THE THERMAL CHARACTERISTICS OF THE ELECTROSLAG REMELTING PROCESS

BY

SATISH V. JOSHI

B.Tech.(Hons), Indian Institute of Technology, Bombay, 1967

A THESIS SUBMITTED IN PARTIAL FULFILMENT OF

THE REQUIREMENTS FOR THE DEGREE OF

DOCTOR OF PHILOSOPHY

in the Department

of

METALLURGY

We accept this thesis as conforming to the

required standard

THE UNIVERSITY OF BRITISH COLUMBIA

July, 1971

In presenting this thesis in partial fulfilment of the requirements for an advanced degree at the University of British Columbia, I agree that the Library shall make it freely available for reference and study. I further agree that permission for extensive copying of this thesis for scholarly purposes may be granted by the Head of my Department or by his representatives. It is understood that copying or publication of this thesis for financial gain shall not be allowed without my written permission.

Department of Metallurgy

The University of British Columbia
Vancouver 8, Canada

Date Aug 17th, 1971

ABSTRACT

The thermal characteristics of the electroslag remelting process have been investigated on a laboratory scale unit.

The heat generation and distribution in the slag bed is discussed. The voltage gradients in the slag bed are predicted using a resistance network analogue and tested against experimental results.

A self-consistent model for electrode temperature gradients in the electroslag remelting process has been tested against experimental results.

An unsteady-state method has been used to determine the electrical resistance and the overall heat transfer coefficient of the interface region, liquid slag/slag skin/copper wall in the electroslag furnace.

An accurate heat balance of the process is carried out on laboratory scale ingots. Attention has been devoted to the influence of various melt parameters i.e. polarity, power input, geometry, atmosphere etc. on the melt rate. The power requirements and the melt rate for industrial ingots are predicted and compared with the data collected from the literature.

The liquid metal pool volumes in ESR ingots are predicted from the operational data. The pool profiles are computed using a finite difference technique and compared with the experimentally obtained profiles.

TABLE OF CONTENTS

Page

Page

Page

Page

Page

LIST OF FIGURES

LIST OF TABLES

LIST OF SYMBOLS

CHAPTER II

A : cross sectional area, cm^2

c : conductivity, $ohm^{-1}cm^{-1}$ $\left(= \frac{1}{r} = \frac{1}{\text{resistivity}} \right)$

e : potential, volts

ℓ : length, cm

r : radial coordinate

R : $\frac{\ell}{A\,c} = \frac{r\ell}{A}$ = resistance, ohms

t_+, t_- : transference numbers, dimensionless

Z : vertical coordinate

CHAPTER III

a : radius of the electrode, cm

A : area, cm^2

C_n : constants

D : $\frac{\sigma \epsilon_1 a\, T_o^3}{K}$, radiation-conduction parameter, dimensionless

F : configuration factor, dimensionless

E : $\frac{\epsilon_2\, T_{slag}^4}{T_o^4}$, dimensionless

h_c : heat transfer coefficient, cal $cm^{-2}sec^{-1}{}^\circ K^{-1}$

K : thermal conductivity of the electrode, cal $cm^{-1}sec^{-1}{}^\circ K^{-1}$

ℓ : length of the electrode, cm

L : $\frac{\ell}{a}$, dimensionless electrode length

N : $\frac{h\,a}{K}$, convection parameter, dimensionless

r,ϕ,z: cylindrical polar coordinates

r,z : length along r,z directions, cm

R,Z : $\frac{r}{a}$, $\frac{z}{a}$, dimensionless

r_2 : mold radius, cm

T : temperature at any point in the electrode, °K

T_o : electrode surface temperature at the slag/gas interface, °K

T_∞ : average temperature of argon, °K

T^* : average temperature of the inside surface of the copper mold, °K

α : coefficient of absorptivity, dimensionless

ε : coefficient of emissivity, dimensionless

σ : Stefan-Boltzmann constant, cal $sec^{-1}cm^{-2}{}^\circ K^{-4}$

β : $\frac{r_2}{a}$, dimensionless

λ : $\frac{T - T_o}{T_o}$, dimensionless temperature at any point in the electrode

λ_∞ : $\frac{T_\infty}{T_o}$, dimensionless average temperature of argon

λ^* : $\frac{T^*}{T_o}$, dimensionless average temperature of inside surface of the copper mold.

Subscripts

1 : electrode surface

2 : slag surface at slag/gas interface

3 : mold surface

∞ : argon bulk

Superscripts

* : effective radiation environment (water cooled copper mold)

CHAPTER IV

A : heat transfer area, cm^2

c : conductivity ($= \frac{1}{\text{resistivity}}$), $ohm^{-1}cm^{-1}$

C_p : specific heat of the copper cylinder, cal $g^{-1}{}^{\circ}C^{-1}$

h_{int} : heat transfer coefficient of the discontinuous interface between the slag skin and the inner face of the mold wall, cal $cm^{-2}sec^{-1}{}^{\circ}C^{-1}$

h_{slag}: heat transfer coefficient, describing the transfer of heat from the bulk slag to the slag skin, cal $cm^{-2}sec^{-1}{}^{\circ}C^{-1}$

k_{slag}: average thermal conductivity of the slag skin, cal $cm^{-1}sec^{-1}{}^{\circ}C^{-1}$

K_{cu} : thermal conductivity of copper, cal $cm^{-1}sec^{-1}{}^{\circ}C^{-1}$

ℓ : characteristic axial length, cm

L : significant dimension of the copper cylinder = $\frac{\text{volume}}{\text{surface area}}$, cm

m : mass of the copper cylinder, g

q : heat transferred per second, cal sec^{-1}

$r_{1,2,3}$: radial dimensions of the copper mold slag-skin system as shown in Fig. (39), cm

R : resistance, ohm

t : time, sec

$T_{C,D,E}$: temperatures at locations as shown in Fig. (40), °C

T_{Cu}: temperature of the inner surface of the copper mold wall, °C

T_o : copper cylinder temperature at t = 0, °C

T_{slag}: bulk slag temperature, °C

T_t : copper cylinder temperature at t = t, °C

U : overall heat transfer coefficient, cal $cm^{-2}sec^{-1}{}^{\circ}C^{-1}$

CHAPTER V

A : area, cm^2

c : conductivity, $ohm^{-1}cm^{-1}$

c_p : specific heat, cal $g^{-1}{}^{\circ}C^{-1}$

d : electrode diameter, cm

D : ingot diameter, cm

D_1, D_2 : dimensions of the annulus, cm

D_b : average bubble diameter, cm

D_H : hydraulic diameter, cm

G : mass velocity of fluid flowing through the annulus, g $cm^{-2}sec^{-1}$

G_b : mass velocity of the bubbles per unit area, g $cm^{-2}sec^{-1}$

h : heat transfer coefficient, cal $cm^{-2}sec^{-1}{}^{\circ}C^{-1}$

h_{nb} : heat transfer coefficient for non-boiling region, cal $cm^{-2}sec^{-1}{}^{\circ}C^{-1}$

h_{sb} : heat transfer coefficient for the surface boiling region, cal $cm^{-2}sec^{-1}{}^{\circ}C^{-1}$

I : current, amperes

k : thermal conductivity, cal $cm^{-1}sec^{-1}{}^{\circ}C^{-1}$

ℓ : length, cm

L : latent heat, cal g^{-1}

m : mass, g

MR : melt rate, g sec^{-1}

Nu : Nusselt number, dimensionless

P : power, Kcal sec^{-1}

Pr : Prandtl number, dimensionless

q : heat transferred per unit time, cal sec^{-1}

q_A, q_B, q_C: total heat transferred across the regions shown in Fig. (49), Kcal sec^{-1}

$Q_{1\to8}$: as defined in Fig. (64), cal sec^{-1}

r : resistivity, ohm cm

R : $\frac{r\,\ell}{A}$, resistance, ohms

Re: Reynolds number, dimensionless

St: Stanton number, dimensionless

T : temperature, °C

V : voltage, volts

W : water rate through the annulus, g sec^{-1}

Z : $\frac{V\,I\,d^2}{D^2(\frac{\ell}{D})\,MR}$, Kcal g^{-1}

ρ : density, g cm^{-3}

μ : viscosity, poise

ΔT : temperature difference, °C

CHAPTER VI

A : area, cm^2

C_p: specific heat, cal $g^{-1}{}^\circ K^{-1}$

h : heat transfer coefficient, cal $cm^{-2}sec^{-1}{}^\circ K$

h_{bottom}: heat transfer coefficient for the bottom surface, cal $cm^{-2}sec^{-1}{}^\circ K^{-1}$

h_{side}: heat transfer coefficient for the flow of heat from the mold wall to the mold cooling water, cal $cm^{-2}sec^{-1}{}^\circ K^{-1}$

h_{top}: heat transfer coefficient for the top surface, cal $cm^{-2}sec^{-1}{}^\circ K^{-1}$

k : thermal conductivity, cal $cm^{-1}sec^{-1}{}^\circ K^{-1}$

k_{eff} : effective thermal conductivity, cal $cm^{-1} sec^{-1} {}^{\circ}K^{-1}$

ℓ : length, cm

L : length of the mold, cm

L_H : latent heat, cal g^{-1}

MR : $\frac{C_p \rho \Delta r^2}{K \Delta T}$, dimensionless

MZ : $\frac{C_p \rho \Delta z^2}{K \Delta T}$, dimensionless

q : heat transferred per unit time, cal sec^{-1}

r, ϕ, z : cylindrical polar coordinates

T : temperature, °K

t : time, sec

α : $\frac{k}{\rho C_p}$, thermal diffusivity, $cm^2 sec^{-1}$

ρ : density, g cm^{-3}

Δr : length of the element along the r axis, cm

Δt : time element, sec

ΔT : temperature difference, °K

Δz : length of the element along the z axis, cm

APPENDIX I

d : diameter of the suspension wire, cm

E : $1 + 3 \{\frac{L_t - L_o}{L_o}\}$, dimensionless

g : acceleration due to gravity, cm sec^{-2}

K_1 : constant

L : length of the inner cylinder immersed in the slag, cm

L_o : length of the cylinder at room temperature, cm

L_t : length of the cylinder at t °C, cm

r_1 : radius of the inner cylinder, cm

r_2 : radius of the outer cylinder, cm

T : temperature, °C

T_r : torque, dynes cm

t : time of rotation, sec

V_o : volume of the bob at room temperature, cm^3

W : weight of the bob, g

ρ : density, g cm^{-3}

γ : surface tension, dynes cm^{-1}

α : coefficient of linear expansion, $°C^{-1}$

η : coefficient of viscosity, poise

ω : $\frac{2\pi}{t}$, angular velocity of the outer cylinder, sec^{-1}

Subscripts

a : air

m : melt

w : water

ACKNOWLEDGEMENTS

The author would like to express his gratitude to his research advisor, Dr. A. Mitchell, for his keen interest and valuable advice during the course of this research project.

Thanks are also due to Dr. J. Cameron and my fellow graduate students of the ESR group, for technical help and innumerable helpful discussions.

The assistance of the departmental technical staff, in particular Mr. A. Thomas, throughout the experimental programme is greatly appreciated.

The financial assistance by the National Research Council of Canada and the American Iron and Steel Institute is gratefully acknowledged.

CHAPTER I

INTRODUCTION

I.1 The Electroslag process

The electroslag remelting process (ESR) has in the past decade received increasing industrial attention.[1,2,3] The demand for superior quality, high performance special alloys has been steadily rising. The chief competitors of the electroslag process are the vacuum arc remelting (VAR) and to a lesser degree, the electron-beam melting and the vacuum induction melting processes.

The struggle to improve the quality of alloy steels and other high melting special alloys and reactive metals is aimed at

(1) reducing the inclusion content

(2) reducing the gas content

(3) reducing the segregation

(4) retaining the reactive elements present.

This is achieved using two methods of approach[4]:

(1) increasing the purity of the liquid metal.

(2) improving the structure of the ingot.

Two groups of methods have found use in the metallurgical industry for increasing the quality of the metal in the fused state:

(1) processing the metal under vacuum,

(2) treatment of the metal with special slags outside the furnace.

The vacuum processing is carried out either during the smelting or outside the furnace. Although this treatment removes substantial amounts of O, N, H and other impurities present, most of these methods have some serious shortcomings. In vacuum induction melting, the contamination from the refractory lining as well as the evaporation of Mn, Si and other elements of high vapor pressure occurs frequently.

The out-of-furnace treatment of the metal with various oxidizing slags of the system CaF_2-CaO-Al_2O_3, on the other hand, is quite effective in reducing the sulfur, phosphorus and the non-metallic inclusion content of the metal.

However, these methods do not provide the possibility of any significant improvement of the ingot structure which is essential for the production of high quality metal.

Various methods are suggested for improving the structure of the ingot. These involve the heating of the ingot top, teeming, rational construction of the casting mold etc. To improve the ingot structure, directional solidification is generally attempted.

The cold-crucible processes i.e. the vacuum arc remelting, electro-slag and the electron beam remelting, combine both the objectives of increasing the general purity of the metal and improving the structure of the ingot and as such have found increasing industrial applications.

The electron-beam melting process uses a concentrated flux of electrons as the source of heat. The presence of high vacuum together with the unidirectional solidification of the liquid metal in a

water-cooled copper mold guarantees an effective purification of the metal from the gases and the non-metallic inclusions. Although possessing the potential for large scale industrial usage, at the present, this process is used only for refining some very high melting metals and alloys. This is due to the complexity of the equipment and the high capital and operating costs.

In the electroslag remelting process (ESR), a metal electrode is melted in a molten superheated slag pool. The slag is rendered molten by resistance heating. High current at low voltages is delivered to the slag through the electrode and the refined molten metal is immediately solidified in a water cooled copper mold (Fig. 1).

The vacuum arc remelting (VAR) process consists of melting a consumable electrode in vacuum or in an atmosphere of inert gas, by means of a high current electric arc maintained between the lower end of the electrode and a pool of molten metal contained in a water cooled copper mold.

Except for the fact that a consumable electrode is remelted and that the metal is solidified in a water cooled metal mold, the electroslag process is distinctly different from the vacuum arc remelting process.

The main advantages of the ESR process over the VAR may be summarized as follows:

(1) good surface quality of the ingot, readily useable for forging

(2) a certain degree of refining (mainly of sulfur) is possible

(3) possible to use either a.c. or d.c. power

(4) lower capital cost

(5) safer in operation than VAR

(6) can tolerate relatively complicated mold shapes.

While it is usually accepted that the electroslag remelting complements VAR by its ability to change the ingot chemistry as well as its structure, the cost factor does not allow one to make a clear choice for industrial operation.[5] The lower capital cost and the slightly higher production rate of the ESR equipment is offset by the higher specific power required and the cost of the slag itself.

The typical power consumption for ESR process is 1200 to 2000 KWH per ton of the metal while for VAR, it is slightly less.[5,6]

ESR ingots have already exceeded the maximum size of VAR ingots, as a producer reports having produced ingots of 23 tons.[7]

Except for Russia, which does not have many VAR installations, in the rest of the world, the ESR process today is, at the best, a complementary process to VAR, for refining high quality alloys. This is mainly due to the installation of large VAR furnaces in the alloy steel industry in the early sixties, prior to the advent of the ESR process.

I.2 Statement of the Problem

The electroslag remelting process is suitable as a modern secondary refining process largely because of its versatility. This is due to the large number of available combinations of slag chemistry, the more flexible power requirements and the greater freedom of choice of electrode characteristics.

Despite rapid advances in the design and application of the

electroslag equipment, much work of a fundamental nature is required before the physical and chemical processes inherent to the electroslag system are understood.

The purpose of the present work is to study the thermal characteristics of the electroslag process. It is necessary to understand the mode of heat generation and distribution in the ESR process to achieve effective control during its operation.

It is convenient to divide the study into six sections.

(1) Heat generation in the slag bath: The slag bath is the most important part of the process. It is the resistive and the refining element. It is therefore necessary to examine the form of heat generation in the slag bath.

(2) Temperature gradients on the electrode: It is necessary to know the temperature gradients on the electrode as it controls the extent of electrode oxidation, structure of the ingot, as well as the degree of thermal instability during electrode changes in large industrial units.

(3) Thermal and electrical characteristics of the slag skin region: As a significant portion of the heat leaves the system across the liquid slag region, the study of heat transfer in the system slag/slag skin/mold is vital to the understanding of the ESR operation. The study of the electrical characteristics of this region is necessary to correlate the observed relative stabilities of the different electrical configurations.

(4) Heat balance of the process: Clites and Beall[8] studied the heat transfer to the water-cooled copper mold during vacuum arc remelting

of zirconium and titanium. No such study is reported on the ESR process. It is essential to carry out an accurate heat balance of the process to understand the mode of heat distribution. This should enable the prediction and correlation of the various operating parameters of the process for industrial scale ingots.

(5) Prediction of pool volumes in ESR ingots: For an effective control, it is necessary to be able to predict the pool volumes in the ESR ingots. The pool volume and its shape, control the surface quality and the structure of the ingot.

(6) Measurement of the physical properties of the slag: The slag serves many purposes, not all of them being compatible. The slag should have the appropriate melting point, vapor pressure, electrical resistivity, viscosity, density, surface tension and thermal capacity or a best possible combination of these properties. Attempt is made here to measure (1) the density and (2) the viscosity of the CaF_2 based slags.

I.3 The U.B.C. Electroslag Unit

For the purpose of investigating the influence of various parameters on the thermal characteristics of the process, experiments have been carried out with the U.B.C. electroslag unit. The design of this unit is specifically adapted to the requirements of a range of research projects and has been described in detail by Etienne.[9] Electroslag remelting is one of the few metallurgical processes which can be scaled down without loosing its intrinsic properties. Thus it is possible to predict the operation characteristics of large industrical scale units by correlating the data obtained on the small laboratory unit.

I.4 Choice of Materials

An important problem has been the selection of suitable alloy and slag compositions for the present study.

Alloy compositions: Vibrac EN 25, 321 stainless steel, Ferrovac E, Armco iron, AISI 1018 steel and AISI 630 steel have been used in the present investigations. Table I gives the composition of the alloys studied.

Table I. Composition of alloys studied

(1) Vibrac EN 25 (supplied by British Steel Corporation)

Fe	C	Mn	Si	S	P	Ni	Cr
Bal	0.28	0.67	0.22	0.058	0.012	2.5	0.72

Mo	Sn	Cu	Al
0.6	0.028	0.27	0.01

(2) Austenitic Stainless Steel: 321 grade. Air melted (supplied by Atlas Steels Company, Welland, Ontario).

Fe	Cr	Ni	Ti	Si	Mn	C	P
Bal	17.78	10.60	0.58	0.56	1.86	0.05	0.031

S	O
0.018	0.0009

(3) Ferrovac E: vacuum melted (supplied by Crucible Steel Company, Sorel, Quebec)

Fe	C	Mn	P	S	Si	Ni	Cr
Bal	0.01	0.001	0.002	0.004	0.006	0.01	<0.01

Mo	N	O	H	Co	Cu	V	W
0.001	0.0002	0.00092	0.000018	0.006	0.006	<0.002	0.02

(4) 1018 Steel: (supplied by Atlas Steel Company)

Fe	C	Mn	P_{max}	S_{max}
Bal	0.15-0.20	0.6-0.9	0.04	0.05

(5) AISI 630 (supplied by Armco)

Fe	C	Mn	Si	P	S	Cr	Ni
Bal	0.07	1.0	1.0	0.025	0.025	16.5	4.0

Co + Ta	Cu	Mo
0.3	4.00	0.5

(6) Armco Iron (supplied by Armco)

Fe	C	Mn	P	S	Si	O
Bal	0.012	0.017	0.005	0.025	trace	0.065

Slags: Calcium fluoride is the basic constituent. Part of this material (flotation concentrate) is used as a dry powder to make up for the required proportion of powder and granules.

Most of the calcium fluoride used is prefused in a graphite crucible. Induction heating and argon blanket are used. The main impurities of CaF_2 are calcium oxide, silica and iron oxide. For the measurement of density and viscosity of CaF_2 base slags, extra pure CaF_2 (British Drug House) was used.

Alumina is used either as powder (Alcan, 99.9% purity) or granules of electrofused alumina (Norton Co.) of equivalent purity.

Calcium oxide is prepared from calcium carbonate (technical grade).

Calcium titanate is commercially available as powder (Cerac Corp.) normally used for spray coating. It is cold pressed and sintered before use.

CHAPTER II

DETERMINATION OF VOLTAGE GRADIENTS IN THE SLAG BED OF THE ESR PROCESS

II.1 Mechanism of Heat Generation

Descriptions[4,10,11] of the electroslag remelting process have attributed the heat generation mechanism variously to 'soft' arcs and to resistive heating, but are not specific as to how the resistance is constituted.

In order to understand the mechanism of heat generation in ESR, it is logical to compare ESR and vacuum arc remelting (VAR) processes since they are apparently similar, in both their metallurgical aims and operations. The major difference between the two processes is the method by which the heat is generated.

In the high intensity arc present in VAR, there are three points of heat generation

(1) cathode fall

(2) anode fall

(3) the transfer resistance of the plasma

The heat generation mechanism in an arc is a mixture of joule heating, due to the transfer resistance of the plasma, and the particle emission and bombardment which gives rise to the observed steep voltage gradients in the terminal regions, called the anode and cathode

fall (Fig. (2)).

It is interesting to consider what effects, if any, will result from the interposition of a liquid slag between the two electrodes which are at a potential difference high enough to cause a sustained arc in the absence of the slag. Whether or not the arc will be extinguished depends upon the relation between the electrical transport effects and the heating effects in the slag. If the heat generated by the various resistances involved is great enough to boil the slag, then the ionizable vapor will provide a very stable arc path. If, on the other hand, the heat can be dissipated at a temperature well below the boiling point, electrical transport is by ionic movement in the slag.

Mitchell and Beynon[12] have shown that a current density of the order of 10^4-10^5 Amp. cm^{-2} is necessary for the sustained existence of an arc in the electroslag process. Mironov et al.[13] have also reported similar findings in their study of the characteristics of the ESR process. As the maximum current density rarely exceeds 150 Amp. cm^{-2} in laboratory scale units (much lower for industrial scale units), one can conclude that the bulk of the heat is generated in the slag bed by the frictional dissipation in ionic movement. Joule heating is generated by the opposing flux of cations and anions. There is every reason[14-17] to suppose that the slags used are entirely ionic with $t_+ \simeq t_- \simeq 0.5$ and that the current is carried by ionic diffusion in the impressed potential gradient. There should be no asymmetry of heat generation in the slag beyond that accounted for by the geometry of the system. This provision

would include skin effects at a large enough crucible size, but it is calculated that the 60 Hz skin depth in liquid calcium fluoride is approximately 40 cm, and thus a crucible diameter larger than 100 cm would be required before the heat generation showed significant radial asymmetry.

As the electrode and the ingot do not constitute a symmetrical arrangement in the slag bath, it is necessary to examine the form of resistive heat generation in the slag bulk. In order to be able to do so, it is first necessary to calculate the isopotential contours in the slag bed. This may be modelled for an axially symmetrical system by the use of a resistance network analogue which will accommodate the temperature dependent resistivity of the slag. As the temperature distribution in the slag bed was unknown, it was first experimentally determined for various electrical configurations.

II.2 Measurement of Temperature in the Slag Bed

The problem of temperature measurement in an operating ESR unit has been studied in several contexts.[18,19] There exists substantial experimental difficulty in measuring millivolt thermocouple potentials in a system containing intense magnetic fields, at a high temperature in a corrosive slag and at a.c. or d.c. potentials significantly above ground. If a bare thermocouple is immersed in the slag (which rapidly dissolves even cermet refractories) it will transiently record the surface temperature before being destroyed by the metallic content of the slag.[20] Since the slag is at a potential above ground, the temperature measuring instruments must be floating and have adequate

common mode rejection. Trials established that boron nitride is an excellent material for thermocouple protection tubes in this context as it is compatible with the W-3Re/W-25Re thermocouple used, is an electrical insulator at the temperatures experienced, and will resist attack by the ESR slag for a considerable time. Measurements of the slag temperature were made with the above combination attached to the electrode surface and reading out to a Sargent Model SR4 recorder. Fig. (3) and Fig. (4) give a schematic diagram of the experimental assembly. Temperature measurement was carried out in both argon atmosphere and air for various electrical configurations using CaF_2-25 wt. % Al_2O_3 slag. In all the cases, 3.81 cm (1.5 inches) diameter EN 25 steel electrode was melted in 8 cm x 45 cm mold. Fig. (5) to Fig. (10) give the observed temperature gradients in the slag bed for the one vertical section investigated.

II.3 Determination of Isopotential Contours in the Molten Slag Bed

II.3.1 Introduction

The isopotential lines are determined here for an experimentally obtained geometrical configuration (I.N. 1, Table V). The extent of electrode immersion and the depth of the slag bed are as shown in Fig. (11).

The resistivity of the slag depends upon the temperature. Appendix I (Fig. (86)) gives the variation of electrical conductivity with temperature for CaF_2-25 wt. % Al_2O_3 slag as obtained by Mitchell and Cameron.[21]

In order to calculate the isopotential contours in the slag bed,

it is necessary to assume a temperature distribution in the slag bed. Fig. (11) gives the assumed temperature distribution based on the experimentally obtained data.

Assuming radial symmetry, it is sufficient to consider the voltage distribution in a segment of the cylindrical slag bath. For convenience, a segment of one radian is chosen. It is subdivided into volume elements as shown in Fig. (12). The vertical height of the volume elements is 0.5 cm while along the radius it is 1.0 cm. The volume of the elements increases away from the centre.

II.3.2 Solution by Electric-Resistance Network.[22]

The effect of each volume element is considered to be concentrated at the central point. In accordance with the electrical resistance concept, the resistance of the volume of the slag may be set up approximately as shown in Fig. (13).

Here, the resistances R_r and R_z represent the resistances in the r and z directions respectively. The composite resistance effect is likewise shown, with separate half elements $\frac{R_r}{2}$ and $\frac{R_z}{2}$ representing r and z directions respectively and totalling R_r and R_z for the entire volume element.

Consider Fig. (12). In d.c. negative (I.N.1), the surface AB is at 23.75 volts while the surface CD is at 0 volts. The resistance at the surface EF (slag/gas interface) is assumed to be infinite. Due to the assumed radial symmetry, surface BC has infinite resistance. In the ESR unit, there is always a solid slag skin against the water cooled mold. As solid slag skin has very high electrical resistance,

it is not unreasonable to assume that there is infinite resistance at the surface A'F'. The effect of finite slag skin resistance on the potential contours will be considered later.

As the solid electrode exists in the slag bed which is at a temperature higher than the melting point of the metal, there exists on the surface ED a very thin layer of solid slag skin. The electrical resistivity of this skin is not known. Initially it will be assumed that this slag skin has zero resistance. The effect of finite resistance of this thin slag skin will be subsequently treated.

Fig. (14) gives the equivalent resistance network for the case where it is assumed that the resistance at A'F' = ∞ and at ED = 0 ohms. It is necessary to calculate the area 'A' and length 'ℓ' for the various volume elements under study ($R = \frac{\ell}{A.c.}$), Appendix II gives the method of calculating the 'ℓ' and 'A' for all the volume elements under consideration.

The numerical solution of the resistance network of Fig. (14), without recourse to the experimental electrical determination is of specific interest, particularly in view of the many network branches involved.

At any junction point, under steady state electrical flow conditions, the sum of the currents flowing 'in' must be zero i.e., there is no accumulation. Accordingly, considering Fig. (15), the point 0 is surrounded by points M, N, P and Q. The resistance of the four corresponding branches is R_m, R_n, R_p, R_q respectively.

The currents in the four different branches, dependent on the difference in potential 'e' between the outlying point and the center

junction are next considered.

The following relationships may be set up

$$\frac{e_M - e_O}{R_m} + \frac{e_N - e_O}{R_n} + \frac{e_P - e_O}{R_p} + \frac{e_Q - e_O}{R_q} = 0 \qquad (2.1)$$

Thus, to satisfy the steady state conditions,

$$e_O = \frac{(\frac{1}{R_m})e_M + (\frac{1}{R_n})e_N + (\frac{1}{R_p})e_P + (\frac{1}{R_q})e_Q}{(\frac{1}{R_m}) + (\frac{1}{R_n}) + (\frac{1}{R_p}) + (\frac{1}{R_q})} \qquad (2.2)$$

In the present case, it is assumed that a voltage of 23.75 volts is impressed between the electrode (0 volts) and the molten metal bath (23.75 volts).

Equations similar to (2.2) can be written for all the 29 junction points. This leads to 29 linear simultaneous equations in 29 unknowns. These can be easily solved with the aid of the computer. Fig. (16) gives the voltage distribution obtained.

II.3.3 Discussion

Fig. (16) illustrates the manner by which the slag volume, the geometry, applied voltage and resistivity combine to determine the voltage gradients and hence the heat input in the slag bath.

The region of steep voltage gradient lies below the electrode tip and most of the heat generation takes place below this level. The slag above the electrode tip, due to low voltage gradients, does not

get heated to the same extent and performs a coolant function in the system.

The curvature in the current lines is largely above the electrode tip, and there is negligible horizontal current vector near the ingot surface. This comment, of course, neglects the a.c. skin effect which would lead to intense curvature in this latter region in a larger ESR unit. The significance of such a current pattern lies in the form of stirring pattern which might be established by a configuration of electromechanical forces imposed on the ESR melt.

In the present analysis it was assumed that the slag skin on the mold has infinite electrical resistance. Fig. (17) shows the effect of considering a finite slag skin resistance ($r \approx 200$-300 ohm. cm). It is clear from Fig. (17) that this consideration does not significantly distort the voltage gradients. Fig. (18) and Fig. (19) consider the effect of finite resistance of the slag skin on immersed electrode. It is clear that except for an unreasonably high value of skin resistance, the effect of finite slag skin resistance on electrode is not significant. It will be shown in Chapter IV that at a high electrode temperature ($> 1000°C$), the slag skin has a relatively low effective resistance due to good contact with the electrode. Hence Fig. (16) is adequate in describing the voltage profiles in the ESR slag bed.

In the present model, the applied voltage was deliberately equated to the potential seen by the slag bulk at the electrode-slag interfaces. However, by doing so, the electrochemical polarization present in ESR was neglected.

II.4 Electrochemical Polarization in ESR

With the exception of the situation where the slag has a substantial electron mobility, ions must be discharged at the electrode and ingot surfaces if the current passes through the system. The passage of current requires both the anodic and cathodic interfacial potentials to be displaced from their equilibrium values, giving rise to over-potentials on both the surfaces.

The anodic process in the d.c. electroslag melting of pure iron has been postulated by Mitchell and Beynon[12] to be the corrosion of iron, giving an interface layer of saturation of Fe^{++}. The cathodic process is postulated to be the deposition of Al or Ca which may subsequently dissolve in either the metal or the slag phases. Fig. (20) and Fig. (21) give the experimentally obtained polarization curves for pure iron.[12] In a.c. electroslag melting, it was found that there is no polarization with $Fe \rightleftharpoons Fe^{++} + 2e$ reaction occurring at both the electrodes.

Fig. (20 and (21) show that the maximum overpotential is approximately 1.0 volt. This will not alter the isopotential lines significantly. However, the heat generation in the metal-slag interfacial region as a result of current passing through this overpotential is very important. This will be considered in detail in Chapter V.

II.5 The Effect of Ca and Al Dissolved in the Slag

The resistivity values used in the analysis are applicable only to a.c. electroslag refining. As discussed earlier, the cathodic reaction product in d.c. operation is Ca and Al. Both these elements are

soluble in the CaF_2 based slags. Addition of these elements significantly increases the electrical conductivity of CaF_2 based slags. Its effect on ESR operation will be discussed in detail in Chapter V. The voltage gradients will remain unaltered if the temperature dependence of the effective resistivity of the slag in d.c. operation is proportionately the same as the slag in a.c. operation. Although the effective resistivity in d.c. operation will be less sensitive to temperature, as the temperature dependence is unknown, it has been assumed here to be proportionately similar to the a.c. operation slag.

II.6 Measurement of Voltage Gradients in the Slag Bed

The predicted voltage gradients were experimentally varified using a voltage probe. Voltage was measured in CaF_2-25 wt. % Al_2O_3 slag (3.81 cm diameter EN 25 steel electrode in 8.0 cm diameter copper mold) between the electrode and a boron nitride insulated molybdenum wire probe. The probe was lowered vertically down into the slag bath at constant speed by a motor and the voltage recorded on a Sargent Model SR 4 recorder. Fig. (22) gives the experimentally obtained voltage gradient across a vertical section and compares it with the predicted gradient. The agreement appears to be reasonably good. Thus, in spite of the many simplifying assumptions made, fig. (16) gives a fair estimate of the voltage gradients in an operating ESR slag bath.

CHAPTER III

ELECTRODE TEMPERATURE GRADIENTS IN THE ELECTROSLAG PROCESS

III.1 Introduction

In the electroslag remelting process, the amount of heat flowing out through the electrode plays a significant part in the process for a number of reasons. Firstly, it is a direct contribution to the heat balance in the melting electrode tip region and therefore to the process operating temperature. It also determines the electrode temperature above the slag/gas interface and thus the amount of possible electrode oxidation in cases where inert atmosphere is not used and the degree of thermal instability during electrode changes in large industrial units. Finally, the time the electrode material spends whilst travelling through the electrode temperature gradient determines the extent to which second phase particles will be dissolved before the matrix melts. This latter effect has not been investigated in either the vacuum arc remelting (VAR) or ESR context, but is likely to have at least three significant metallurgical consequences described as follows. The second phase may be oxide inclusions, such as silica, which should dissolve progressively in a steel as the temperature increases.

Thus the silica inclusion distribution present in the melting electrode tip will be closer to that in the bulk electrode than would be predicted by an equilibrium analysis of the heating process. The way in which this may affect ingot inclusion content has been briefly outlined.[23] Alternately, if the second phase is a more soluble material, such as a carbide (TiC in a stainless steel, for example), then the major effect of retaining this through the liquid period in both VAR and ESR (due to a low solution rate compared to the liquid metal residence time) will be that any electrode carbide particles persisting to the ingot stage will act as nuclei for subsequent carbide growth. Thus the structure of the ingot produced would depend upon the carbide distribution in the electrode. In the case where the second phase has a lower melting point than the matrix (as for example, an eutectic carbide) then the point at which this melts relative to the tip of the electrode will largely determine whether or not large pieces of electrode become physically detached and fall to the ingot solidifying-front without melting. This latter defect is well known in the ESR processing high-speed steels.

The problem of the electrode temperature gradient in ESR may be divided conveniently into two sections, relating to the heat transfer regimes above and below the slag/gas interface. The present study relates to the gradients above the slag/gas interface and compares the experimental results obtained, with the theoretical computation of this gradient for AISI 1018 steel and 321 stainless steel electrodes.

III.2 Experimental

III.2.1 Temperature Measurement

A schematic diagram for the arrangement used is shown in Fig. (23). Measurements of the slag temperature were made with the W3Re/W25Re thermocouple protected by boron-nitride. The thermocouple was attached to the electrode surface as shown in fig. (23) and read out to a Sargent Model SR 4 recorder. Measurements of the temperature gradient in the electrode were made using chromel-alumel thermocouples placed in wells drilled in the electrode in axial sets of four at known intervals. The thermocouple measuring the slag temperature was placed one centimeter ahead of the leading electrode thermocouple, and provided an accurate "marker" of the slag/gas interface relative to electrode position. The electrode thermocouple readout was on a Texas Instruments Model FMW6B multi-channel recorder.

II.2.2 ESR Operating Conditions

Two sets of ingot and electrode sizes were used:

2.54 cm (1") diameter electrode, 5.85 cm x 40 cm mold

3.81 cm (1.5") diameter electrode, 8.0 cm x 45 cm mold

with two materials, AISI 1018 steel and 321 stainless steel. The experimental ESR unit has been earlier described[9] and was operated with either electrode positive or negative, with the negative pole at ground potential. The electrode current densities used were approximately 100 $A.cm^{-2}$ for 2.54 cm diameter electrodes and 75 $A.cm^{-2}$ for 3.81 cm diameter electrodes. The slag used in each case was CaF_2-30 wt. % calcium aluminate, and in a quantity to give a 4 cm deep slag bath. The electrode

position was measured by a remote incremental counter to a precision of $\pm$ 5 x 10^{-2} cm. In all cases, the electrode feed rate was held constant during the measurement period, but as the operation had previously stabilized for some time using a constant-current control mechanism, this override condition did not result in significant departure in current density.

The electrode temperature profiles are shown in Fig. (24) to (29). These are obtained by a non-linear (cubic) regression analysis of the sequential-readings record from the multi-channel recorder.

The slag temperature varied between 1775°K $\pm$ 20°K at the surface, and a maximum of 1975°K $\pm$ 50°K, at a point several millimeters below the electrode tip.

III.3 Discussion

III.3.1 Formulation of the Problem

The general formulation of the problem in the present case is similar to that of a cylindrical fin dissipating heat from its surface by convection and radiation with no heat transfer through the end of the fin.[24] However, there are more complex boundary conditions in the present case than are encountered in the usual formulation. The electrode is immersed in the slag as shown in Fig. (30). The temperature gradient at B is assumed to exist across the thin (2 x 10^{-2} cm) layer of solid slag skin, similar to that found between the slag and the water cooled mold wall. The boundary temperature T_o at z = 0 is known from the experimental measurements and is specific to the melting conditions used. It is also assumed that:

(1) the slag surface temperature is uniform over all the effective radiant area; black body conditions are assumed

(2) the system has complete radial symmetry

(3) the physical and surface properties of the electrode are temperature invariant

(4) no heat transfer occurs from the cold end of the electrode

(5) the electrode has radiation interaction with the slag, but multiple interactions are absent

(6) steady state conditions

(7) water cooled copper mold and the gas atmosphere are at known constant temperatures

(8) two dimensional heat transfer

One may then write the energy equation as:

$$\frac{\partial^2 T}{\partial r^2} + \frac{1}{r}\left(\frac{\partial T}{\partial r}\right) + \frac{\partial^2 T}{\partial z^2} = 0 \qquad (3.1)$$

which has boundary conditions

$$\text{at } z = 0, \quad T = T_o \qquad (3.2)$$

$$\text{at } z = \ell, \quad \frac{\partial T}{\partial z} = 0 \qquad (3.3)$$

$$\text{at } r = 0, \quad \frac{\partial T}{\partial r} = 0 \qquad (3.4)$$

and a fourth condition at r = a. This condition involves an energy balance over an element of electrode surface area dA_1, discussed below.

A heat balance through dA_1 involves three heat transfer terms through the electrode surface, and the electrode volume conduction term.

Firstly, the electrode surface element has radiant energy interchange with water cooled copper mold

$$dA_1 F_{dA_1 \rightarrow *} \; \varepsilon_1 \; \sigma \; T^4_{r=a} - \alpha_1 \; \varepsilon_3 \; \sigma \; (T^*)^4 \; A_* F_{* \rightarrow dA_1} \tag{3.5}$$

Also, there is convective interchange with the gas atmosphere within the mold

$$dA_1 \; h \; (T_{r=a} - T_\infty) \tag{3.6}$$

and finally, radiant interchange with liquid slag surface

$$\varepsilon_1 \; \sigma \; dA_1 F_{dA_1 \rightarrow A_2} \; T^4_{r=a} - \varepsilon_2 \; \sigma \; A_2 F_{A_2 \rightarrow dA_1} \; T^4_{slag} \alpha_1 \tag{3.7}$$

(The configuration factor $F_{m \rightarrow n}$ introduced above denotes the fraction of the total energy emitted by surface m that is intercepted by surface n).

Using the reciprocity theorem for configuration factors:

$$A_2 F_{A_2 \rightarrow dA_1} = dA_1 F_{dA_1 \rightarrow A_2} \tag{3.8}$$

$$A_* F_{* \rightarrow dA_1} = dA_1 F_{dA_1 \rightarrow *} \tag{3.9}$$

and the summation theorem

$$F_{dA_1 \rightarrow *} = 1 - F_{dA_1 \rightarrow A_2} \tag{3.10}$$

and assuming grey body properties for the electrode (i.e., $\alpha_1 = \varepsilon_1$) the energy balance equation reduces to

$$-K\, dA_1 \left.\frac{\partial T}{\partial r}\right|_{r=a} = dA_1(1 - F_{dA_1 \to A_2})\, \varepsilon_1\, \sigma\, T^4_{r=a}$$

$$-\varepsilon_1\varepsilon_3\, \sigma\, dA_1 (T^*)^4 (1 - F_{dA_1 \to A_2}) + dA_1\, h\, (T_{r=a} - T_\infty)$$

$$-dA_1 F_{dA_1 \to A_2}\, \varepsilon_2\, \sigma\, T^4_{slag}\, \varepsilon_1 + dA_1 F_{dA_1 \to A_2}\, \varepsilon_1\, \sigma\, T^4_{r=a} \qquad (3.11)$$

where each side gives the amount of heat leaving the surface.

On rearrangement:

$$\left.\frac{\partial T}{\partial r}\right|_{r=a} = -\frac{\varepsilon_1\sigma}{K} T^4_{r=a} + \frac{\varepsilon_1\varepsilon_3\sigma}{K} (T^*)^4 \quad (1 - F_{dA_1 \to A_2})$$

$$-\frac{h}{K}(T_{r=a} - T_\infty) + \frac{\varepsilon_1\varepsilon_2\sigma}{K} T^4_{slag}\, F_{dA_1 \to A_2} \qquad (3.12)$$

Equation (3.12) may be conveniently re-expressed using the following dimensionless terms:

$$\lambda = \frac{T-T_o}{T_o}, \qquad \lambda_\infty = \frac{T_\infty}{T_o}, \qquad \lambda^* = \frac{T^*}{T_o}$$

$$N = \frac{ha}{K}, \qquad D = \frac{\varepsilon_1 a T_o^3 \sigma}{K}, \qquad R = \frac{r}{a}$$

$$L = \frac{\ell}{a}, \qquad Z = \frac{z}{a}$$

In terms of these new variables, eq. (3.1) and the boundary conditions (3.2), (3.3), (3.4) and (3.11) become respectively,

$$\frac{\partial^2 \lambda}{\partial R^2} + \frac{1}{R} \frac{\partial \lambda}{\partial R} + \frac{\partial^2 \lambda}{\partial Z^2} = 0 \tag{3.13}$$

where

$$\lambda \Big|_{Z=0} = 0 \tag{3.14}$$

$$\frac{\partial \lambda}{\partial Z}\Big|_{Z=L} = 0 \tag{3.15}$$

$$\frac{\partial \lambda}{\partial R}\Big|_{R=0} = 0 \tag{3.16}$$

$$\frac{\partial \lambda}{\partial R}\Big|_{R=1} = - D(1 + \lambda_{R=1})^4 + D(\lambda^*)^4 \left(1 - F_{dA_1 \to A_2}\right) \varepsilon_3$$

$$- N(1 + \lambda_{R=1}) + N\lambda_\infty + D\varepsilon_2 \frac{T_{slag}^4}{T_o^4} F_{dA_1 \to A_2} \tag{3.17}$$

Putting $\varepsilon_2 \dfrac{T_{slag}^4}{T_o^4} = E$, equation (3.17) becomes

$$\frac{\partial \lambda}{\partial R}\Big|_{R=1} = -D (1 + \lambda_{R=1})^4 + D\, \varepsilon_3 (\lambda^*)^4 \left(1 - F_{dA_1 \to A_2}\right)$$

$$- N(1 + \lambda_{R=1}) + N\lambda_\infty + DEF_{dA_1 \to A_2} \tag{3.18}$$

Let the solution of eq. (3.13) be of the form

$$\lambda = P(R)\ Q(Z) \tag{3.19}$$

Substituting the value of λ from (3.19) in eq. (3.13) and simplifying yields

$$\frac{1}{P}\ \frac{d^2P}{dR^2} + \frac{1}{PR}\ \frac{dP}{dR} = -\frac{1}{Q}\ \frac{d^2Q}{dZ^2} = m^2 \tag{3.20}$$

Separating the variables, the two resulting equations are

$$\frac{d^2Q}{dZ^2} = -Qm^2 \tag{3.21}$$

$$\frac{d^2P}{dR^2} + \frac{1}{R}\ \frac{dP}{dR} = Pm^2 \tag{3.22}$$

The solution to (3.21) is of the form

$$Q = C_1 \cos mZ + C_2 \sin mZ \tag{3.23}$$

where C_1, C_2 are constants.

Equation (3.22) is of a type reducible to Bessel's equation[25] and its solution is of the form

$$P = C_3\ I_o(mR) + C_4 K_0(mR) \tag{3.24}$$

where C_3 and C_4 are unknown constants, I_o is the modified Bessel function

of the first kind of order zero and K_o is the modified Bessel function of the second kind of order zero.

An approximate solution of the energy equation (3.13) is

$$\lambda = (C_1 \cos mZ + C_2 \sin mZ)(C_3 I_o(mR) + C_4 K_o(mR)) \tag{3.25}$$

The use of eq. (3.14) in (3.25) yields $C_1 = 0$, then

$$\lambda = [C_5 I_o(mR) + C_6 K_o(mR)]\sin mZ \tag{3.26}$$

where C_5 and C_6 are unknown constants. Applying boundary condition (3.16) to (3.26) yield $C_6 = 0$. Therefore,

$$\lambda = C_5 I_o(mR)\sin mZ \tag{3.27}$$

Assuming no heat transfer from the cold end of the electrode i.e., applying boundary condition (3.15) to (3.27) yields

$$\lambda = m \cos(mL) = 0 \tag{3.28}$$

Equation (3.28) is satisfied for all values of m given by

$$m = \frac{(2n+1)\pi}{2L} \quad , \qquad n = 0, 1, 2 \ldots\infty \tag{3.29}$$

Thus the general solution of eq. (3.13) is

$$\lambda = \sum_{n=0}^{\infty} [C_n I_o \left(\frac{2n+1}{2L} \pi R\right) \sin \left(\frac{2n+1}{2L}\right) \pi Z)] \tag{3.30}$$

The unknown coefficients C_n (n = 0, 1, 2...∞) can be determined by least square fitting at a finite number of points on the boundary,

choosing equally spaced points along the electrode i.e., the z axis and fitting them to the boundary condition (3.18).

In the present analysis 7 coefficients C_n (n = 0, 1, 2,...6) and 100 boundary points were used. The problem to be solved was to determine the values of the 7 coefficients so as to satisfy the boundary condition (3.18) for the 100 boundary points in the best possible manner.

From the boundary condition (3.18) the expression to be minimized is obtained as[26]

$$S = \sum_1 \{\left.\frac{\partial\lambda}{\partial R}\right|_{R=1} - [- D(1 + \lambda_{R=1})^4 + D(\lambda^*)^4(1 - F_{dA_1 \to A_2}) - N(1 + \lambda_{R=1}) + N\lambda_\infty + DEF_{dA_1 \to A_2}]\}^2 \quad (3.31)$$

where $\sum_1$ denotes summation over all points in the region $0 < Z < L$.

Using the series solution for λ as expressed in (3.30), eq. (3.31) takes the form

$$S = \sum_1 \{ \sum_{n=0}^{\infty} [C_n(\frac{2n+1}{2L}) I_1[\frac{(2n+1)\pi}{2L}] \sin [\frac{(2n+1)}{2L} Z]] + D \{1 + \sum_{n=0}^{\infty} [C_n I_o[\frac{(2n+1)\pi}{2L}] \sin[\frac{(2n+1)\pi}{2L} Z]]\}^4 + N \{1 + \sum_{n=0}^{\infty} [C_n I_o[\frac{(2n+1)\pi}{2L}] \sin[\frac{(2n+1)\pi}{2L} Z]]\} - D\varepsilon_3\lambda^{*4}(1 - F_{dA_1 \to A_2}) - N\lambda_\infty - DEF_{dA_1 \to A_2}\}^2 \quad (3.32)$$

The function to be fitted to zero at various boundary points is $\sqrt{S}$. Since the function is non-linear in the unknown parameters C_n, it is first locally linearized and then the least-square fit criteria applied to get a system of linear algebraic equations which are solved to give the coefficients C_n. Initial guess is made for the values of C_n and the process is then iterated upon until

$$\left| \frac{C_n^{new} - C_n^{old}}{C_n^{old}} \right| < 10^{-7}$$

The computer programme written to obtain the calculated temperature distribution is given in Appendix (III). The subroutine LQF, used in the programme was obtained from U.B.C. programme library.[27]

The configuration factor used was evaluated by Sikka[24] and is given by the following expression

$$F_{dA_1 \to A_2} = \frac{Z}{\pi} \left\{ \frac{1}{2} \cos^{-1}\left(\frac{1}{\beta}\right) - \frac{\phi}{\sqrt{\phi^2 - 4\beta^2}} \tan^{-1} \left[\sqrt{\frac{(\beta-1)(\phi+2\beta)}{(\beta+1)(\phi-2\beta)}} \right] \right\}$$

$$+ \frac{1}{\pi} \tan^{-1} \left[\frac{\sqrt{\beta^2-1}}{Z} \right] \qquad (3.33)$$

where $\phi = Z^2 + \beta^2 + 1$ and $\beta = r_2/a$. Fig. (31) gives the plot of $F_{dA_1 \to A_2}$ against axial length for various values of β.

III.3.2 Calculated Temperature Profiles

Profiles obtained by the above computation depend significantly on the three dimensionless parameters β, D and N (experimental values of T_o, T_{slag} and the process geometry were used).

The parameter D, for a particular value of β, depends upon the thermal conductivity of the electrode material and the temperature T_o. Assuming an average thermal conductivity K = 0.075 $cal.cm^{-1}{}^{\circ}K^{-1}sec^{-1}$ for mild steel and K = 0.058 $cal\,cm^{-1}{}^{\circ}K^{-1}sec^{-1}$ for stainless steel, the value of D obtained for the experimentally observed T_o values is in the range of $0.02 < D < 0.035$ for different β values.

The parameter N ($= \frac{h_c\, a}{K}$) is not the Nusselt number at the electrode surface, but may be evaluated by considering h_c for a similar geometrical heat transfer situation. h_c is typically in the range of 0.6×10^{-3} to 6×10^{-3} $cal.cm^{-2}{}^{\circ}K^{-1}sec^{-1}$ depending upon the type of convection, giving values for N of $0.05 < N < 0.5$. Typical profiles for two sets of parameters are shown in Fig. (24) to (29).

III.3.3 Correlation with Experiment

Curves of the type shown in Figs. (24) to (29) were computed for the existing experimental boundary conditions. The parameters used in the computation of the theoretical curves are listed in Table II. The correlation between the theoretically computed and the experimentally observed curves is found to be very good.

The slight difference in the two curves may be attributed to experimental error (especially in the measurement of T_o) and to the fact that only an average value of the thermal conductivity of the

Table II. Parameters used in the computations of the curves shown in Figs. (24) to (29).

ESR Condition	L	λ_∞	λ^*	ε	K	h_c	T_{slag}	T_o	β	D	N
2.54 cm (1") 1018 steel electrode negative	16.0	0.308	0.29	2.2	0.075	0.0041	1775	1225	2.25	0.0255	0.07
3.81 cm (1 1/2") 1018 steel electrode negative	16.0	0.318	0.302	2.6	0.075	0.0041	1775	1175	2.167	0.032	0.10
2.54 cm (1") 321 steel electrode negative	16.0	0.366	0.346	4.5	0.058	0.0041	1775	1025	2.25	0.0225	0.09
2.54 cm (1") 1018 steel electrode positive	16.0	0.306	0.240	2.2	0.075	0.0041	1775	1225	2.25	0.0255	0.07
3.81 cm (1 1/2") 1018 steel electrode positive	16.0	0.318	0.302	2.6	0.075	0.0041	1775	1175	2.167	0.032	0.10
2.54 cm (1") 321 steel electrode positive	16.0	0.366	0.348	4.5	0.058	0.0041	1775	1025	2.25	0.0225	0.09

electrode material was considered in the analysis. Secondly, only approximate values of emissivity were used. The model would require extensive refinement to accommodate a temperature dependent thermal conductivity. Accordingly one can not comment on the value used beyond the fact that it is numerically equal to that calculated using an average thermal conductivity for the pertinent temperature ranges.

The value of N is higher than expected as it requires an average heat transfer coefficient, h of 4.1×10^{-3} cal. $cm^{-2}{}^{\circ}K^{-1}sec^{-1}$ for the electrode surface. The argon gas flow rate through the system would give a maximum average velocity of 4 cm sec^{-1} over the electrode. This would lead to a much lower h_c value in free convection conditions and thus we have either selected too low a value for the average gas temperature, or there exists significant local variation in the value of N due to changes in the gas flow regime along the electrode.

Relation to Process Variables: The observed gradients in the electrode show the expected trends in that the gradients in electrode negative mode differ only slightly from the equivalent electrode positive condition. At a feed rate of 3×10^{-2} cm sec^{-1}, the electrode material spends approximately 60 sec between 950°K and the melting point, and 30 sec below the slag surface in the region 1300°K to melting point. Under these conditions it seems likely that in any solution process only very small particles (probably sub-micron sizes) of the dissolving phase will maintain equilibrium composition and phase relationship through the temperature gradient.

Two further aspects of the model are worthy of note. A steady state model was chosen, in spite of the fact that the electrode is being

consumed, and is, therefore moving with respect to the slag/metal interface. The rate at which the electrode moves affects the temperature gradients predicted by the model through the boundary value of T_o, and possibly also through T_{slag}. Both of these values are experimental parameters and will be specific to the melting conditions used. If the melt rate and power input are changed these temperatures will vary in a way controlled by the complex heat transfer regime existing on the electrode surface submerged below the slag/gas interface. Recently[28,29] attempts have been made to calculate the temperature distribution in the submerged portion of the electrode using assumed heat transfer coefficients. No attempt has been made here to predict the complex heat transfer regime and hence of including the melt-rate parameter in this analysis.[30]

Due to the small diameter of electrode used in the present laboratory experiments, any radial temperature gradient should be small (10-20°C). This was found to be the case. However, in large electrode/ingot configurations, a significant radial gradient exists and can be predicted by the present two dimensional analysis.

It was initially postulated that the electrode's time-temperature relationship would affect the amount of electrode surface oxidation, and therefore the reactive alloy element loss on melting. Using the data of Kubashewski and Evans[31] for the oxidation of iron in this temperature range, the oxide thickness for an electrode being melted in air was calculated. This was done by considering the electrode surface above 1000°K, summing the appropriate parabolic growth-rates for the experimental melt rate of 3×10^{-2} cm sec^{-1}, and thus deriving

an integrated oxide coating at point B in Fig. (30). This thickness is approximately 10^{-4} cm, which in the present electrode size range would account for only 10^{-2} wt. % loss of, say, titanium in an iron-titanium alloy. As the electrode surface-volume ratio decreases with electrode diameter, this oxidation source becomes still less important in large ESR units.

One can briefly comment on the possible differences which might be observed between VAR and ESR electrode temperature gradients, in spite of the fact that there exists no convenient demarcation line in VAR equivalent to the slag/gas interface in ESR. The relative parts played by radiation, conduction and convection are illustrated in Fig. (32). Here it has been assumed that VAR electrode is exposed to a uniform surface at 1900°K at z = 0, with T_o = 1800°K and with no electrode thermal term due to convection. The equivalent ESR gradient at an equivalent distance from the ingot surface is also shown. Although the two situations are not strictly comparable, the difference between the gradients illustrates the significant cooling effect of the convective gas flow in ESR.

CHAPTER IV

MEASUREMENT OF ELECTRICAL AND THERMAL PROPERTIES OF THE SLAG-SKIN REGION

IV.1 Introduction

One of the advantages claimed for the ESR processing of metals is held to be the resulting control in the directionality of ingot solidification.[32] This arises in a controllable proportion of radial to axial heat flow in the solidifying ingot. Since the radial flow is determined largely by the heat transfer characteristics of the mold-wall region, it is of interest to have numerical values of the appropriate heat transfer coefficients for calculation purposes.[33] The electrical properties of the same interface region determine the current distribution. In the insulated mold configuration (Fig. 33(a)), although there is no net current flow out of the system, a potential difference exists along the path slag/mold/ingot, so as to give the current path shown. Should this current be large, the local joule heating, or arcing, will result in the ingot welding to the mold, or in a severe case, in mold-wall puncture. In the situation shown in Fig. (33(b)), with the mold grounded, the above effects are only of importance in the region where the slag has a potential significantly above ground. Thus, the slag-skin should have a sufficiently high electrical resistivity to prevent

the above effects. A second result of the current passing from the slag to the mold is to provide the horizontal current component necessary for conventional electromechanical stirring.[34] Whether stirring from this latter cause is significant is still unknown. The numerical values obtained are used in explaining the results relating to a partial heat balance of the process and a current distribution model in Chapter V.

IV.2 Experimental

IV.2.1 Electrical and Thermal Measurements

The apparatus used is shown in Fig. (34) and consists of a graphite crucible containing a large volume ($\sim$ 1 litre) of liquid slag, heated by an induction coil. The copper cylinder (of diameter 3 cm, length 3 cm) was immersed at time zero, and its temperature measured simultaneously with the slag temperature and the electrical resistance between the graphite counter-electrode and the cylinder. The copper cylinder was cleaned by mechanical abrasion. The electrical resistance was measured on successive occasions at both 40 Hz and 1 KHz, with the same result, indicating that polarization contributions were negligible. The 1.0 KHz instrument is a phase-discriminating bridge which registers only the ohmic contributions to the test impedance, and the close correlation between the 40 Hz and 1.0 KHz measurements also therefore indicates that reactive contributions to the impedance were negligible. The temperature was measured using W3Re/W25Re thermocouple.

In order to eliminate the electrical interference from the induction generator, all the measurements were made with r.f. power off,

and with ungrounded instrumentation. This latter step also allowed high impedance recorders to be used in the thermocouple circuits whilst the thermocouples were in contact with the resistance measuring circuits.

The slag skin thickness was determined using a micrometer, after removing the copper block from the slag, following a 10 seconds immersion time. In order to establish that the slag skin thickness remained constant during the experimental period, the block was immersed for periods varying between one and ten seconds, and the skin thickness measured. It was found that the equilibrium thickness was established in less than one second.

Results of the resistivity measurement are shown in Fig. (35) and Fig. (36) as a function of the cylinder temperature. The equivalent dimensionless temperature vs. time measurements are shown in Fig. (37) and Fig. (38).

Several features not shown in these graphs are worthy of comment. Firstly, the slag temperature was measured continuously during the runs, so that the slight fall in the temperature could be accounted for in the subsequent calculation. This temperature decrease was approximately 20°C and remained essentially constant during the time of the experiment. At high temperatures (1730°C) it was found that CaF_2 did not form a coherent skin, but formed a discontinuous "patchy" film on the cylinder surface. The consequent heat transfer was high and non-reproducible. Finally, a calculation of the amount of heat liberated in the solidification of slag showed that the copper block would undergo a temperature rise of approximately 100°C if all this heat was absorbed by the block. However the subsequent analysis indicates that the rate of heat exchange

between the liquid and solid slag is high in comparison to that between the solid slag and the block. Thus, most of the heat of fusion should be transferred to the liquid slag bath.

A slight curvature could be detected in the initial part of the experimental time/temperature trace, but as this was in a time period close to the reaction time of the recording system, this can not be unequivocally attributed to the solidification step.

The derivation of the ruling expression for heat transfer in the experimental situation used is a standard one.[35]

For the transient heat flow in systems, with negligible internal resistance

The change of internal energy of the copper cylinder during 'dt' = Net flow of heat from slag to the copper cylinder

$$C_p \, m \, dT = U \, A \, [T_{slag} - T]dt \tag{4.1}$$

integrating,

$$\int_o^t dt = \frac{C_p \, m}{U \, A} \int_{T_o}^{T_t} \frac{dT}{T_{slag} - T} \tag{4.2}$$

simplifying (4.2),

$$t = C_p \frac{m}{U \, A} \ell n \, \frac{T_{slag} - T_o}{T_{slag} - T_t} \tag{4.3}$$

Figs. (37) and (38) show the time dependence of the cylinder temperature, processed following eq. (4.3).

In applying eq. (4.3) to the present experimental situation, several assumptions are made. Firstly, although the system undergoing the heat transfer reaction contains two surface and a volume term, it is assumed here that it may be described by an overall heat transfer coefficient, U. The terms comprising U are outlined and discussed subsequently. Secondly an average value for $(C_p)_{copper}$ is used over the temperature range considered. Thirdly, it is assumed that the copper cylinder contains no significant gradients, in spite of the unsteady-state condition used. The justification for this lies in the fact that the Biot number ($\frac{UL}{K_{Cu}}$, where L = significant dimension, volume/surface area; K_{Cu} = thermal conductivity of copper) of the system is less than 0.01. Only if this value exceeds 0.1 will the assumption introduce significant (>5%) error[35] into a subsequent calculation of U. Values of U obtained this way are listed in Table III.

IV.2.2 ESR Experimental Data

The method of obtaining the total electrical resistance between the mold, electrode and the ingot, in an operating ESR unit has been previously described.[36] Table IV gives the various operating resistances in the ESR unit used in this study as obtained by Cameron et al.[36]

Table III. Values of the overall heat transfer coefficient, U, calculated from the data of Figs. 37 and 38.

Slag Composition	Slag Temperature °C	Skin Thickness mm ± 0.2	U x 10^2 cal. $s^{-1}cm^{-2}°C^{-1}$ ± 0.02
CaF_2	1460	4.4	0.92
"	1440	4.2	1.15
"	1500	3.56	1.15
"	1600	2.30	1.23
"	1666	1.20	1.28
"	1720	1.02	1.25
CaF_2 + 25 wt. % Al_2O_3	1640	4.05	1.07
CaF_2 + 35 wt. % $CaTiO_3$	1530	5.0	1.00

Table IV. Operating resistances in the ESR process.[36]

Ingot dia. (cm)	Electrode dia. (cm)	No. of ingots x determin-ation	Slag skin thickness (cm)	Mold-electrode resistance (ohms)	Mold-ingot resistance (ohms)	Ingot-electrode resistance (ohms)	Slag composi-tion	Unshunted current in mold (amps)	Unshunted current in slag (amps)	Electrode Polarity
5.08	2.54	3 x 4	0.12	0.77±0.1	0.45±0.02	0.035±0.005	CaF_2	13±5	659±10	-ve
5.08	2.54	5 x 5	0.08	0.60±0.1	0.05±0.02	0.037±0.005	CaF_2 + CA	38±5	650±10	-ve
5.08	2.54	5 x 4	0.09	0.15±0.05	1.0 ±0.1	0.036±0.005	CaF_2 + CA	9±2	630±10	+ve
7.62	3.81	4 x 4	0.12	0.7 ±0.1	0.13±0.05	0.020±0.005	CaF_2	13±5	1205±15	-ve
7.62	3.81	5 x 4	0.08	0.55±0.1	0.06±0.02	0.019±0.005	CaF_2 + CA	19±5	1180±15	-ve
7.62	3.81	5 x 4	0.09	0.15±0.02	0.4 ±0.1	0.020±0.005	CaF_2 + CA	20±5	1180±15	+ve

IV.3 Discussion

IV.3.1 The Thermal Resistance of the Slag Skin

The present experimental set up and an ESR system are similar with one difference. In ESR process the copper mold is water cooled where as the copper block was not and consequently heated up. However as U was experimentally found to be independent of copper block temperature, it is justified to use the data obtained from the present experimental set up in describing the ESR thermal characteristics in the slag-skin region.

The overall heat transfer coefficient of the system, U, is made up of the two surface terms and the volume conductance of the slag skin. The numerical value of U so defined is seen to be approximately 10^{-2} cal. $cm^{-2}sec^{-1}{}^{\circ}C^{-1}$. This is almost the same value as that found for the metal/solid-metal/copper mold wall system, as in continuous casting practice,[37] or in a VAR unit. Although the ESR system will necessarily contain a thermal resistance due to either free or forced convection in the liquid slag adjacent to the solid skin, which will not be the same as the equivalent term at the liquid/solid metal interface in, for example, a VAR system, it is noteworthy that the overall heat transfer coefficients are close in magnitude.

In steady state, from Fig. (39) and Fig. (40)

$$q = 2\pi r_3 \, \ell h_{slag} [T_{slag} - T_E] \tag{4.4}$$

$$= \frac{2\pi k_{slag} \, \ell}{\ell n(\frac{r_2}{r_3})} [T_E - T_D] \tag{4.5}$$

$$= 2\pi r_1 \, \ell h_{int} \, [T_D - T_C] \tag{4.6}$$

From (4.4), (4.5) and (4.6) one obtains

$$q = U \, A_o (T_{slag} - T_{Cu}) \tag{4.7}$$

where $A_o = 2\pi r_1 \, \ell$

$$U = \frac{1}{\frac{r_1}{r_3}\frac{1}{h_{slag}} + \frac{r_1 \, \ell n \, (r_2/r_3)}{k_{slag}} + \frac{1}{h_{int}}} \tag{4.8}$$

In the following calculations for 8.0 cm copper mold, ℓ is taken as unity and $r_1 \simeq r_2$.

By using a method of approximation, one can deduce the component values of eq. (4.8) and hence the temperature profile in the mold-wall region. One must make the assumption here that T_{Cu} is approximately 140°C. This value is estimated from the mold wall thickness, and the observation that the mold wall outer temperature is approximately 110°C (Chapter V). In a typical case, such as that illustrated by Table III for a CaF_2 slag, T_{slag} = 1650°C and the slag skin thickness is 0.12 cm. This leads to a value for q of 480 cal. $cm^{-1}sec^{-1}$ for a 8 cm diameter copper mold using the observed value for U of 1.28×10^{-2} $cal.cm^{-2}sec^{-1}{}^{\circ}C^{-1}$. At this value, one obtains a self-consistent correlation between the mold wall inner and outer temperatures.

Fig. (40) shows schematically the system at hand. In the present case all the temperatures except that at D are known as the temperature at E is the melting point of CaF_2.

It is now possible to separate the terms in equation (4.8), and calculate the values for h_{int}, h_{slag} and T_D, using the data developed above.

Thus, in the liquid slag:

$$q = A_o' \, \Delta T_{EF} \, h_{slag} \tag{4.9}$$

where $A_o' = 2\pi r_3 \, \ell$

r_3 = radial dimension shown in Fig. (39)

ΔT_{EF} = temperature difference between points E and F of Fig. (40).

Substituting the values in eq. (4.9) one gets

$$h_{slag} \simeq 7.5 \times 10^{-2} \text{ cal.cm}^{-2}\text{sec}^{-1}{}^{\circ}\text{C}^{-1} \tag{4.10}$$

In order to calculate the temperature at D, i.e. T_D, a value for k_{slag} must be assumed.

The value of $k_{slag} = 0.8 \times 10^{-2}$ cal. $\text{cm}^{-1}\text{sec}^{-1}{}^{\circ}\text{C}^{-1}$, estimated from the values of crystalline ionic solids found in literature[38] is used for the calculation. Substituting the values of k_{slag} and h_{slag} in (4.8) one obtains

$$h_{int} \simeq 2.05 \times 10^{-2} \text{ cal. cm}^{-2}\text{sec}^{-1}{}^{\circ}\text{C}^{-1} \tag{4.11}$$

Substituting the known values in eq. (4.5) and (4.6) leads to the value

$$T_D \simeq 1100°C$$

Varying the values of k_{slag} one obtains

for $k_{slag} = 10^{-2}$ cal. $cm^{-1}sec^{-1}{}^{\circ}C^{-1}$

$T_D \simeq 1160°C$

and for $k_{slag} = 0.6 \times 10^{-2}$ cal. $cm^{-1}sec^{-1}{}^{\circ}C^{-1}$

$T_D \simeq 1000°C$

with corresponding changes in h_{int}. One may thus draw the profile shown in Fig. (40), with the temperature at D approximately equal to 1100°C. The two heat transfer coefficients have values:

$$h_{slag} = 7.5 \times 10^{-2} \text{ cal. } cm^{-2}sec^{-1}{}^{\circ}C^{-1}$$

$$h_{int} = 2.05 \times 10^{-2} \text{ cal. } cm^{-2}sec^{-1}{}^{\circ}C^{-1}$$

Since the major factor in determining the values of the overall parameter, U, is seen to be the surface discontinuity term, it is not surprising that the ESR system closely resembles the other cold-mold processes in its heat transfer characteristics. As both h_{slag} and k_{slag} are functions of slag composition and temperature, this will lead to the variations in slag skin thickness observed in practice.

However, it is unlikely that either of these parameters significantly affect h_{int} and thus U will be relatively insensitive function of the process variables, as was observed and shown in Table III.

IV.3.2 The Electrical Resistance of the Slag Skin

The curves in Fig. (35) and Fig. (36) clearly show that the slag skin resistance is quite high. At cylinder temperature of 140°C, the resistance is ≃ 50 ohms. This gives a resistivity value of 14,600 ohm.cm assuming a slag skin thickness of 0.12 cm and the surface area of the copper block as 35 cm^2. At a cylinder temperature of 500°C, the value drops drastically to 292 ohm. cm (R ≃ 1 ohm).

Using these values to calculate the slag skin resistance for the laboratory ESR unit slag bath (diameter = 8.0 cm, ℓ = 3.5 cm) yields R = 20 ohms for 140°C and R = 0.39 ohms for 500°C. The value of R obtained experimentally in earlier study[36] of 0.55-0.77 ohms is comparable to $R_{500°C}$. However as the copper mold temperature is below 150°C, the experimentally obtained value of R = 0.55-0.77 ohms has to be explained by a different mechanism.

The experimentally obtained value of the resistance of slag skin in this study can be considered as a combination of two resistances in series, the slag skin resistance and the contact resistance. Extrapolating the values of resistivity for CaF_2-Al_2O_3 system from Fig. (86), for slag temperature of 1000-1200°C (average slag skin temperature as obtained from Fig. (40)), one obtains values ranging from r = 0.5 to 20 ohm. cm. From these values it is clear that the main resistance is the contact resistance. At 500°C, there is a better contact between

the slag skin and the copper cylinder yielding a value of the combined resistance 50 times smaller than at 140°C.

Thus in the ESR unit if there is good contact between slag skin and the mold over even a small area of 0.1-2 sq. cm, the experimentally observed value of slag skin resistance in ESR unit can be obtained.

With the inner mold-wall temperature above 150°C, the probability of a good contact between the slag skin and the mold is higher. This may make the electrode-mold, and the ingot-mold resistances comparable in magnitude to the working resistance of the liquid slag. Thus, the main current path would be electrode → mold → ingot, with consequent mold wall failure. This probably accounts for the explosions, or ingot-mold welding, observed in the ESR practice using steel molds.

The second point to be observed in Fig. (35) and Fig. (36) is that there is an apparent resistance drop at low temperatures. This arises from the fact that the reported temperature is processed from a time-temperature record, and the apparent resistance drop is the initial contact of the cylinder and the slag. The significance of this is a momentary low-resistance contact arising either from the cooling of the initial slag skin, or the speed of formation of the skin. During the ESR processing, the liquid slag continually forms a skin at the mold-slag-air interface in a region where potential difference of at least 15 V exists between the slag and the mold wall. The momentary low resistance contact will result in small areas of transient high current-density and possible arcing. This has been observed in industrial ESR units as small, transient "bright spots" around the slag surface boundary with the mold wall.

CHAPTER V

HEAT BALANCE OF THE PROCESS

V.1 Introduction

The electroslag refining process is a relatively inefficient operation in terms of thermal efficiency. However, the factors which make this process inefficient are the same ones which give this process some unique advantages. In an ESR furnace, the efficiency is sacrificed for the sake of ingot structure by melting the metal in a metal mold which is very effectively cooled by a water jacket.

It is not surprising, therefore, that power consumption figures for electroslag remelting of 1200 to 2000 kilowatt hours per metric ton are reported,[39] although the theoretical power required to melt ferrous alloys is about 400 KWH/metric ton. For laboratory scale process, the efficiency is still lower (16-25%). Most of the heat energy supplied to the process is passed immediately to the cooling water by conduction from the sides of the slag pool.

An analysis of the heat balance of some of the electroslag heats made at the Mellon Institute[11] has indicated that about 50-55% of the heat is held in the molten metal pool which is extracted through the ingot and the water-cooled copper stool. About 10 to 15% heat is extracted through mold cooling, while 25% is used in heating the electrode. The balance of the heat was accounted for as being

lost by radiation and convection.

Holzgruber[40] found that for 110 mm square ESR ingots (42 V, 4500 amp), 66% of the total heat introduced is removed by the cooling water of the mold. A slight amount (≈5%) remains as heat in the ingot, while about 29% of the total heat is lost by radiation from the slag surface.

It is quite clear that the analyses of heat distribution done to date[11,39,40,41] do not agree closely. An accurate knowledge of the distribution of heat in the electroslag remelting unit is vital to the better understanding and control of the process.

As discussed earlier, there are a number of different ways in which the electrical energy can be supplied to the unit. The process can be operated using A.C. or D.C. supply. In D.C., one has the choice of having the electrode as the cathode (referred to as electrode negative) or anode (electrode positive). It has been established for some time now[12] that both the anode and cathode are polarized to different extents in an ESR unit. The two types of arrangement give different operating characteristics. The mold can be insulated from or connected (referred to as 'live') to the ingot. The current path has been found[36] to be different in the two cases for electrode positive arrangement.

Significant disagreement exists in the literature as to the power required to melt in a particular configuration.[17] The range of figures quoted[6,42] for steels and nickel-base alloys is a function of absolute size, polarity and electrode/mold diameter ratio, as well as of the material. Kammel et al.[42] have reported that D.C. with electrode

negative is the most efficient mode, whilst Holzgruber et al.[6] found that D.C. with electrode positive was the most efficient.

Although the electrical energy can be supplied in different ways, it is necessary to adjust the power supplied to the melt to within fine limits if an ingot having good surface and structure is to be produced.

The same power input can be achieved by various combinations of voltage and current. The choice of current within the required power limitation is rather critical, because while increased current increases the melt rate, it also deepens the slag pool, giving a less satisfactory ingot structure.[4,43] The effect of change in voltage is not as great as that of current. In certain cases, high voltage gives a better solidification front and hence an improvement in ingot properties. Medovar et al.[4] report that the main effect of voltage is to raise the temperature of the slag bath and a high voltage intensities desulphurization.

The power input to the process is generally chosen such that the melt rate corresponds to a stable electroslag process. At a very low rate of delivery of the electrode, the ESR process periodically turns into an electric arc process. At the moment when the drop breaks off, an arc discharge is observed between the electrode and slag surface.[4] At very high rate of electrode feed, periodic arc discharge occurs between the end of the electrode and the surface of the metallic bath, arising at the moment when the drop breaks off. This ultimately leads to short-circuiting of the electrode on the metallic bath.

The volume of the slag bath also controls the structure of the

ingot obtained. As the depth of the slag bath is increased (without changing the melt rate), the depth of the metallic bath is reduced.

As the materials processed by the ESR process are quite expensive, very often it is not economically feasible to try out various working conditions to determine the optimum working parameters. An attempt is made here to predict the working conditions for industrial scale ingots.

Distribution of Heat in the ESR Unit

In a dynamic steady state, the heat generated in the slag bath by resistance heating is distributed in the unit in the following manner

(1) heat consumed in heating the consumable electrode to the melting point, its fusion and further heating of the drops of the electrode material as they fall through the slag bed

(2) heat given to cooling water across the slag bed

(3) heat given to cooling water across the length of the ingot

(4) heat accumulated in the ingot

(5) heat given to base plate cooling water

(6) heat lost by radiation from the surface of the slag bath to the furnace atmosphere

(7) heat radiated by the slag bath on to the walls of the mold

(8) heat radiated by the slag bath on to the electrode.

V.2 Experimental

V.2.1 ESR Ingot Schedule

V.2.1.1 Melt Record

Experiments were carried out on the U.B.C. electroslag unit. Fig. (41a) gives the general view of the laboratory unit. The starting procedure has been described in detail by Etienne.[9] After steady operating conditions were established, readings of current, voltage, electrode travel, slag feed rate etc., were recorded at known time intervals.

V.2.1.2 Molds

Six different water-cooled copper molds ((i) I.D.: 5.85 cm, ht: 40 cm, wall thickness: 0.5 cm; (ii) I.D.: 6.35 cm, ht: 40 cm, wall thickness: 0.5 cm; (iii) I.D.: 6.35 cm, ht: 80 cm, wall thickness: 0.5 cm; (iv) I.D.: 8.0 cm, ht: 45 cm, wall thickness: 0.5 cm; (v) I.D.: 8.0 cm, ht: 80 cm, wall thickness 0.5 cm; (vi) I.D.: 9.5 cm, ht: 90 cm, wall thickness 0.4 cm). were used in the present study.

V.2.1.3 Electrodes

Electrodes of different composition (EN 25 steel, 321 S.S., 1018 steel, AISI 630, Ferrovac E, Armco iron) and size (2.54 cm to 6.35 cm diameter) were remelted. In the non-consumable electrode experiment, 3.81 cm diameter EN 25 steel electrode was threaded to the 3.81 cm diameter molybdenum electrode. The process went non-consumable after the EN 25 steel melted and formed an ingot at the bottom.

V.2.1.4 Slag Composition

Slag composition CaF_2 ∿ 25 wt. % Al_2O_3 was used in the study of the heat balance of the process. For some auxilliary studies, 100% CaF_2 and CaF_2 ∿ 30 wt. % TiO_3 compositions were also used.

V.2.1.5 Polarity

Ingots were made using either a.c. or d.c. (with electrode of either polarity) power. Fig. (42) gives the three possible mold connections.

V.2.1.6 Continuous Slag Addition[9]

A specially designed rotating table (Fig. (41b)) allowed the continuous delivery of the slag during the melt. A vertical cannister whose base is closed by the rotating plate delivered the material (powder or small granules) through a calibrated grate. The stream of material was then wiped over the edge of the plate into the mold. The continuous addition of slag using this apparatus was carried out only while making tall ingots.

V.2.1.7 Atmosphere Control

Three types of hoods were used for melts done under argon atmosphere:

Type I: Fig. (43) gives a schematic diagram of the hood, used in the initial melts, which provided an argon blanket and extraction of fumes.

Type II: A more elaborate design included a sealed chamber in

which the electrode was held onto a water cooled stub. The rubber bellows clamped to the stub at the top of the assembly provided the moving seal (Figure (44)). Spring clamps and blowout windows allowed for a quick release of inside pressures in case of explosion.

Type III: This was used in melts where continuous addition of the slag was necessary (Fig. (45)).

V.2.1.8 Experimental Data

The experimental data obtained is tabulated in Table V. The reported values of the process parameters are the average values during stable working conditions. Table (VI) gives the analysis of the electrode and ingot compositions for some of the EN 25 steel melts. This was carried out by the Mineral Sciences Division, Mines Branch, Ottawa. Fig. (46) gives the percentage of current going to the mold during a d.c. positive (with live mold) melt.

V.2.2 Measurement of Temperature Profiles on the Mold

In order to calculate the heat leaving the mold, measurement of the temperature profiles on the mold was carried out for various experimental conditions. Copper-constantan thermocouples were used to measure the temperature distribution on the mold. Constantan wire (0.0254 cm diameter) were embedded in 0.1 cm diameter x 0.125 cm deep holes in the copper mold, plugged by 0.1 cm diameter copper wire. Forty-eight constantan wires were embedded in the copper mold located in a spiral at fixed distances apart, as shown in Fig. (47). The copper mold itself was used as the positive terminal, for all the 48 thermocouples. The 300 cm long constantan wires were individually enclosed

Table V. ESR melt record

Ingot no.	mold diameter (cm)	electrode diameter (cm)	electrode comp.	electrode polarity	atmosphere	starting slag wt. and composition (g)	voltage (volt)	current (amp)	melt rate ($g.sec^{-1}$)	wt. of the slag cap at the end of the run (g)	Total electrode descend (cm)
1	8	3.81	EN 25	-ve	Argon[III]	660 g CaF_2-27.3 wt. % Al_2O_3	23.75	1150	3.35	535	106.5
2	8	3.81	EN 25	-ve	Air	720 g CaF_2-25 wt. % Al_2O_3	22.25	1150	3.8	495	38.2
3	8	5.08	EN 25	-ve	Air	660 g CaF_2-27.3 wt. % Al_2O_3	23.0	1100	4.15	461	37.0
4	8	3.5	EN 25	-ve	Argon[I]	680 g CaF_2-26.5 wt. % Al_2O_3	22.5	1130	2.20	411	56.8
5	8	3.81	EN 25	-ve	Argon[II]	660 g CaF_2-27.3 wt. % Al_2O_3	23.5	1250	2.2	400	55.9
6	8	3.81	EN 25	-ve	Argon[II]	720 g CaF_2-25 wt. % Al_2O_3	23.0	1175	2.64	485	30.8
7	6.35	3.5	EN 25	-ve	Argon[I]	440 g CaF_2-25 wt. % Al_2O_3	22.8	960	2.67	325	99.9

Table V. (Continued)

Ingot no.	mold diameter (cm)	electrode diameter (cm)	electrode comp.	electrode polarity	atmosphere	starting slag wt. and composition (g)	voltage (volt)	current (amp)	melt rate ($g.sec^{-1}$)	wt. of the slag cap at the end of the run (g)	Total electrode decend (cm)
8	9.5	5.08	EN 25	-ve	Air	960 g CaF_2-25 wt. % Al_2O_3	23.5	1575	4.10	875	66.8
9	6.35	3.18	Armco Iron	-ve	Air	440 g CaF_2-25 wt. % Al_2O_3	22.0	880	1.26	380	122.8
10	8.0	3.81	EN 25	+ve	Argon[III]	660 g CaF_2-27.3 wt. % Al_2O_3	23.0	920	2.58	530	86.2
11	8	3.81	EN 25	+ve	Argon[II]	720 g CaF_2-25 wt. % Al_2O_3	22.0	975.0	2.58	517	30.2
12	8	3.81	EN 25	+ve	Argon[II]	"	22.5	925.0	2.58	480	48.3
13	8	3.81	EN 25	+ve live	Argon[III]	660 g CaF_2-27.3 wt. % Al_2O_3	23.25	1175	2.59	602	80.0
14	8	3.81	EN 25	+ve live	Argon[II]	720 g CaF_2-25 wt. % Al_2O_3	23.5	950	2.58	400	36.3
15	8	3.81	EN 25	a.c.	Air	"	26.0	840	4.15	442	29.5

Table V. (Continued)

Ingot no.	mold diameter (cm)	electrode diameter (cm)	electrode comp.	electrode polarity	atmosphere	starting slag wt. and composition (g)	voltage (volt)	current (amp)	melt rate ($g.sec^{-1}$)	wt. of the slag cap at the end of the run (g)	Total electrode decend (cm)
16	8	3.81	En 25	a.c.	Argon[III]	660 g CaF_2-27.3 wt. % Al_2O_3	23.5	850	3.5	355	95.7
17	8	3.81	EN 25	a.c.	Argon[II]	720 g CaF_2-25 wt. % Al_2O_3	25.5	810	3.7	340	63.0
18	8	3.5	EN 25	a.c.	Argon[I]	680 g CaF_2-26.5 wt. % Al_2O_3	23.1	780	2.8	367	70.0
19	8	3.81	EN 25 + Mo	a.c.	Argon[III]	660 g CaF_2-27.3 wt. % Al_2O_3	25.0	1100	non-consumable	375	72.4
20	8	3.81	AISI 630	-ve	Argon[II]	600g CaF_2-13.3 wt. % Al_2O_3	23.5	1300	3.4	400	50.0
21	9.5	6.35	EN 25	-ve	Air	980 g CaF_2-25 wt. % Al_2O_3	23.5	1575	6.36	772	80.0
22	5.85	2.54	321 SS	+ve	Argon[I]	380 g 100 % CaF_2	22.3	650	1.22	345	40.0

Table V. (Continued)

Ingot no.	mold diameter (cm)	electrode diameter (cm)	electrode comp.	electrode polarity	atmosphere	starting slag wt. and composition (g)	voltage (volt)	current (amp)	melt rate ($g.sec^{-1}$)	wt. of the slag cap at the end of the run (g)	Total electrode decend (cm)
23	5.85	2.54	321 SS	+ve	Argon[I]	380 g CaF_2-31.6 wt. % $CaTiO_3$	22.3	630	2.0	195	45.0
24	5.85	2.54	321 SS	+ve	Argon[I]	380 g CaF_2-31.6 wt. % $CaTiO_3$	22.3	640	1.69	286	40.1
25	5.85	3.18	FVE	-ve	Air	380 g CaF_2-23.7 wt. % Al_2O_3	23.3	1010	2.5	217	32.5
26	5.85	3.18	FVE	-ve	Argon[II]	400 g CaF_2-25 wt. % Al_2O_3	23.5	1000	1.735	192	26.5
27	5.85	3.18	FVE	+ve	Air	360 g CaF_2-25 wt. % Al_2O_3	20.2	780	1.56	252	31.4
28	5.85	3.18	FVE	+ve BN insulated	Argon[II]	340 g CaF_2-25 wt. % Al_2O_3	22.2	975	2.45	327	28.1
29	5.85	3.18	FVE	+ve BN insulated	Argon[II]	340 g CaF_2-25 wt. % Al_2O_3	22.4	910	1.75	272	28.0

Table V. (Continued)

Ingot no.	mold diameter (cm)	electrode diameter (cm)	electrode comp.	electrode polarity	atmosphere	starting slag wt. and composition (g)	voltage (volt)	current (amp)	melt rate ($g.sec^{-1}$)	wt. of the slag cap at the end of the run (g)	Total electrode decend (cm)
30	5.85	3.18	FVE	+ve live	$Argon^{II}$	340 g CaF_2-25 wt. % Al_2O_3	21.5	870	1.3	158	26.6
31	5.85	3.18	FVE	a.c.	$Argon^{II}$	340 g CaF_2-25 wt. % Al_2O_3	24.2	650	2.25	167	28.2
32	5.85	3.18	FVE	a.c. BN insulated	$Argon^{II}$	340 g CaF_2-25 wt. % Al_2O_3	23.0	810	2.43	158	28.6

Atmosphere: $Argon^{I}$: Argon atmosphere using shield of type I

$Argon^{II}$: Argon atmosphere using shield of type II

$Argon^{III}$: Argon atmosphere using shield of type III

Table VI. Chemical analysis of the EN 25 steel ingots

Ingot no.	composition of the	Alloy composition	electrode polarity	Atmosphere	composition (wt. %)											
					C	Mn	Si	S	P	Ni	Cr	Mo	Sn	Cu	Al	Fe
1	Electrode	EN 25	-ve	Argon^{III}	0.29	0.675	0.225	0.06	0.013	2.475	0.72	0.60	0.028	0.27	0.01	bal
1	Ingot	EN 25	-ve	Argon^{III}	0.285	0.51	0.135	0.05	0.013	2.50	0.66	0.62	0.028	0.275	0.13	"
2	Electrode	EN 25	-ve	Air	0.28	0.69	0.24	0.062	0.012	2.55	0.73	0.65	0.028	0.29	0.01	"
2	Ingot	EN 25	-ve	Air	0.275	0.56	0.155	0.056	0.013	2.37	0.185	0.61	0.028	0.265	0.13	"
3	Electrode	EN 25	-ve	Air	0.275	0.645	0.32	0.025	0.013	2.42	0.74	0.60	0.026	0.23	0.01	"
3	Ingot	EN 25	-ve	Air	0.29	0.53	0.165	0.026	0.013	2.38	0.20	0.56	0.027	0.225	>0.2	"
5	Electrode	EN 25	-ve	Argon^{II}	0.28	0.675	0.235	0.056	0.012	2.5	0.725	0.61	0.027	0.27	0.015	"
5	Ingot	EN 25	-ve	Argon^{II}	0.295	0.61	0.165	0.06	0.013	2.42	0.70	0.65	>0.10	0.29	0.14	"
6	Electrode	EN 25	-ve	Argon^{II}	0.28	0.67	0.235	0.059	0.012	2.55	0.72	0.63	0.028	0.28	0.01	"
6	Ingot	EN 25	-ve	Argon^{II}	0.30	0.59	0.17	0.05	0.015	2.42	0.79	0.62	0.03	0.27	0.15	"
10	Electrode	EN 25	+ve	Argon^{III}	0.28	0.675	0.24	0.056	0.012	2.475	0.73	0.625	0.028	0.285	0.015	"
10	Ingot	EN 25	+ve	Argon^{III}	0.27	0.57	0.11	0.049	0.013	2.45	0.20	0.59	0.029	0.275	0.03	"
11	Electrode	EN 25	+ve	Argon^{II}	0.28	0.66	0.23	0.058	0.013	2.55	0.72	0.60	0.028	0.275	0.015	"
11	Ingot	EN 25	+ve	Argon^{II}	0.275	0.63	0.15	0.040	0.013	2.5	0.20	0.57	0.028	0.27	0.015	"

Table VI. (Continued)

Ingot no.	composition of the	Alloy composition	electrode polarity	atmosphere	composition (wt. %)											
					C	Mn	Si	S	P	Ni	Cr	Mo	Sn	Cu	Al	Fe
12	Electrode	EN 25	+ve	Argon^{II}	0.29	0.665	0.225	0.058	0.013	2.475	0.72	0.598	0.029	0.265	0.01	"
12	Ingot	EN 25	+ve	Argon^{II}	0.27	0.65	0.185	0.051	0.013	2.50	0.20	0.59	0.029	0.27	0.015	"
13	Electrode	EN 25	+ve live	Argon^{III}	0.295	0.675	0.235	0.064	0.014	2.50	0.725	0.61	0.029	0.275	0.010	"
13	Ingot	EN 25	+ve live	Argon^{III}	0.30	0.33	0.09	0.062	0.013	2.57	0.63	0.66	0.029	0.29	>0.2	"
14	Electrode	EN 25	+ve live	Argon^{II}	0.275	0.675	0.23	0.062	0.012	2.45	0.725	0.625	0.027	0.28	0.01	"
14	Ingot	EN 25	+ve live	Argon^{II}	0.28	0.35	0.055	0.067	0.013	2.47	0.19	0.60	0.029	0.27	0.04	"
15	Electrode	EN 25	a.c.	Air	0.28	0.66	0.225	0.06	0.012	2.45	0.715	0.61	0.017	0.27	0.01	"
15	Ingot	EN 25	a.c.	Air	0.275	0.61	0.18	0.032	0.013	2.50	.215	0.62	0.029	0.27	0.04	"
16	Electrode	EN 25	a.c.	Argon^{III}	0.28	0.66	0.23	0.058	0.012	2.475	0.72	0.60	0.028	0.27	0.010	"
16	Ingot	EN 25	a.c.	Argon^{III}	0.285	0.66	0.20	0.064	0.014	2.52	0.74	0.66	0.03	0.29	0.03	"
17	Electrode	EN 25	a.c.	Argon^{II}	0.28	0.675	0.235	0.057	0.012	2.475	0.73	0.61	0.028	0.275	0.01	"
17	Ingot	EN 25	a.c.	Argon^{II}	0.27	0.62	0.195	0.045	0.012	2.48	0.195	0.60	0.028	0.27	0.035	"

in 0.2 cm dia. plastic tubings (made by ICORE, California). The cold junctions were maintained at 0°C by immersing them in ice cooled glass tubes containing mercury.

For melts using d.c. positive (live mold) configuration, a significant fraction of the total current flows through the mold and as such it is not possible to determine the temperature distribution on the mold using copper mold as the +ve terminal for all the thermocouples. A number of insulated thermocouple grade copper wires were embedded near the constantan wires in the mold to give an accurate temperature distribution on the mold.

Fins were attached to the mold to regulate the water flow over the copper mold, at the same time, enabling chromel-alumel thermocouples to be located in a spiral along the length of the mold. These thermocouples (15 in total) were used to determine the temperature distribution in the mold cooling water.

Fig. (48) shows the thermocouples clad copper molds. The e.m.f. generated was recorded on a Texas instrument model FM W6B multichannel recorder.

As the ingot progressively built up, appropriate thermocouples were connected to the 24 terminals recorder to give the temperature distribution on the mold.

Fig. (49) to Fig. (56) gives the temperature distribution on the mold for different experimental configurations. Fig. (57) gives the temperature distribution in the mold cooling water.

V.2.3 Measurement of the Heat Leaving Through the Bottom of the Mold

In order to calculate the amount of heat leaving through the bottom of the mold, in some melts, two chromel/alumel thermocouples were placed, known distance apart (1 cm), in grooves made in the steel base plate. Fig. (58) gives the temperature distribution obtained.

V.3 Distribution of Heat Input in the Slag Bed

V.3.1 Power Input

In this section, a detailed analysis of the heat input into the unit will be carried out. It will be carried out for a typical melt (I.N. 1 of Table V). The voltage gradients for this experimental set up were determined in Chapter II and will be used here.

There are 3 sources of heat input.

(1) resistance heating of the slag

(2) polarization of the electrode and the ingot

(3) oxidation of the electrode or the cathode reaction product in air.

From Table V, the amount of heat input (due to (1) and (2)) can be calculated. The a.c. ripple in a d.c. operation is not a sine wave, but has an r.m.s. equivalent, registered by the 'r.m.s.' meters.

D.C. power: V = 23.75 volts; A = 1150 amps.

A.C. ripple: r.m.s. voltage = 2.65 V

r.m.s. current = 142 amp

Power input = 23.75 x 1150 + 2.65 x 1.42

= 27.60 Kwatts

Heat Input = 27.60 x 0.24 = 6.65 $Kcal.sec^{-1}$.

V.3.2 Resistance Heating of the Slag

Fig. (59) gives the voltage gradients in the slag bed for melt of Ingot No. 1. The slag bath is subdivided into five sections as shown. The average temperature and conductivity of each section are shown in Fig. (59). The conductivity data was experimentally determined by Mitchell and Cameron.[21] The effect of Ca and Al on conductivity will be discussed subsequently.

Each section is assumed to have a constant current density

$$\text{Power} = I^2R \text{ watts}$$

$$= \frac{V^2}{R}$$

$$= \frac{V^2}{\ell^2} \text{ volume x c}$$

Region A: $\text{Power} = \frac{V^2}{\ell^2} \times \text{volume} \times c$

$V \simeq 8$ volts

$\text{volume} = 2\pi \text{ cm}^3$

$\ell \simeq 0.9$ cm

$c = 2.46 \text{ ohm}^{-1}\text{cm}^{-1}$

$$P_A = \frac{(8)^2}{(0.9)^2} \times 2\pi \times 2.46 \times 0.24 = 0.295 \text{ Kcal.sec}^{-1}$$

Table VII gives the heat input distribution in the five different regions considered here.

$$\text{Total heat input} = \sum_{A \to E} P_A$$

$$= 4.75 \text{ Kcal.sec}^{-1}.$$

Table VII. Calculation of heat input distribution in the slag bed using a.c. electrical conductivity

Region	ΔV (volts)	volume $(cm)^3$	length (cm)	a.c. electrical conductivity $(ohm^{-1}cm^{-1})$	Amount of heat generated $(Kcal.\ sec^{-1})$	Total heat generated $(Kcal.\ sec^{-1})$
A	8	2π	≃0.9	2.46	.295	0.295 + 1.27 +1.60 + 1.10 +0.485 = 4.75
B	18	8π	≃2.1	2.85	1.27	
C	12.87	24π	≃2.22	2.64	1.60	
D	13.0	12π	≃1.8	2.30	1.10	
E	8.75	18π	≃2.1	2.08	0.485	

V.3.3 Effect of Dissolved Ca and Al on the Conductivity of the Slag

As discussed earlier in Chapter II, the cathodic reaction product in a d.c. ESR operation is Ca, Al or Al^+ and these are soluble to different extents, in both the liquid metal and the slag.

Ca has complete misibility in CaF_2 slag at the ESR operating temperatures.[44] Although the effect of Ca on the electrical conductivity of CaF_2 has not been studied, data is available on the effect of Na addition to NaF and similar halide systems.[44] From this data it is clear that 30-40% increase in conductivity for 2-5 mole % addition of Ca or Al in the slag is not unreasonable.

To obtain a more realistic value for the increase in conductivity due to the dissolution of Ca and Al in slag the following approach is adopted.

From Table V, it is clear that both for I.N. 1 (d.c. negative) and I.N. 16 (a.c.), the ESR cell geometry below the electrode tip was very similar. Using this assumption, it is possible to calculate the cell constant from the a.c. melt and substitute it in the calculations for d.c. melt to give the value of resistivity of the slag.

For I.N. 16 (a.c. $V = 23.5$ V

$I = 850$ amp.

$R = \frac{V}{I} = .0276$ ohms

$R = r_{a.c.}(\frac{\ell}{A}) = 0.0276$

$$(\frac{\ell}{A}) = \frac{.0276}{r_{a.c.}}$$

For I.N. 1 (d.c. negative) $V \simeq 23.5$ V (actually 23.75 V)

$$I = 1150 \text{ amp}$$

$$R = \frac{23.5}{1150} = 0.0204 \text{ ohm}$$

$$r_{d.c.} \left(\frac{\ell}{A}\right) = 0.0204$$

$$\left(\frac{\ell}{A}\right) = \frac{0.0204}{r_{d.c.}}$$

Equating the two values of $\left(\frac{\ell}{A}\right)$

$$\frac{0.0276}{r_{a.c.}} = \frac{0.0204}{r_{d.c.}}$$

$$r_{d.c.} = \frac{0.0204}{0.0276} \; r_{a.c.}$$

$$r_{d.c.} = .74 \; r_{a.c.}$$

$$c_{d.c.} = 1.35 \; c_{a.c.}$$

Thus the conductivity of the slag in d.c. operation is increased by 35%. The temperature variation of d.c. resistivity is unknown. Although it will be less sensitive to temperature variation, to simplify the analysis, it is assumed here that the temperature variation of d.c. resistivity is similar to a.c. resistivity. The voltage gradients will therefore remain unaltered.

Table VIII gives the heat input distribution in the various regions based on the d.c. conductivity values.

Table VIII. Calculation of heat input distribution in the slag bed using d.c. electrical conductivity

Region	a.c. electric conductivity ($ohm^{-1}cm^{-1}$)	amount of heat generated ($Kcal.sec^{-1}$)	d.c. electric conductivity =1.35 x a.c. electric cond. ($ohm^{-1}cm^{-1}$)	amount of heat generated ($Kcal.sec^{-1}$)	Total heat generated by resistance heating of the slag ($Kcal.sec^{-1}$)
A	2.46	0.295	3.32	0.40	0.40 + 1.72 + 2.16 + 1.485 + 0.665 = 6.43
B	2.85	1.27	3.85	1.72	
C	2.64	1.60	3.57	2.16	
D	2.30	1.10	3.11	1.485	
E	2.08	0.485	2.81	0.665	

V.3.4 Heat Generation Due to Polarization

As discussed earlier in Chapter II, in d.c. ESR process, both the ingot and electrode are polarized. Although polarization data is not available for EN 25 steel, it is not unreasonable to use the data for pure iron (Fig. (21)). Using this data, for the current densities existing on the electrode and ingot for d.c. negative configuration, one obtains $\eta \simeq 0.5$ V for both cathode and anode processes.

The amount of heat generated due to these polarizations = $0.5 \times 1150 \times .24 + 0.5 \times 1150 \times .24 = 0.275$ Kcal.sec^{-1}.

Adding the heat input values for resistance heating and polarization one gets

$$\text{heat input} = 6.43 + 0.275 = 6.705 \text{ Kcal.sec}^{-1}$$

The value of 6.705 Kcal/sec compares very favourably with 6.65 Kcal.sec^{-1} obtained from the electrical energy input data.

V.4 An Analysis of the Heat Transferred to Mold Cooling Water

V.4.1 Introduction

In order to carry out an accurate heat balance of the process, one must know the amount of heat transferred to mold cooling water at each point on the mold outer surface.

On examining the temperature distribution on the copper mold, it is clear that the temperature of the copper mold containing the liquid slag and metal pool is above the boiling point of water at atmospheric pressure. When the surface temperature exceeds the

saturation temperature, local boiling in the vicinity of the surface may take place even if the bulk water temperature is below the boiling point. The boiling process in a liquid whose bulk temperature is below the saturation temperature but whose boundary layer is sufficiently superheated that bubbles form next to the heating surface is usually called heat transfer to a subcooled boiling liquid or surface boiling.[35] Various mechanisms of heat transfer in surface boiling are put forward but the vapor-liquid mechanism[45] is the presently accepted mechanism as it is able to explain most of the observed phenomena.

Thus the analysis has to be carried out in the two regions of the mold/water interface which are separately in the:

1. non-boiling region
2. surface boiling region.

V.4.2 Non-boiling Region

V.4.2.1 Introduction

The final expressions obtained from more advanced analogies are very complicated and the evaluation of the Nusselt number under given flow and thermal boundary conditions usually requires a numerical integration. For this reason it is more convenient for the purpose at hand to use semi-empirical equations, or graphs based on advanced analogies. Secondly, as will be apparent subsequently, the amount of heat transferred to the cooling water in the non-boiling region, is quite small when compared to surface boiling region.

V.4.2.2 Calculation of the Reynolds Number

Tables IX and X give the experimental data and the relevant physical properties of water respectively.

$$\text{Reynolds number} = \frac{G\, D_H}{\mu}$$

where G = mass velocity of the fluid flowing through the annulus ($g.sec^{-1}cm^{-2}$)

$$G = \frac{W\ 4}{\pi[D_2^{\,2}-D_1^{\,2}]}$$

where W = water rate through the annulus ($g\ sec^{-1}$)

$$W = \frac{21 \times 10^3 \times 1}{60} = 350\ g\ sec^{-1}$$

D_1 and D_2 : dimensions of the annulus (cm)

$G = 5.87\ g\ sec^{-1}cm^{-2}$

D_H = hydraulic diameter (cm)

$$= \frac{4 \times \text{flow cross sectional area}}{\text{wetted perimeter}}$$

$= 3.55$ cm

μ = viscosity of water (poise)

$$Re = \frac{5.87 \times 3.55}{0.00657}$$

$\simeq 3200$

The flow is laminar when the Reynolds number is below 2100.[35] In the range of Reynolds number between 2100 and 10,000, the transition from laminar to turbulent flow takes place. The flow in this

Table IX. Experiment data for ingot no. 1 (Table V)

Inlet water temperature:	32°C
Outlet water temperature:	50°C
Water flow rate:	21 litres min^{-1}
Cross-sectional dimensions of the water jacket:	D_1 = 8.9 cm
	D_2 = 12.45 cm

Table X. Physical properties of water at 40°C-50°C

Coefficient of viscosity at 40°C:	0.00657 poise
Coefficient of viscosity at 50°C:	0.0055 poise
Specific heat:	1 cal $g^{-1}{}^{\circ}C^{-1}$
Thermal conductivity:	15.2 x 10^{-4} cal $cm^{-1}sec^{-1}{}^{\circ}C^{-1}$
Density:	1 g cm^{-3}

regime is called 'transitional'. At a Reynolds number of about 10,000, the flow becomes fully turbulent.

Thus the experimental flow rate is in the 'transitional region'. There are no well developed empirical formulae for this region. For the purpose of calculations, 'turbulent flow' condition will be assumed. Naturally, the heat transfer coefficient obtained in this way would be the upper limit.

V.4.2.3 Calculation of the Heat Transfer Coefficient in the Non-boiling Region

Colburn's equation[35] for heat transfer coefficient for turbulent flow in annular tubes is

$$St.(Pr)^{2/3} = 0.023\ (Re)^{-0.2} \qquad (5.1)$$

where St = Stanton number = $\frac{h_{nb}}{c_p G}$

Re = Reynolds number = $\frac{G\ D_H}{\mu_f}$

Pr = Prandtl number = $\frac{\mu_f\ c_p}{k_f}$

where all the symbols have the usual meaning.

To account for the variation in physical properties due to the temperature gradient, McAdams[35] recommends that all the physical properties except c_p be evaluated at the average film temperature of the fluid defined as

$$T_f = 0.5[T_s + T_b] \tag{5.2}$$

where T_s = surface temperature of copper (°C)

T_b = bulk water temperature (°C).

In the present case, both T_s and T_b are variables. However, for accuracy required in the present calculations, it is a reasonable approximation to assume $T_f \simeq 50°C$.

$$\frac{h_{nb}}{c_p G} = 0.023 \left[\frac{\mu_f}{D_H G}\right]^{0.2} \left[\frac{\mu_f c_p}{k_f}\right]^{-2/3} \tag{5.3}$$

substituting the values and simplifying, one obtains

$$h_{nb} = 1.15 \times 10^{-2} \text{ cal cm}^{-2}\text{°C}^{-1}\text{sec}^{-1} \tag{5.4}$$

Alternatively, Sieder and Tate[46] suggest the following empirical relationship to calculate h_{nb}:

$$\left[\frac{h_{nb} D_H}{k}\right]\left[\frac{c \mu}{k}\right]^{-1/3} \left[\frac{\mu_W}{\mu}\right]^{0.14} = 0.023 \left[\frac{D_H G}{\mu}\right]^{0.8} \tag{5.5}$$

All the physical properties are evaluated at the average bulk temperature of the water (≃40°C) except μ_W which is evaluated at the average surface temperature of the copper (≃60°C).

$$\mu_{W_{60°C}} = 0.00469 \text{ poise} \tag{5.6}$$

On substituting the values in (5.5) and simplifying, one obtains:

$$h_{nb} = 1.145 \times 10^{-2} \text{ cal cm}^{-2}{}^{\circ}\text{C}^{-1}\text{sec}^{-1} \qquad (5.7)$$

Thus one may approximate the heat transfer coefficient for the non-boiling region to be = 1.15×10^{-2} cal $cm^{-2}{}^{\circ}C^{-1}sec^{-1}$.

V.4.3 Surface Boiling Region

V.4.3.1 Introduction

The analysis for the heat transfer coefficient in the surface boiling conditions, is at present, semi-empirical.[45,47,48] In all cases, the analysis was carried out for distilled water. The normal tap water used as a coolant in the present experiments has a considerable amount of dissolved air. The solubility of air in water decreases with an increase of temperature. The air escapes in the form of bubbles. As a result of the increase in the bubble population, the agitation of the liquid caused by the motion of the bubbles is more intense. This increases the heat transfer from the mold wall to the cooling water quite significantly.

As a first step, the distilled water analysis will be considered.

The experimental data for forced convection without boiling can be correlated by a relation of the type[35]

$$Nu = \phi(Re)\ \psi\ (Pr) \qquad (5.8)$$

Eq. (5.8) can be modified for nucleate boiling into the form

$$Nu_b = \frac{h_b D_b}{k_\ell} = \phi(Re_b)\ \ \psi\ \ (Pr_\ell) \qquad (5.9)$$

where Pr_ℓ is the Prandtl number of the saturated liquid; h_b is the nucleate boiling heat transfer coefficient and $Re_b = \frac{D_b G_b}{\mu_\ell}$ is a measure of the agitation of the liquid in nucleate-boiling heat transfer

D_b = average bubble diameter (cm)

G_b = mass velocity of the bubbles per unit area (g $sec^{-1} cm^{-2}$)

μ_ℓ = viscosity of the liquid (poise)

The mechanisms of bubble formation and heat transfer are quite similar in nucleate and surface boiling and thus the analysis for nucleate boiling is applicable for surface boiling conditions.

Using experimental data, Rohsenow[47] modified eq. (5.9) by means of simplifying assumptions to obtain

$$\frac{C_\ell \Delta T_{sat}}{h_{fg}(Pr_\ell)^{1.7}} = C_{sf}\left[\frac{q/A}{\mu_\ell h_{fg}} \sqrt{\frac{g_c \sigma}{g(\rho_\ell - \rho_v)}}\right]^{0.33} \qquad (5.10)$$

where C_ℓ = specific heat of saturated liquid, BTU $lb^{-1} {}^\circ F^{-1}$

q/A = heat flux, BTU $hr^{-1} ft^{-2}$

h_{fg} = latent heat of vaporization, BTU lb^{-1}

g_c = gravitational acceleration, ft hr^{-2}

ρ_ℓ = density of saturated liquid, lb_m ft^{-3}

ρ_v = density of saturated vapor, lb_m ft^{-3}

σ = surface tension of the liquid-to-vapor interface, lb_f ft^{-1}

Pr_ℓ = Prandtl number of the saturated liquid

μ_ℓ = viscosity of the liquid, lb_m $hr^{-1} ft^{-1}$

C_{sf} = empirical constant which depends upon the nature of the heating surface/fluid combination (C_{sf} = 0.013 for a water/copper combination).

ΔT_{sat} = temperature excess of the heated wall over the saturated water temperature: $(t_w - t_{sat})$, °F

Fig. (60) gives the experimental plot obtained for (q/A) vs. ΔT_{sat} by Rohsenow.[47] Using eq. (5.10) for ΔT_{sat} = 10°C (18°F), one obtains

$$q/A = 1.5 \times 10^3 \text{ BTU/sq.ft.hr.} \tag{5.11}$$

However, from fig. (60) the value is

$$q/A = 2.2 \times 10^4 \text{ BTU/sq.ft.hr.} \tag{5.12}$$

Thus the (5.10) does not fit the experimental data very accurately.

Fig. (61), as plotted by Rohsenow clearly shows all the experimental points for 14.7 PSIA lying above those predicted by eq. (5.10).

Using Engelberg-Forster and Grief's[45] analysis, for ΔT_{sat} = 10°C (18°F) one obtains

$$(q/A) = 4 \times 10^4 \text{ BTU ft}^{-2}\text{hr}^{-1} \tag{5.13}$$

Fig. (60) shows the plot for (q/A) vs. ΔT_{sat} obtained from Engelberg-Forster and Grief's analysis superimposed on Rohenow's experimental data.

McAdams et al.,[48] in their analysis use the following expression:

$$(q/A) = c' \Delta t_{sat}^{3.86} \qquad (5.14)$$

where both c' and 3.86 were determined empirically as 'best fits' to the experimental data.

From the above discussion it is very clear that the predicted correlations are very approximate and that the best approach is to use the experimental plot obtained by Rohsenow[47] (Fig. (60)).

V.4.3.2 Effect of Dissolved Air

As mentioned earlier, all the previous analyses were carried out for distilled water. The evolution of air bubbles increases the heat flux. There is no detailed study made as yet which would predict the resulting increase in heat flux. McAdams et al.[48] have experimentally determined the effect of dissolved air on the heat flux (Fig. (62)). In the present analysis a similar increase in flux will be assumed.

The total heat flux in surface boiling region = $q_{surface\ boiling} + q_{convection}$. The experimental (q/A) values used here give the total heat flux for surface boiling.

V.4.4 Calculations

V.4.4.1 Introduction

Figure (63) gives the plot for (q/A) vs. ΔT for both non-boiling and surface boiling conditions. ΔT in Fig. (63) is the temperature difference between copper mold and bulk water temperature.

Curve 1 in Fig. (63) represents the relation between (q/A) and ΔT for non-boiling conditions. It is obtained by using the value of h = 1.15×10^{-2} cal $cm^{-2} sec^{-1} {}^{\circ}C^{-1}$.

Curve 2 represents the relation between (q/A) and ΔT for surface boiling, using distilled water. This plot was obtained from the experimental data of Rohsenow.[47] The water temperature is assumed to be 50°C.

Curve 3 gives the correlation between (q/A) and ΔT for surface boiling, using tap water (containing dissolved air). This is drawn similar to the experimentally obtained curve of Fig. (62).

Using Fig. (63) it is now possible to calculate the amount of heat transferred to mold cooling water at every section.

The calculations will be carried out for Ingot No. 1. Fig. (49) gives the experimentally obtained temperature profile on the copper mold for Ingot No. 1. The curve will be subdivided into three regions A, B and C as shown in the figure. Regions A and C have non-boiling conditions whereas in region B surface boiling is present.

V.4.4.2 Region A

The average water temperature in this region = 32°C. The outside radius of copper mold = 4.45 cm. The height of the copper mold will be subdivided into elements 0.5 cm high and it will be assumed that each element has a constant temperature. For each element

$$q = h A \Delta T$$

where $h = 1.15 \times 10^{-2}$ cal. $cm^{-2} sec^{-1} {}^{\circ}C^{-1}$

$$A = 2\pi r\ell \quad cm^2$$

$$\Delta T = T_{copper} - 32.0, (°C)$$

$$= 2 \times \pi \times 4.45 \times 0.5$$

$$= 14 \ cm^2$$

$$\sum_i^n q = h A \sum_i^n \Delta T_i$$

$$= 0.161 \sum_i^n \Delta T_i$$

Region A is 30 cm high (i.e. 60 ΔT terms)

$$\sum_i^n q = 0.161[3 \times 30 + 4 \times 4 + 4 \times 6 + 8 \times 4 + 11 \times 4 + 14 \times 4 + 19 \times 4 + 25 \times 4 + 32 \times 4 + 39 \times 4]$$

$$= 0.161 \times 876$$

$$q_A = 0.141 \ Kcal \ sec^{-1}$$

V.4.4.3 Region C

Average temperature of water = 50°C, height of region C = 29.0 cm. A calculation similar to that performed for region A leads to

$$q_C = 0.102 \ Kcal \ sec^{-1}$$

Therefore, the total heat transferred to cooling water in the non-boiling region = $0.141 + 0.102 = 0.243 \ Kcal \ sec^{-1}$.

V.4.4.4 Region B

Average temperature of water = 50°C, total length of the region B = 16 cm.

In figure (63) the location of the curves 2 and 3 depends upon the water temperature. The water temperature is assumed to be 50°C, as from Fig. (57) it is clear that the water temperature in the surface boiling region rapidly increases to 50°C and then remains approximately constant.

$$q_B = \sum_{i=1}^{32} q_i = A \sum_{i=1}^{32} h_i \Delta T_i$$

where $A = 14\ cm^2$.

From Fig. (63), the values for $h\Delta T$ (= q/A) are read for ΔT of each element

$$\begin{aligned} q_B &= 14\ [2 \times 0.75 + 2 \times 1.5 + 2 \times 5 + 2 \times 14 + 12 \times 22.5 \\ &\quad + 2 \times 21.5 + 2 \times 15 + 2 \times 8 + 2 \times 3.5 + 2 \times 1.6 \\ &\quad + 2 \times 0.65] \\ &= 14 \times 413.0 \\ &= 5.782\ \text{Kcal sec}^{-1}. \end{aligned}$$

Total amount of heat given to mold cooling water

$$\begin{aligned} &= q_A + q_B + q_C \\ &= 6.025\ \text{Kcal sec}^{-1} \end{aligned}$$

From Fig. (63), it is clear that the present heat distribution analysis critically depends upon the curve 3 which is empirically obtained. The following calculations justify the location of curve 3 in Fig. (63).

(1) Knowing the cooling water flow rate and rise in water temperature, it is possible to calculate the total heat accumulated by the cooling water

water flow rate: 20.5 - 21 litres min^{-1}

specific heat of water: 1 cal $g^{-1}{}^{\circ}C^{-1}$

density of water: 1 g cm^{-3}

ΔT water: 18°C

q = flow rate x density x sp. heat x ΔT

= 6.15-6.3 Kcal sec^{-1} for a flow rate of 20.5 and 21.0 litres min^{-1} respectively.

With the existing accuracy in flow rate and ΔT measurement, the agreement with the value of 6.025 Kcal sec^{-1} obtained from Fig. (63) analysis appears to be very good.

(2) According to the present location of curve 3, the maximum heat flux going to the cooling water (near the slag/metal interface) has a value of

$$(q/A) = 22.5 \text{ cal } cm^{-2} sec^{-1}$$

$$q/A = h \Delta T$$

$$h\Delta T = 22.5 \text{ cal } cm^{-2} sec^{-1}.$$

In the 'copper cylinder' experiments discussed in Chapter IV, the value of the overall heat transfer coefficient was obtained as 1.28×10^{-2} cal $cm^{-2}{}^{\circ}C^{-1} sec^{-1}$ with $\Delta T = 1610°C$

$$q/A = 1610 \times 1.28 \times 10^{-2} = 20.6 \text{ cal } cm^{-2} sec^{-1}.$$

As the two values of (q/A) obtained from the two different analysis are quite close (7-8% error) one is justified in using Fig. (63)

in spite of the empirical derivation of the curves.

V.5 A Detail Analysis of the Heat Distribution in the Laboratory ESR Unit

V.5.1 Indroduction

As most of the previous calculations were done for I.N. 1, the present analysis will also be carried out for the experimental conditions of ingot no. 1.

The total heat input into the unit, as calculated earlier is 6.65 Kcal/sec.

Fig. (64) gives the possible ways this heat leaves the unit.

V.5.2 Heat Balance of the Slag Bed Region

V.5.2.1 Heat Input

As all the heat is generated in the slag bed, the total heat input in the slag bed region = 6.65 Kcal/sec. Fig. (65) gives the heat generation distribution in the slag bed as calculated earlier in this chapter.

V.5.2.2 Heat Output

V.5.2.2.1 Heat Required to Melt the Electrode

Q_{1A}, cal sec^{-1}

melt rate in I.N. 1 = 3.0 cm/100 sec of electrode travel

length of the electrode melted = $\frac{3.81}{2.81}$ x 3.0 = 4.06 cm/100 sec.

length of the electrode melted in 1 second = 0.0406 cm.

Although the electrode gets heated by conduction, convection and radiation gradually; in steady state, when the temperature of the electrode far away from the slag surface is at room temperature, one can assume that 0.0406 cm length of the electrode was heated from room temperature to melting point in one second.

Table (XVI) gives the average physical properties of iron used in the calculation. As the data on the physical properties of EN 25 steel was not available, the average physical properties of iron are used (except for melting point).

Mass of the electrode melted in one second

$$= \pi r^2 \ell \rho$$

$$= 3.36 \text{ g sec}^{-1}$$

$$Q_{1A} = m c_p \Delta T + m L$$

$$= 1000 \text{ cal sec}^{-1}$$

V.5.2.2.2 Heat Lost by Radiation from the Slag Surface: Q_2, cal sec^{-1}

The heat lost by radiation from the slag surface Q_2 can be subdivided (fig. (66)) into:

Q_{2A} = heat radiated to the water cooled copper mold

Q_{2B} = heat lost to air or gases

Q_{2C} = heat radiated to the electrode.

Q_{2C} has already been considered in the heat taken up for heating of the electrode.

Q_{2B} is the heat carried away by the air or the gases present. A significant part of the heat acquired by the gases is however lost by

convection to the copper mold and the electrode. As it is difficult to calculate the net heat carried away by the gases it is a reasonable assumption to have Q_{2B} = 0.0 cal sec^{-1}.

Heat lost by radiation from the slag surface to copper mold: Q_{2A}

The temperature profile on the copper mold above the slag/gas inferface is known (fig. (49)). Q_{2A} can be calculated using Fig. (63)

$$Q_{2A} = 14[2 \times 8 + 2 \times 3.5 + 2 \times 1.6 + 2 \times 0.65] + 102.0$$

$$= 487 \text{ cal } sec^{-1}.$$

V.5.2.2.3 Heat Lost to Cooling Water Across the Slag Bed: Q_3, cal sec^{-1}

Using Fig. (63) and Fig. (49), Q_3 can be calculated similar to previous calculations.

$$Q_3 = 14[5 \times 22.5 + 2 \times 21.5 + 2 \times 15]$$

$$= 2597.0 \text{ cal } sec^{-1}.$$

V.5.2.2.4 Heat Picked up by the Falling Liquid Metal Drops: Q_{1B}, cal sec^{-1}

Assuming that the liquid metal droplets are superheated by 100°C during their descent through the slag bed, the amount of heat picked up by the droplets:

$$Q_{1B} = C_{p\ell} \times m \times \Delta T$$

$$= 0.18 \times 3.36 \times 100$$

$$= 60.5 \text{ cal } sec^{-1}.$$

$$Q_{4A} = Q_{1A} + Q_{1B} = 1000 + 66.5$$

$$= 1060.5 \text{ cal sec}^{-1}.$$

Although Q_{4A} is the heat consumed in melting the electrode and its subsequent heating, it is not lost. It enters the liquid metal bed as sensible heat. Thus for calculating the total transferred across the slag/metal interface, this heat has to be considered.

Fig. (67) gives a block diagram for the heat balance of the slag region.

The amount of heat leaving across the slag/metal interface per second

$$= 6650 - 487 - 2597$$

$$= 3566 \text{ cal sec}^{-1}.$$

Amount of heat transferred across the slag/metal interface by convection per second

$$= 3566 - 1060.5$$

$$Q_{4B} \simeq 2505.5 \text{ cal sec}^{-1}$$

V.5.2.3 Heat Distribution in the Slag Bed

V.5.2.3.1 Introduction

Following the calculation of the heat balance for the entire slag bed, it is interesting to see how the heat is distributed in the various regions of the slag bed.

The slag bed can be subdivided into two regions, above and below the electrode tip.

V.5.2.3.2 Heat Balance of the Region Above the Electrode Tip

Consider the heat balance of region AJKB (Fig. (65)).

Heat Input: $Q_A + Q_D + Q_E$ + heat generated in the cathodic polarization

$= 400 + 1485 + 665 + 137$

$= 2687 \text{ cal sec}^{-1}$.

Heat Output: $Q_{1A} = 1000 \text{ cal sec}^{-1}$

$Q_{2A} = 487 \text{ cal sec}^{-1}$

Q_{3A} = heat going to mold cooling water across the slag bed = $14[2 \times 15 + 2 \times 21.5 + 22.5]$

$= 1337.0 \text{ cal sec}^{-1}$

Total heat output = $1337 + 1000 + 487$

$= 2824 \text{ cal sec}^{-1}$

Amount of heat obtained by this region from the lower region JKCD by convection

$= 2824 - 2687$

$= 137 \text{ cal sec}^{-1}$.

V.5.2.3.3 Heat Balance of the Region Below the Electrode Tip

Heat Input: $Q_B + Q_C$ + heat generated in anodic polarization

$= 1720 + 2160 + 137 = 4017 \text{ cal sec}^{-1}$

Heat Output: Q_{3B} = heat going to mold cooling water across the slag bed = $14[4 \times 22.5]$

$= 1260 \text{ cal sec}^{-1}$.

Q_{1B} = heat required to super heat the falling liquid metal drops by 100°C = 60.5 cal sec^{-1}

heat transferred to AJKB region by convection = 137 cal sec^{-1}

Total heat output = 1260 + 60.5 + 137

= 1457.5 cal sec^{-1}

heat transferred by convection across the slag/metal interface = 4017 - 1457.5

= 2559.5 cal sec^{-1}.

The difference of 54.0 cal sec^{-1} observed in the two analyses, is the error involved in the heat input distribution analysis.

V.5.3 Approximate Calculation of the Heat Transfer Coefficient Across the Liquid Slag-Liquid Metal Interface

The amount of heat transferred across the liquid slag-liquid metal interface $\simeq$ 2500 cal sec^{-1}

$$q = h.A.\Delta T$$

where $A = \pi r^2 \simeq 50\ cm^2$

Assuming (1) uniform heat transfer coefficient across the section; (2) uniform temperature in the slag and metal bath across the entire cross section at the slag/metal interface, one can write

$$h\Delta T = \frac{q}{A} = \frac{2500}{50} = 50\ cal\ cm^{-2} sec^{-1}$$

If ΔT = temperature difference between liquid slag and metal $\simeq$ 25-50°C

$$h = 1 - 2 \text{ cal cm}^{-2}{}^{\circ}\text{C}^{-1}\text{sec}^{-1}.$$

V.5.4 Heat Balance of the Liquid Metal Region

Fig. (68) gives the block diagram for the heat balance of the liquid metal region.

Heat Input: $Q_4 = Q_{4A} + Q_{4B}$

$= 3566.0 \text{ cal sec}^{-1}.$

Heat Output: The amount of heat going to mold cooling water across

$CN = Q_5 = 14[7 \times 22.5 + 1 \times 14]$

$= 2401 \text{ cal sec}^{-1}.$

Heat leaving the section ON downwards

$Q_9 = Q_4 - Q_5$

$= 3566.0 - 2401.0$

$= 1165.0 \text{ cal sec}^{-1}.$

V.5.5 Heat Balance of the Solidified Ingot Region

Fig. (69) gives the block diagram for the heat balance of this region.

V.5.5.1 Heat Input: $Q_9 = 1165.0$ cal/sec

V.5.5.2 Heat Output:

V.5.5.2.1 Heat Going to Mold Cooling Water; Q_6, cal sec^{-1}

$Q_6 = 14[2 \times 0.75 + 2 \times 1.5 + 2 \times 5 + 1 \times 14] + 141$

$= 540 \text{ cal sec}^{-1}.$

V.5.5.2.2 Heat Going to Base Plate Cooling Water: Q_7

Fig. (58) gives the experimentally obtained temperature profiles with respect to slag/metal interface position for two thermocouples located at the base of the ingot, known distance apart.

$$Q_7 = \frac{k\,A}{\Delta x}\ \Delta T$$

where k = average thermal conductivity of iron

$= 0.075$ cal $cm^{-1} sec^{-1} {}^{\circ}C^{-1}$

A = cross sectional area $= 34.4\ cm^2$

Δx = distance between the two thermocouples = 1 cm

The present heat balance is carried out after a significant amount of ingot has been formed. Therefore the value of ΔT = difference in temperature between the two thermocouples = 160°C.

$$Q_7 = \frac{34.4 \times .075}{1.0} \times 160$$

$$Q_7 = 410 \text{ cal } sec^{-1}.$$

V.5.5.2.3 Sensible Heat Retained by the Ingot: Q_8

Under steady state conditions, all the heat supplied in the slag region is taken away by the mold and base plate cooling water except that which is retained in the solidified ingot as sensible heat. The sensible heat of the escaping gases is neglected in the present analysis.

Amount of heat retained as sensible heat by the ingot/sec = Q_8

= mass of ingot formed per sec x C_p x ΔT

where ΔT = average temperature of the ingot

$$Q_8 = 3.36 \times 0.16 \times \Delta T$$
$$= 0.538 \times \Delta T \text{ cal sec}^{-1}.$$

The value of ΔT is unknown and one must make a reasonable estimate.

Assuming $\Delta T = 750°C$

$$Q_8 = 0.538 \times 750$$
$$Q_8 = 404 \text{ cal sec}^{-1}.$$

V.5.5.2.4 Total Heat Output

The total heat output $= Q_6 + Q_7 + Q_8$
$= 540 + 410 + 404$
$= 1354 \text{ cal sec}^{-1}.$

The difference in heat input and output values is only 188.5 cal sec^{-1}.

With the various approximations and assumptions made, a difference of 188.5 cal sec^{-1} for a total heat input of 6650 cal sec^{-1} is less than 3% and this is well within the accepted limits.

V.5.6 Heat Balance for Ingot Nos. 1, 10 and 16

Table XI gives the heat balance for ingots made with d.c. negative, d.c. positive and a.c. polarities.

V.6. Discussion

V.6.1 Comparison of the Different Electrical Configurations

As mentioned earlier, there has been a considerable disagreement between different workers on the efficiency of the ESR process for

Table XI. Heat balance for ingot no. 1, 10 and 16

Ingot No.		1	10	16
Melt rate g sec^{-1}		3.36	2.58	3.50
Dimensions (cm) refer Fig.(64)	X	1.5	0.4	0.25
	Y	1.0	1.6	0.85
	Z	4.5	4.5	3.1
	A	2.5	0.75	0.5
	B	1.5	2.00	2.5
Heat Input cal sec^{-1}		6650	5100	4800
Heat Output Q_1 (cal sec^{-1})		1060.5	785	1110
	%	15.6%	15.50%	23.3%
Q_{2A} (cal sec^{-1})		487	738	637.2
	%	7.15%	14.5%	13.4%
Q_3 (cal sec^{-1})		2597	2606	1872.5
	%	38.0%	51.4%	39.4%
Q_4 (cal sec^{-1})		3566.0	1756	2290
	%	52.3%	34.6%	48%

Table XI. (Continued)

Ingot No.	1	10	16
Q_{4A} (cal sec^{-1})	1060.5	785	1110
%	15.6%	15.5%	23.3%
Q_{4B} (cal sec^{-1})	2505.5	971	1180
%	36.7%	19.10%	24.7%
Q_5 (cal sec^{-1})	2401	704	1081.5
%	35.1%	13.7%	22.6%
Q_6 (cal sec^{-1})	540	316	333
%	7.8%	6.2%	7.0%
Q_7 (cal sec^{-1})	410	410	410
%	6.1%	8.10%	8.7%
Q_8 (cal sec^{-1})	404	310	420
%	5.85%	6.1%	8.9%

different electrical configurations. The efficiency of the process is usually expressed in terms of the amount of metal remelted per KWH. Using the available experimental data, an attempt is made here to explain the observed differences.

There are 9 possible different types of electrical configurations.[36]

(1) d.c. with electrode as the negative pole (commonly referred to as d.c. negative).

(2) d.c. with electrode as the positive pole (commonly referred to as d.c. positive).

(3) a.c.

Each of these can have the mold (a) insulated from the ingot or (b) floating or (c) connected to the ingot (referred to as 'live'). Fig. (42) gives the schematic diagrams for the different arrangements.

In the present set of experiments, the remelting of the ingots was carried out with the process parameters (i.e., voltage, current and melt rate) so adjusted, as to achieve stable operating conditions. An attempt was made to maintain approximately the same melt rate for the different electrical configurations under similar conditions. However in cases where the process became unstable while attempting a constant melt rate, the process parameters were so adjusted as to achieve stable remelting conditions.

Ingots 1, 10, 13 and 16 can be compared to study the effect of electrical configuration. Attempt was made here to achieve a constant melt rate of approximately 3.4-3.5 g sec^{-1} (30 mm of electrode travel for every 100 seconds). This was achieved in both d.c. negative and a.c. In the present set of experiments, the voltage was kept approximately

constant (20-24 volts). It was observed that to achieve a similar melt rate, it was necessary to maintain a similar gap (≃ 2.0 cm) between the electrode tip and the slag/metal interface in the two cases. As discussed earlier, for the same slag and similar geometry, the working resistance of the d.c. -ve operation slag is 35% less than the a.c. case. This is due to the presence of the dissolved calcium and aluminum in the slag. This results in a higher current input in the d.c. -ve configuration as compared to a.c. (1150 amp for d.c. -ve and 850 amp for a.c.).

It is now possible to explain the observed deep cylindrical portion of the liquid metal pool in d.c. negative configuration (Fig. (80), Fig. (84)). To maintain a dynamic steady state, it is necessary to remove the extra heat introduced in the slag bed in the d.c. negative case. It has been shown earlier that the amount of heat transferred to the mold cooling water across the liquid slag bed is quite insensitive to the extent of heat produced in the slag bed. Thus the extra heat produced is transferred to the mold cooling water by maintaining a deep cylindrical portion of the liquid metal pool which has a good surface contact with the mold.

It was found that in both d.c. positive with mold 'floating' and 'live', it was not possible to achieve the desired melt rate of ≃3.4 g sec^{-1} under stable working conditions. On examining the extent of electrode immersion it was found that for the stable working of the unit it was necessary to maintain a larger gap between the electrode tip and slag/metal inferface (2.6 cm for ingot no. 10 and 2.3 cm for ingot no. 13). The total power input was also correspondingly less. Thus the low melt rate (≃2.58 g sec^{-1}) obtained was a result of the low power

input and the large gap between the electrode tip and the slag/metal interface. The necessity of maintaining these to obtain stable working conditions can be explained as follows.

Fig. (70) gives the ESR unit's analog circuit. Table IV gives the experimental results and the values of the various resistances as calculated by Cameron et al.[36]

There are two paths for the flow of current in Fig. (70)

(1) electrode → liquid slag → ingot
(working resistance)

(2) electrode → mold → ingot.

The magnitude of the current following in each circuit depends on the relative values of the resistances R_1, R_2 and R_3. Resistances R_1 and R_3 are in series and they together are in parallel with R_2.

In the case of d.c. positive with mold floating, the potential on the mold was experimentally determined as ≈18 V (Table XII).[36] The flow of current is as shown in Fig. (70a). The observed value of 18 V on the mold can be explained. Under stable working conditions the electrode is not significantly immersed in the slag bath. The temperature at the slag/gas interface is quite high. The value of the resistance R_1 is quite low as new slag skin is continuously formed at the slag/gas interface having a momentary low value of resistance. The voltage drop of 5 volts occurs mostly in the slag bath between the electrode and the slag skin as shown in Chapter II. Table IV gives the calculated values of R_1, R_2 and R_3.

There is thus a considerable potential difference between the mold and the ingot. Arcing would occur between the mold and the ingot

Table XII. Experimental results for the insulated mold unshunted and shunted to ground through 0.5 ohm resistor[36]

Ingot Size	Slag System	Applied Voltage	Electrode Polarity	Mold Potential	Unshunted Current	Mold Potential 1/2 shunt to ground	Shunted Current	Slag skin Average thickness
2"	CaF_2	23.7	-ve	22.4	672	20.5	704	0.040"
2"	CaF_2 + CA	24.5	-ve	21.9	688	20.1	720	0.025"
2"	CaF_2 + CA	22.8	+ve	19.0	640	15.4	710	0.035"
3"	CaF_2	22.5	-ve	18.7	1 220	17.3	1 300	0.040"
3"	CaF_2 + CA	22.8	-ve	20.6	1 200	18.6	1 265	0.030"
3"	CaF_2 + CA	22.5	+ve	17.0	1 200	16.1	1 240	0.035"

if significant amount of current flows through via path 2. To avoid this, the value of R_3 should be maintained high. The existence of a deep cylindrical portion of the liquid metal pool results in a low value of R_3. Thus to achieve stable working conditions, the working parameters are so adjusted as to avoid the existance of a deep cylindrical portion of the liquid metal pool. This is achieved by maintaining a larger gap between the electrode tip and the slag metal interface resulting in lower power input and hence a lower melt rate.

If the argument put forward here is true then for the d.c. positive case with insulated mold, it should be possible to achieve a melt rate comparable to a.c. and d.c. negative configurations. The mold was insulated by coating the inside surface of the mold with boron nitride paste and allowed to dry. Comparing FVE ingots 25, 28, 29, 31, 32 it is found that the melt rates are comparable.

In the case of d.c. positive with live mold, as the ingot and the mold are connected, they are both at the same potential (= 0 volts) with R_3 = 0 ohms. The potential difference between the mold and the electrode is 23.0 volts. As the value of R_1 is quite low, significant portion of the current goes to the mold (as much as 80% as shown in Fig. (46)). The effect of the horizontal current component on the magnetohydrodynamics of the region is not yet clear, but is outside the scope of the present work. Metal drops are drawn towards the mold by the horizontal current component and are embedded in the slag skin. Continuous arcing occurs between the mold and the slag bath and is unavoidable. The melt rate is low as the current going to the mold is not effectively used to heat the slag bath.

In the d.c. negative case with mold floating, it was found that the mold had a potential of 21 volts. This is expected since the value of R_3 is low due to the existance of a deep cylindrical portion of the liquid metal pool. There is thus a significant potential difference between the electrode and the mold. To avoid arcing between the mold and the slag, the value of R_1 is maintained high. This is achieved by maintaining the electrode deeply immersed in the slag bath (2.5 cm in ingot no. 1). This decreases the temperature at the slag/gas interface resulting in a thicker slag skin at the slag/gas interface. Comparing the values of R_1, R_2 and R_3 (Table IV) it is seen that the value of R_1 is maintained high (0.7 ohms) for d.c. negative as compared to d.c. positive (0.15 ohms). The value of R_3 on the other hand is low for d.c. negative (0.1-0.2 ohms) as compared to d.c. positive (0.4-1.0 ohm).

As there exists, only a slight potential difference between the mold and ingot in d.c. negative with mold 'floating', there is no significant difference observed between operations using d.c. negative with 'floating' mold and 'live' mold configurations. In the case of insulated mold, as there is no problem of mold-slag arcing, it is possible to operate having the electrode only slightly immersed in the slag bath.

Measurement of the current flowing through the circuit, electrode→mold→ingot for a.c. with mold 'floating and 'live' has shown that only a very small fraction of the total current flows through this circuit. This is expected since the slag skin is always thick in operations using a.c. mode thereby maintaining a high value for both R_1 and R_3.

V.6.2 Effect of the Electrochemical and Chemical Reactions

In the electroslag remelting of FVE electrodes, Mitchell and Beynon[12] have shown that the following electrochemical reactions occur at the two poles using CaF_2-25 wt.% Al_2O_3 slag.

Reactions at the cathode

$$\begin{aligned} &(1)\quad Al^{+++} + 2e \longrightarrow Al^{+} \\ &(2)\quad Al^{+++} + 3e \longrightarrow Al \\ &(3)\quad Ca^{++} + 2e \longrightarrow Ca \end{aligned} \qquad (5.15)$$

Reaction at the anode

$$(1)\quad Fe \longrightarrow Fe^{++} + 2e$$

In the case of remelting of EN 25 steel, the following reactions also may occur at the anode

$$\begin{aligned} &Cr \longrightarrow Cr^{++} + 2e \\ &Cr \longrightarrow Cr^{+++} + 3e \\ &Mn \longrightarrow Mn^{++} + 2e \\ &Si \longrightarrow Si^{4+} + 4e \qquad \text{etc...} \end{aligned} \qquad (5.16)$$

In the electro-positive configuration, the anodic reactions occur at the electrode, i.e. Fe, Cr, Mn, etc. are oxidized at the electrode.

At the ingot surface, the cathodic reactions (reduction of Al^{+++} and Ca^{++}) occur. The anodic reaction product, due to convection and

higher density, comes in contact with the cathodic reaction product and reduction of Fe, Cr, Mn, etc. occurs

$$\begin{array}{lllll} Al & Fe^{++} & \longrightarrow & Fe & Al^{+++} \\ Ca & Cr^{+++} & & Cr & Ca^{++} \\ Al^{+} & Si^{4+} & & Si & \\ & Mn^{++} & & Mn & \end{array} \qquad (5.17)$$

There is no net change in the slag composition if the back reaction (5.17) is complete. However it is found that this reaction does not go to completion, resulting in a net change of the slag composition.

Table (VI) gives the analysis of the ingot and the electrode compositions. It can be seen that remelting with d.c. positive always results in the loss of the alloying element chromium (reduced from $\simeq$ 0.7 wt.% to $\simeq$ 0.2 wt.%). This is due to the incompletion of reaction (5.17). As the oxidation is electrochemical in nature, it does not depend upon the atmosphere present.

In the ESR remelting using d.c. negative, the situation is quite different. At the electrode, the cathodic reduction of Ca^{++} and Al^{+++} occurs. As the liquid metal is present on the electrode in the form of a thin film, the reduced aluminum is very effectively dissolved in the liquid metal before it falls down as a droplet. At the ingot site, the anodic oxidation of Fe, Cr, Mn, Si, etc. occurs. However, as the aluminum is dissolved to a considerable extent in the liquid metal, the back reaction (5.17) occurs very effectively. There is thus practically no change in the slag composition. Here it was assumed that an argon atmosphere prevailed over the slag to avoid atmospheric

oxidation of the reduced Al and Ca. The ESR remelted ingots under argon using d.c. negative configuration show no loss of alloying elements as can be seen from Table (VI).

In ESR processing in air using d.c. negative configuration, it is found that there is a loss of the alloying element chromium on remelting. This can be easily explained.

Etienne[9] has shown the existance of the convection patterns in the slag at the slag/air interface of the type which may suggest that a significant amount of the electrochemically reduced Al and Ca has an opportunity to become reoxidized by the atmospheric oxygen. This oxidation prevents the effective reduction of the anodic product at the ingot resulting in the loss of alloying element chromium (reduced from ≈0.7 wt. % to ≈0.2 wt. %).

It is proposed by Mitchell and Beynon[12] that in the a.c. electroslag remelting of pure iron (FVE), reaction (5.18) occurs at both the ingot

$$Fe \rightleftharpoons Fe^{++} + 2e \qquad (5.18)$$

and electrode surfaces. More experimental data is needed to draw any definite conclusions regarding the effect of the atmosphere in this configuration.

V.6.3 Effect of Polarity on the Slag Skin Thickness

It is interesting to study the effect of the polarity on the thickness of the slag skin. Fig. (71) and (72) show pictures of the vertical section of the slag cap and the slag skin formed.

It is observed that in the remelting of pure iron (FVE) using d.c. positive (both air and argon) and d.c. negative (air), the slag skin is extremely thin. There is also a considerable amount of iron oxide at the bottom of the slag cap. The above observations can be explained in terms of the electrochemical and chemical reactions discussed earlier. In all the three cases, the back reaction (5.17) does not occur very significantly. This builds up the iron-oxide content in the slag bed. This iron-oxide attacks the alumina rich slag skin and dissolves it partially, forming a low melting eutectic. This results in a thin slag skin. This can also be varified from the experimental data of Table (V). It is observed that d.c. positive (argon and air) and d.c. negative (air) melts have a thicker slag cap after remelting approximately the same length of the electrode.

In remelting EN 25 steel, the presence of chromium oxide prevents the formation of lower melting eutectic. The slag skin is therefore not very thin.

V.6.4 Correlation and Prediction of Operating Parameters for Electroslag Processing

In industry, very often, large scale ingots have to be made without carrying out trial runs to establish the working conditions. One is therefore interested in knowing the approximate process parameters (i.e. current, voltage and melt rate) for remelting these large scale ingots. An attempt is made here to predict these process parameters for the industrial scale ingots from the available laboratory and industrial data.

On observing the temperature profiles on the mold for the various electrical and geometrical configurations (Fig. (49) to Fig. (56)), it is clear that the temperature profiles on the mold and hence the amount of heat going to the mold cooling water per unit area does not depend upon the electrical and the geometrical configurations. It is thus possible to assume an approximate temperature profile on the mold and calculate the heat input for any industrial scale ingot. Appendix (IV) gives the detail calculation of the power requirement for a 61 cm (24 inches) diameter ingot.

The melt rate depends upon the following parameters:

(1) slag composition

(2) electrode composition

(3) electrical configuration

(4) atmosphere

(5) diameter of the electrode

(6) diameter of the ingot

(7) distance between the electrode tip and the slag/metal interface.

Empirical equations are available in literature[49,50] giving the dependence of the melt rate on the power input, electrode diameter etc.

Klein[49] gave the following empirical equation to fit his experimental data for Hastelloy X ingots

$$R = -2.64 + 0.473\ D + 0.391 \times 10^{-3} I + 0.689 \times 10^{-1} E - 0.0558\ S \qquad (5.19)$$

where R = melt rate (lb min^{-1})

D = electrode diameter (inches)

I = current (amperes)

E = voltage (volts)

S = slag weight (lbs)

The equation (error $\pm$ 20%) was only valid for a narrow range of ingot sizes.

Sun and Pridgeon[50] arrived at the following empirical equation:

$$R = 0.3\ E_D + 1.57 \times 10^{-3} I - 0.18\ S_G - 1.167 \qquad (5.20)$$

where R = melt rate (ft hr^{-1})

E_D = ingot diameter (inches)

I = current (amperes)

S_G = slag weight (lbs).

The above equation was valid for (1) $2.75 < E_D < 4.25$, (2) $1.85 < I \times 10^{-3} < 3.0$, (3) $7.0 < S_G < 9.3$ ranges.

Present analysis

The melt rate can be correlated to the other process parameters in the following manner

$$M.R \quad \alpha \quad \frac{V^a I^b d^c}{D^e (\ell/D)^f} \qquad (5.21)$$

where M.R = melt rate (g sec^{-1})

V = applied voltage (volts)

I = current x 10^{-3} (amperes)

d = diameter of the electrode (cm)

D = diameter of the ingot (cm)

ℓ = distance betweeen the electrode tip and the slag/metal interface (cm).

For an approximate correlation, one can assume $a = b = f \simeq 1.0$ and $c = e \simeq 2.0$.

Relation (5.21) reduces to

$$M.R \propto \frac{V I d^2}{D^2 (\ell/D)} \tag{5.22}$$

or

$$M.R = \text{constant} \quad \frac{V I d^2}{D^2 (\ell/D)}$$

or

$$Z = \frac{V I d^2}{D^2 (\ell/D) MR} \tag{5.23}$$

where Z is a constant. The value of Z depends upon the slag composition, electrode composition, electrical configuration and the atmosphere.

Before going into the details of establishing the validity of equation (5.23), the general form of the equation will be discussed.

The units of the constant Z are K cal g^{-1}. Thus one would expect a higher value for Z, higher the melting point of the material being remelted.

In equation (5.23) it is proposed that, the other parameters remaining constant, the melt rate is proportional to the square of the electrode diameter. As most of the heat necessary to melt the electrode is transferred to the electrode by convection, it is logical to expect the melt rate to be proportional to the cross-sectional area of the electrode.

The correlation that the melt rate is inversely proportional to

the square of the ingot diameter can be qualitatively justified. Keeping a constant (d/D) ratio, an increase in the diameter of the ingot by a factor of 2 results in a similar increase in power input. This is justified since most of the heat leaves the ESR unit through the side walls of the mold to the mold cooling water. The increase in surface area of the mold wall is proportional to the diameter of the ingot. However as some heat also leaves through the mold bottom, an increase in the diameter of the ingot by a factor of 2, keeping the (d/D) ratio constant will result in an increase in the power input and hence the melt rate by a factor of 2.0 to 2.2.

Fig. (73) gives the experimentally obtained correlation between the melt rate and the ingot diameter by Holzgruber et al.[6] From Fig. (73) one can see that an increase in the diameter of the ingot from 15 inches to 30 inches, results in an increase in the melt rate from 800 lbs hr^{-1} to 1700 lbs hr^{-1}.

The effect of the localized heat input on the melt rate is included in the equation (5.23) by the correlation that the melt rate is inversely proportional to (ℓ/D). Decreasing the distance 'ℓ' localizes a significant portion of the total heat input in the narrow region between the electrode tip and the slag/metal interface, resulting in an increase in the melt rate.

The validity of equation (5.23) is checked (error $\pm$ 10%) against the available laboratory and industrial experimental data. All the laboratory experiments were carried out using CaF_2~25 wt.% Al_2O_3 slag. Tables XIII and XIV give the calculated values of Z for the different ingots.

Table XIII. Calculated values of Z for the laboratory made ingots

Ingot no.	Polarity	Atmosphere	Electrode material	ℓ (cm)	Z (Kcal g^{-1})
1	-ve	$Argon^{III}$	EN 25	2.0	2.28
2	-ve	Air	EN 25	2.0	1.7
3	-ve	Air	EN 25	3.0	1.81
4	-ve	$Argon^{I}$	EN 25	2.0	2.46
5	-ve	$Argon^{II}$	EN 25	2.0	3.36
6	-ve	$Argon^{II}$	EN 25	1.5	3.42
7	-ve	$Argon^{I}$	EN 25	1.8	2.35
8	-ve	Air	EN 25	2.6	1.8
10	+ve	$Argon^{III}$	EN 25	2.6	1.585
11	+ve	$Argon^{II}$	EN 25	2.8	1.52
12	+ve	$Argon^{II}$	EN 25	2.6	1.56
13	+ve live	$Argon^{III}$	EN 25	2.3	2.32
14	+ve live	$Argon^{II}$	EN 25	1.4	3.08
15	a.c.	Air	EN 25	1.8	1.48
16	a.c.	$Argon^{III}$	EN 25	1.9	1.50
17	a.c.	$Argon^{II}$	EN 25	1.7	1.65
18	a.c.	$Argon^{I}$	EN 25	1.6	1.49
20	-ve	$Argon^{II}$	AISI 630	2.0	2.26
25	-ve	Air	FVE	1.6	3.16
26	-ve	$Argon^{II}$	FVE	1.6	4.15

Table XIII. (Continued)

Ingot no.	Polarity	Atmosphere	Electrode material	ℓ (cm)	Z ($Kcal\ g^{-1}$)
27	+ve	Air	FVE	1.6	3.10
28	+ve (BN ins)	Argon^{II}	FVE	1.3	3.19
29	+ve (BN ins)	Argon^{II}	FVE	1.7	3.33
30	+ve live	Argon^{II}	FVE	1.7	4.12
31	a.c.	Argon^{II}	FVE	1.2	2.86
32	a.c. (BN ins)	Argon^{II}	FVE	1.1	3.12

Table XIV. Calculated values of Z for industrial ingots

Ingot no.	Mold diameter (cm)	Electrode diameter (cm)	Electrode Composition	Polarity	Power input (Kwatts)	Melt rate (g sec^{-1})	ℓ/D	Z (Kcal g^{-1})
$I1^{51}$	30.5	15.25	1020	a.c.	240	24	≈0.262	2.3
$I2^{51}$	30.5	22.8	1020	a.c.	240	50.5	≈0.262	2.46
$I3^{49}$	20.3	15.25	Hastelloy X	a.c.	66	19.4	≈0.30	1.53
I4	60.96	45.72	EN 25	a.c.	760	258	≈0.24	1.65
I5	60.95	41.57	EN 25	a.c.	720	157	≈0.24	1.65

(1) To study the effect of the electrode composition one can compare the ingots (5), (20) and (26). As expected, the ingot (26) with the highest melting point (1539°C) has the highest value of Z. The values of Z calculated for industrial ingots also show a similar pattern.

(2) To study the effect of the ingot diameter, one can compare the ingots (3) and (8),and (4) and (7). The calculated values of Z are very similar, thereby establishing the relationship $R \alpha 1/D^2$.

(3) Comparing the ingots (2) and (3) to study the effect of the electrode diameter, the distance between the electrode tip and the slag/metal interface it is seen that the calculated value of Z in both the cases is approximately the same. The AISI 1020 ingots I1 and I2 (Table XIV) also show a similar value for Z for different (d/D) ratios.

(4) On comparing the ingots having the same composition but different electrical configuration and atmosphere, it is seen that except for the d.c. negative with argon and d.c. positive live (both with air and with argon) configurations, all have approximately the same value of Z ($Z \simeq 1.65$ for EN 25 and $Z \simeq 3.0$ for FVE). An attempt is made here to explain the observed behaviour.

In d.c. positive 'live' configuration, as shown by Fig. (46), a significant portion of the current goes to the mold wall. This portion of the total current is not efficiently utilized in the heating the slag bath. The current density below the electrode tip is also relatively low. As a result, the temperature of the slag in the vicinity of the electrode is not very high. The melt rate is thereby reduced, and the value of Z increased.

In remelting with d.c. having the electrode as negative pole, the presence of the argon atmosphere prevents the oxidation of the Al and Ca at the slag/gas interface. The non-availability of the heat of oxidation in the vicinity of the electrode results in a lower melt rate and an increase in the value of Z.

In the d.c. positive configuration, both with air or argon, the electrode is significantly more polarized than the d.c. negative configuration. However in the laboratory scale ingots, the extra heat liberated at the electrode surface in the d.c. positive due to the higher polarization is compensated in the d.c. negative in air configuration by the exothermic heat of oxidation of Al and Ca at the slag/gas interface. This results in both configurations having approximately the same value of Z. In remelting larger scale ingots however, d.c. negative in air would have a lower value of Z. The increase in the electrode size, decreases the current density on the electrode thereby decreasing the relative contribution by the polarization in the d.c. positive configuration.

In remelting steels using a.c. ($\simeq$ 50 cycles) there is no contribution by polarization or oxidation. However, due to the higher effective slag resistance (because of the absence of dissolved Ca or Al) it is possible to achieve a localized heat generation (by reducing the value of ℓ) in the slag bed. This results in a similar value for Z as in d.c. negative in air or d.c. positive (insulated).

Prediction of the Melt Rate

It is possible to approximately predict the melt rate for large scale ingots from the available experimental data.

For a 60.95 cm (24 inches) diameter ingot of EN 25 (d/D = 0.75; ingot I4, Table XIV), the value of the melt rate is obtained, using the approximate power input calculated in Appendix (IV) and the average value of Z for EN 25 steel of 1.65. Substituting the values of the various parameters in equation (5.23) yields a value for the melt rate of $\simeq$258 g sec^{-1}.

To compare the predicted values of the melt rate with the experimentally obtained values by Holzgruber et al.,[6] melt rate is calculated for a 60.95 cm diameter ingot (I5) of EN25 with d/D = 0.6 (Fig. (73) data is for d/D = 0.6) using the approximate power input calculated in Appendix IV). A melt rate of 157 g sec^{-1} is calculated as compared to 177 g sec^{-1} (1400 lb hr^{-1}) obtained experimentally. The correlation appears reasonable, considering the various approximations involved. Secondly Fig. (73) is obtained basically from data on highly alloyed steels. As shown earlier, lower melting compositions have a smaller value of Z and hence a higher melt rate.

CHAPTER VI

PREDICATION OF POOL VOLUMES IN ESR INGOTS

VI.1 Introduction

One of the main advantages claimed by electroslag melting technique is the improvement of the ingot structure. The manner by which an ingot would solidify depends upon the mode of heat extraction. The liquid metal pool profile which is controlled by the rate and mode of heat extraction, is a good indicator of the manner in which the ingot would solidify.

Consider the two extreme cases as shown in Fig. (74). A high melt rate is generally characterized by a deep liquid pool. As the dendrites grow perpendicular to the interface, a higher melt rate results in a radical orientation of the dendrites. This is not favoured for subsequent working. On the other extreme, a very slow melt rate results in a flat liquid pool having significant microsegregation due to larger dendritic arm spacing. Thus one would like to have an optimum shape of the liquid pool.

The pool volume of an ESR ingot can be subdivided into two distinct regions as shown in Fig. (75). Besides the shape of the curved portion of the liquid pool, it is important to have an optimum height for the cylindrical portion of the pool volume. In industrial scale ingots

this height is about 10-15 cm. This is necessary to achieve a good surface quality for the ingot. If the process is stopped suddenly after a desired length of the ingot is made, the liquid metal volume present at the time of shut off would solidify in the conventional manner i.e., with equiaxed structure in the centre. As the ESR process is generally used for refining expensive alloys, it is not economical to reject the last 10-15 cm of the ingot every time. In industry, this is oyercome by adopting the practice of 'hot topping'. The power and feed rate are gradually reduced towards the end, so that the cylindrical portion is reduced to a minimum and then the process is stopped. It is quite important from this point of view to know the exact pool volume for a normal set of working conditions.

Now that the ESR process is accepted in the industry as a batch process, efforts are being made to make it continuous; similar to continuous casting. In designing the copper mold for the continuous process, it is necessary to know the volume of the liquid metal pool and the position of the solid/liquid interface in the copper mold.

Having discussed the importance of knowing the pool volume, an attempt is now made to predict it for some known operating conditions. As shown in Fig. (75), the pool volume can be subdivided into two regions. The cylindrical portion can be predicted on the basis of a dynamic heat balance of the unit while the curved portion can be predicted using a finite difference technique.

VI.2 Prediction of the Height of the Cylindrical Portion of the Pool Volume

In Chapter V, an accurate heat balance of the process was carried out. From it, it is clear that knowing the operating conditions, the geometry and the volume of the slag cap, it is possible to calculate the height of the cylindrical portion of the liquid metal pool.

Fig. (76) shows the macrographs of ingots (26) and (32). The observed difference in height of the cylindrical portion in the two cases is ≈3.5 cm. Using similar boundary conditions as obtained experimentally for ingots (1), (10) and (16), a heat balance of the two ingots yields a value for the difference in the height of the cylindrical portion of 3.0-3.3 cm.

Similar calculations were carried out for ingots (4) and (18). A value of ≈3.0 cm was obtained which compared very favourably with the experimentally observed difference in height of the cylindrical portion of 3.0-3.2 cm.

Having being able to predict the height of the cylindrical portion of the liquid metal pool in laboratory scale ingots, attempt is now made to predict this height for an industrial scale ingot. Table (XV) gives the operating conditions for an industrial scale ingot.[51] On carrying out a heat balance similar to the one done in Appendix (IV), a value of 15 cm is obtained for the height of the cylindrical portion of the liquid metal pool. Considering the approximations involved, this value agrees very well with the experimentally obtained value of 15-18 cm.

Table XV. Operating conditions for an industrial scale ingot.[51]

Mold dia. (cm)	Electrode dia. (cm)	Electrode comp.	Electrode polarity	Atm.	Slag comp.	Volts	Amp.
50.8	40.5	Hastelloy X	a.c.	Air	CaF_2-25 wt.% Al_2O_3	32	15000

Melt Rate (g/sec)	Z* (cm)	A* (cm)	B* (cm)
160	15	15-18	20

* Refer to Fig. (75)

VI.3 Prediction of Pool Profiles Using Explicit Finite Difference Method

VI.3.1 Introduction

Mathetmatical models for predicting the solidification pattern in castings have been studied by many investigators.[37,50,52,53] Sun and Pridgeon[50] used the finite difference method to predict the pool profiles in Hastelloy-X ingots. The model presented here can be considered as a refinement of the Sun and Pridgeon analysis.

For rounded ingots, the cylindrical polar system (r, ϕ , Z) is generally used. Two dimensional heat transfer along the r and Z axes is adequate in describing the heat flow in an electroslag refining unit as angular symmetry exists in the temperature distribution.

The Fourier equation reduces to

$$\frac{\partial T}{\partial t} = \alpha\{\frac{\partial^2 T}{\partial r^2} + \frac{1}{r}\cdot\frac{\partial T}{\partial r} + \frac{\partial^2 T}{\partial Z^2}\} \tag{6.1}$$

$$\text{where } \alpha = \frac{k}{\rho C_p} \tag{6.2}$$

Equation (6.1) can be solved by means of definite difference methods knowing the appropriate boundary conditions. Both the Dusinberre[54] (explicit) and the Crank and Nicolson[55] (implicit) methods can be used. Use of the Dusinberre's explicit method is made in the following analysis.

In the electroslag process, the ingot is continuously built up. The versatility of the finite difference technique permits one to simulate the liquid metal dropped continuously into the pool by adding at the top, a thin disc layer of liquid metal of a given size after every unit time interval.

VI.3.2 Derivation of the Formulae for the Explicit Finite Difference Method

The first question concerns the subdivision of the system. The simple and obvious method is in equal increments of the radius. The system is then laid out as in Fig. (77).

For convenience, an arc of one radian is used and each element has the dimensions of 'Δr' along the 'r' axis and 'Δz' along the 'z' axis.

As seen in Fig. (77), there are, in total nine different types of elements. Symbolically, they can be represented as follows

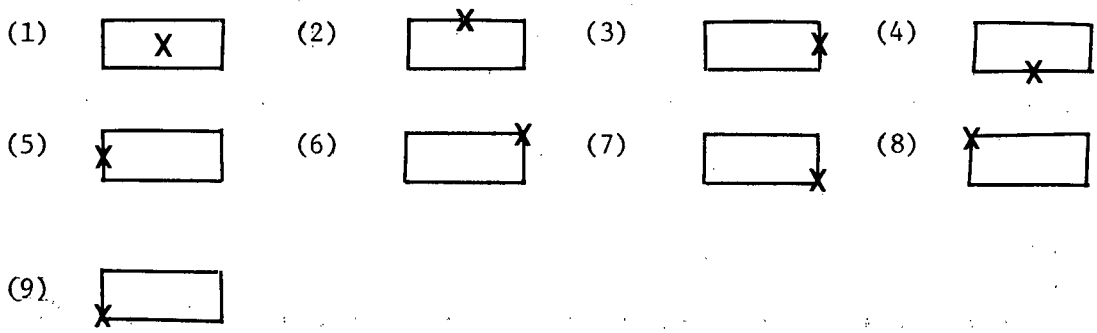

The arcs halfway between the reference points are taken as defining the width of the heat flow path and also the volumes of the respective regions.

Appendix (V) gives the derivation of the formulae for each of the nine different types of elements.

VI.3.3 Salient Features of the Computer Programme

The dependence of the pool shape on the thermophysical properties of a given alloy is obvious. Hence in developing the computation model, the pool shape is considered as a function of both the ingot melt rate and the thermo-physical properties of the alloy. The following are the salient features of the programme.

(1) It is assumed that the temperature of the top layer elements remains constant, i.e. the top layer elements are assumed to be in steady state equilibrium with the elements below them and the liquid slag or metal above them.

(2) The temperature distribution in the top layer elements is assumed. The temperature distribution depends upon the height of the cylindrical portion of the liquid metal pool above them. The cylindrical portion acts as a buffer region and reduces the radial temperature gradient in the top layer elements.

(3) A constant temperature at the bottom of the ingot is assumed after sufficient ingot is built up. Although it is possible to calculate the heat leaving at the bottom of the ingot from the available experimental data, the assumption simplifies the analysis without scarificing accuracy.

(4) The current passing through the ingot does not produce significant heating of the ingot; hence its effect is neglected by assuming $I^2R = 0$.

(5) As documented earlier in Chapter V, temperature profiles were obtained on the copper mold for various mold sizes, mold/electrode ratios and polarities. It is possible to non-dimensionalize the temperature vs. distance from the liquid metal/solid metal interface plots for distance. Fig. (78) shows the average temperature distribution on the mold across the solidified ingot. It is necessary to express this curve in the form of an equation. A polynomial of 8th degree was fitted to the curve quite accurately. However, this polynomial cannot be used as a boundary condition for industrial scale ingots as Fig. (78) is valid only for 'L' $\simeq$ 35.0 cm.

One is interested in calculating the heat going to the mold cooling water in elements of cases 3, 6 and 7 discussed in Appendix (V). For case 3, the temperature of a nodal point $X_{r,z}$ at time t = k + 1, i.e. $T_{r,z,k+1}$ is given by the following equation

$$\frac{C_p \rho \text{ volume}}{\Delta t} [T_{r,z,k+1} - T_{r,z,k}] = \frac{k_1 A_1}{\Delta r} [T_{r-1,z,k} - T_{r,z,k}]$$

$$+ h_{side} A_2 [T_{r+1,z,k} - T_{r,z,k}] + \frac{k_3 A_3}{\Delta z} [T_{r,z+1,k} - T_{r,z,k}]$$

$$+ \frac{k_4 A_4}{\Delta z} [T_{r,z-1,k} - T_{r,z,k}] \qquad (6.3)$$

In Eq. (6.3), one is interested in calculating the term $h_{side} A_2 [T_{r+1,z,k} - T_{r,z,k}]$

$$\text{Let } q = h_{side} A_2 [T_{r+1,z,k} - T_{r,z,k}]$$

$$\frac{q}{A_2} = h_{side} [T_{water} - T_{r,z,k}] \qquad (6.4)$$

In steady state

$$\frac{q}{A_2} = h \Delta T \qquad (6.5)$$

where $h \Delta T$ is obtained from Fig. (63), ΔT being the temperature difference between the mold wall and the water temperature.

As discussed earlier in Chapter V, the heat transfer to the mold cooling water can be subdivided into two regions

(a) surface boiling region

(b) non-boiling region

(a) Surface Boiling Region:. The heat flux in the surface boiling region can be expressed in an equation form as follows

$$\left(\frac{q}{A}\right) = \exp\{6.12\ \ln[(T-50) - 22.18]\} \qquad (6.6)$$

Where T is the temperature on the copper mold in degrees centrigrade. Using (6.6) it is possible to calculate the heat going to the mold cooling water for elements across the surface boiling region.

(b) Non-Boiling Region: As calculated earlier in Chapter V $h_{non\text{-}boiling} = 1.15 \times 10^{-2}$ cal $cm^{-2}{}^{\circ}C^{-1}sec^{-1}$. Knowing the temperature difference between mold and water temperature, the heat transferred to the mold cooling water for elements across the non-boiling region can be calculated.

(6) As the thermophysical properties of the various steels at elevated temperatures are not available in literature, attempt is made here to predict the pool profiles in pure iron and EN 25 steel ingots only. EN 25 steel has approximately 5% alloying elements and as such, except for the melting point ($\simeq$ 50°C lower), it is assumed to have the same thermophysical properties as pure iron.

(7) The latent heat of solidification and also the allotropic transformations in the case of pure iron are taken into account by adjusting the specific heat, in the calculation, as follows:

$$C_p(\text{adjusted}) = C_p(\text{metal}) + \frac{L_H}{\Delta T} \qquad (6.7)$$

where ΔT is the temperature range over which the transformation occurs.

(8) The data for thermal conductivity is not available in literature above 1600°K even for pure iron. The thermal conductivity is estimated above 1600°K by making use of the Loren's relationship, as the data for electrical resistivity is available up to 2100°K.

Loren's relationship:

$$\frac{\text{electrical resistivity x thermal conductivity}}{\text{temperature}} = \text{constant} \quad (6.8)$$

In the range where both the thermal and electrical conductivity data is available, the validity of the Loren's relationship is checked (error < 5%).

In the liquid iron temperature range, it is very difficult to calculate the contribution of convection. It is taken into account by way of the concept of 'effective thermal conductivity'

$$k_{eff} = k_{conv} + k_{cond} \quad (6.9)$$

$$k_{eff} = f\, k_{cond} \quad (6.10)$$

It is extremely difficult to estimate the value of 'f'. It is a function of temperature and flow conditions. Sun and Pridgeon[50] use f = 3-5. Using Stewart's[56] non-dimensional analysis for the present case yields a similar value for 'f' and is used in the analysis. However the validity of using his analysis to the present case is in doubt. In the present case, the temperature gradients are such that denser liquid is at the bottom and lighter at the top. Table XVI gives the physical properties of pure iron used in the analysis.[57]

(9) The time interval 'Δt' between successive temperature evaluations at a node is chosen such that the stability criteria is satified.

In Fig. (79), the temperature at the nodal point 'a' after time Δt

Table XVI. Physical properties of pure iron used in the analysis.[57]

Temperature Range (°K)	Density ($g\ cm^{-3}$)	Specific Heat ($cal\ g^{-1}{}^{\circ}K^{-1}$)	Thermal Conductivity ($cal\ cm^{-1}{}^{\circ}K^{-1}sec^{-1}$)
300-900	7.75	0.14	0.13
900-1350	7.59	0.18	0.072
1350-1660	7.45	0.15	0.076
1660-1670	7.35	0.53	0.082
1670-1800	7.31	0.164	0.085
1800-1801	7.187	65.7	0.12
1801-1825	7.073	0.18	0.24
1825-1900	7.04	0.182	0.30
1900-2050	6.94	0.183	0.40

can be written as

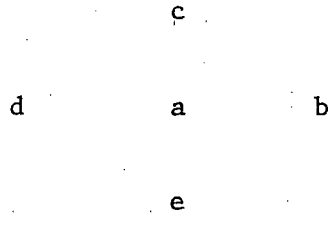

Fig. (79) nodal points configuration

$$\frac{C_a\,[T'_a - T_a]}{\Delta t} = k_{ba}(T_b - T_a) + k_{ca}(T_c - T_a) + \cdots \qquad (6.10)$$

where $C_a = \rho C_p$

On simplifying

$$T'_a = \frac{k_{ba}\,\Delta t}{C_a} T_b + \frac{k_{ca}\,\Delta t}{C_a} T_c + .. + [1 - \frac{\Sigma k_a\,\Delta t}{C_a}]T_a \qquad (6.11)$$

$$T'_a = F_{ba}T_b + F_{ca}T_c + \ldots + F_{aa}T_a \qquad (6.12)$$

In equation (6.12) all F_{ba} etc. are inherently positive but

$$F_{aa} = 1 - \frac{\Sigma k_a\,\Delta t}{C_a} \qquad (6.13)$$

and this may become negative if Δt is chosen large enough. This would be absurd physically, because it would say that, the warmer the region 'a' is now, the colder it is going to be after the time interval Δt. More sophisticated criteria have been devised for systems to which differential equations are applicable and can be solved. But, as a practical matter, it is easy to obey a simple rule: 'avoid negative coefficients'.[54]

Of the possible F_{aa} values, the worst value is selected to evaluate Δt. In the present analysis, as constant temperature is assumed at both the top and bottom, the value of F_{aa} to be considered is obtained from eq. (A.V.7) [Appendix V].

$$F_{aa} = \frac{4}{MR_2} + \frac{1}{MZ_3} + \frac{1}{Mz_4} \qquad (6.14)$$

The maximum allowable value of Δt is obtained by solving

$$F_{aa} = 1 = \frac{4}{MR_2} + \frac{1}{MZ_3} + \frac{1}{MZ_4} \tag{6.15}$$

where $MR_2 = \dfrac{C_p \rho \Delta r^2}{k_2 \Delta t}$

$$MZ_3 = \frac{C_p \rho \Delta z^2}{k_3 \Delta t}$$

$$MZ_4 = \frac{C_p \rho \Delta z^2}{k_4 \Delta t}$$

$$\therefore \quad \frac{4.0\, k_2 \Delta t}{\rho C_p \Delta r^2} + \frac{k_3 \Delta t}{\rho C_p \Delta z^2} + \frac{k_4 \Delta t}{\rho C_p \Delta z^2} = 1 \tag{6.16}$$

The minimum value of $(-\frac{\rho C_p}{k})$ is chosen for evaluation, as it leads to the maximum allowable value of Δt in the worst case.

$$\rho = 6.88 \text{ g cm}^{-3}$$

$$C_p = 0.18 \text{ cal g}^{-1}{}^{\circ}\text{C}^{-1}$$

$$k = 0.4 \text{ cal cm}^{-1}{}^{\circ}\text{C}^{-1}\text{sec}^{-1}$$

Substituting these values in (6.16) yields

$$\Delta t = \frac{1.55}{[\frac{2}{\Delta r^2} + \frac{1}{\Delta z^2}]} \tag{6.17}$$

Using (6.17) it is possible to calculate the value of Δt for any size of the element.

VI.3.4 Results

Appendix VI gives the computer programme written to predict the pool profiles in ESR ingots. Pool profiles for EN 25 steel and FVE ingots were computed. Table XVII gives the assumed temperature distribution in the top elements and the values of the various parameters used in the computation.

Fig. (80) to Fig. (85) show the predicted pool profiles superimposed on the experimentally obtained profiles. The agreement appears to be good in spite of the numerous assumptions made. In ingot no. 21 (Fig. (83)), tungsten powder was added to define the pool profile.

To predict the pool profiles for industrial scale ingots, it is necessary, either to experimentally determine or assume, a temperature profile on the mold across the solidified ingot.

Table XVII. Parameters used in the prediction of pool profiles in EN25 and FVE ingots

Ingot no.	DELR cm	DELZ cm	DELT sec	NRATE	H_{SIDE} cal $cm^{-2}sec^{-1}{}^{\circ}C^{-1}$	Temperature distribution in the top layer (°K) Ingot Centre				Ingot Edge
1	1.22	1.0	0.5	178	0.0116	1800	1790	1780		1750
10	1.22	1.0	0.5	232	0.0116	1810	1795	1780		1750
16	1.22	1.0	0.5	178	0.0116	1825	1785	1770		1750
21	1.1625	1.0	0.5	169	0.0116	1800	1795	1790	1780	1750
26	0.9	0.5	0.18	308	0.0116	1830	1815	1810		1800
28	0.9	0.5	0.18	185	0.0116	1850	1825	1815		1800

CHAPTER VII

CONCLUSIONS

(1) The heat generation pattern in the slag bed has been analysed using a resistance network analogue to predict the voltage gradients in the slag bed. Most of the heat generation takes place below the electrode tip. Self consistency between current, voltage, temperature, resistance and q is obtained in the slag bed.

(2) It is possible to predict the temperature gradient on the electrode. This may be used to calculate the degree of thermal instability during electrode changes in large industrial ingots and the electrode oxidation. The results indicate that when melting steel in the electrode and mold sizes studied, the electrode material spends approximately 30 seconds in the temperature gradient 1000°C to the melting point. It is suggested that this would lead to a significant non-equilibrium retention of second-phase precipitates in a melting alloy which contained these precipitates at a lower temperature in the solid.

(3) The overall heat transfer coefficient of the interface region, liquid slag/slag skin/copper mold is found to have a slight

dependence on the slag temperature, slag composition and the slag skin thickness. It is postulated that the major resistance to the transfer of heat across this composite interface lies in the discontinuity between the slag-skin and the mold wall.

(4) The electrical resistivity of the slag skin primarily depends upon the contact resistance and is a sensitive function of the mold wall temperature.

(5) An approximate thermal gradient in the slag skin region has been determined.

(6) An accurate heat balance of the process is carried out on laboratory scale ingots. The results indicate that a significant portion of the heat leaves the unit across the liquid slag and the liquid metal regions.

(7) The power requirements and the melt rate for industrial scale ingots are predicted. Good agreement is obtained between the predicted values and the data collected from literature.

(8) Real differences are observed between different melting modes. It is observed that in d.c. negative, there is a marked difference between melting under argon and air.

(9) The liquid metal pool volumes in ESR ingots can be predicted from the operational data. Good agreement is obtained between pool profiles computed using a finite difference technique and the experimentally obtained profiles.

APPENDIX I

PHYSICAL PROPERTIES OF ESR SLAGS

A.I.1 Introduction

The correct choice of slag composition is of prime importance in the electroslag refining process.

The slag bath is the most important unit in the process. It is the resistance and refining element. The correct choice of slag is therefore governed by the physical considerations such as electrical conductivity, liquidus temperature, viscosity, density, vapor pressure etc., and also the chemical considerations such as desulphurization and removal of large oxide inclusions.

No coherent picture has yet emerged from the published data as to what constitutes the requirements for a useable ESR slag, but one may establish several boundary conditions.[17]

(1) the slag must be chemically compatible with the metal being processed.

(2) the slag must have a liquidus temperature below the melting point of the metal but a primary phase melting point above that of the metal.

(3) the physical properties must be such that the heat generation is established in a uniform volume, of a size compatible with the required heat balance.

The first condition is imposed by one of the prime objectives of the process i.e., capability of improving the cleanliness of the metal. Inclusions such as sulphides, oxides, silicates etc. can be removed. Generally speaking, the process is one of oxidation, hence

precautions are necessary to minimize oxidation losses of these alloying elements such as Si, Ti, Al which are particularly prone to oxidation.

The second boundary condition is imposed by the requirement that one must be able to immerse the electrode in the slag while also allowing a metal pool to be bounded by a solid slag skin.

The third condition represents the dependence of process parameters i.e., melt rate, voltage and current on the physical properties of the slag.

However, the requirements of a suitable electrical conductivity, viscosity, vapor pressure, liquidus temperature etc., must be satisfied before the selection according to the chemical properties desired of the slag for a specific metallurgical application is made.

Slag components are selected primarily on account of their low vapor pressure and high temperature stability. The slag should also have the appropriate electrical conductivity to achieve the desired temperature. Other important criteria are those of viscosity, density, thermal conductivity, liquidus temperature, vapour pressure, interfacial tension and thermal capacity. Electrical conductivity, density and kinematic viscosity are interrelated. Thus a low electrical conductivity necessary for high resistance heating is accompanied by high viscosity. Although the viscous slag may slow down the oxidation of reactive elements, it also slows down the removal of unwanted components.

The most common choice of slag constituents is between CaF_2, CaO, Al_2O_3, MgO and SiO_2. However, MgF_2, BaF_2, TiO_2 etc. are sometimes added in small quantities to achieve a close control of a particular

element.

Although many slag compositions may represent equally acceptable optima, in industry, only a few slag compositions, selected by empirical means, are used. Knowing the physical properties of the slags, it is possible to simplify the multicomponent slags used in industry and at the same time propose several alternative compositions.

At the present time, insufficient data is available on the various physical properties of the slags. Table XVIII summarises the available literature on the physical properties of ESR slags. Fig. (86) gives the electrical conductivity data for CaF_2-Al_2O_3 slags.[21]

Attempt is made here to measure the density and viscosity of CaF_2 based slags.

A.I.2 Measurement of Density of CaF_2 Based Slags

A.I.2.1 Introduction

In addition to its use in the analysis of such properties as viscosity and electrical conductivity, density measurement is of considerable value in the investigations of the structure of liquids. It is quite difficult to measure accurately the density of liquids at temperatures of 1450-1750°C. Previous measurements of the density of CaF_2-Al_2O_3 and CaF_2-CaO binary systems have been restricted to below 1600°C and confined mostly to the Russian literature.[68-72]

In the present work, density measurements have been made in the two binary compositions: CaF_2-Al_2O_3, CaF_2-CaO over the temperature range 1450-1750°C.

Table XVIII. Physical properties of ESR slags

Property	System	Reference
Phase structure	CaF_2-Al_2O_3, CaF_2-CaO, CaF_2-CaO-Al_2O_3	58
Phase structure	CaF_2-CaO-Al_2O_3	59
Phase structure	CaF_2-CaO	60
Phase structure	CaF_2-CaO	61
Phase structure	CaF_2-Al_2O_3	62
Phase structure	CaO-CaF_2-2CaO·SiO_2	63
Phase structure	CaF_2-CaO; CaF_2-Al_2O_3; CaF_2-CaO-Al_2O_3; CaF_2-CaO-2CaO.SiO_2; CaO-MgO; CaO-Al_2O_3	65
Phase structure	2CaO.SiO_2-CaF_2	64
Phase structure	Ca_3O_3-Ca_3F_6-$Si_{1.5}F_6$-$Si_{1.5}O_3$	66
Phase structure	CaF_2-CaO-Al_2O_3	67
Density	CaF_2-MF_2, MF	68
Density	CaF_2-Al_2O_3-CaO	69
Density	CaF_2-Al_2O_3; CaF_2-CaO; CaF_2-Al_2O_3-CaO; CaF_2-CaO-SiO_2; CaF_2-CaO-Al_2O_3-MgO	70
Density	CaF_2; CaF_2-MgO; CaF_2-CaO; CaF_2-Al_2O_3; CaF_2-SiO_2; CaF_2-ZrO_2; CaF_2-SiO_2	71
Density	CaF_2-CaO-Al_2O_3; CaF_2-SiO_2-CaO	72
Interphase and interfacial tension	CaF_2-CaO-Al_2O_3	69
Interphase and interfacial tension	CaF_2-MgO; CaF_2-CaO; CaF_2-Al_2O_3; CaF_2-SiO_2; CaF_2-ZrO_2	70

Table XVIII. (Continued)

Property	System	Reference
Interphase and interfacial tension	CaF_2-CaO-Al_2O_3	71
Viscosity	CaF_2-CaO-Al_2O_3	73,74
Viscosity	CaO-Al_2O_3-SiO_2	75
Electrical conductivity	CaO-Al_2O_3-CaF_2; CaF_2-CaO, BaO, MgO, TiO_2, ZrO_2, Al_2O_3	69
Electrical conductivity	CaF_2	76
Electrical conductivity	CaO-SiO_2-CaF_2	77
Electrical conductivity	CaF_2-CaO-Al_2O_3	21
Electrical conductivity	CaF_2-Al_2O_3-CaO	66
Specific heat and heat content	CaF_2-CaO; CaF_2-CaO-Al_2O_3-MgO CaF_2-Al_2O_3	78
Vapour pressure	CaF_2	79

A.I.2.2 Experimental

A.I.2.2.1 Apparatus

The apparatus is based on 'the measurement of the buoyancy force'. It is shown schematically in Fig. (87). It was supported on a stainless steel base plate with rigid support on the two sides. The molybdenum lined graphite crucible K (5 cm ϕ, 10 cm high) was supported by a hollow alumina tube N carrying a thermocouple O which was attached to the controller of the induction furnace. The entire assembly was enclosed in a Vycor glass tube P (7.8 cm dia., 48 cm long) lined with graphite felt L in the heating zone. Oxidation at elevated temperature was prevented by maintaining a slight positive argon atmosphere in the apparatus.

The water cooled induction coil M enabled the maintainence of a uniform temperature over the entire volume of the slag in the crucible. Precise temperature measurement of the slag was made by inserting a W-3Re/W-25Re thermocouple E (in a twin bored alumina tubing with a boron-nitride sheath protection) in the melt J.

A transducing cell 'A' (Statham's Universal transducing cell model UC3) was used to measure the weight change of the bob. Fig. (88) gives the external circuitry required to operate the transducer. A change in weight of the bob caused a change in the resistance. This was measured in millivolts and was calibrated to give the weight change in grams. A molybdenum bob I ($\simeq$5 grams) in the form of a ring was suspended from the transducer by a tungsten wire H (0.025 cm dia.). Both the weight change and temperature were simultaneously recorded by two Sargent Model SR6 recorders. The absence of large systematic errors

owing to the thermal lag between the melt and temperature sensing element on continuous measurement was varified. In all the density measurements, the bob was completely immersed in the melt, leaving surface forces acting only on the wire. The problem of bubbles getting attached to the bob, as indicated by erratic buoyancies, necessitated the process of removal, cleaning and re-immersion of the bob. The process was repeated until reproducible and minimum values of buoyancy were obtained. Fig. (89) shows the experimental setup.

A.I.2.2.2 Calibration and Measurement

The transducer was calibrated by suspending known weights and observing the change in millivolts. Eq. (A.1.1) gives the calibration

$$1\ g = 1.3\ mV \qquad (A.1.1)$$

expression and this was verified frequently.

The volume of the bob at room temperature, determined from its apparent weight loss upon immersion in distilled water was obtained from the equation.[80]

$$V_o = \left[\frac{W_a - W_w}{\rho_w}\right] + \left[\frac{\pi \gamma_w d}{g \rho_w}\right] \qquad (A.1.2)$$

where the subscripts 'a' and 'w' refer to air and water respectively and

V_o = volume of bob at room temperature (cm^3)

W = weight of the bob (g)

ρ = density ($g\ cm^{-3}$)

γ = surface tension (dynes/cm)

d = diameter of suspension wire (cm)

g = acceleration due to gravity (cm sec^{-2})

The volume of the bob at room temperature was determined each time before an experiment.

The density of the melt was calculated from the following equation

$$\rho_m = \frac{W_a - W_m}{V_o[1 + 3\alpha(T-25)]} + \frac{\pi\gamma_m d}{V_o g} \qquad (A.1.3)$$

where the subscripts 'a' and 'm' refer to air and melt respectively and

T = temperature of the melt (°C)

α = linear coefficient of expansion for the material of the bob. For molybdenum,[81]

$$\alpha \times 10^6 = 5.05 + 0.31 \times 10^{-3}T + 0.36 \times 10^{-6}T^2 \qquad (A.1.4)$$

where T = temperature (°C).

The surface tension data from the literature[70,71] for 1450-1600°C range was used at all the temperatures (Fig. (90)).

A.I.2.3 Results

CaF_2 rich side of two binary systems CaF_2-Al_2O_3 and CaF_2-CaO was investigated. In all the cases $\Delta\rho$ was linear with temperature. Fig. (91) and Fig. (92) give the experimental data obtained.

A.I.3 Measurement of Viscosity of CaF_2 Based Slags

A.I.3.1 Introduction

Viscosity is an important physical property of fused salts. It determines, in part, the rate of fall of metal droplets through the liquid slag and may also influence the rates of certain refining reactions through its interrelations with diffusion rates.

As in the case of most of the other physical properties of CaF_2 based slags, previous work is sparse and inconclusive.[73,74] Davies and Wright[73] in their recent paper have reported the viscosity data for some CaF_2 based slags up to 1500°C. As the operating temperatures in ESR process are higher than 1500°C, measurement of viscosity at higher temperatures (1500-1650°C) is attempted here.

A.I.3.2 Experimental

A.I.3.2.1 Apparatus

The apparatus is based on the rotating crucible principle. In this method, the torque exerted on the suspension wire through the inner cylinder immersed in the liquid slag contained in the rotating outer cylindrical crucible is measured by the deflection of a beam of light incident on the mirror attached to the suspended assembly.

Fig. (93) gives a schematic diagram of the apparatus. The molybdenum lined outer cylindrical graphite crucible V was supported on a shaft W connected to a variable speed motor (Boston Gear Ratiotrol 1/8 H.P. Motor, made by Boston Gear Works, Quincy, Mass., U.S.A.).

The inner molybdenum cylinder T was attached to the end of the alumina tube M carrying a thermocouple O (W/W-26% Re thermocouple in

a twin bored alumina sheath). The entire assembly was attached to the suspension wire G (0.012 cm dia. tungsten wire) by a stainless steel frame I carrying the mirror H. The leads of the thermocouple O were brought out through a slit in I and connected to molybdenum wires K supported in a brass ring J.

When the inner molybdenum cylinder T was immersed in the liquid slag, the molybdenum leads K were immersed in separate pools of mercury L which were connected to a Sargent recorder (Model SR 6) for temperature measurement. Fig. (94) gives a close-up view of the assembly.

The entire assembly is enclosed in two Vycor tubes F and Q with water cooled bases N and X respectively. Constant immersion of the inner cylinder was achieved by having a graduated stem A. To avoid oxidation, argon gas was flushed continuously through B at slight positive pressure.

Uniform heating of the slag bath U was achieved by induction heating. The Vycor tube Q was protected with a graphite felt lining S in the heating zone.

A gas laser was used as a light source to obtain a undiffused reflected beam from the mirror H. Fig. (95) shows experimental equipment. The deflection of the beam of light caused by the torque exerted on the suspension wire is measured on a scale mounted behind the laser.

A.I.3.2.2 Procedure

Weighed amount of slag was melted in outer crucible under argon by induction heating. After the slag was molten, the inner molybdenum

cylinder was slowly lowered into a desired position by lowering the shaft A. The outer graphite crucible was rotated at various known speeds and the deflection measured. Both clockwise and anticlockwise rotation was used and a mean deflection measured for each speed of rotation.

By changing the power input, the slag was heated to various temperatures. Measurement was carried out after steady temperature had been obtained.

A.I.3.2.3 Calibration

It has been shown[82] for the ideal case of infinitely long cylinders that when the outer cylinder is rotated at constant velocity, the torque produced on the inner cylinder is

$$T_r = \frac{4\pi L W \eta r_1^2 r_2^2}{r_2^2 - r_1^2} \qquad (A.1.5)$$

The torque is measured by the angle of twist caused in the calibrated suspension. It is equal to $K\theta$ where θ is the angular displacement of the inner cylinder.

If absolute measurement of the coefficient of viscosity is desired, corrections for stem of the inner cylinder, end effect due to finite length of cylinders etc. have to be accurately calculated. However, a much easier approach is to calibrate the apparatus against liquids of known viscosity. If dimensions of the cylinders, depth of immersion, bottom clearance and torsion wire are kept constant, equation (A.1.5) reduces to

$$\eta = K_1 \theta t \qquad (A.1.6)$$

where K_1 is found experimentally. The value of K_1 was determined by calibrating the apparatus against light oils, Hydrodrive and Dinonylphathalate. The viscosity of these oils was first determined accurately using Brookfield syncho-lectric viscometer.

A.I.3.2.4 Errors Involved

(1) Dimensions of the Cylinders: As the calibration of the apparatus was done at room temperature, correction has to be made for the expansion of the inner cylinder

$$\eta = \frac{K_1 \theta t}{E} \qquad (A.1.7)$$

where $$E = 1 + 3\left\{\frac{L_t - L_o}{L_o}\right\} \qquad (A.1.8)$$

where L_t = length of cylinder at t°C

L_o = length of cylinder at room temperature.

For molybdenum cylinder, the error introduced, if the expansion factor is omitted was 2.7 % at 1600°C.

(2) Depth of Immersion: The inner cylinder was lowered to the same extent in each experiment. To achieve constant depth of immersion, the volume of the liquid slag had to be kept constant as well. Knowing the density at 1600°C for CaF_2-Al_2O_3 binary slags, the total weight of the slag was so chosen, as to give a constant volume for each slag

composition at 1600°C. However, an error (≃ 1%) is introduced by the increase in the depth of immersion due to the decrease in slag density with increase in temperature of the slag from 1600°C and vice-versa.

(3) The other possible sources of error are

(a) lack of alignment of the cylinders

(b) temperature measurement

(c) turbulent motion in slag at high speeds of rotation

(d) slip between cylinders and slag due to non-wetting

(e) the suspension wire being not perfectly elastic over the torion angles involved.

Care was taken to see that errors due to (a), (b) and (c) were avoided. As the CaF_2-Al_2O_3 slags do wet molybdenum, error due to slip was not present. The error introduced by the non-ideal behaviour of the tungsten suspension wire is negligible.

A.I.3.3 Results

Viscosity measurement of the CaF_2 rich side of CaF_2-Al_2O_3 binary system was carried out. Fig. (96) gives the variation of coefficient of viscosity with composition at 1600°C. Fig. (97) gives the variation of coefficient of viscosity with temperature and compares the experimental data with the data of Davies and Wright.[73]

APPENDIX II

CALCULATION OF THE RESISTANCE OF THE VOLUME ELEMENTS IN THE VOLTAGE GRADIENT ANALYSIS

A.II.1 Introduction

A segment of one radian of the slag bath is subdivided into volume elements as shown in Fig. (12).

A.II.2 Calculation of R_z :

$$R_z = \frac{r\,\ell}{A}$$

Calculation of 'A':

Fig. (98) gives a schematic diagram of the segment of the slag bath. The volume elements are classified into groups M, N, O and P as shown. The volume elements 9 and 13 will be considered subsequently.

$$A_M = \frac{180}{\pi} \times \frac{1}{360} \times \pi[(4\Delta r)^2 - (3\Delta r)^2]$$

$$= \frac{7}{2}\Delta r^2$$

Similarly

$$A_N = \frac{5}{2}\Delta r^2; \qquad A_O = \frac{3}{2}\Delta r^2; \qquad A_P = \frac{\Delta r^2}{2}$$

Calculation of ℓ : $\ell = \Delta z$ for each of the volume elements. It is possible to subdivide the resistance R_z into two equal halves of $R_z/2$.

A.II.3 Calculation of R_r :

$$R_r = \frac{r\,\ell}{A}$$

Calculation of ℓ : $\ell = \frac{\Delta r}{2}$ for each of the two subdivisions of R_r .

Calculation of A : The value of A is different for the two subdivisions of R_r (Fig. (99)).

$$A_{M_{LHS}} = \frac{180}{\pi} \times \frac{1}{360} \times \frac{2\pi}{1} \left[\frac{4\Delta r + \frac{7}{2}\Delta r}{2}\right] \Delta z$$

$$= \frac{15}{4}\ \Delta r\ \Delta z$$

$$A_{M_{RHS}} = \frac{13}{4}\ \Delta r\ \Delta z$$

LHS: left hand side; RHS: right hand side. Similarly

$$A_{N_{LHS}} = \frac{11}{4}\ \Delta r\ \Delta z; \qquad A_{N_{RHS}} = \frac{9}{4}\ \Delta r\ \Delta z$$

$$A_{O_{LHS}} = \frac{7}{4}\ \Delta r\ \Delta z\ ; \qquad A_{O_{RHS}} = \frac{5}{4}\ \Delta r\ \Delta z$$

$$A_{P_{LHS}} = \frac{3}{4}\ \Delta r\ \Delta z; \qquad A_{P_{RHS}} = \frac{1}{4}\ \Delta r\ \Delta z$$

A.II.4 Calculation of R_9 and R_{13}

The exact calculation of 'A' and 'ℓ' for elements 9 and 13 is complicated. Approximate values of A and ℓ are used in the analysis and are given below:

$R_{9\to12}$: $A = \frac{5}{4}\,\Delta r^2;\quad \ell = \frac{\Delta z}{3}$

$R_{9\to8}$: $A = \frac{5}{3}\,\Delta r\,\Delta z;\quad \ell = \frac{1}{3}\,\Delta r$

$R_{9\to\text{electrode}}$: $A = \frac{5\sqrt{5}}{2}\,\Delta z^2;\quad \ell \simeq \frac{\sqrt{5}}{6}\,\Delta z$

$R_{13\to17}$: $A = \frac{5}{12}\,\Delta r^2;\quad \ell = \Delta z/3$

$R_{13\to12}$: $A = \frac{5}{6}\,\Delta r\,\Delta z;\quad \ell = \frac{1}{3}\,\Delta r$

$R_{13\to\text{electrode}}$: $A = \frac{5\sqrt{5}}{6}\,\Delta z^2;\quad \ell \simeq \frac{\sqrt{5}}{6}\,\Delta z$

APPENDIX III

COMPUTER PROGRAMME TO DETERMINE THE TEMPERATURE GRADIENTS ON THE MOLD

```
FORTRAN IV G COMPILER        MAIN            05-23-71        12:07:08        PAGE 0001

                C
                C
                C     PROGRAM : PREDICTION OF TEMPERATURE PROFILES ON E.S.R. ELECTRODES
                C
                C     PROGRAMMER : SATISH JOSHI
                C
                C
                C                LIST OF ABBREVIATIONS USED
                C
                C     LQF : LEAST SQUARE FIT ROUTINE AVAILABLE IN UBC'S GENERAL
                C           PROGRAMME LIBRARY
                C
                C           REFER TO THE WRITE-UP LQF FOR THE MEANING OF THE PARAMETERS
                C           NOT DEFINED IN THE PROGRAMME
                C
                C     F = SHAPE FACTOR
                C
                C     LI= LAMDA INFINITY
                C
                C     LS= LAMDA STAR
                C
                C     MA= NUMBER OF TERMS IN THE SERIES
                C
                C     NA= NUMBER OF POINTS ON THE BOUNDARY
                C
                C     A = D AS DEFINED IN THE TEXT
                C
                C     L = L AS DEFINED IN THE TEXT
                C
                C     E = E AS DEFINED IN THE TEXT
                C
                C     B = BETA AS DEFINED IN THE TEXT
                C
                C     TO= TO AS DEFINED IN THE TEXT
                C
                C     T(I)= TEMP AT THE CENTRE OF THE ELECTRODE
                C
                C     TS(I)= TEMP AT THE SURFACE OF THE ELECTRODE
                C
                C     NU= NU AS DEFINED IN THE TEXT
                C
                C
0001                    REAL X(300),Y(300),YF(300),W(100),E1(100),E2(100),P(100),T(300),
                       1TS(300),A,L,NU,LI,LS,E
0002                    COMMON A,L,PY,MA,NU,LI,LS,E,B
0003                    COMMON/A1/P
0004                    EXTERNAL AUX
0005                    PY=3.141593
0006                    READ(5,1)EP
0007          1         FORMAT(E10.5)
0008                    READ(5,2)L,LI,LS,E,TO
0009          2         FORMAT(8F10.3)
0010                    WRITE(6,3)L,LI,LS,E,TO
0011          3         FORMAT(1HO,4HL = ,F8.2,3X,11HLAMDAINF = ,F8.2,3X,12HLAMDASTAR = ,
                       1F8.2,3X,13HEMISSIVITY = ,F8.2,3X,5HTO = ,F10.3)
```

```
FORTRAN IV G COMPILER        MAIN            05-23-71        12:07:08        PAGE 0002

0012                  READ(5,4) MA,NA,NI
0013            4     FORMAT(10I5)
0014                  WRITE(6,5) MA
0015            5     FORMAT(1H ,32HNUMBER  OF  TERMS  IN  SERIES = ,I5)
0016                  WRITE(6,6) NA
0017            6     FORMAT(1H ,35HNUMBER  OF  POINTS  ON  BOUNDARY = ,I5)
0018                  DO 7 I=1,NA
0019            7     X(I)=(L/FLOAT(NA))*(0.5+FLOAT(I-1))
0020            8     READ(5,9)B,NU,A,(P(I),I=1,MA)
0021            9     FORMAT(3F8.3,(7E8.1))
0022                  IF(B.EQ.0.0)GO TO 20
0023                  WRITE(6,10)B,NU,A
0024           10     FORMAT(1HO,7HBETA = ,F16.7,5X,5HNU = ,F8.2,5X,4HA = ,F16.7)
0025                  DO 11 I=1,NA
0026           11     Y(I)=0.0
0027                  CALL LQF(X,Y,YF,W,E1,E2,P,0.0,NA,MA,NI,ND,EP,AUX)
0028                  IF(ND.EQ.0)GO TO 18
0029                  WRITE(6,12)
0030           12     FORMAT(69H ESTIMATES  OF  ROOT  MEAN  SQUARE  TOTAL  ERROR  IN  TH
                     1E  PARAMETERS)
0031                  WRITE(6,13) (E2(I),I=1,MA)
0032           13     FORMAT(1X,(8E15.5))
0033                  WRITE(6,14)
0034           14     FORMAT(12X,1HX,17X,10HAXIAL TEMP,12X,12HSURFACE TEMP)
0035                  DO 17 I=1,NA
0036                  SUM=0.0
0037                  SUM1=0.0
0038                  DO 15  NN=1,MA
0039                  N=NN-1
0040                  F1=(2.0*FLOAT(N)+1.0)*PY/(2.0*L)
0041                  S1=P(NN)*SIN(F1*X(I))
0042                  SUM=SUM+S1
0043                  SUM1=SUM1+ S1*BESSI0(F1)
0044           15     CONTINUE
0045                  T(I)=1.0+SUM
0046                  T(I)= TO*T(I)
0047                  TS(I)=1.0+SUM1
0048                  TS(I)=TO*TS(I)
0049                  WRITE(6,16) X(I),T(I),TS(I)
0050           16     FORMAT(7X,F12.7,8X,F14.7,8X,F14.7)
0051           17     CONTINUE
0052                  GO TO 8
0053           18     WRITE(6,19)
0054           19     FORMAT(1X,19HEQUATIONS  UNSOLVED//)
0055                  GO TO 8
0056           20     CONTINUE
0057                  END

 TOTAL MEMORY REQUIREMENTS 00241C BYTES

 COMPILE TIME =       2.7  SECONDS
```

```
FORTRAN IV G COMPILER        AUX              05-23-71        12:07:10        PAGE 0001

0001                 FUNCTION AUX(P,D,X,I)
0002                 COMMON A,L,PY,MA,NU,LI,LS,E,B
0003                 DIMENSION  P(100),D(100)
0004                 REAL L,NU,LI,LS
0005                 ALPHA=X*X+B*B+1.0
0006                 IF(((SQRT(B*B-1.0))*1.0E-36).GT.X) GO TO 21
0007                 C=ATAN(SQRT(B*B-1.0)/X)/PY
0008                 GO TO 22
0009           21    C=0.5
0010           22    F=C+(X/PY)*(0.5*(ATAN(SQRT(B*B-1.0))-(ALPHA/SQRT(ALPHA*ALPHA-4.0*B
                    1*B))*ATAN(SQRT((B-1.0)*(ALPHA+2.0*B)/((B+1.0)*(ALPHA-2.0*B))))))
0011                 DO 24 NN=1,MA
0012                 N=NN-1
0013                 F1= (2.0*FLOAT(N)+1.0)*PY/(2.0*L)
0014                 F2= BESSI1(F1)*SIN(F1*X)
0015                 F3= BESSI0(F1)*SIN(F1*X)
0016                 SUM2=0.0
0017                 SUM3=0.0
0018                 DO 23 JJ=1,MA
0019                 J=JJ-1
0020                 F4=(2.0*FLOAT(J)+1.0)*PY/(2.0*L)
0021                 F5=F4*X
0022                 F6=SIN(F5)
0023                 F7=BESSI0(F4)
0024                 F8=BESSI1(F4)
0025                 SUM2=SUM2 +P(JJ)*F4*F8*F6
0026                 SUM3=SUM3 +P(JJ)*F7*F6
0027           23    CONTINUE
0028                 AUX=SUM2+A*(1.0+SUM3)**4-A*(1.-F)*LS**4+NU*(1.0+SUM3)-NU*LI-A*E*F
0029                 D(NN)=F1*F2+4.0*A*(1.0-SUM3)**3*F3 +NU*F3
0030           24    CONTINUE
0031                 RETURN
0032                 END

 TOTAL MEMORY REQUIREMENTS 0005D8 BYTES

 COMPILE TIME =       1.4  SECONDS
```

APPENDIX IV

CALCULATION OF POWER REQUIREMENT FOR MAKING AN INDUSTRIAL SCALE INGOT

Assumed Data:

1.	diameter of the electrode:	45.72 cm (18 inches)
2.	diameter of the ingot:	61.0 cm (24 inches)
3.	electrode composition:	Vibrac EN 25 (B.S.C.)
4.	slag composition:	CaF_2-25 wt. % Al_2O_3
5.	height of slag cap:	16 cm
6.	Electrode immersion:	1.5 cm
7.	height of the cylindrical portion of the liquid metal pool:	7.5 cm
8.	height of the ingot	250 cm
8.	approximate melt rate:	258 g sec^{-1}

To calculate the power requirements, the total heat leaving the system will be calculated and then equated to the required heat input. From the experimental data (Fig. (49) to Fig. (56)) it is clear that the themperature profiles on the mold are independent of the size of the electrode and the ingot. Thus assuming an approximate temperature profile it is possible to calculate the heat leaving the system.

A temperature profile on the mold, similar to Fig. (49) will be assumed. The heat leaving the 61 cm diameter mold will be assumed proportional to the ratio of the areas between the 61 cm diameter industrial scale ingot and the 8 cm diameter ingot (ingot no. 1).

Heat Output:

(1) Q_1 = heat required to melt the electrode and superheat the metal droplets by 100°C

$$= \frac{1066.5}{3.36} \times 258$$

$$\simeq 82 \text{ Kcal sec}^{-1}$$

(2) Q_{2A} = heat lost by radiation from the slag surface to the mold cooling water

$$= 0.650 \times \frac{61.0}{8}$$

$$\simeq 5.0 \text{ Kcal sec}^{-1}$$

(3) Q_3 = heat lost to mold cooling water across the slag bed

$$= 2.597 \times (\frac{61.0}{8}) \times (\frac{16}{4.5})$$

$$\simeq 70 \text{ Kcal sec}^{-1}$$

(4) Q_5 = heat lost to the cooling water across the liquid metal pool

$$= \frac{2401}{1} \quad (\frac{61.0}{8}) \times (\frac{10}{4})$$

$$\simeq 45.6 \text{ Kcal sec}^{-1}$$

(5) Q_6 = heat lost to the cooling water across the solidified ingot

$$= 540 \times (\frac{61.0}{8}) = 4.1 \text{ Kcal sec}^{-1}$$

The increase in the length of ingot should also be considered. However, it is reasonable to assume $Q_6 \simeq 5.0$ Kcal sec^{-1} as very little

heat leaves across the extra length of the solidified ingot to the mold cooling water.

(6) Q_7 = heat lost to base plate cooling water

$$= 0.410 \times \left(\frac{61.0}{8}\right)^2$$

$$= 31.2 \text{ Kcal sec}^{-1}$$

However as the heat leaving the bottom of the ingot decreases as the height of the ingot increases, a value of $Q_7 \simeq 25$ Kcal sec^{-1} appears more reasonable.

(7) Q_8 = Sensible heat retained by the ingot

$$= \frac{258}{3.36} \times 0.404 = 31.4 \text{ Kcal sec}^{-1}$$

Total heat output = $Q_{2A} + Q_3 + Q_5 + Q_6 + Q_7 + Q_8$ =

$$= 182 \text{ Kcal sec}^{-1}$$

Thus the total heat input should be approximately 182 Kcal sec^{-1}. The above calculation is very approximate. However most of the error can be accommodated in the term Q_5 i.e., heat lost to the cooling water across the liquid metal pool. The height of the cylindrical portion of the liquid metal pool adjusts itself to the actual power input.

Total power input = 182 Kcal sec^{-1}

= 760 Kwatts

If V = 40 volts, the total current input should be ≈19000 amperes.

APPENDIX V

DERIVATION OF THE FORMULAE FOR THE EXPLICIT FINITE DIFFERENCE METHOD

Case 1

The element is surrounded on all sides by homogeneous material (Fig. 100(a)). The temperature of a general nodal point $X_{r,z}$ at time t = k is designated as $T_{r,z,k}$. One is interested in calculating the temperature of this nodal point at time t = k + 1, knowing the temperatures of the surrounding nodal points at t = k.

Using the finite difference form of eq. (6.1),[54] the temperature of the nodal point $X_{r,z}$ at t = k + 1 is given by the following equation

$$\frac{C_p \rho}{\Delta t} \text{ volume } [T_{r,z,k+1} - T_{r,z,k}] = \frac{k_1 A_1}{\Delta r} [T_{r-1,z,k} - T_{r,z,k}]$$

$$+ \frac{k_2 A_2}{\Delta r} [T_{r+1,z,k} - T_{r,z,k}] + \frac{k_3 A_3}{\Delta z} [T_{r,z+1,k} - T_{r,z,k}] + \frac{k_4 A_4}{\Delta z} [T_{r,z-1,k} - T_{r,z,k}] \qquad \text{(A.V.1)}$$

where (1) k_1 is the average conductivity for the temperature range of $T_{r-1,z,k}$ to $T_{r,z,k}$ etc.

(2) volume of the element:

volume = area of the base x height

$$= \frac{\pi}{2\pi} \left[\left(r\Delta r + \frac{\Delta r}{2}\right)^2 - \left(r\Delta r - \frac{\Delta r}{2}\right)^2 \right] \Delta z = r \, \Delta r^2 \, \Delta z$$

(3) calculation of the area A_1

Fig. (100(b)) gives a schematic diagram for the area A_1

$$A_1 = \text{shaded area}$$

$$= \frac{2\pi}{2\pi}\left[\left(\frac{r + r - 1}{2}\right)\Delta r\right] \Delta z$$

$$= \left(\frac{2r - 1}{2}\right) \Delta r \, \Delta z$$

similarly $A_2 = \left(\frac{2r + 1}{2}\right) \Delta r \, \Delta z$

$$A_3 = r \, \Delta r^2$$

$$A_4 = r \, \Delta r^2$$

Let $$MR_1 = \frac{\rho \, C_p \, \Delta r^2}{k_1 \, \Delta t}$$

$$MR_2 = \frac{\rho \, C_p \, \Delta r^2}{k_2 \, \Delta t}$$

$$MZ_3 = \frac{\rho \, C_p \, \Delta z^2}{k_3 \, \Delta t}$$

$$MZ_4 = \frac{\rho \, C_p \, \Delta z^2}{k_4 \, \Delta t}$$

On substituting these values in eq. (A.V.1), one obtains

$$T_{r,z,k+1} - T_{r,z,k} = \left(\frac{2r-1}{2rMR_1}\right)[T_{r-1,z,k} - T_{r,z,k}] + \left(\frac{2r+1}{2rMR_2}\right)[T_{r+1,z,k} - T_{r,z,k}]$$

$$+ \frac{1}{MZ_3}[T_{r,z+1,k} - T_{r,z,k}] + \frac{1}{MZ_4}[T_{r,z-1,k} - T_{r,z,k}] \qquad \text{(A.V.2)}$$

Case 2

For a general point on the upper surface as shown in Fig. (101), the temperature at t = k+1 is given by the following equation.

$$\frac{C_p\ \rho\ \text{volume}}{\Delta t}\ [T_{r,z,k+1} - T_{r,z,k}] = \frac{k_1 A_1}{\Delta r}\ [T_{r-1,z,k} - T_{r,z,k}] + \frac{k_2 A_2}{\Delta r}\ x$$

$$[T_{r+1,z,k} - T_{r,z,k}] + h_{top}\ A_3\ [T_{r,z+1,k} - T_{r,z,k}] + \frac{k_4 A_4}{\Delta z}\ [T_{r,z-1,k} -$$

$$T_{r,z,k}] \qquad \text{(A.V.3)}$$

where volume = $\frac{r\ \Delta r^2}{2}\ \Delta z$

$A_1 = (\frac{2r-1}{4})\ \Delta r\ \Delta z$

$A_2 = (\frac{2r+1}{4})\ \Delta r\ \Delta z$

$A_3 = r\ \Delta r^2$

$A_4 = r\ \Delta r^2$

h_{top} is the heat transfer coefficient for the top surface.

On substituting these values in (A.V.3) one obtains

$$T_{r,z,k+1} - T_{r,z,k} = (\frac{2r-1}{2rMR_1})[T_{r-1,z,k} - T_{r,z,k}] + (\frac{2r+1}{2rMR_2})[T_{r+1,z,k} -$$

$$T_{r,z,k}] + \frac{2h_{top}\ \Delta t}{\rho\ C_p\ \Delta z}\ [T_{r,z+1,k} - T_{r,z,k}] + \frac{2}{MZ_4}\ [T_{r,z-1,k} - T_{r,z,k}]$$

(A.V.4)

Case 3

For a general point as shown in Fig. (102)

$$T_{r,z,k+1} - T_{r,z,k} = \frac{4(2r-1)}{MR_1(4r-1)} [T_{r-1,z,k} - T_{r,z,k}] + \frac{8\, h_{side}\, r\, \Delta t}{(4r-1)\, \rho\, C_p\, \Delta r} \times$$

$$[T_{r+1,z,k} - T_{r,z,k}] + \frac{1}{MZ_3} [T_{r,z+1,k} - T_{r,z,k}] + \frac{1}{MZ_4} [T_{r,z-1,k} -$$

$$T_{r,z,k}] \qquad \text{(A.V.5)}$$

Case 4

$$[T_{r,z,k+1} - T_{r,z,k}] = (\frac{2r-1}{2rMR_1}) [T_{r-1,z,k} - T_{r,z,k}] + (\frac{2r+1}{2rMR_2}) [T_{r+1,z,k} -$$

$$T_{r,z,k}] + \frac{2\, h_{bot}\, \Delta t}{C_p\, \rho\, \Delta z} [T_{r,z-1,k} - T_{r,z,k}] + \frac{2}{MZ_3} [T_{r,z+1,k} -$$

$$T_{r,z,k}] \qquad \text{(A.V.6)}$$

Case 5

For a general point as shown in Fig. (103)

$$T_{r,z,k+1} - T_{r,z,k} = \frac{4}{MR_2} [T_{r+1,z,k} - T_{r,z,k}] + \frac{1}{MZ_3} [T_{r,z+1,k} -$$

$$T_{r,z,k}] + \frac{1}{MZ_4} [T_{r,z-1,k} - T_{r,z,k}] \qquad \text{(A.V.7)}$$

Case 6

For a general point as shown in Fig. (104)

$$T_{r,z,k+1} - T_{r,z,k} = \{\frac{4(2r-1)}{(4r-1)MR_1}\} [T_{r-1,z,k} - T_{r,z,k}] + \{\frac{8\ r\ h_{side}\ \Delta t}{(4r-1)\rho C_p\ \Delta r}\}$$

$$[T_{r+1,z,k} - T_{r,z,k}] + \{\frac{2\ h_{top}\ \Delta t}{\rho\ C_p\ \Delta t}\} [T_{r,z+1,k} - T_{r,z,k}] +$$

$$\{\frac{2}{MZ_4}\} [T_{r,z-1,k} - T_{r,z,k}] \qquad \text{(A.V.8)}$$

Case 7

$$T_{r,z,k=1} - T_{r,z,k} = \{\frac{4(2r-1)}{(4r-1)MR_1}\} [T_{r-1,z,k} - T_{r,z,k}] + \{\frac{8\ r\ h_{side}\ \Delta t}{(4r-1)\ \rho\ C_p\ \Delta r}\}$$

$$[T_{r+1,z,k} - T_{r,z,k}] + \{\frac{2}{MZ_3}\} [T_{r,z+1,k} - T_{r,z,k}] + \{\frac{2\ h_{bot}\ \Delta t}{\Delta z\ \rho\ C_p}\}$$

$$[T_{r,z-1,k} - T_{r,z,k}] \qquad \text{(A.V.9)}$$

Case 8

For a general point as shown in Fig. (105)

$$T_{r,z,k+1} - T_{r,z,k} = \{\frac{4}{MR_2}\} [T_{r+1,z,k} - T_{r,z,k}] + \{\frac{2\ h_{top}\ \Delta t}{\rho\ C_p\ \Delta z}\}$$

$$[T_{r,z+1,k} - T_{r,z,k}] + \{\frac{2}{MZ_4}\} [T_{r,z-1,k} - T_{r,z,k}] \qquad \text{(A.V.10)}$$

Case 9

$$T_{r,z,k+1} - T_{r,z,k} = \{\frac{4}{MR_2}\} [T_{r+1,z,k} - T_{r,z,k}] + \{\frac{2}{MZ_3}\} [T_{r,z+1,k} - T_{r,z,k}] + \frac{2\, h_{bot}\, \Delta t}{\rho\, C_p\, \Delta z} [T_{r,z-1,k} - T_{r,z,k}] \quad \text{(A.V.11)}$$

APPENDIX VI

COMPUTER PROGRAMME TO DETERMINE THE POOL PROFILES IN ESR INGOTS

Flow chart of the computer programme

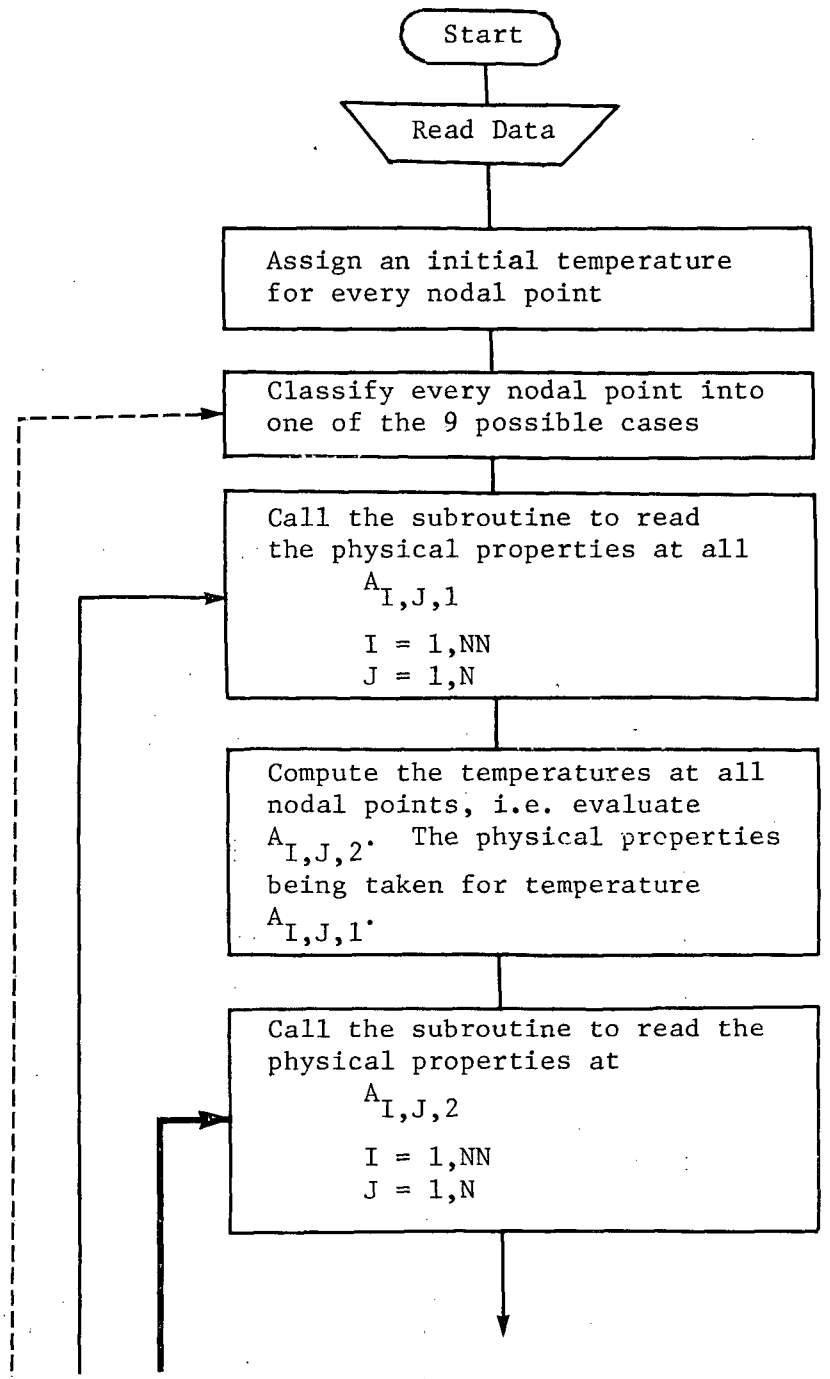

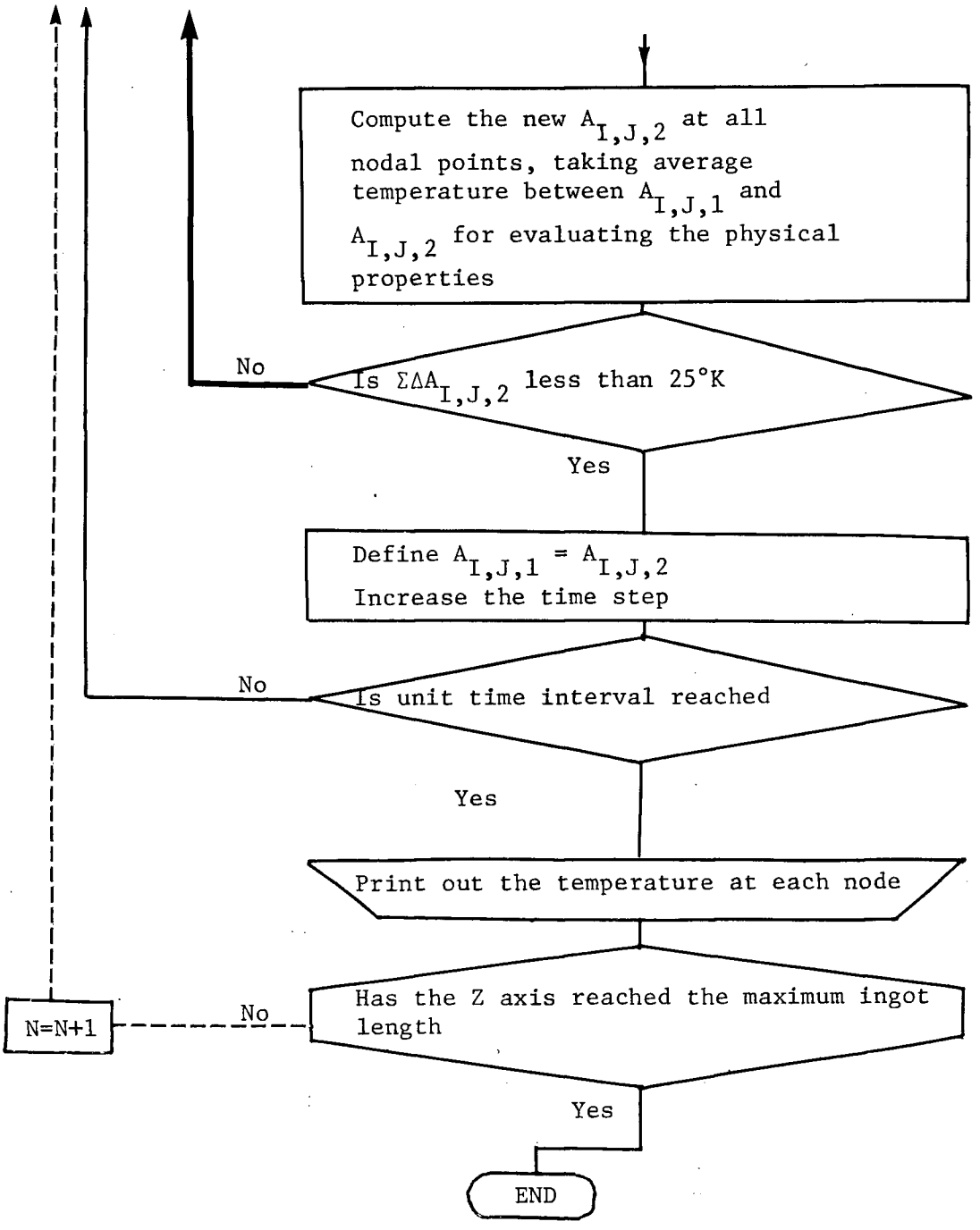
Compute the new $A_{I,J,2}$ at all nodal points, taking average temperature between $A_{I,J,1}$ and $A_{I,J,2}$ for evaluating the physical properties
No
Is $\Sigma\Delta A_{I,J,2}$ less than 25°K
Yes
Define $A_{I,J,1} = A_{I,J,2}$
Increase the time step
No
Is unit time interval reached
Yes
Print out the temperature at each node
N=N+1
No
Has the Z axis reached the maximum ingot length
Yes
END

```
C        3.81CM DIA END ELECTRODE IN A 5M DIA COPPER MOLD
C
C
C
C                        TEMPERATURE PROFILES IN AN E.S.R. INGOT
C
C
C
C
C
C                                   ABBREVIATIONS USED
C
C
C          I     :RADIAL AXIS
C
C          J     :LONGITUDINAL AXIS
C
C          K     :TIME AXIS
C
C       A(I,J,K):TEMPERATURE AT NODAL POINT (I,J,K)
C
C       T(I,J,K)=TEMPORARY TEMPERATURE LOCATION FOR NODAL POINT (I,J,K)
C
C       S(I,N,K)=TEMPERATURE OF THE ELEMENTS IN THE TOP LAYER
C
C       D(I,J,K)=DENSITY OF VOLUME ELEMENT AT (I,J,K)
C
C       CP(I,J,K):SPECIFIC HEAT OF VOLUME ELEMENT AT (I,J,K)
C
C       C(I,J,K):THERMAL CONDUCTIVITY OF VOLUME ELEMENT AT (I,J,K)
C
C        DELT   :TIME INCREMENT
C
C        DELR   :SIZE OF THE VOLUME ELEMENT IN R DIRECTION
C
C        DELZ   :SIZE OF THE VOLUME ELEMENT IN Z DIRECTION
C
C          N    : NDELZ: HT OF INGOT AT ANY TIME
C
C          NN   :NUMBER OF ELEMENTS IN THE RADIAL DIRECTION
C
C        NF     : NF*DELZ: MAXIMUM INGOT HEIGHT
C
C       ZY    : CUMMULATIVE ALLOWABLE ERROR
C
C       NAJRY  : 1 FOR APPROXIMATE EVALUATION
C       NAJRY  : 2 FOR ACCURATE EVALUATION
C
C       NRATE  : NRATE*DELT:TIME BETWEEN NEW VOLUME ELEMENT ADDITION
C
C       HSIDE  : HEAT TRANSFER COEFFICIENT FOR THE SIDE WALLS
C
C       QSUR   : (Q/A) ACROSS THE ELEMENT A(N,NN,K) FOR SURFACE BOILING
C
```

```
C     QQYA  : Q/A)  FOR SURFACE BOILING
C
C      HBOT  :  J/A ACROSS THE BOTTOM OF THE INGOT
C
C     HTOP: J/A   ACROSS THE SLAG/METAL INTERFACE
C
C     HMOT  :  J/A FOR MOLD COOLING WATER AT THE BOTTOM
C
C     PHYPRO  : SUBROUTINE TO EVALUATE THE PHYSICAL PROPERTIES
C
C
C
C                         ASSUMPTIONS
C
C
C     T  WATER  : 295.0
C
C     T  BOTTOM  :295.0
C
C     T CO WAT : 308.0
C
C
      DIMENSION A(10,50,3),T(10,50,5),B(10),      M(10,50),D(10,50,2),
     1CP(10,50,2),C(10,50,2)
      COMMON A,D,CP,C,N,NN,I,J,K
      READ(5,1)DELR ,DELZ,HSIDE,HTOP,HBOT,HMOT,DELT,HSDT
1     FORMAT(8F10.5)
      WRITE(6,50)DELR,DELZ,DELT
50     FORMAT(5X,7HDELR = ,F10.5,2HCM,5X,7HDELZ = ,F10.5,2HCM,5X,
     17HDELT = ,F10.5,3HSEC)
      WRITE(6,51)HSIDE,HTOP,HBOT,HMOT,HSDT
51    FORMAT(5X,3HHSIDE = ,F10.5,5X,7HHTOP = ,F10.5,5X,7HHBOT = ,F10.5,
     15X,7HHMOT = ,F10.5,5X,7HHSDT = ,F10.5)
      READ(5,52)NRATE,NF,N,NN,ZY
52    FORMAT(4I3,F6.2)
      WRITE(6,53)NRATE,NF,N,NN,ZY
53    FORMAT(5X,8HNRATE = ,I3,5X,5HNF = ,I2,5X,4HN = ,I2,5X,5HNN = , I2,
     15X,5HZY = ,F6.2)
      NAJRY=1
      Y=J.0
      N1=N-1
      N2=NN-1
      WRITE(6,64)
64    FORMAT(10X,40HASSUMED INITIAL TEMPERATURE DISTRIBUTION)
      DO 2 J=1,N1
      READ(5,98)(T(I,J,1) ,I=1,NN)
98     FORMAT(5F15.0)
      WRITE(6,98)(T(I,J,1) ,I=1,NN)
2     CONTINUE
      DO 99 I=1,NN
      DO 99 J=1,N1
      A(I,J,1)=T(I,J,1)
99    CONTINUE
      READ(5,98)(B(I),I=1,NN)
      WRITE(6,65)
```

```
0030        65    FORMAT     (10X,49HASSUMED TEMPERATURE DISTRIBUTION IN THE TOP LAY
                  1ER )
0031              WRITE(6,98)(B(I),I=1,NN)
0032        3     NTURN=0
0033              DO 211 I=1,NN
0034              A(I,N,1)=B(I)
0035              A(I,N,2)=B(I)
0036              T(I,N,1)=B(I)
0037              T(I,N,2)=B(I)
0038        211   CONTINUE
0039                DO 212 I=1,NN
0040               A(I,1,2)=A(I,1,1)
0041               T(I,1,2)=A(I,1,1)
0042        212          CONTINUE
0043              N1=N-1
0044              N2=NN-1
0045              DO 4  I =2,N2
0046              DO 4  J, =2,N1
0047        4     M(I,J)=1
0048              DO 5  I=2,N2
0049              J=N
0050        5     M(I,J)=2
0051              DO 6  J=2,N1
0052              I=NN
0053        6     M(I,J)=3
0054              DO 7 I=2,N2
0055              J=1
0056        7     M(I,J)=4
0057              DO 8 J=2,N1
0058              I=1
0059        8     M(I,J)=5
0060              M(NN,N)=6
0061              M(NN,1)=7
0062              M(1,N) =8
0063              M(1,1) =9
0064        9     NC=0
0065              DO 10 I=1,NN
0066              DO 10 J=1,N
0067              K=1
0068              CALL PHYPRO
0069        10    CONTINUE
0070              DO 21 I=1,NN
0071              DO 21 J=2,N1
0072              K=1
0073              KKK=M(I,J)
0074              AM=(D(I,J,1)*CP(I,J,1)*DELK**2.0)/DELT
0075              AN=(D(I,J,1)*CP(I,J,1)*DELZ**2.0)/DELT
0076              S1=(2.0*I-1.0)/(2.0*I*AM)
0077              S2=(2.0*I+1.0)/(2.0*I*AM)
0078              S3=(4.0*(2.0*I-1.0))/((4.0*I-1.0)*AM)
0079              S4=(8.0*I*DELK)/((4.0*I-1.0)*AM)
0080              S5=(2.0/AN)
0081              S6=(2.0*DELZ/AN)
0082              GO TO(11,12,13,14,15,16,17,18,19),KKK
0083        11    C1=(C(I-1,J,1)+C(I,J,1))/2.0
```

```
                C2=(C(I+1,J,1)+C(I,J,1))/2.0
                C3=(C(I,J+1,1)+C(I,J,1))/2.0
                C4=(C(I,J-1,1)+C(I,J,1))/2.0
                A1=(A(I-1,J,1)-A(I,J,1))
                A2=(A(I+1,J,1)-A(I,J,1))
                A3=(A(I,J+1,1)-A(I,J,1))
                A4=(A(I,J-1,1)-A(I,J,1))
                X=A(I,J,1)+C1*S1*A1+C2*S2*A2+C3*A3/AN+C4*A4/AN
                GO TO 20
   12           C1=(C(I-1,J,1)+C(I,J,1))/2.0
                C2=(C(I+1,J,1)+C(I,J,1))/2.0
                C4=(C(I,J-1,1)+C(I,J,1))/2.0
                A1=(A(I-1,J,1)-A(I,J,1))
                A2=(A(I+1,J,1)-A(I,J,1))
                A4=(A(I,J-1,1)-A(I,J,1))
                X=A(I,J,1)+C1*S1*A1+C2*S2*A2+S3*C4*A4+S5*HTJP
                GO TO 20
   13           A1=N-J
                AN=N
                AJ=A1/AN
                A4= ALOG10(AJ)
                C1=(C(I-1,J,1)+C(I,J,1))/2.0
                C3=(C(I,J+1,1)+C(I,J,1))/2.0
                C4=(C(I,J-1,1)+C(I,J,1))/2.0
                A1=(A(I-1,J,1)-A(I,J,1))
                A3=(A(I,J+1,1)-A(I,J,1))
                A4=(A(I,J-1,1)-A(I,J,1))
                A(I+1,J,1)=32.117*1+24.081*A4+207.213*A4**2+904.91749*A4**3
               +5291.1+57*A4**4+6559.9918*A4**5+5651.3092*A4**6+3293.8672*A4
               1**7+653.6138*A4**8
                IF(A(I+1,J,1).GT.82.0) GO TO 132
                A(I+1,J,1)=A(I+1,J,1)+273.0
                X=A(I,J,1)+C1*S3*A1+C3*A3/AN+C4*A4/AN-S4*(A(I+1,J,1)-303.)*HSIDE
                GO TO 20
  132           JOYA= (EXP(0.12*ALOG(A(I+1,J,1)-50.0)-22.18))
                X=A(I,J,1)+C1*S3*A1+C3*A3/AN+C4*A4/AN-S4*QBYA
                GO TO 20
   14           C1=(C(I-1,J,1)+C(I,J,1))/2.0
                C2=(C(I+1,J,1)+C(I,J,1))/2.0
                C3=(C(I,J+1,1)+C(I,J,1))/2.0
                A1=(A(I-1,J,1)-A(I,J,1))
                A2=(A(I+1,J,1)-A(I,J,1))
                A3=(A(I,J+1,1)-A(I,J,1))
                X=A(I,J,1)+C1*S1*A1+C2*S2*A2+C3*S3*A3-S5*HBUT
                GO TO 20
   15           C2=(C(I+1,J,1)+C(I,J,1))/2.0
                C3=(C(I,J+1,1)+C(I,J,1))/2.0
                C4=(C(I,J-1,1)+C(I,J,1))/2.0
                A2=(A(I+1,J,1)-A(I,J,1))
                A3=(A(I,J+1,1)-A(I,J,1))
                A4=(A(I,J-1,1)-A(I,J,1))
                X=A(I,J,1)+C3*A3/AN+C4*A4/AN+.5*C2*A2/AM
                GO TO 20
   16           C1=(C(I-1,J,1)+C(I,J,1))/2.0
                C4=(C(I,J-1,1)+C(I,J,1))/2.0
```

```
0137              A1=(A(I-1,J,1)-A(I,J,1))
0138              A4=(A(I,J-1,1)-A(I,J,1))
0139              X=A(I,J,1)
0140              GO TO 20
0141        17    C1=(C(I-1,J,1)+C(I,J,1))/2.0
0142              C3=(C(I,J+1,1)+C(I,J,1))/2.0
0143              A1=(A(I-1,J,1)-A(I,J,1))
0144              A3=(A(I,J+1,1)-A(I,J,1))
0145              X=A(I,J,1)+C1*S3*A1+S5*C3*A3-S6*HBDT-S4*HMDT
0146              GO TO 20
0147        18    C2=(C(I+1,J,1)+C(I,J,1))/2.0
0148              C4=(C(I,J-1,1)+C(I,J,1))/2.0
0149              A2=(A(I+1,J,1)-A(I,J,1))
0150              A4=(A(I,J-1,1)-A(I,J,1))
0151              X=A(I,J,1)+4.0*C2*A2/AM+S6*HTOP+C4*A4*S5
0152              GO TO 20
0153        19    C2=(C(I+1,J,1)+C(I,J,1))/2.0
0154              C3=(C(I,J+1,1)+C(I,J,1))/2.0
0155              A2=(A(I+1,J,1)-A(I,J,1))
0156              A3=(A(I,J+1,1)-A(I,J,1))
0157              X=A(I,J,1)+4.0*C2*A2/AM+A3*C3*S5-S6*HBDT
0158        20    T(I,J,2)=X
0159        21    CONTINUE
0160              DO 22 I=1,NN
0161              DO 22 J=2,N1
0162              A(I,J,2) =T(I,J,2)
0163        22    CONTINUE
0164              IF(NAURY.EQ.1) GO TO 38
0165        23    ZZ=0.0
0166              DO 24 I=1,NN
0167              DO 24 J=1,N
0168              K=2
0169              CALL PHYPRO
0170        24    CONTINUE
0171              DO 35 I=1,NN
0172              DO 35 J=2,N1
0173              KKK=M(I,J)
0174              K=2
0175              AM=((D(I,J,1)+D(I,J,2))*(CP(I,J,1)+CP(I,J,2))*DELR**2.0)/(4.*DELT)
0176              AN=((D(I,J,1)+D(I,J,2))*(CP(I,J,1)+CP(I,J,2))*DELZ**2.0)/(4.*DELT)
0177              S1=(2.0*I-1.0)/(2.0*I*AN)
0178              S2=(2.0*I+1.0)/(2.0*I*AM)
0179              S3=(4.0*(2.0*I-1.0))/((4.0*I-1.0)*AM)
0180              S4=(8.0*I*DELR)/((4.0*I-1.0)*AM)
0181              S5=(2.0/AN)
0182              S6=(2.0*DELZ/AN)
0183              GO TO (25,26,27,28,29,30,31,32,33),KKK
0184        25    C1=(C(I-1,J,1)+C(I-1,J,2)+C(I,J,1)+C(I,J,2))/4.0
0185              C2=(C(I+1,J,1)+C(I+1,J,2)+C(I,J,1)+C(I,J,2))/4.0
0186              C3=(C(I,J+1,1)+C(I,J+1,2)+C(I,J,1)+C(I,J,2))/4.0
0187              C4=(C(I,J-1,1)+C(I,J-1,2)+C(I,J,1)+C(I,J,2))/4.0
0188              A1=(A(I-1,J,1)-A(I,J,1))
0189              A2=(A(I+1,J,1)-A(I,J,1))
0190              A3=(A(I,J+1,1)-A(I,J,1))
0191              A4=(A(I,J-1,1)-A(I,J,1))
```

```
0192            X=A(I,J,1)+C1*S1*A1+C2*S2*A2+C3*A3/AN+C4*A4/AN
0193            GO TO 34
0194       25   C1=(C(I-1,J,1)+C(I-1,J,2)+C(I,J,1)+C(I,J,2))/4.)
0195            C2=(C(I+1,J,1)+C(I+1,J,2)+C(I,J,1)+C(I,J,2))/4.0
0196            C4=(C(I,J-1,1)+C(I,J-1,2)+C(I,J,1)+C(I,J,2))/4.0
0197            A1=(A(I-1,J,1)-A(I,J,1))
0198            A2=(A(I+1,J,1)-A(I,J,1))
0199            A4=(A(I,J-1,1)-A(I,J,1))
0200            X=A(I,J,1)+C1*S1*A1+C2*S2*A2+S5*C4*A4+S6*HTOP
0201            GO TO 34
0202       27   ANN=N-J
0203            AN=N
0204            AJ=ANN/ANN
0205            AH= ALOG10(AJ)
0206            C1=(C(I-1,J,1)+C(I-1,J,2)+C(I,J,1)+C(I,J,2))/4.0
0207            C3=(C(I,J+1,1)+C(I,J+1,2)+C(I,J,1)+C(I,J,2))/4.0
0208            C4=(C(I,J-1,1)+C(I,J-1,2)+C(I,J,1)+C(I,J,2))/4.0
0209            A1=(A(I-1,J,1)-A(I,J,1))
0210            A3=(A(I,J+1,1)-A(I,J,1))
0211            A4=(A(I,J-1,1)-A(I,J,1))
0212            A(I+1,J,K)=35.11761+24.3814*AH+267.218*AH**2+904.51749*AH**3
                1+3291.1+27*AH**4+6509.9914*AH**5+6051.3092*AH**6+3293.8672*AH
                1**7+833.3109*AH**8
0213            IF(A(I+1,J,1).GT.82.0) GO TO 272
0214            A(I+1,J,1)=A(I+1,J,1)+273.0
0215            X=A(I,J,1)+C1*S3*A1+C3*A3/AN+C4*A4/AN-S4*(A(I+1,J,1)-303.)*HSIDE
0216            GO TO 34
0217       272  GOYA= (EXP(6.42*ALOG(A(I+1,J,1)-50.0)-22.18))
0218            X=A(I,J,1)+C1*S3*A1+C3*A3/AN+C4*A4/AN-S4*GOYA
0219            GO TO 34
0220       28   C1=(C(I-1,J,1)+C(I-1,J,2)+C(I,J,1)+C(I,J,2))/4.0
0221            C2=(C(I+1,J,1)+C(I+1,J,2)+C(I,J,1)+C(I,J,2))/4.0
0222            C3=(C(I,J+1,1)+C(I,J+1,2)+C(I,J,1)+C(I,J,2))/4.0
0223            A1=(A(I-1,J,1)-A(I,J,1))
0224            A2=(A(I+1,J,1)-A(I,J,1))
0225            A3=(A(I,J+1,1)-A(I,J,1))
0226            X=A(I,J,1)+C1*S1*A1+C2*S2*A2+C3*S5*A3-S6*HBOT
0227            GO TO 34
0228       29   C2=(C(I+1,J,1)+C(I+1,J,2)+C(I,J,1)+C(I,J,2))/4.0
0229            C3=(C(I,J+1,1)+C(I,J+1,2)+C(I,J,1)+C(I,J,2))/4.0
0230            C4=(C(I,J-1,1)+C(I,J-1,2)+C(I,J,1)+C(I,J,2))/4.0
0231            A2=(A(I+1,J,1)-A(I,J,1))
0232            A3=(A(I,J+1,1)-A(I,J,1))
0233            A4=(A(I,J-1,1)-A(I,J,1))
0234            X=A(I,J,1)+C3*A3/AN+C4*A4/AN+4.0*C2*A2/AM
0235            GO TO 34
0236       30   C1=(C(I-1,J,1)+C(I-1,J,2)+C(I,J,1)+C(I,J,2))/4.0
0237            C4=(C(I,J-1,1)+C(I,J-1,2)+C(I,J,1)+C(I,J,2))/4.0
0238            A1=(A(I-1,J,1)-A(I,J,1))
0239            A4=(A(I,J-1,1)-A(I,J,1))
0240            X=A(I,J,1)
0241            GO TO 34
0242       31   C1=(C(I-1,J,1)+C(I-1,J,2)+C(I,J,1)+C(I,J,2))/4.0
0243            C3=(C(I,J+1,1)+C(I,J+1,2)+C(I,J,1)+C(I,J,2))/4.0
0244            A1=(A(I-1,J,1)-A(I,J,1))
```

```
0245              A3=(A(I,J+1,1)-A(I,J,1))
0246              X=A(I,J,1)+C1*S3*A1+S5*C3*A3-S6*HBDT-S4*HMDT
0247              GO TO 34
0248         32   C2=(C(I+1,J,1)+C(I+1,J,2)+C(I,J,1)+C(I,J,2))/4.0
0249              C4=(C(I,J-1,1)+C(I,J-1,2)+C(I,J,1)+C(I,J,2))/4.0
0250              A2=(A(I+1,J,1)-A(I,J,1))
0251              A4=(A(I,J-1,1)-A(I,J,1))
0252              X=A(I,J,1)+4.0*C2*A2/AM+S6*HTOP+C4*A4*S5
0253              GO TO 34
0254         33   C2=(C(I+1,J,1)+C(I+1,J,2)+C(I,J,1)+C(I,J,2))/4.0
0255              C3=(C(I,J+1,1)+C(I,J+1,2)+C(I,J,1)+C(I,J,2))/4.0
0256              A2=(A(I+1,J,1)-A(I,J,1))
0257              A3=(A(I,J+1,1)-A(I,J,1))
0258              X=A(I,J,1)+4.0*C2*A2/AM+A3*C3*S5-S6*HBDT
0259         34   YY=A(I,J,2)-X
0260              ZZ=ZZ +ABS(YY)
0261              T(I,J,2) =X
0262         35   CONTINUE
0263              DO 36 I=1,NN
0264               DO 36 J=2,N1
0265              A(I,J,2)=T(I,J,2)
0266         36   CONTINUE
0267              IF(ZZ-ZY)38,36,37
0268         37   NC=NC+1
0269              GO TO 23
0270         38   Y=Y+DELT
0271              NTURN=NTURN +1
0272              DO 41  I=1,NN
0273              DO 41 J=2,N1
0274              A(I,J,1) = A(I,J,2)
0275              T(I,J,1)=A(I,J,1)
0276         41   CONTINUE
0277              IF(NTURN-NRATE)40, 42,42
0278         40   GO TO 9
0279         42   CM=N*DELZ
0280              WRITE(6,39)CM
0281         39   FORMAT(10X,18HLENGTH OF INGOT = ,F6.2)
0282              WRITE (6,44)
0283         44   FORMAT(10X,26HTEMPERATURE AT THE NODES   )
0284              DO 46  J=1,N
0285              WRITE(6,45)(A(I,J,2),I=1,NN)
0286         45   FORMAT (8F15.4)
0287         46   CONTINUE
0288              N=N+1
0289              IF(N-NF)3,47,47
0290         47   STOP
0291              END
```

TOTAL MEMORY REQUIREMENTS 004582 BYTES

COMPILE TIME = 20.4 SECONDS

```
FORTRAN IV G COMPILER        PHYPRO          06-24-71        16:13:26        PAGE 0001

0001                SUBROUTINE  PHYPRO
0002                 DIMENSION A(10,50,3),T(10,50,3),B(10),      M(10,50),D(10,50,2),
                   1CP(10,50,2),C(10,50,2)
0003                 COMMON A,D,CP,C,N,NN,I,J,K
0004                 IF(A(I,J,K).LT.900.0 )GO TO  101
0005                 IF(A(I,J,K).LT.1350.0) GO TO 102
0006                 IF(A(I,J,K).LT.1660.0)GO TO  103
0007                 IF(A(I,J,K).LT.1570.0)GO TO  104
0008                 IF(A(I,J,K).LT.1750.0)GO TO 105
0009                 IF(A(I,J,K).LT.1751.0)GO TO 106
0010                 IF(A(I,J,K).LT.1825.0)GO TO  107
0011                 IF(A(I,J,K).LT.1900.0)GO TO  108
0012                 IF(A(I,J,K).LT.2050.0)GO TO  109
0013          101    D(I,J,K)= 7.75
0014                 CP(I,J,K)= 0.14
0015                 C(I,J,K) = 0.13
0016                 GO TO 155
0017          102    D(I,J,K)= 7.59
0018                 CP(I,J,K)= 0.16
0019                 C(I,J,K) = 0.072
0020                 GO TO 155
0021          103    D(I,J,K)= 7.42
0022                 CP(I,J,K)= 0.15
0023                 C(I,J,K) = 0.076
0024                 GO TO 155
0025          104    D(I,J,K)= 7.35
0026                 CP(I,J,K)= 0.53
0027                 C(I,J,K) = 0.082
0028                 GO TO 155
0029          105    D(I,J,K)= 7.31
0030                 CP(I,J,K)=0.164
0031                 C(I,J,K) = 0.065
0032                 GO TO 155
0033          106    D(I,J,K)= 7.1869
0034                 CP(I,J,K)=65.7
0035                 C(I,J,K)=0.12
0036                 GO TO 155
0037          107    D(I,J,K)= 7.073
0038                 CP(I,J,K)= 0.18
0039                 C(I,J,K)=0.24
0040                 GO TO 155
0041          108    D(I,J,K)= 7.04
0042                 CP(I,J,K)= 0.182
0043                 C(I,J,K)=0.30
0044                 GO TO 155
0045          109    D(I,J,K)= 6.94
0046                 CP(I,J,K)= 0.183
0047                 C(I,J,K)=0.40
0048          155    RETURN
0049                 END

 TOTAL MEMORY REQUIREMENTS 002708 BYTES

 COMPILE TIME =       2.2  SECONDS
```

BIBLIOGRAPHY

1. G.K. Bhat: Proc. Second Int. Symp. on ESR Technology, Vol. I, Mellon Institute, Pittsburgh, (IX, 1969).

2. W. Holzgruber, A. Schneidhofer, M. Kroneis: Proc. Second Int. Symp. on ESR Technology, Vol. I, Mellon Institute, Pittsburgh, (IX, 1969).

3. B.E. Paton, B.I. Medovar, Yu. V. Latash, L.V. Chekotilo: Proc. Second. Int. Symp. on ESR Technology, Vol. III, Mellon Institute, Pittsburgh, (IX, 1969).

4. B.I. Medovar, Yu. V. Latash, B.I. Maksimvich, L.M. Stupak: Electroslag Remelting, State Scientific and Techn. Publ. House of Literature on Ferrous and Non-ferrous Metallurgy, Moscow (1963).

5. W.E. Duckworth and P.J. Wooding: Trans. Vacuum Metallurgy Conference, Am. Vac. Soc. N.Y., pp 479-498 (1968).

6. W. Holzgruber, K. Petersen, P.E. Schneider: Trans. Vacuum Metallurgy Conference, Am. Vac. Soc. N.Y., pp 499-523 (1968).

7. W. Holzgruber: Proc. First Int. Symp. on ESR Technology, Vol. **II**, Mellon Institute, Pittsburgh, (VIII, 1967).

8. P.G. Clites and R.A. Beall: U.S. Bureau of Mines, Report of Investigations No. 7035 (X, 1967).

9. M. Etienne: Ph.D. Thesis, Department of Metallurgy, Univer. of British Columbia, Canada (X, 1970).

10. R.K. Hopkins: U.S. Pat. No's. 3 067 473, 2 191 479, 3 152 372.

11. G.K. Bhat: Proc. First Int. Symp. on ESR Technology, Vol I, Mellon Institute, Pittsburgh, (VIII, 1967).

12. A. Mitchell and G. Beynon: unpublished research, Dept. of Metallurgy, Univer. of British Columbia, Canada (1970).

13. Yu. M. Mironov, M.M. Klyuev, V.V. Topilin: Izv. Vysshikh Uchebn. Zavedenii Chernaya Met., 5, pp 51-56 (1965).

14. G.D. Robbins: J. Electrochem. Soc., 116, pp 813-817 (VI, 1969).

15. A. Klemm: Molten Salt Chemistry, Ed. M. Blander, Interscience Publishers, pp 535-606 (1964).

16. J. Bockris and S.N.S. Reddy: Modern Electrochemistry, Plenum Press, New York (1970).

17. A. Mitchell: J. Vacuum Science and Technology, 7 (6), pp 563-573 (1970).

18. B.E. Paton: Electroslag Welding, Am. Welding Society, Inc., N.Y., pp 22-24 (1962).

19. B.S. Speranskii, Yu. A. Szulte, I.A. Harevskich: Avt. Svarka, 16(1), pp 9-14 (1963).

20. A. Mitchell: A.S.M. Technical Report No. g. 98-7.4 (1968).

21. A. Mitchell and J. Cameron: unpublished research, Dept. of Metallurgy, Univer. of British Columbia, Canada (1970).

22. C.F. Kayan: Trans. ASME, 71, pp 9-16 (I, 1949).

23. D.A.R. Kay: Proc. First Int. Symp.on ESR Technology, Vol II, Mellon Institute, Pittsburgh (VIII, 1967).

24. S. Sikka: M.A.Sc. Thesis, Dept. of Mechanical Eng., Univer. of British Columbia, Canada (IV, 1969).

25. C.R. Wylie Jr.: Adv. Engineering Mathematics, 3rd Ed., McGraw-Hill Book Co., USA, pp 363-64 (1966).

26. D.D. McCracken and W.S. Dorn: Numerical Methods and Fortran Programming, John Wiley and Sons Inc., pp 262-275 (1964).

27. A.G. Fowler and C.F. Moore: Univer. of British Columbia Computer Center Writeup no. 44.2, UBC LQF, (I, 1970).

28. M.A. Maulvault and J.F. Elliott: private communication.

29. J. Szekely, J. Mendrykowski, J. Poveromo, A. Mitchell: paper presented at the 100th AIME Conference in New York (III, 1971).

30. A. Mitchell, S. Joshi, J. Cameron: Metallurgical Transactions, 2, pp 561-567 (II, 1971).

31. O. Kubashewski and B.E. Hopkins: Oxidation of Metals and Alloys, Butterworths, London, pp 230-240 (1962).

32. B.I. Medovar, Yu. V. Latash, B.I. Maksimvich, L.M. Stupak: Electroslag Remelting, State Scientific and Techn. Publ. House of Literature on Ferrous and Non-ferrous Metallurgy, Moscow, pp 23-35 (1963).

33. A. Mitchell and S. Joshi: Met. Transactions, 2, pp 449-455 (II, 1971).

34. B.I. Medovar, Yu. V. Latash, B.I. Maksimvich, L.M. Stupak: Electroslag Remelting, State Scientific and Techn. Publ. House of Literature on Ferrous and Non-ferrous Metallurgy, Moscow, pp 158-160 (1963).

35. F. Kreith: Principles of Heat Transfer (2nd Ed), Int. Textbook Co., Scranton, Pa., (1969).

36. J. Cameron, M. Etienne, A. Mitchell: Metallurgical Transactions, 1, pp 1839-44 (1970).

37. E.A. Mizikar: TMS AIME, 239, pp 1747-53 (1967).

38. W.D. Kingery: Progress in Ceramic Science, Vol. 2, Pergamon Press, N.Y., pp 192 (1962).

39. R.J. Roberts: Proc. Second Int. Symp. on ESR Technology, Vol. II, Mellon Institute, Pittsburgh (IX, 1969).

40. W. Holzgruber: Doctoral Dissertation, Mont. Hochschule, Leoben, Austria (VI, 1967).

41. W. Holzgruber and E. Plockinger: Stahl und Eisen, 88, pp 638-48 (1968).

42. R. Kammel and H. Winterhager: Refining by ESR, Erzmetall., 21 pp. 339 (1968).

43. D.A. Whittaker: Ph.D. Thesis, McMaster University, Canada (VIII, 1967).

44. M. Blander: Molten Salt Chemistry, Interscience Publishers, pp 367-421 (1964).

45. K. Engelberg-Forster and R. Grief: J. Heat Transfer (Trans ASME), 81, pp 43-53 (II, 1959).

46. E.N. Sieder and G.E. Tate: Ind. and Eng. Chem., 28, pp 1429-36 (1936).

47. W.M. Rohsenow: Trans ASME, 74, pp 969-76 (VIII, 1952).

48. W.H. McAdams, W.E. Kennel, C.S. Minden, R. Carl, P.M. Picornell, J.E. Dew: Ind. and Eng. Chem., 41, pp 1945-53 (IX, 1949).

49. H.J. Klein: The effect of a variation of melt parameters on the electroslag remelting of a nickel-base alloy, Stellite Division, Cabot Corporation, Kokomo, Indiana USA (1970).

50. R.C. Sun and J.W. Pridgeon: Proc. Second Int. Symp. on ESR Technology, Vol III, Mellon Institute, Pittsburgh (IX, 1969).

51. A. Mitchell: private communication (1971).

52. J.G. Henzel, Jr. and J. Keverian: Proc. of the Electric Furnace Conference (1964).

53. J.G. Henzel, Jr. and J. Keverian: Metals Engineering Quarterly, ASM, pp 39-44 (V, 1965).

54. G.M. Dusinberre: Heat Transfer Calculations by Finite Differences, Chapter 2 and 6, Haddon Craftsmen Inc., Scranton, Pennsylvania (1961).

55. J. Crank: The Mathematics of Diffusion: Chapter 10, Oxford (1956).

56. M.J. Stewart: Ph.D. Thesis, Dept. of Metallurgy, Univer. of British Columbia (XII, 1970).

57. Metals Handbook Committee: Metals Handbook, Am. Soc. for Metals Vol I (8th Ed.), pp 1206-12 (VII, 1967).

58. G.I. Zhmoidin: Isv. Acad. Nauk, S.S.S.R. Met. 6, 9, (1969).

59. B.M. Nikitin and T.I. Litvinova: Russ. Met. 6, (1966) (U.D.C. 669-017-11).

60. T. Baak: Acta Chem. Scand., 8, 1727 (1954).

61. P.P. Budnikov and S.G. Trieswiatskii: Sov. Phys.-Dokl., 89, 479 (1953).

62. A. Mitchell and B. Burel: J. Iron Steel Inst. (London), 208, 407 (1970).

63. J. Mukerji: Mem. Sci. Rev. 60, 785-96 (1963).

64. W. Gutt and G.J. Osbourne: Trans. Brit. Ceram. Soc., 65, 521 (1966).

65. E.M. Levin, H.F. McMurdie, E.P. Hall, Ed.: Phase Diagrams for Ceramists, Amer. Ceram. Soc., (1956).

66. B.M. Nikitin: Izvestia Akademi Nauk., S.S.S.R, 4, pp 222-225 (1970).

67. D.A. Povolotski, B.A. Mishenko, A.P. Byamkin, A.B. Puzirev: Izvestia Vysshikh Uchebnik Zavednii Chevnaya Metallurgia, 13 (12), pp 8, 12 (1970).

68. A.D. Kirshenbaum J.A. Cahill, C.S. Stokes: J. Inorg. Nucl. Chem., 15, 297-304 (1960).

69. P.P. Evseer: Artomat. Svarka 176, 42-45 (1967).

70. V.V. Stepanov and B.E. Lopaev: Avtomat. Svarta, 176, pp 46-50 (1967).

71. S.B. Yakobashvili and I.I. Frimin: Avtomat. Svarka, 171, pp 39-41 (1962).

72. N.M. Gogiberizde, T.I. Dzlincharadze, Sh. M. Mikiaslvilly: Bull. Acad. Sci. Georg. U.S.S.R., 3, pp 696 (1968).

73. M.W. Davies and F.A. Wright: Chem. and Industry, 4, pp 359-63 (1970).

74. V.V. Stepanov, B.E. Lopaev, S.V. Shtengel'meier: Avtomat. Svarka, 174, pp 1128 (1965).

75. M. Sakai, T. Katsuda, R. Manikawa: Sci. Rep. Shiga. Pref. Coll., 8, pp 10-13 (1967).

76. G.D. Robbing: J. Electrochem. Soc., 116, pp 813 (1969).

77. M. Kato and S. Minowa: Trans. Iron Steel Inst. (Tokyo), 9, pp 39 (1969).

78. S.E. Vaisburd, P.P. Evseer, I.N. Sedina, A. Ia, Stomahin: Izv. Vysshikh. Uchebn. Zavedonii (Ferr. Met.), 5, p 54-56 (1969).

79. D.A. Shulz and A.W. Searcy: J. Phys. Chem., 67, pp 103-106 (1963).

80. S. Cantor, W.T. Ward, C.T. Moynihan: J. Chem. Phys., 50(7), pp 2874-79 (1969).

81. J. Om Bockris, J.L. White, J.D. Mackenzie: Physico-chemical Measurements at High Temperatures, Butterworth's Scientific Pub., London, p. 347 (1959).

82. J.R. Rait: Trans. Brit. Ceram. Soc., 40, pp 1941 (1941).

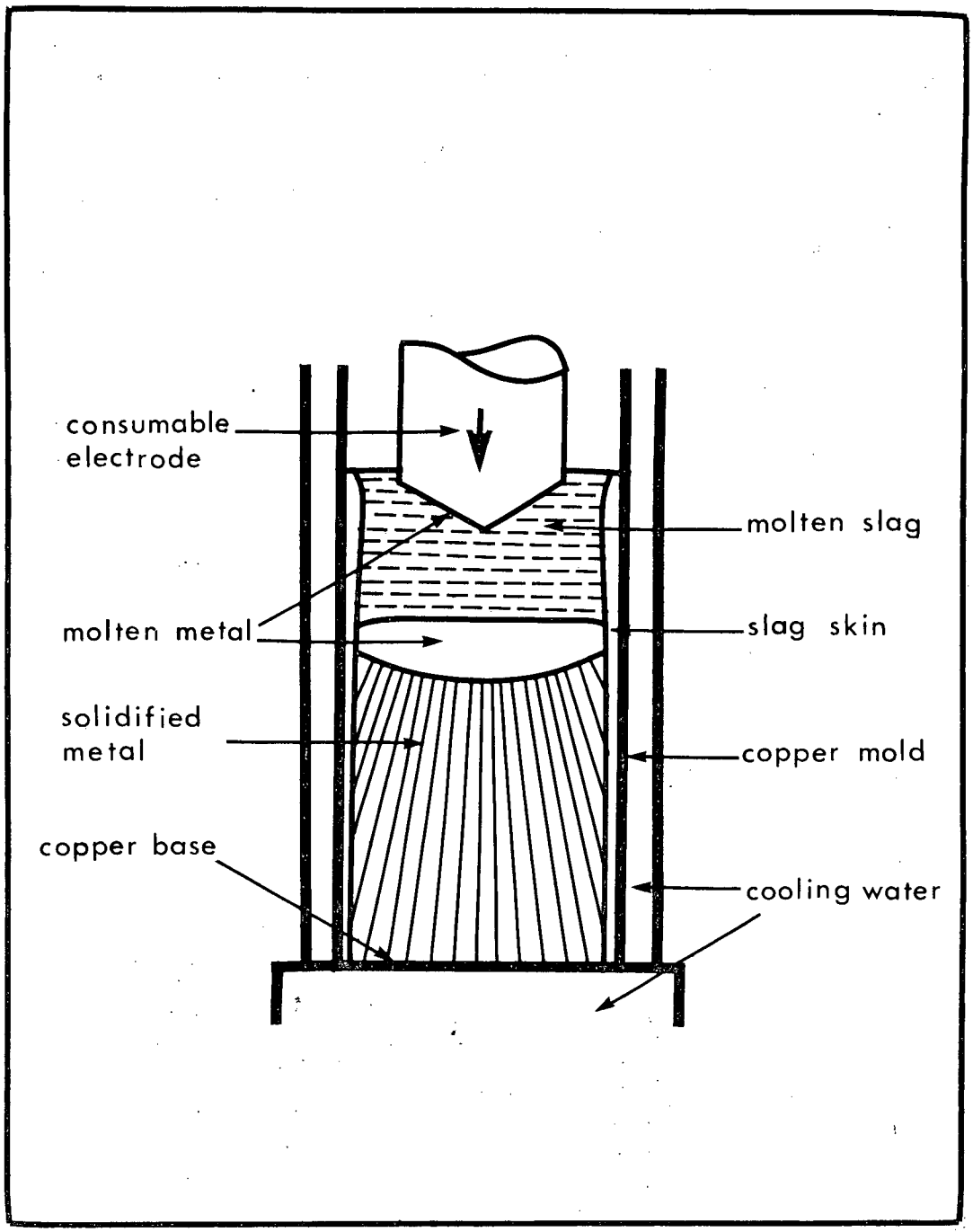

Figure 1. Schematic diagram of the electroslag remelting unit.

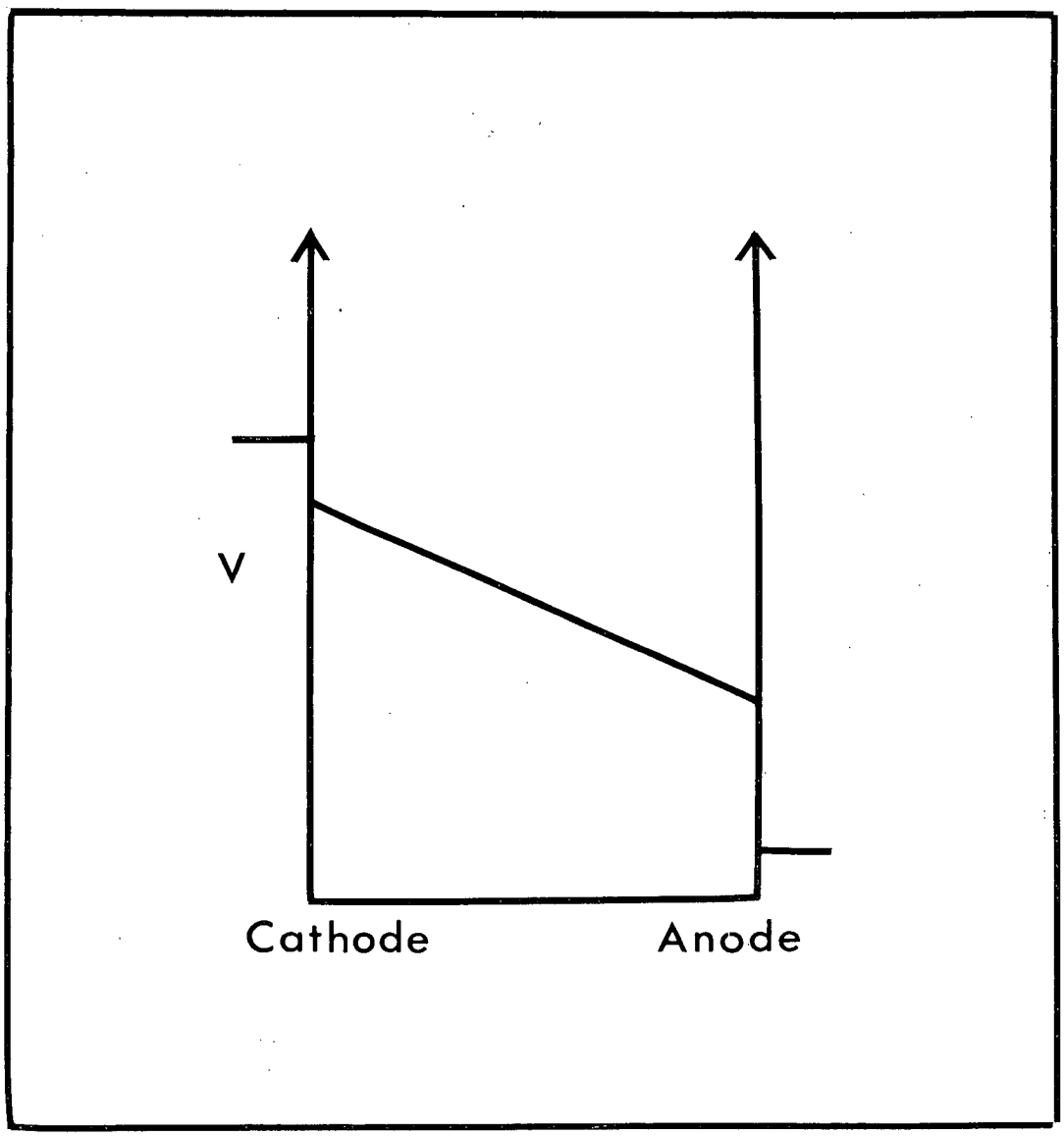

Figure 2. Voltage gradient in an arc.

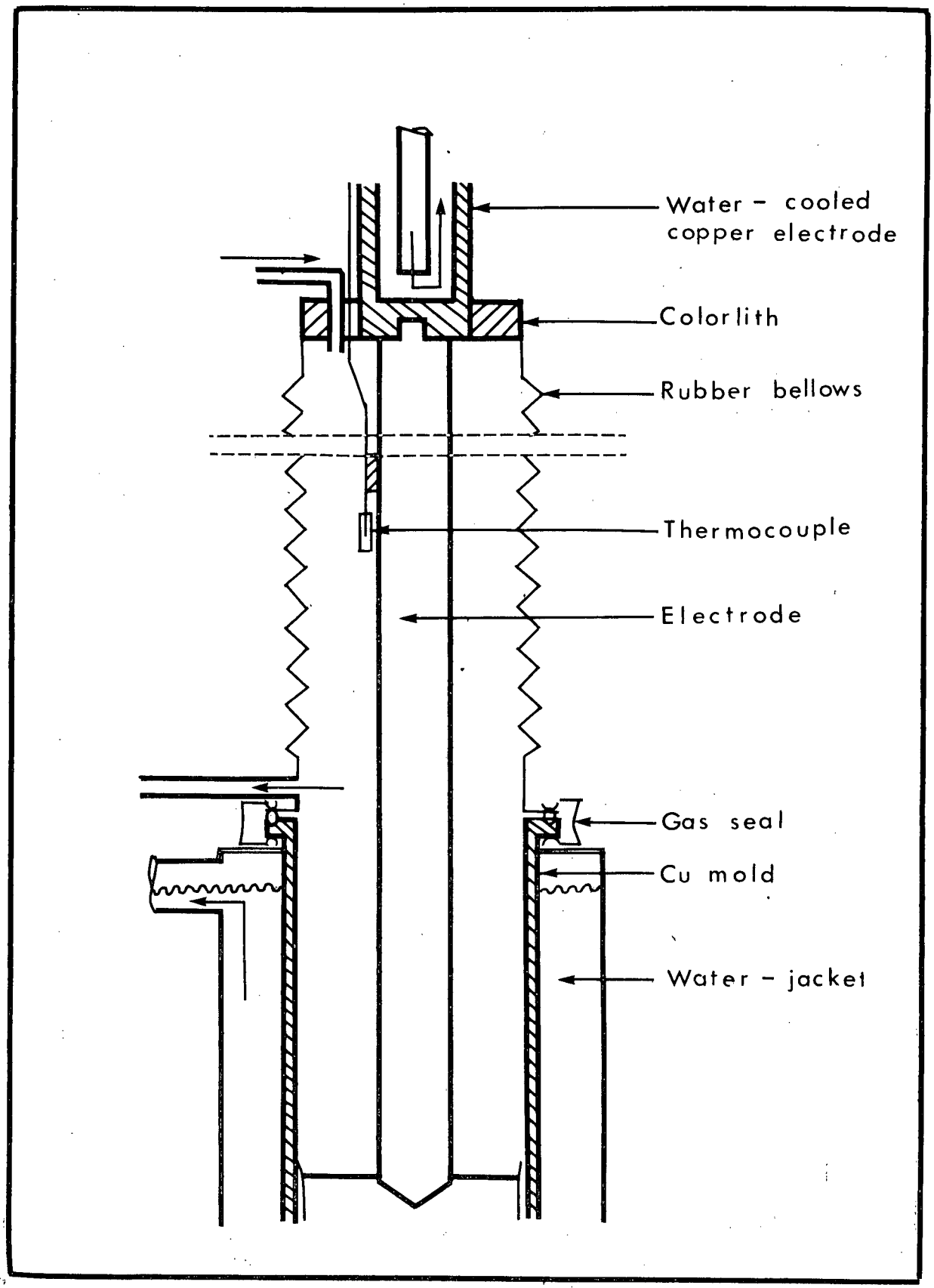

Figure 3. ESR experimental setup for temperature measurement under an argon atmosphere.

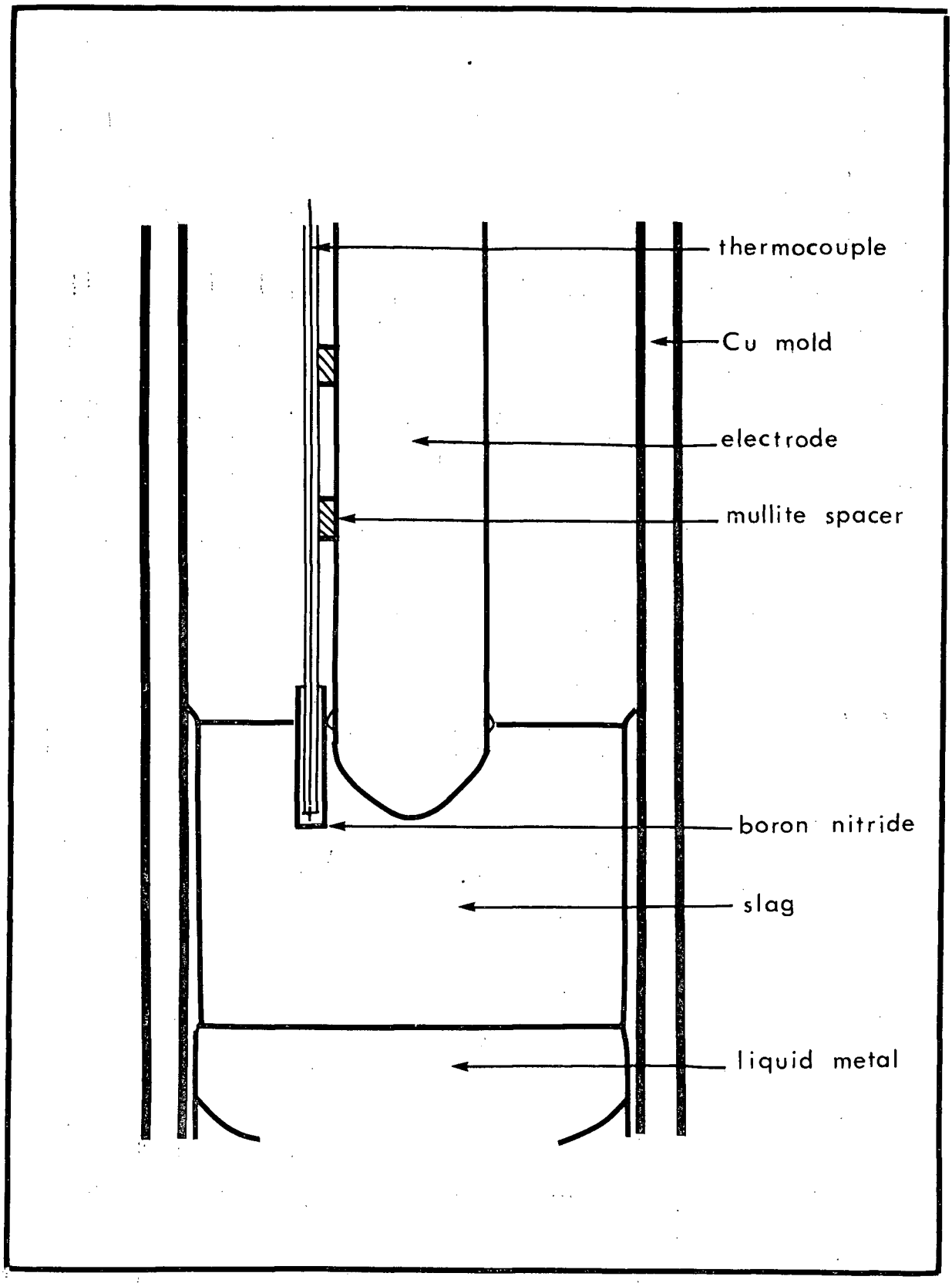

Figure 4. Details of the thermocouple arrangement.

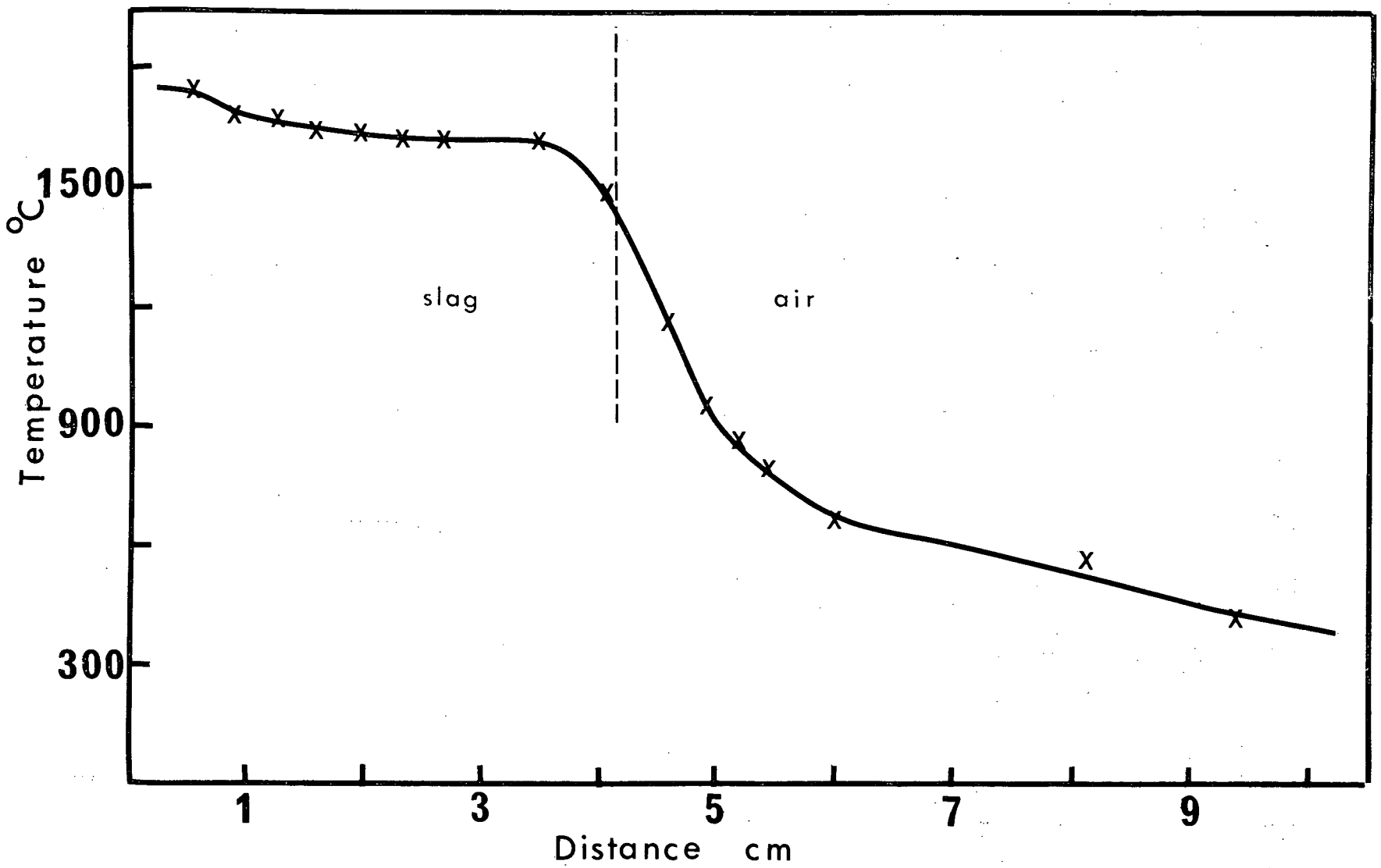

Figure 5. Temperature distribution in the slag bed for d.c. negative (air).

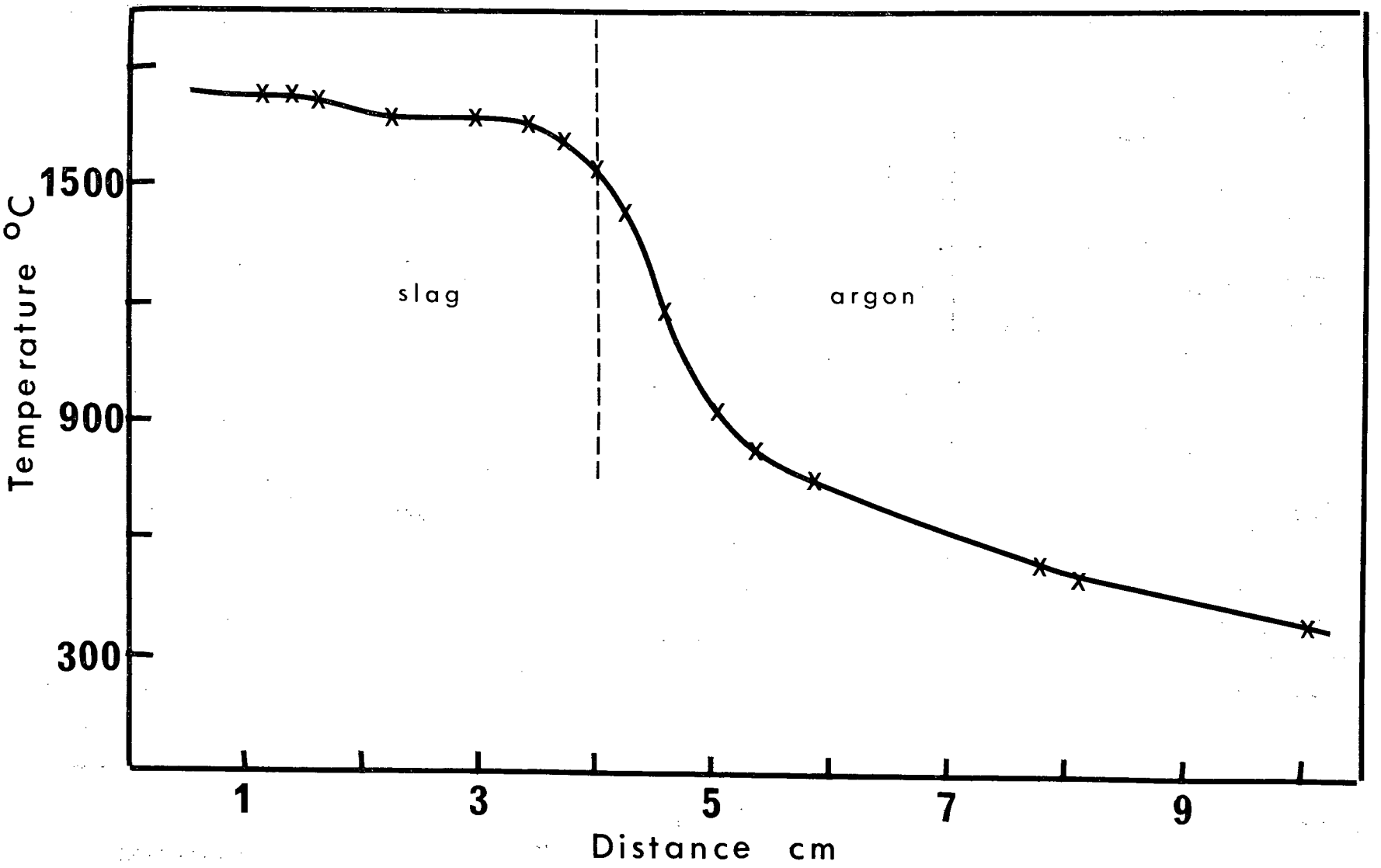

Figure 6. Temperature distribution in the slag bed for d.c. negative (argon).

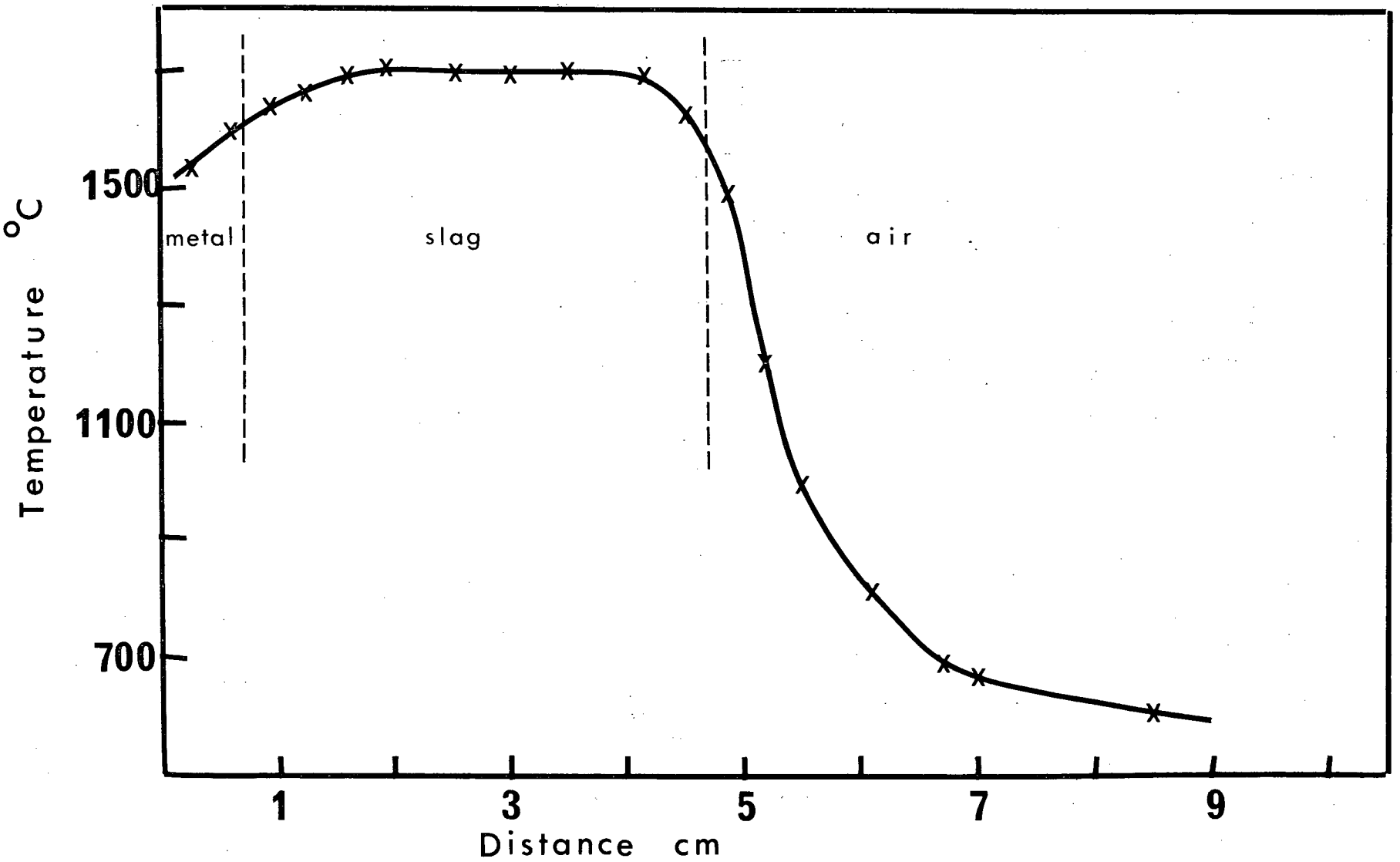

Figure 7. Temperature distribution in the slag bed for a.c. (air).

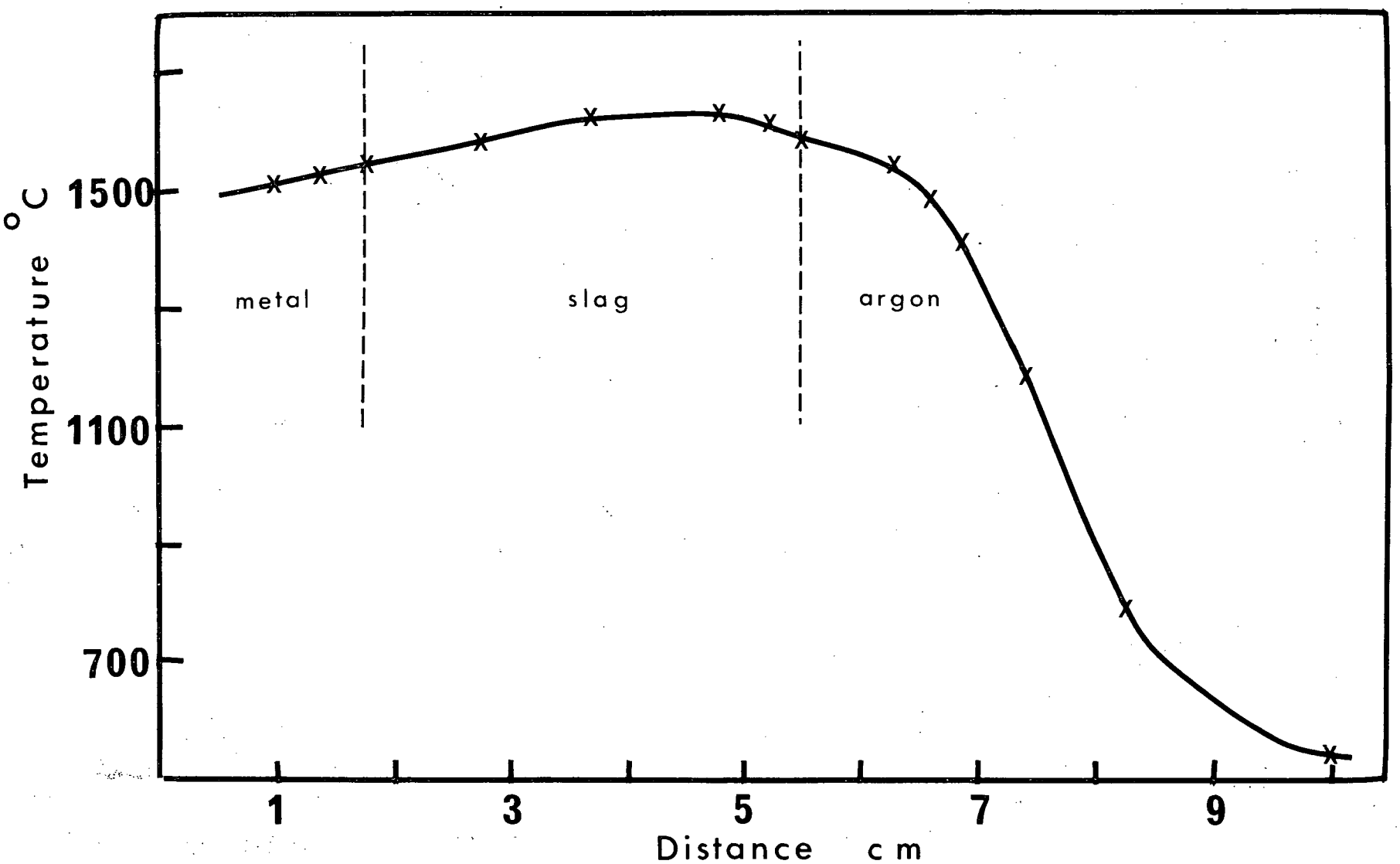

Figure 8. Temperature distribution in the slag bed for a.c. (argon).

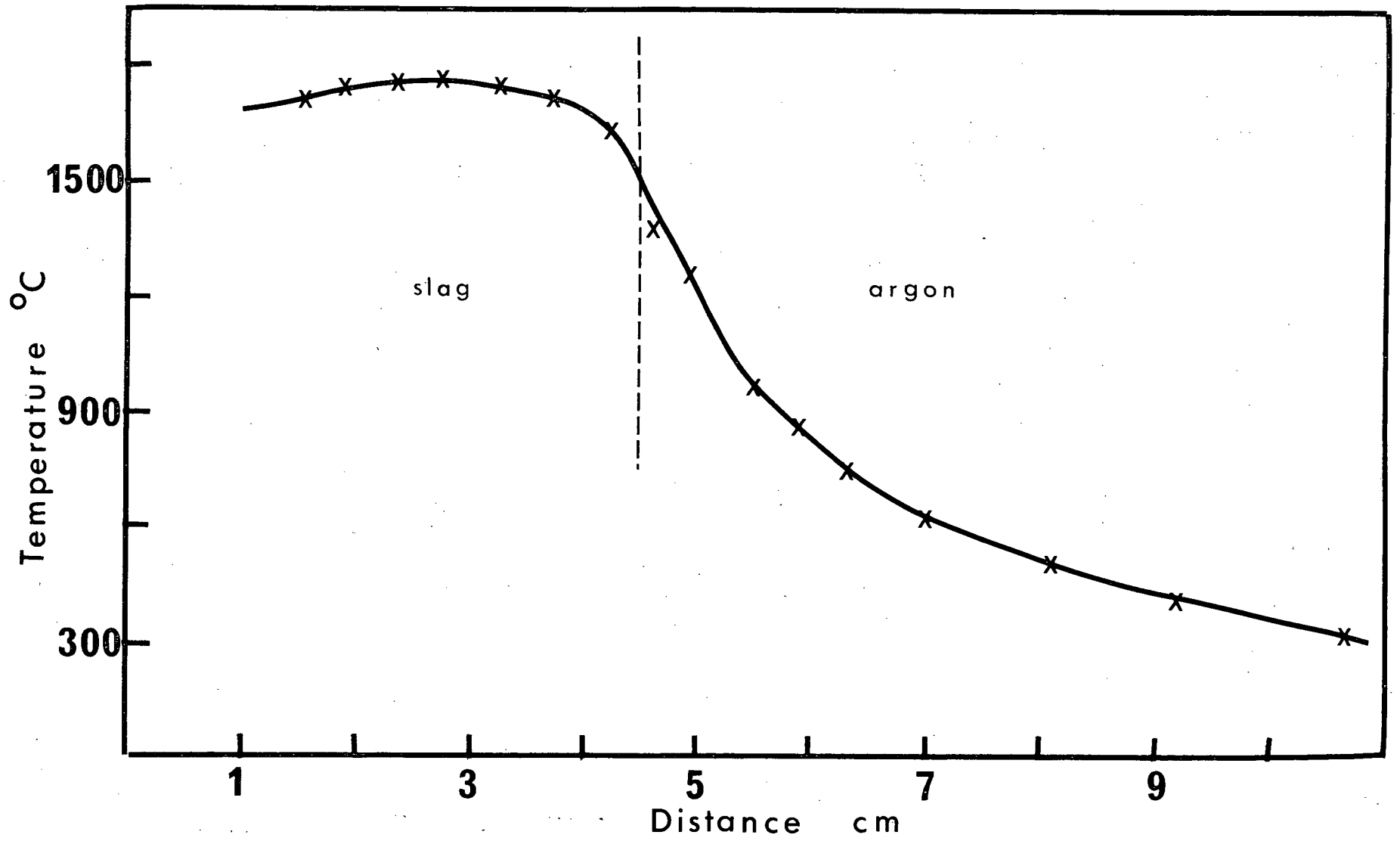

Figure 9. Temperature distribution in the slag bed for d.c. positive (argon).

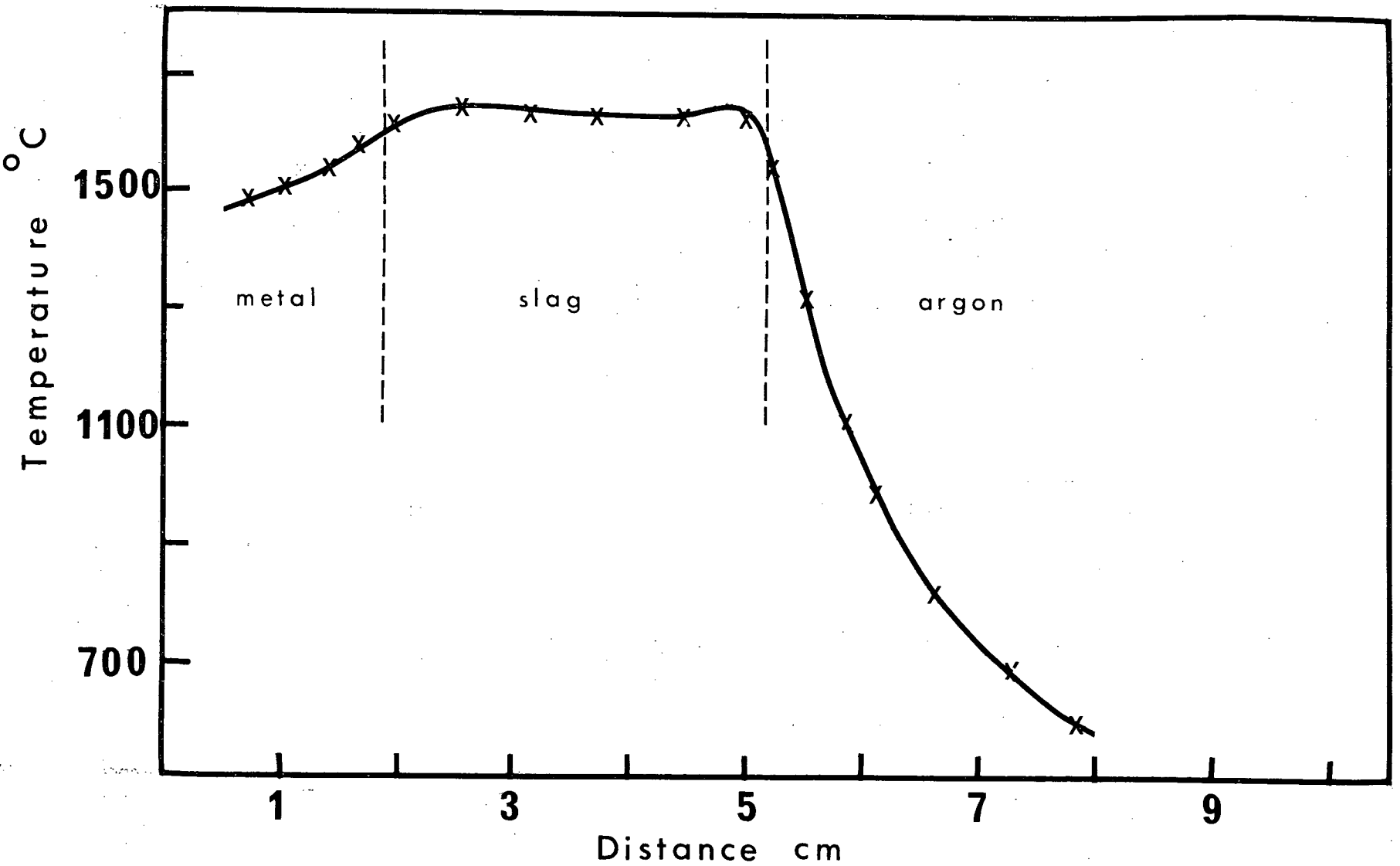

Figure 10. Temperature distribution in the slag bed for d.c. positive - 'live' mold (argon).

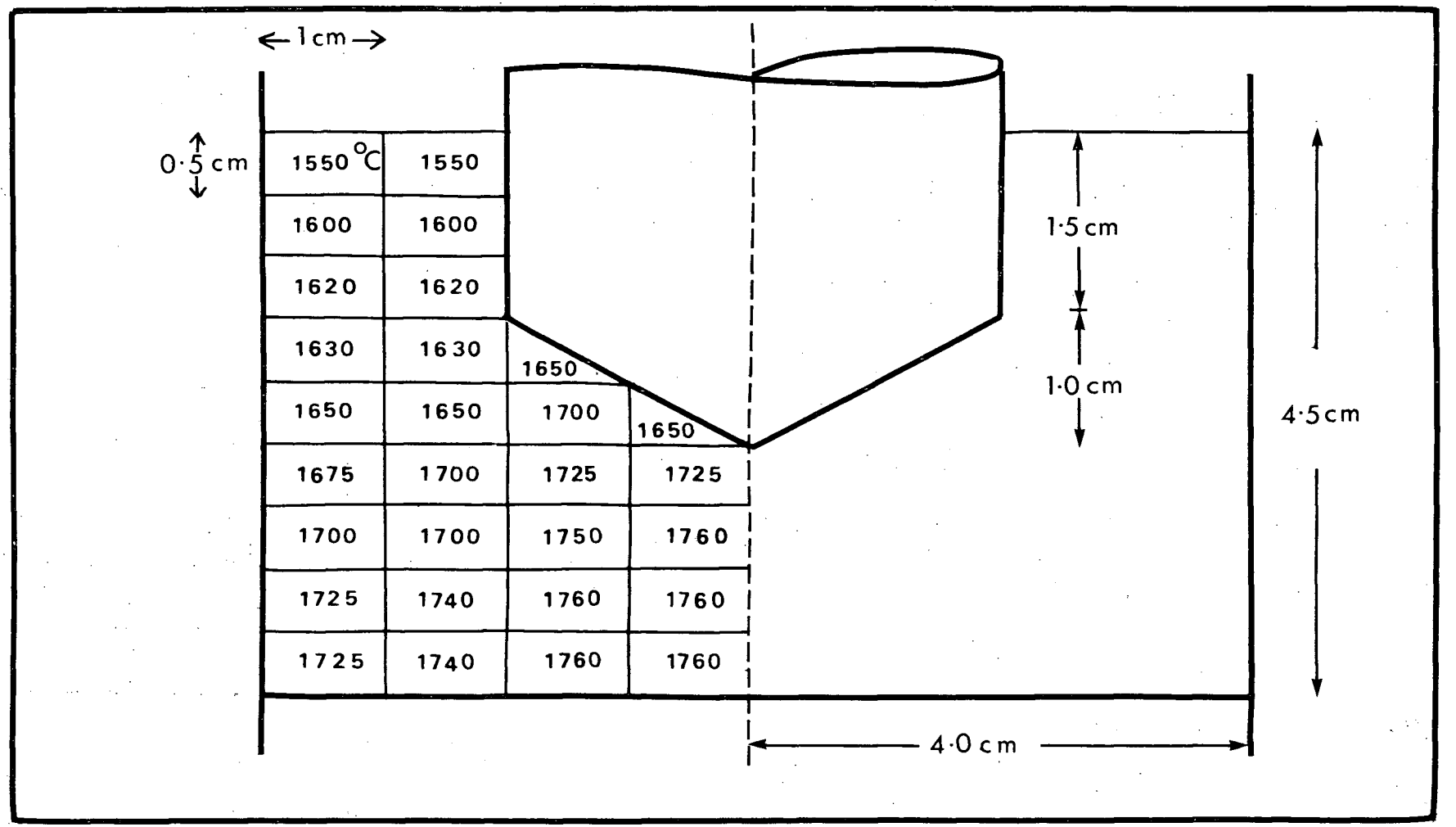

Figure 11. Assumed temperature distribution in the slag bed (ingot no. 1).

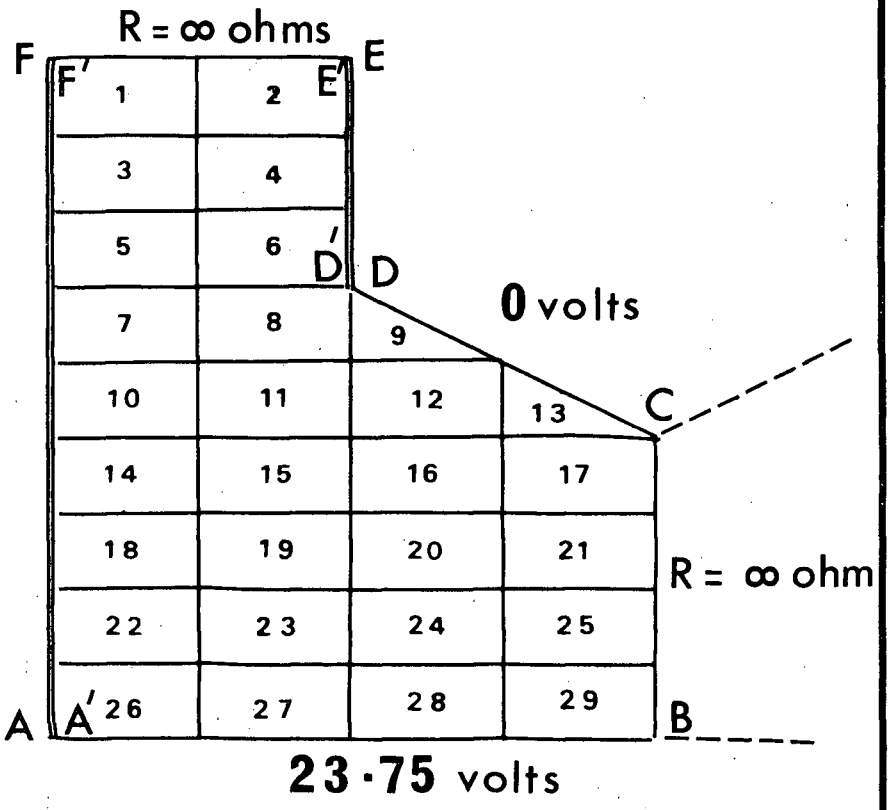

Figure 12. Subdivision of the slag bed.

Figure 13. Resistance of a volume element.

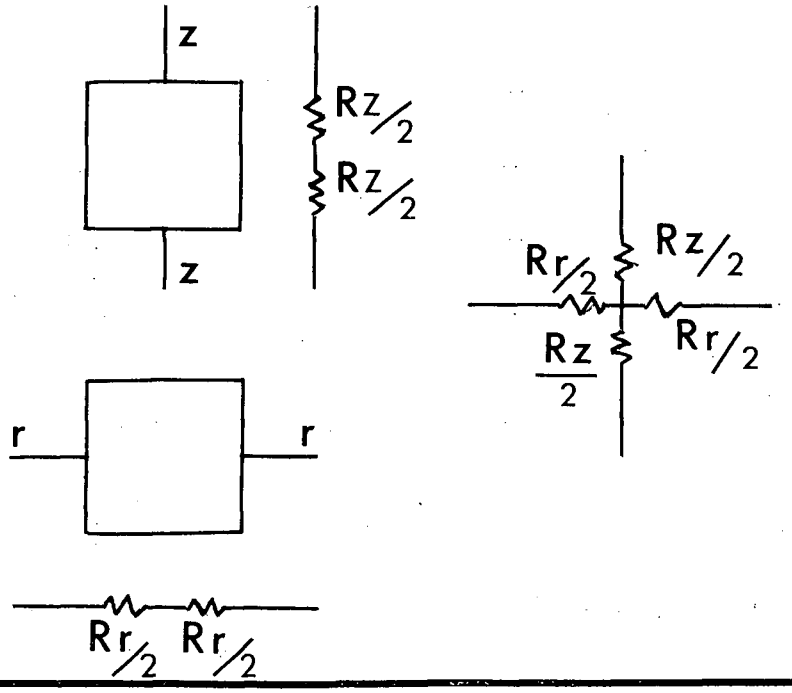

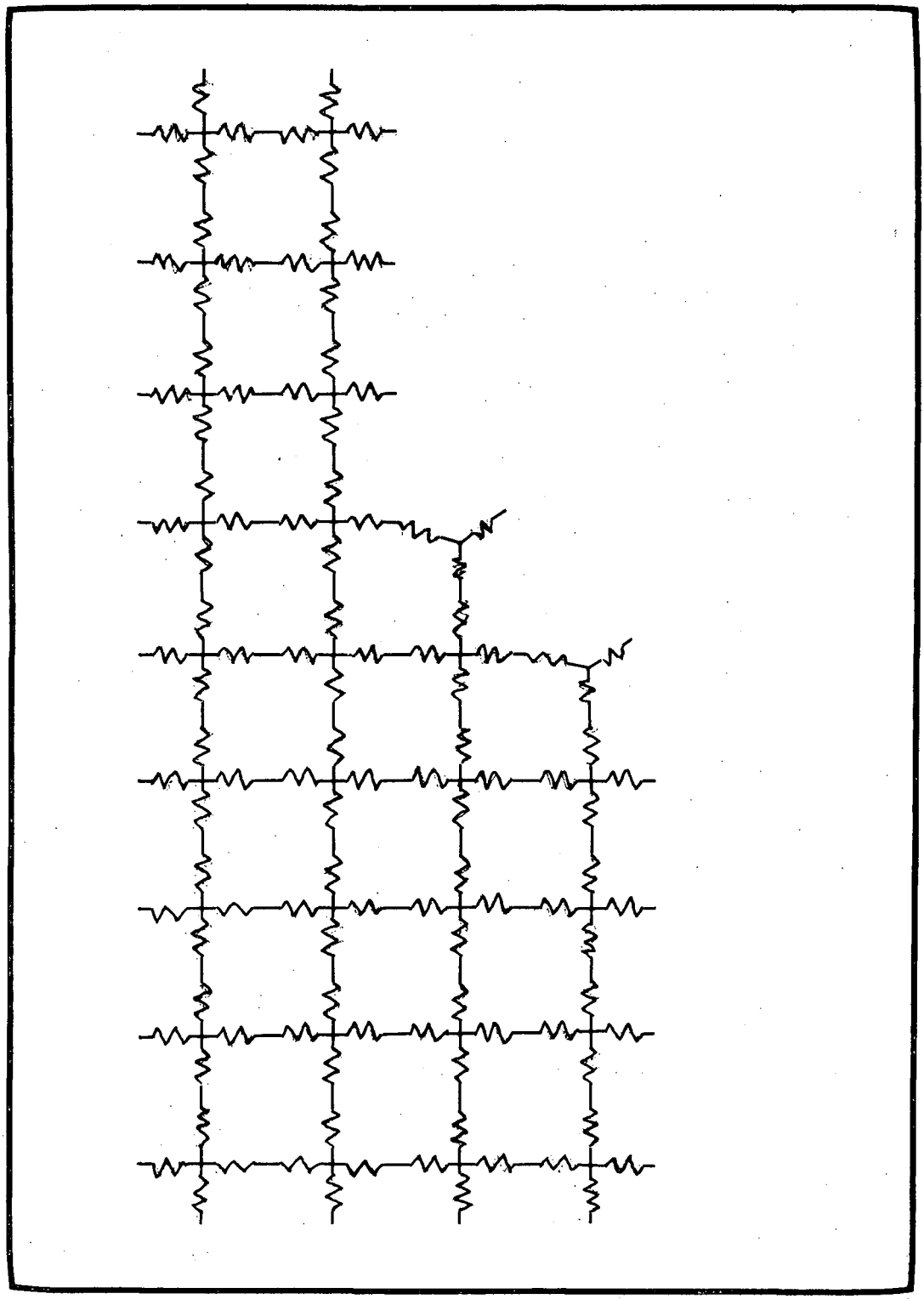

Figure 14. Resistance network.

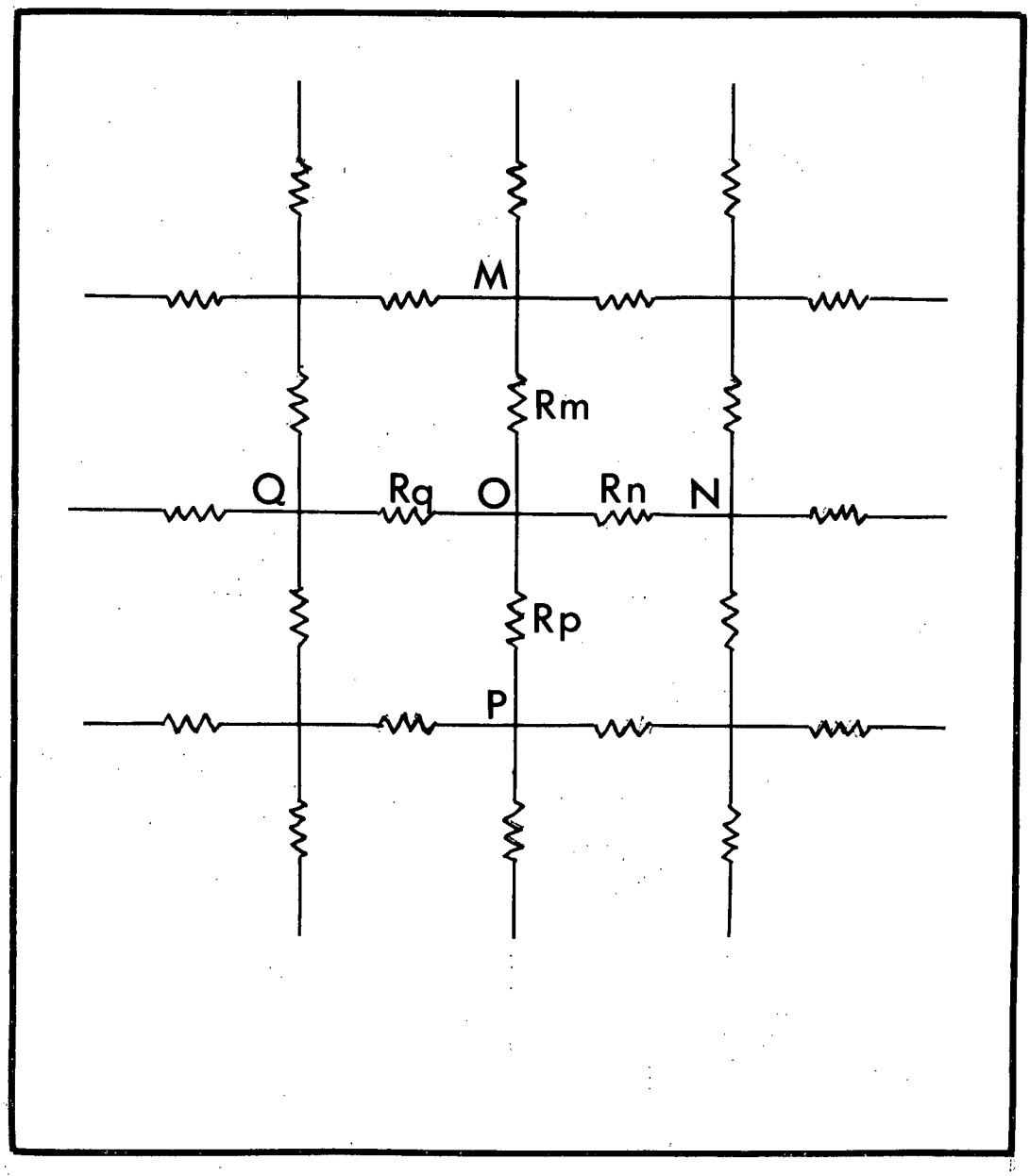

Figure 15. Network resistance for a single junction.

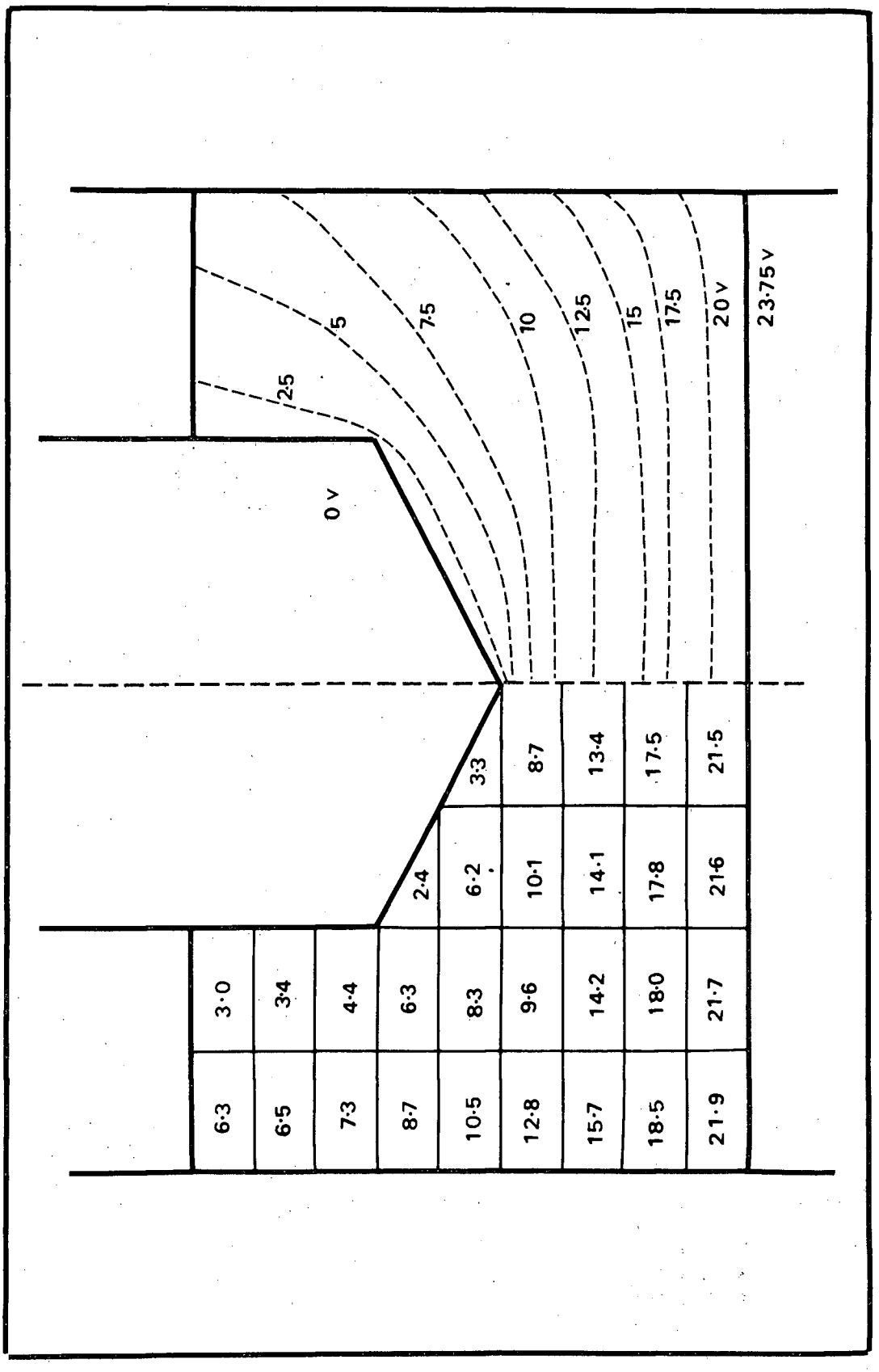

Figure 16. Isopotential contours in the ESR slag bed.

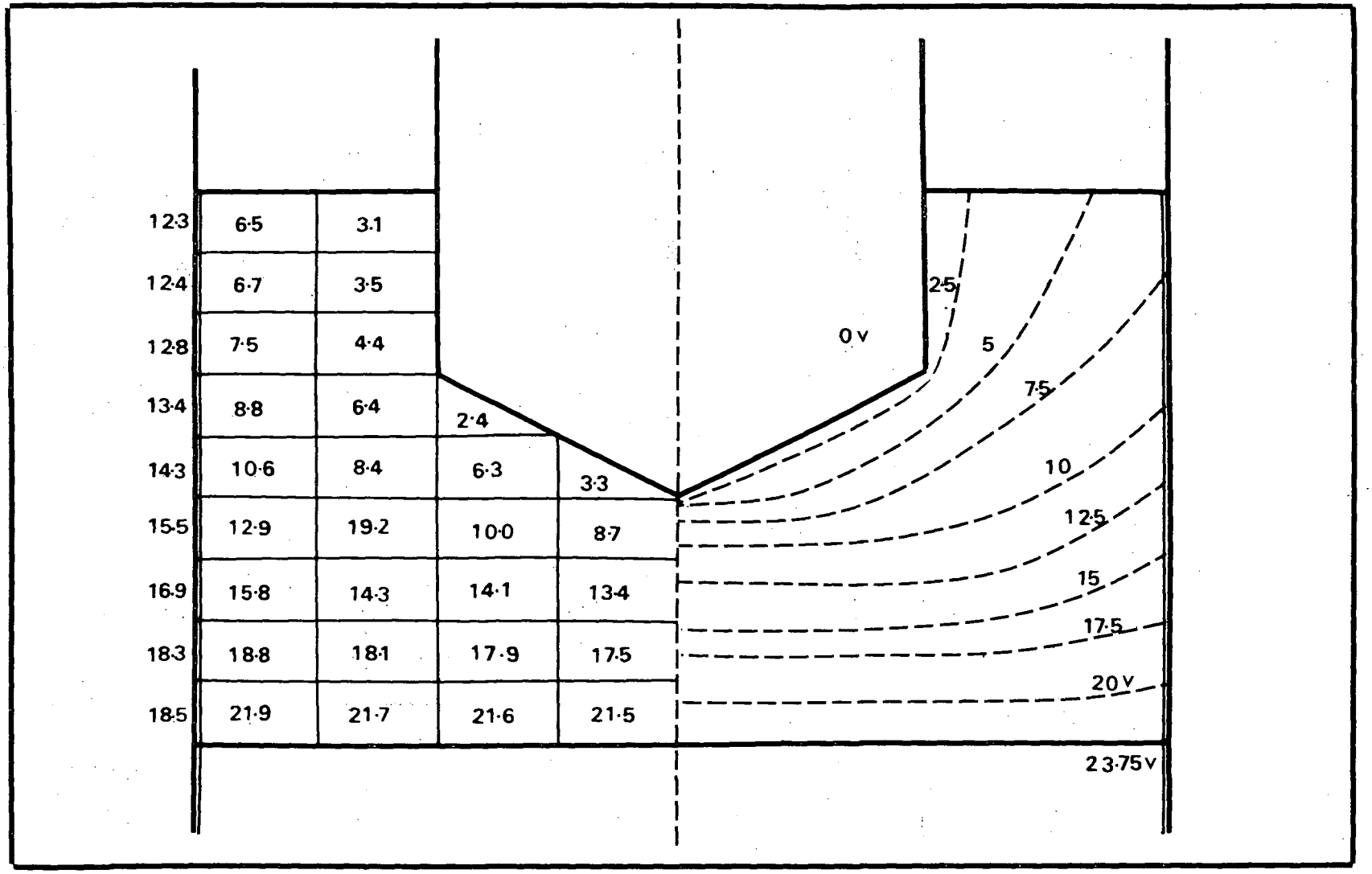

Figure 17. Effect of finite mold wall-slag skin resistance on the isopotential contours (slag skin resistivity = 250 ohm cm).

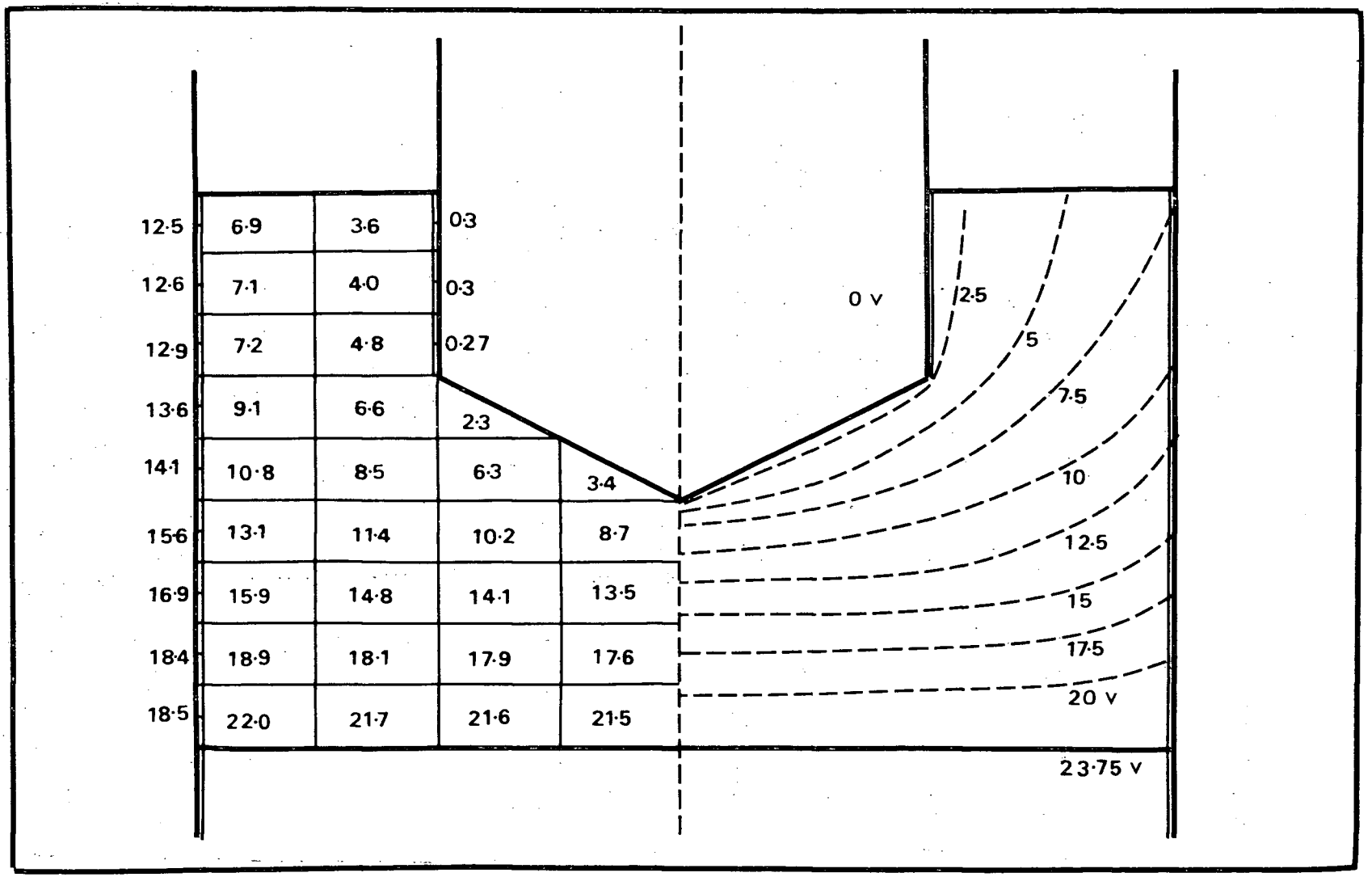

Figure 18. Effect of finite electrode-slag skin resistance on the isopotential contours (slag skin resistivity = 0.2 ohm cm).

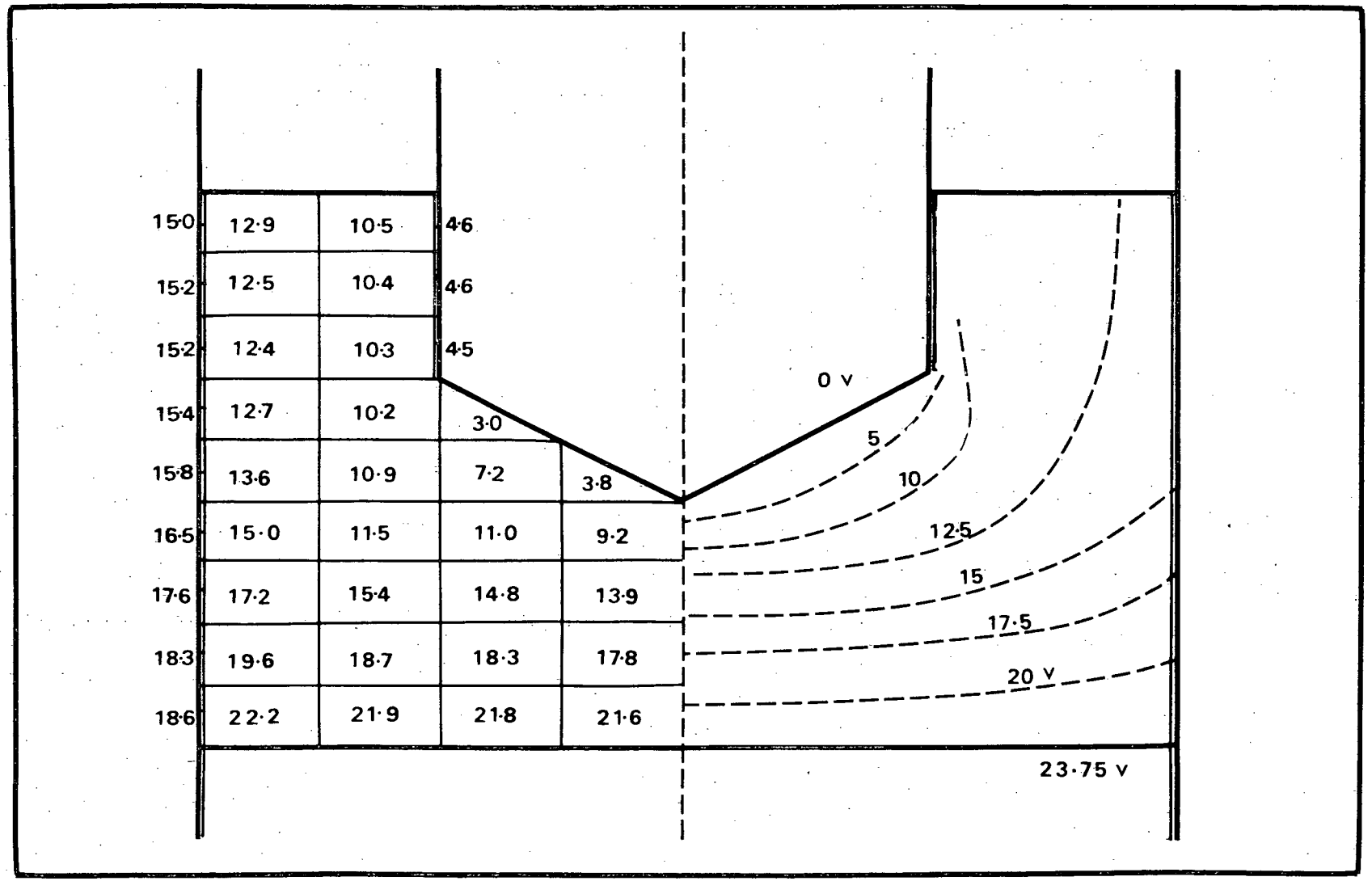

Figure 19. Effect of finite electrode-slag skin resistance on the isopotential contours (slag skin resistivity = 20 ohm cm).

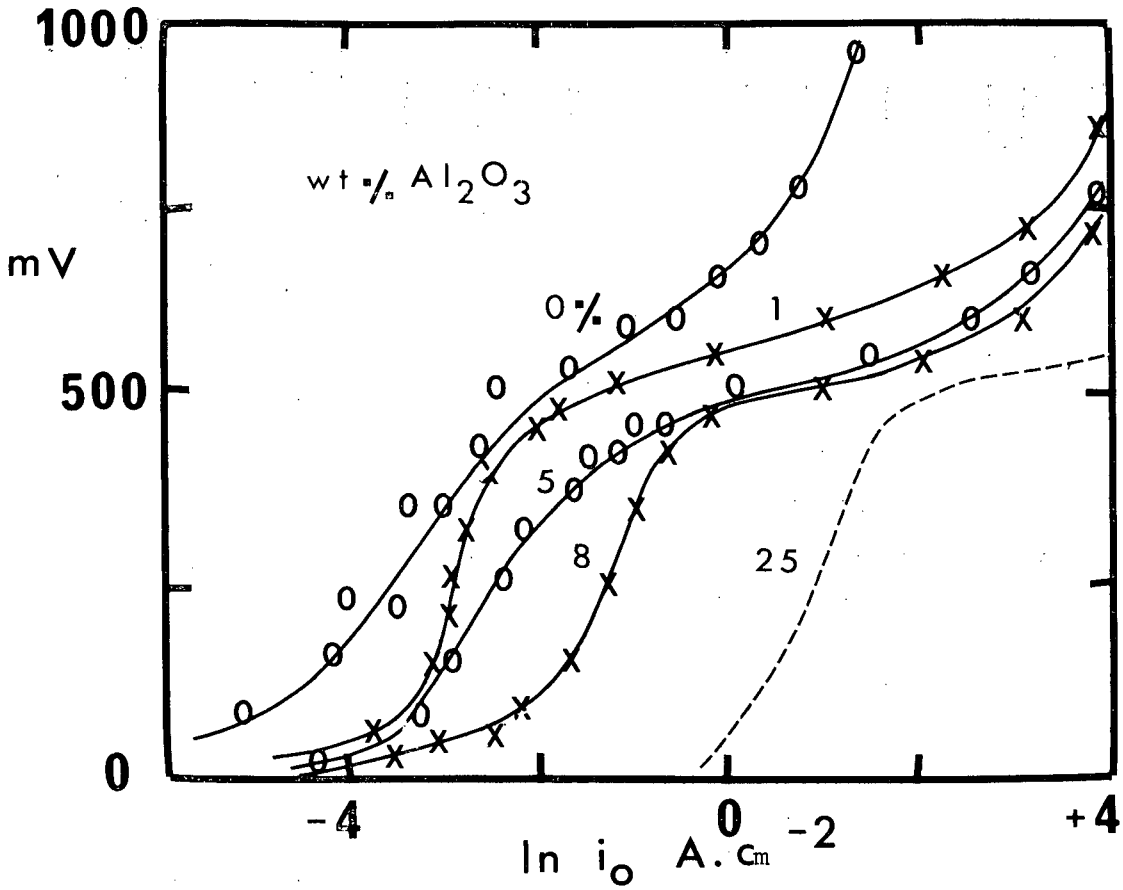

(a) Anodic polarization curves for CaF_2-Al_2O_3 slags determined by galvanostatic experiments.[12]

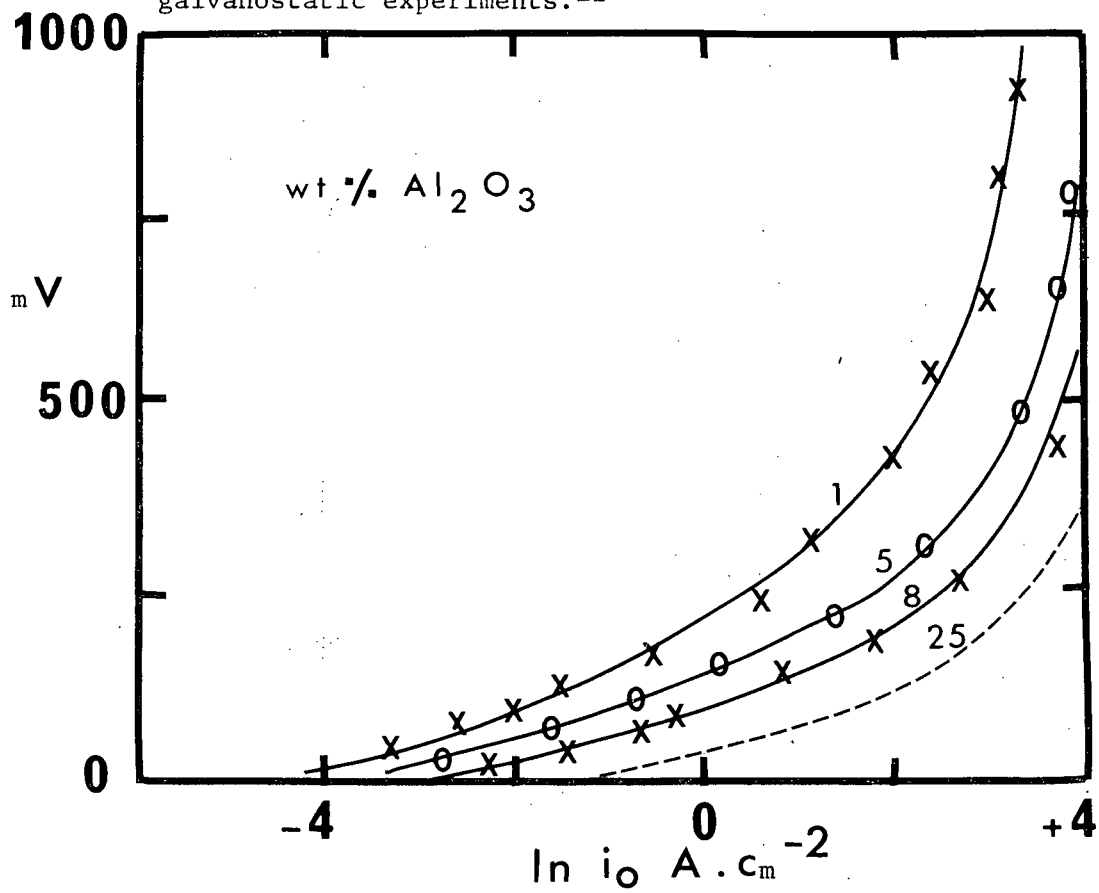

(b) Cathodic polarization curves for CaF_2-Al_2O_3 slags determined by galvanostatic experiments.[12]

Figure 20.

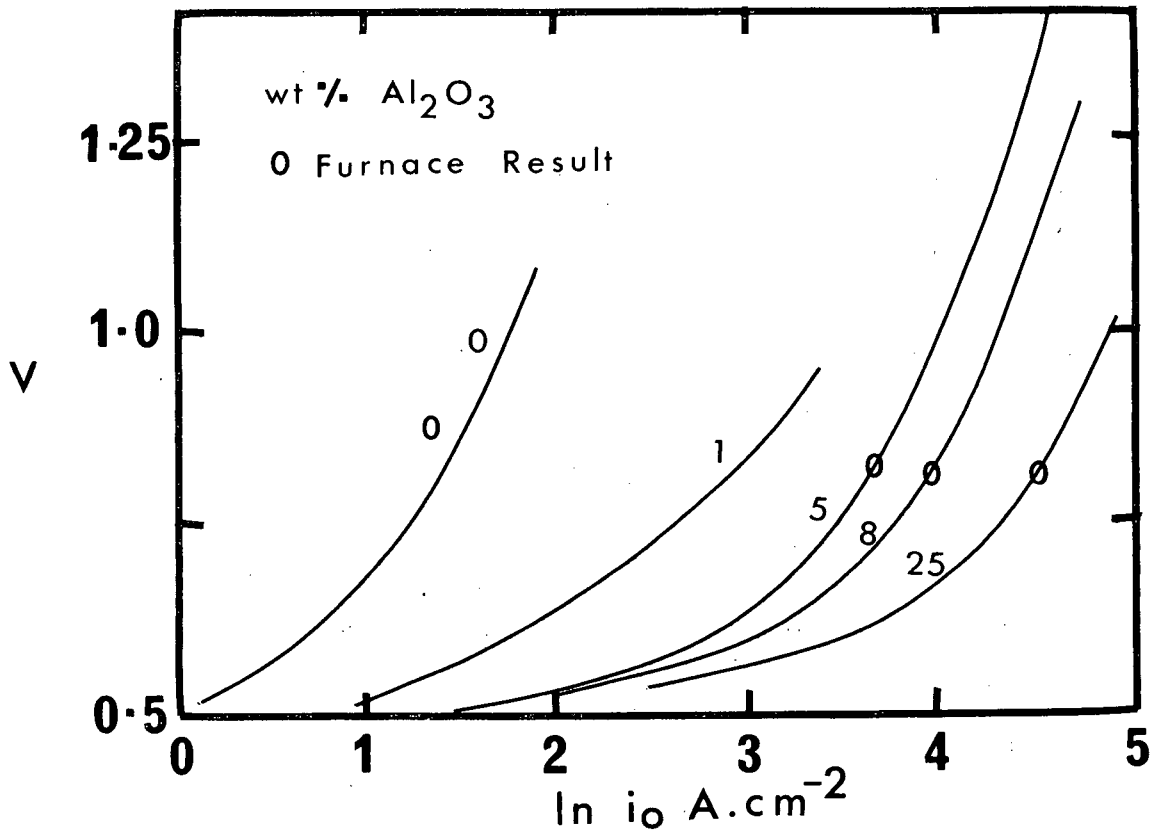

(a) Anodic polarization cruves on ESR electrodes in CaF_2-Al_2O_3 slags.[12]

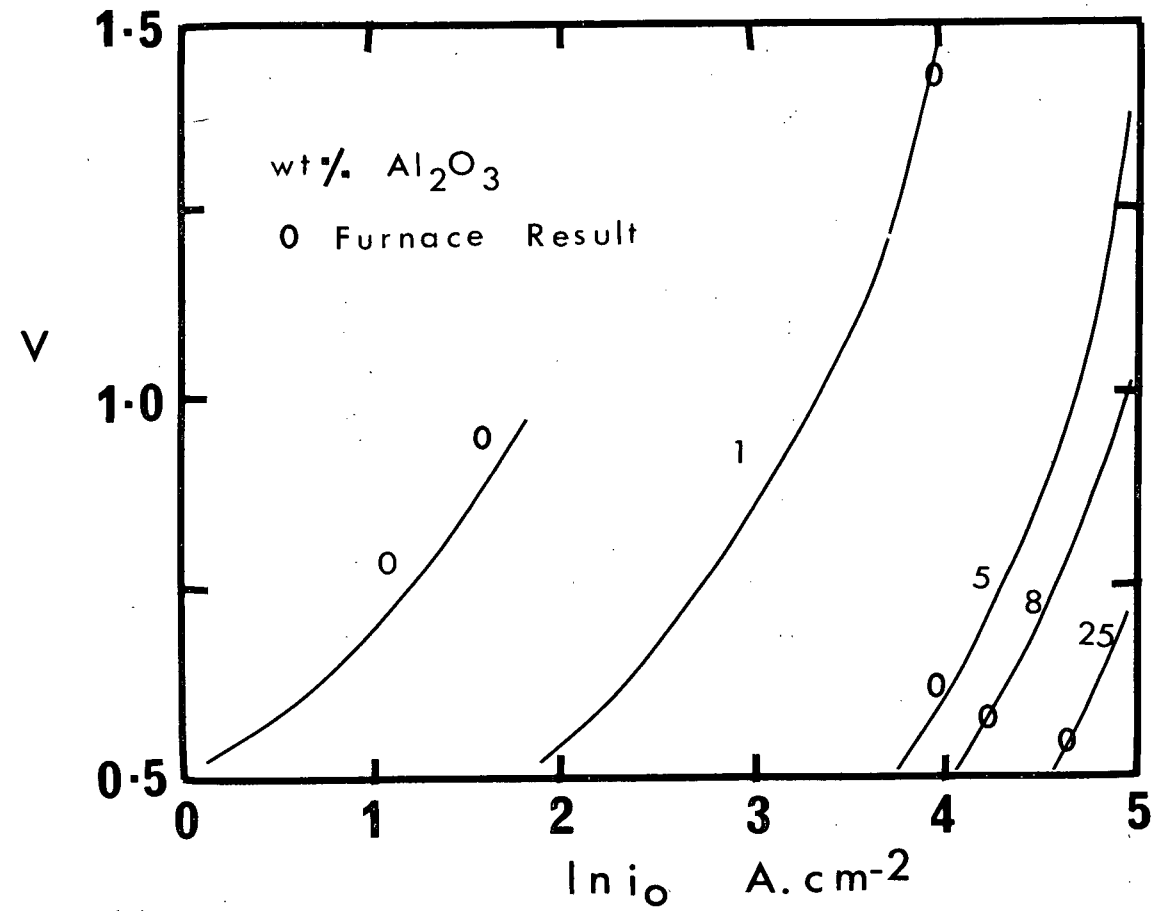

(b) Cathodic polarization curves on ESR electrodes in CaF_2-Al_2O_3 slags.[12]

Figure 21.

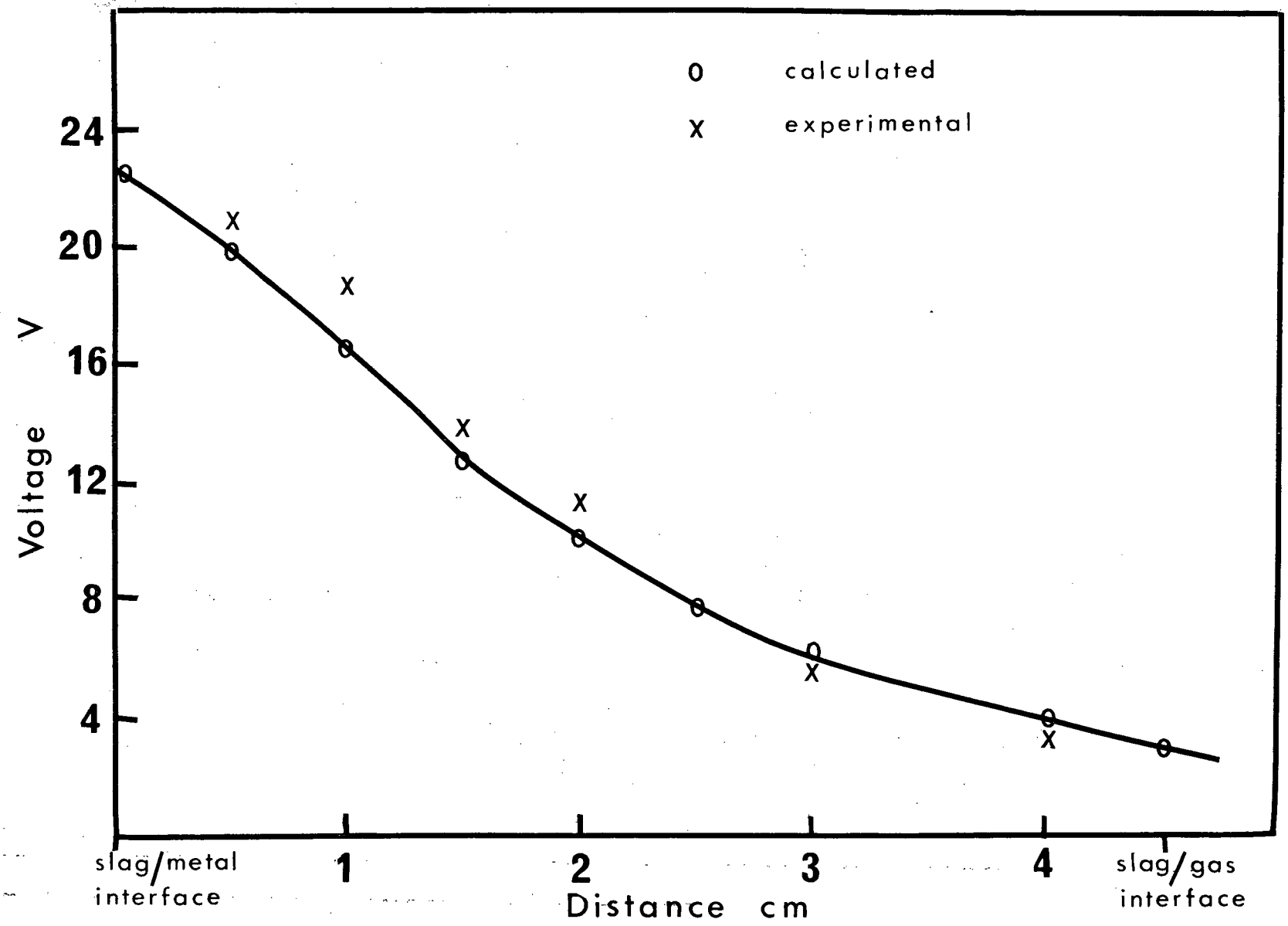

Figure 22. Experimentally obtained voltage gradient in the slag bath.

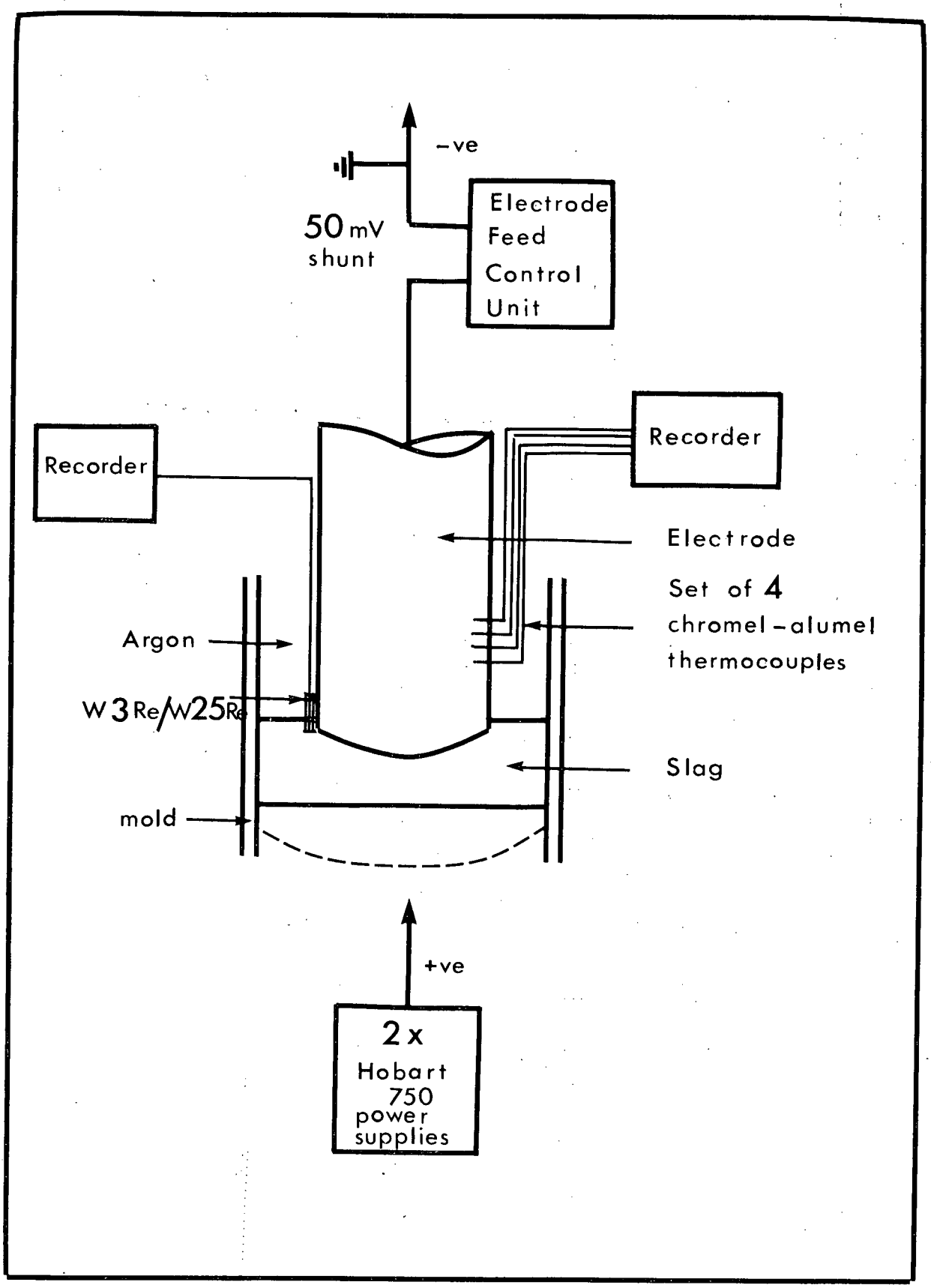

Figure 23. Schematic outline of the experimental set up for electrode temperature measurement.

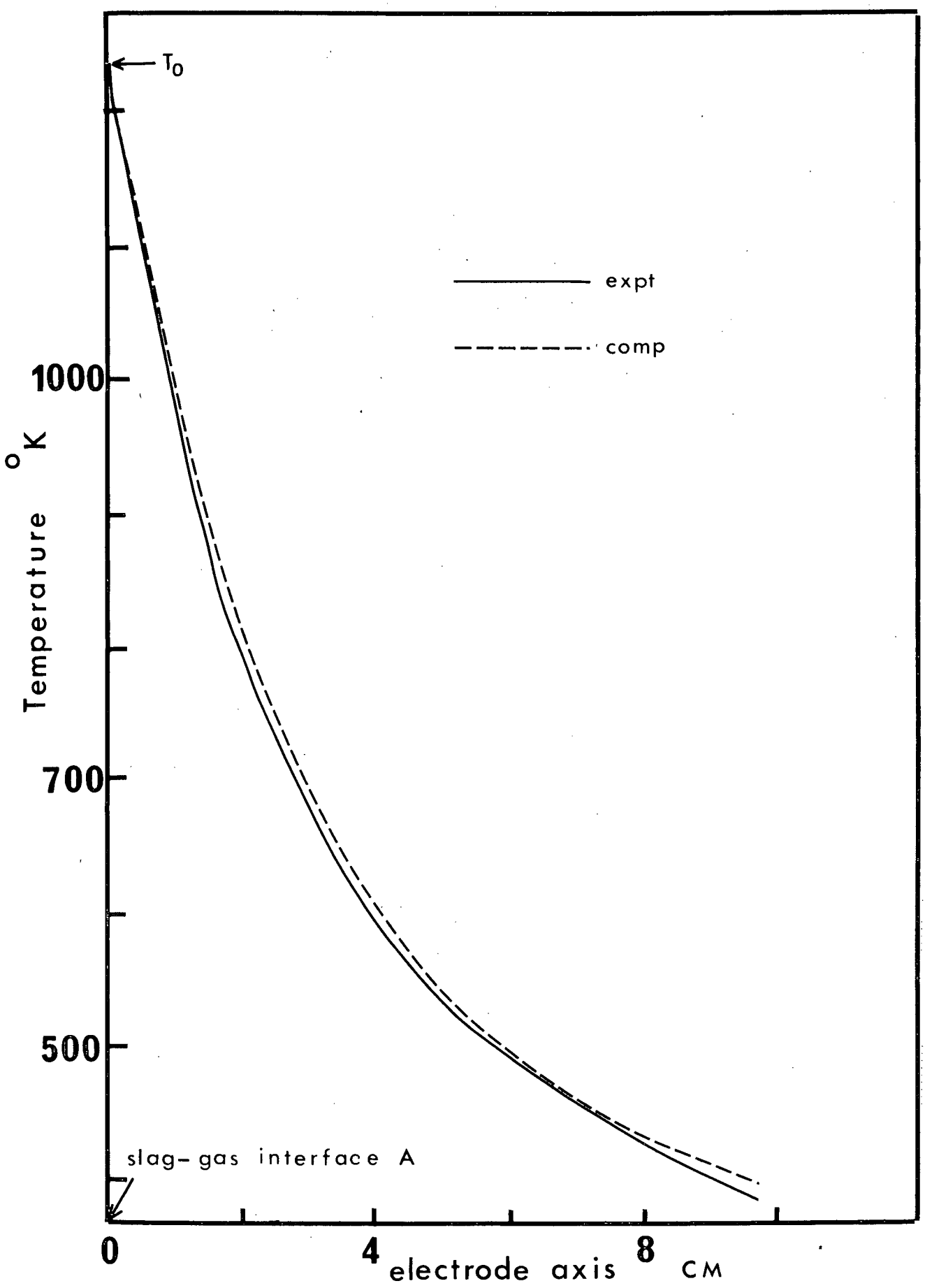

Figure 24. Electrode temperature gradient for 2.54 cm diameter electrode of AISI 1018 steel in electrode negative polarity.

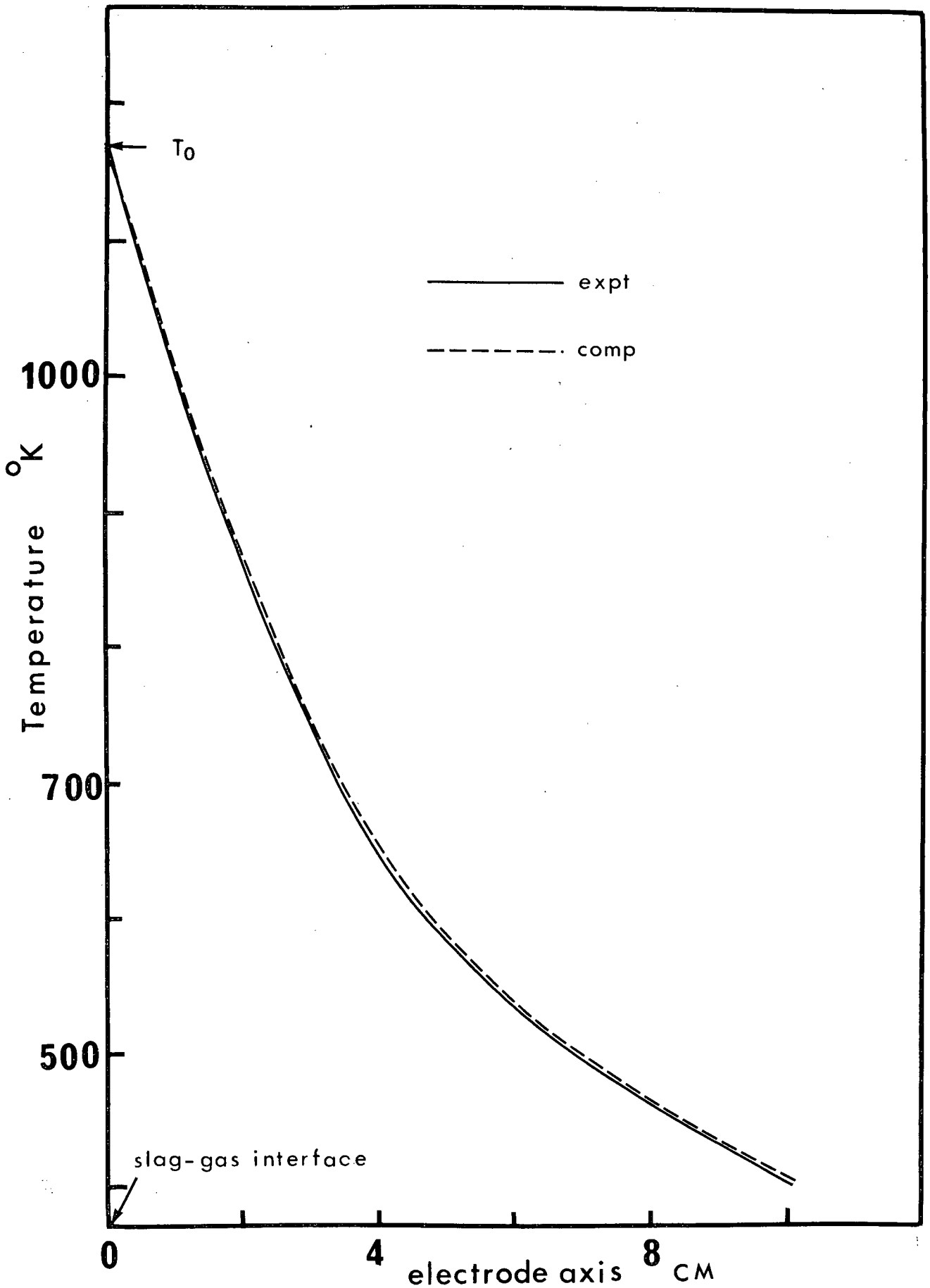

Figure 25. Electrode temperature gradient for 3.81 cm diameter electrode of AISI 1018 steel in electrode negative polarity.

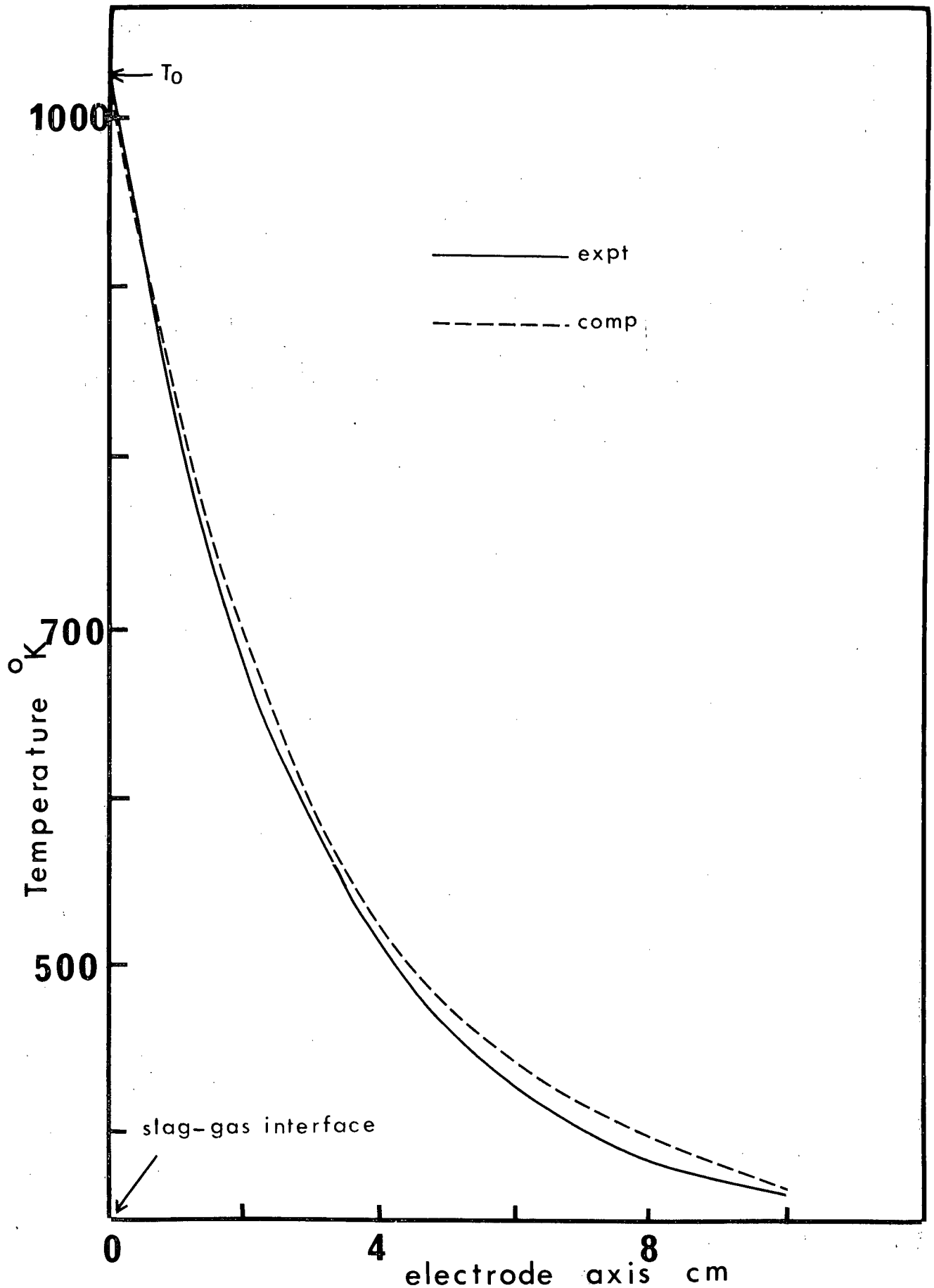

Figure 26. Electrode temperature gradient for 2.54 cm diameter electrode of AISI 321 steel in electrode negative polarity.

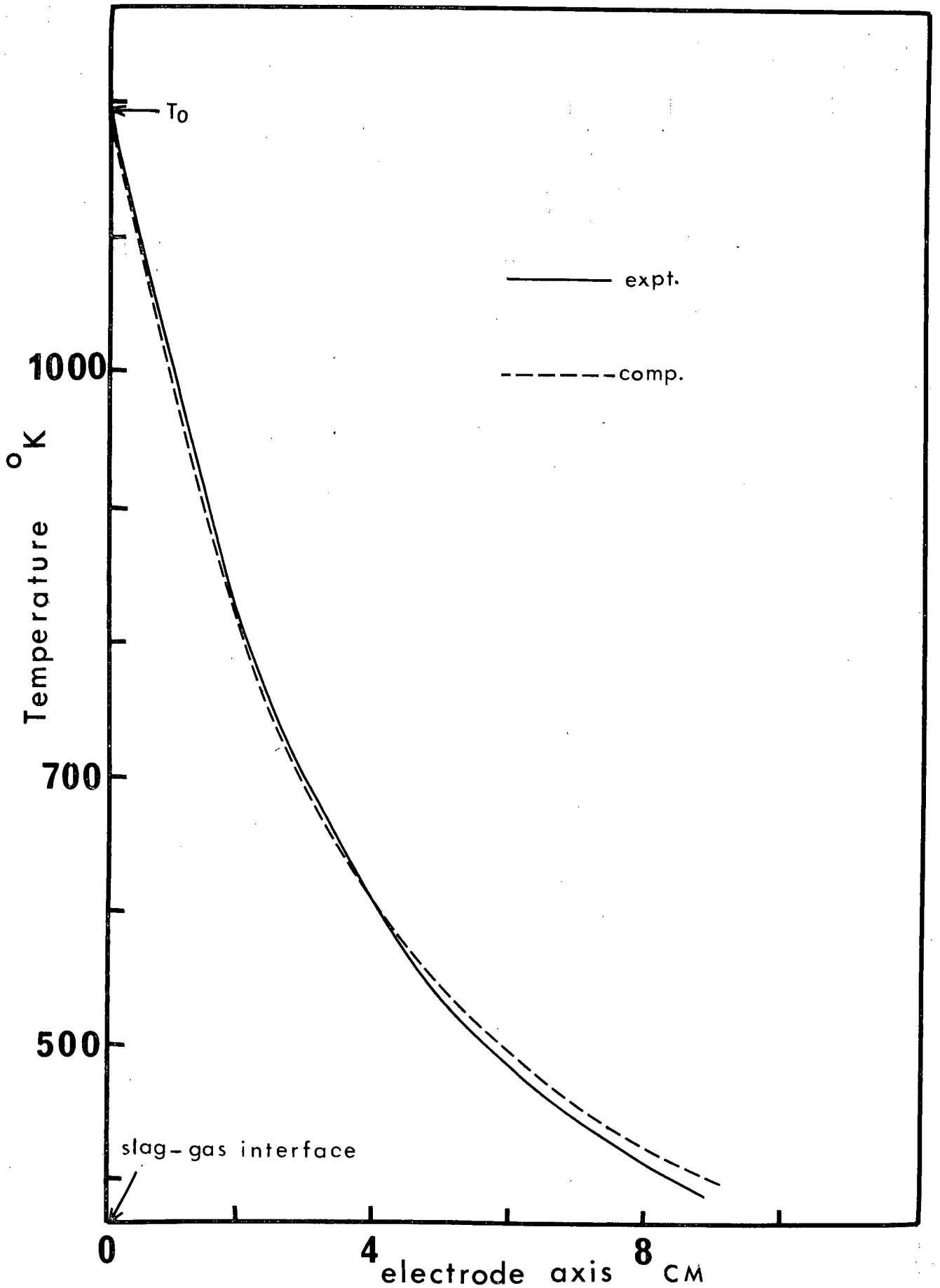

Figure 27. Electrode temperature gradient for 2.54 cm diameter electrode of AISI 1018 steel in electrode positive polarity.

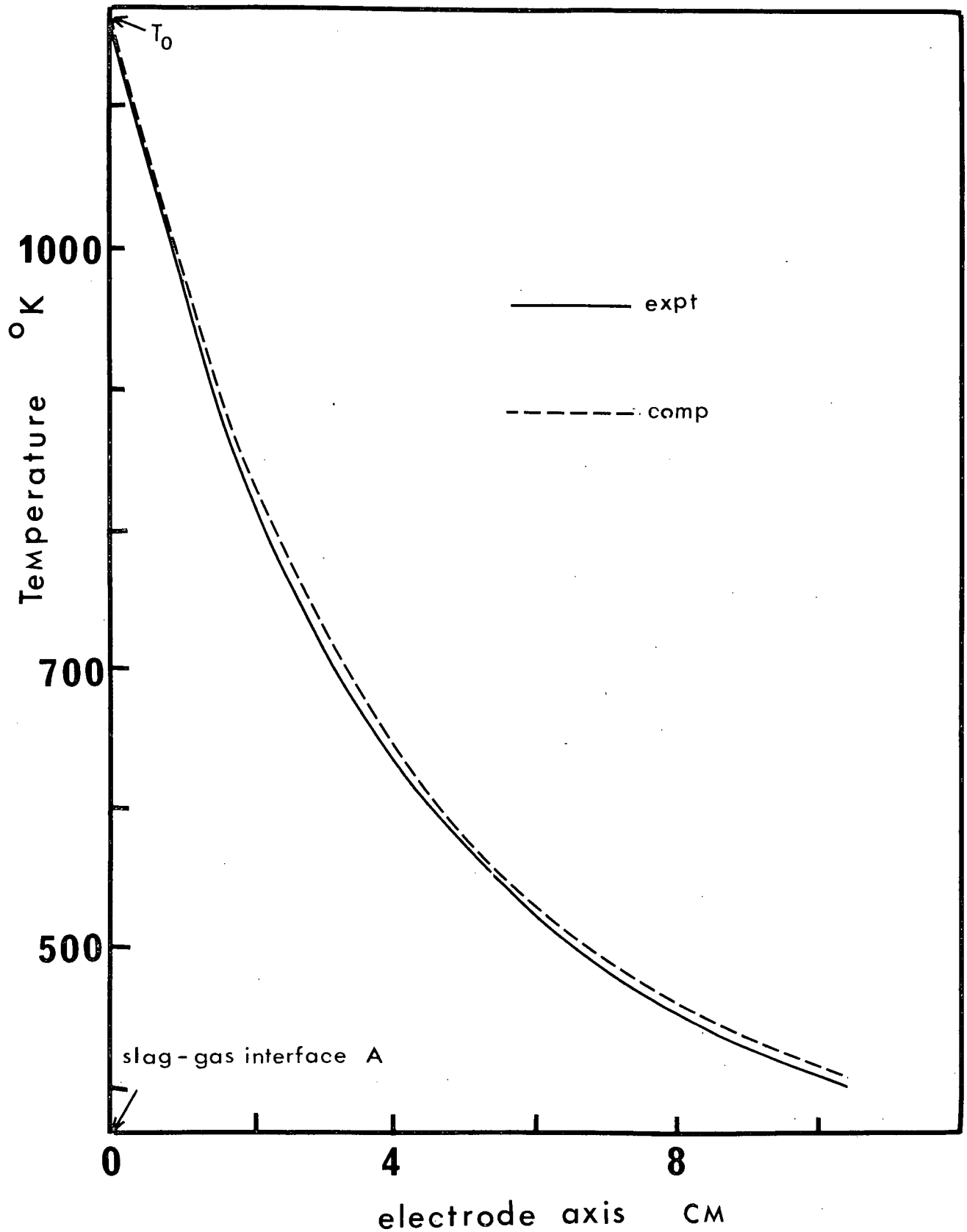

Figure 28. Electrode temperature gradient for 3.81 cm diameter electrode of AISI 1018 steel in electrode positive polarity.

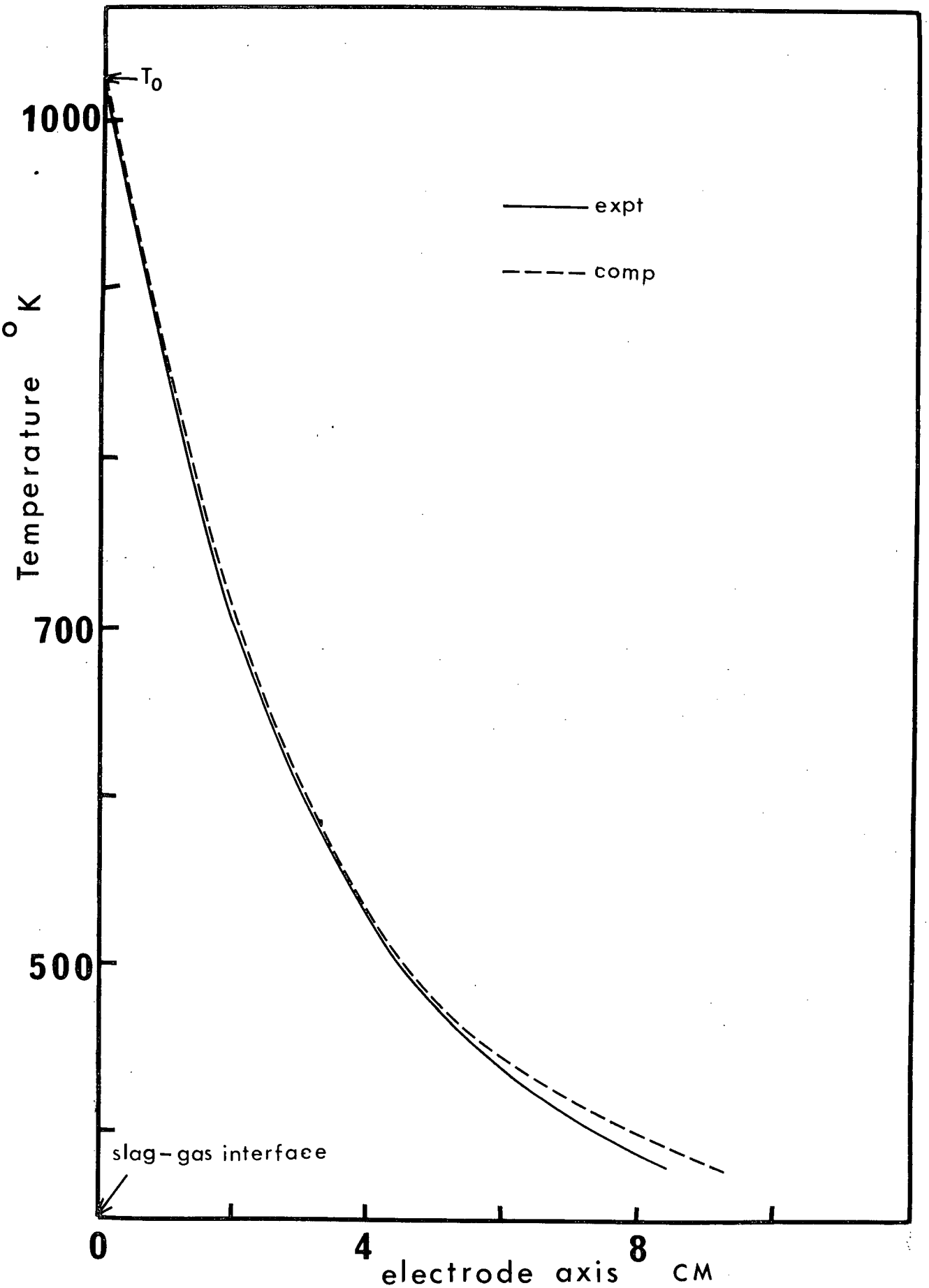

Figure 29. Electrode temperature gradient for 2.54 cm diameter electrode of AISI 321 steel in electrode positive polarity.

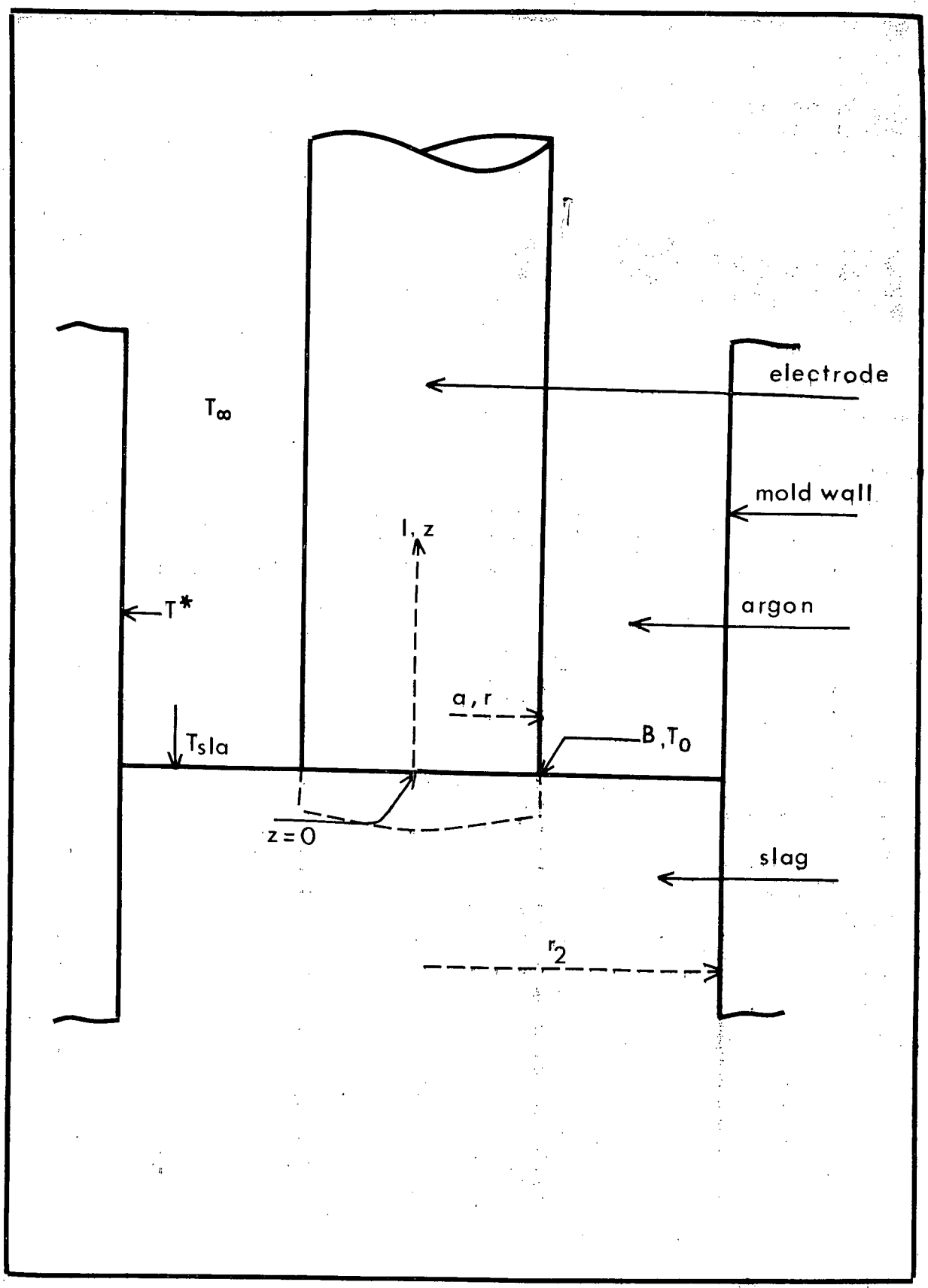

Figure 30. Outline diagram to illustrate the parameters used in the computation of the electrode temperature gradient.

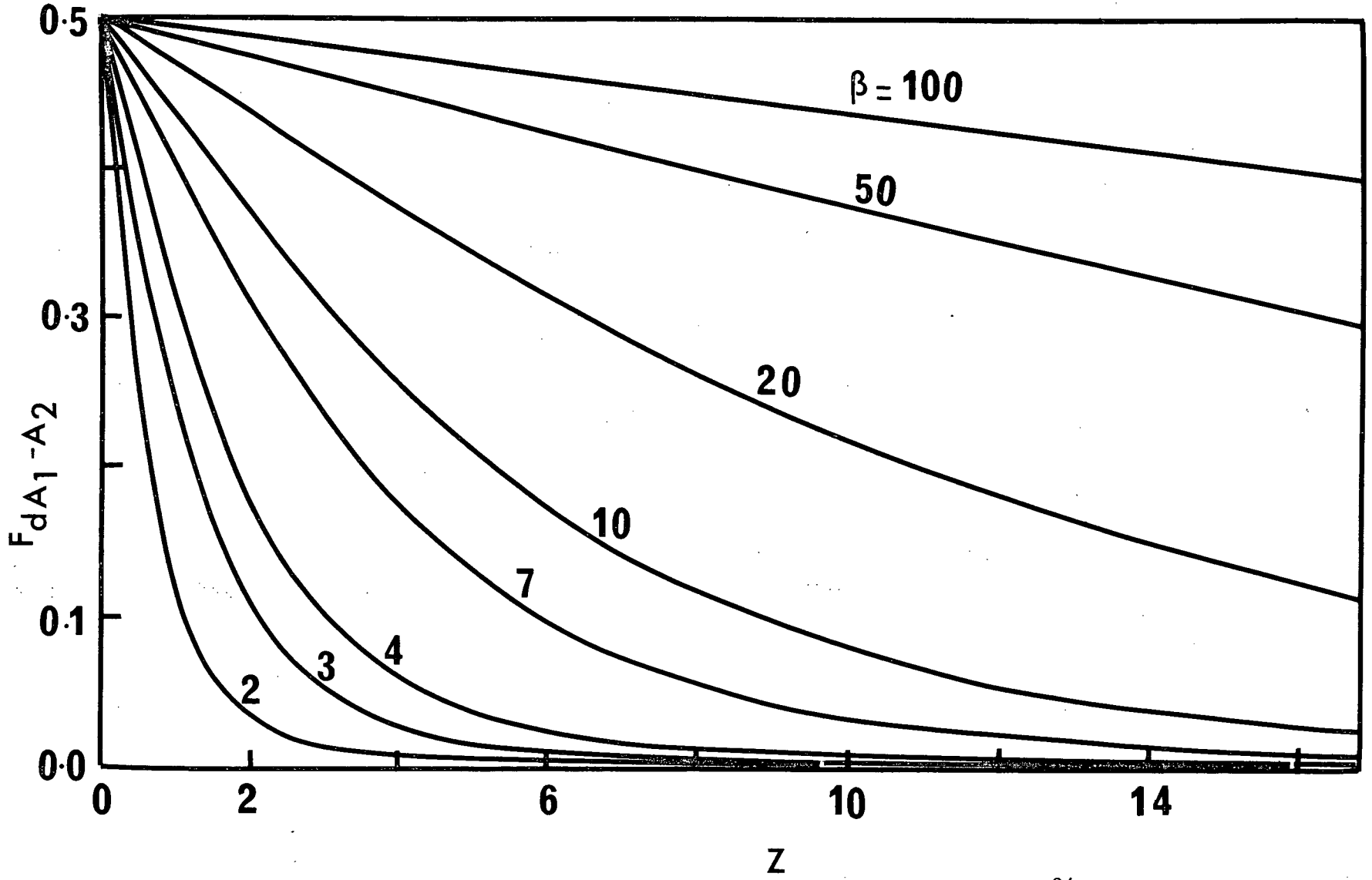

Figure 31. Variation of configuration factor with axial length and β.[24]

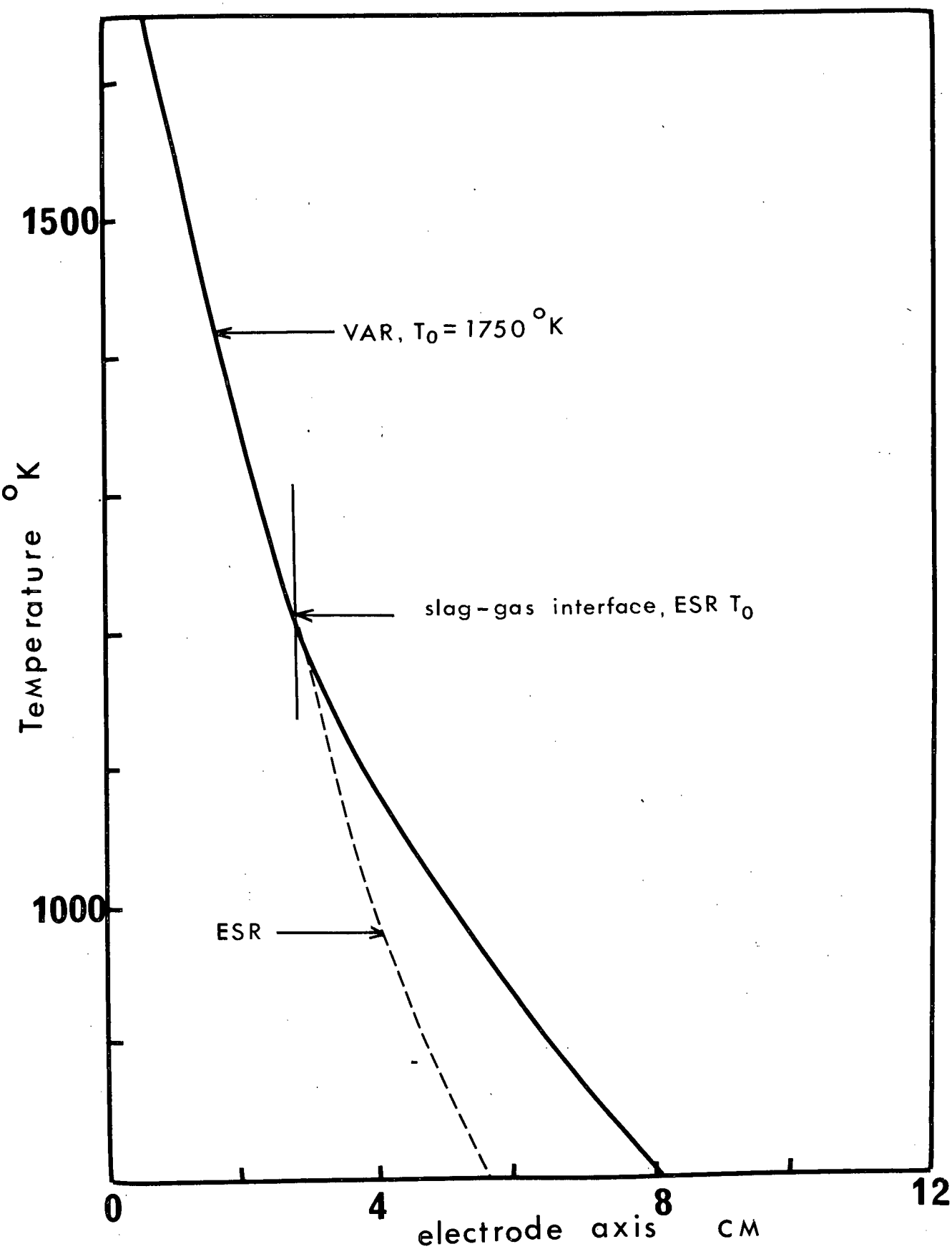

Figure 32. Electrode temperature gradients for 3.81 cm diameter electrode of AISI 1018 steel in electrode negative polarity in VAR and ESR processes.

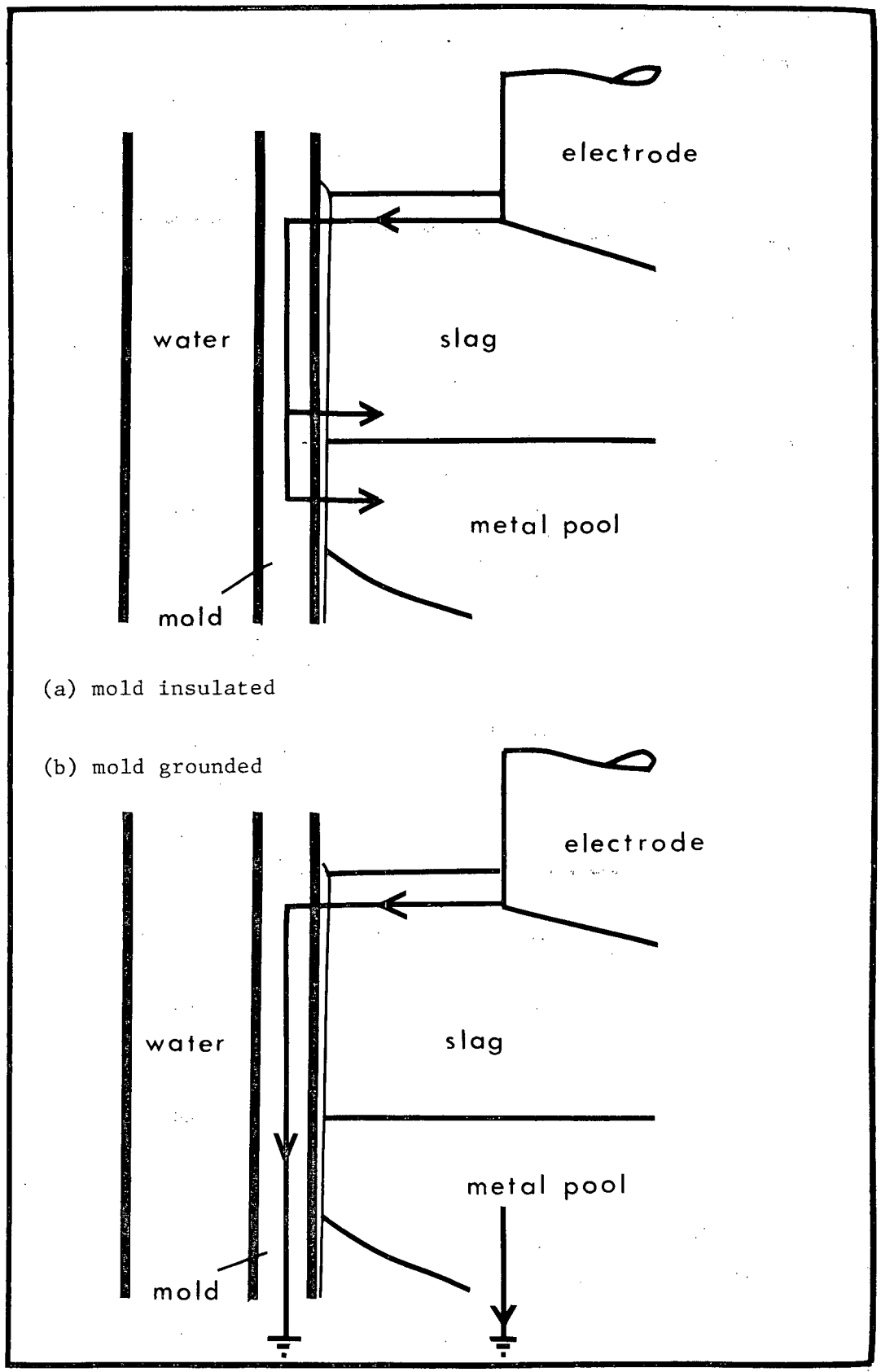

Figure 33. Current paths in an ESR mold

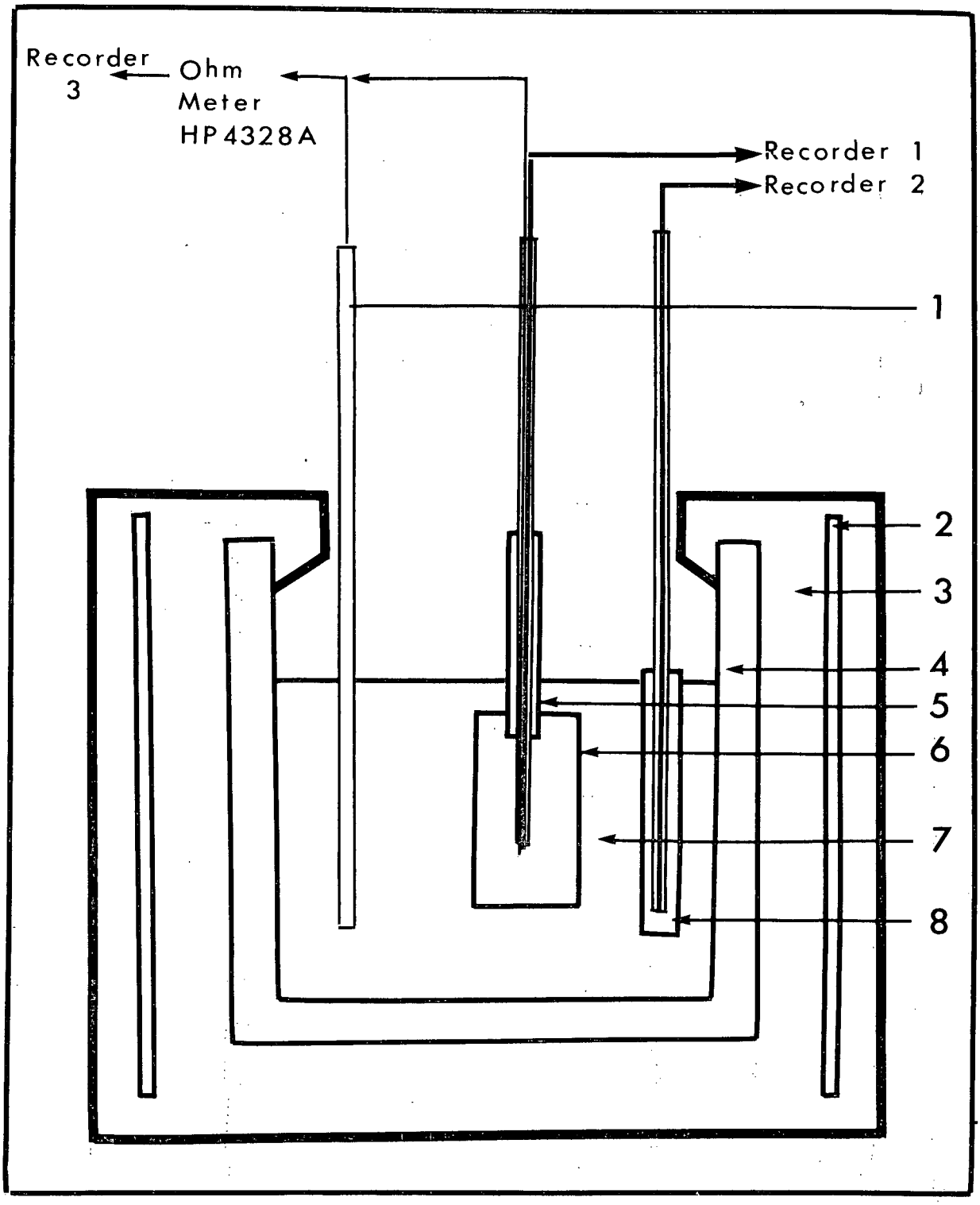

Figure 34. Experimental apparatus for measuring the electrical and thermal resistance of the slag skin. (1) 0.5 cm diameter graphite rod, (2) 450 kHz induction coil, (3) thermal insulation, (4) graphite crucible, (5) boron nitride insulating sleeve, (6) 3.0 cm diameter x 3 cm high copper cylinder, (7) approximately 1 ltr. of liquid slag, (8) boron nitride insulator for slag temperature thermocouple.

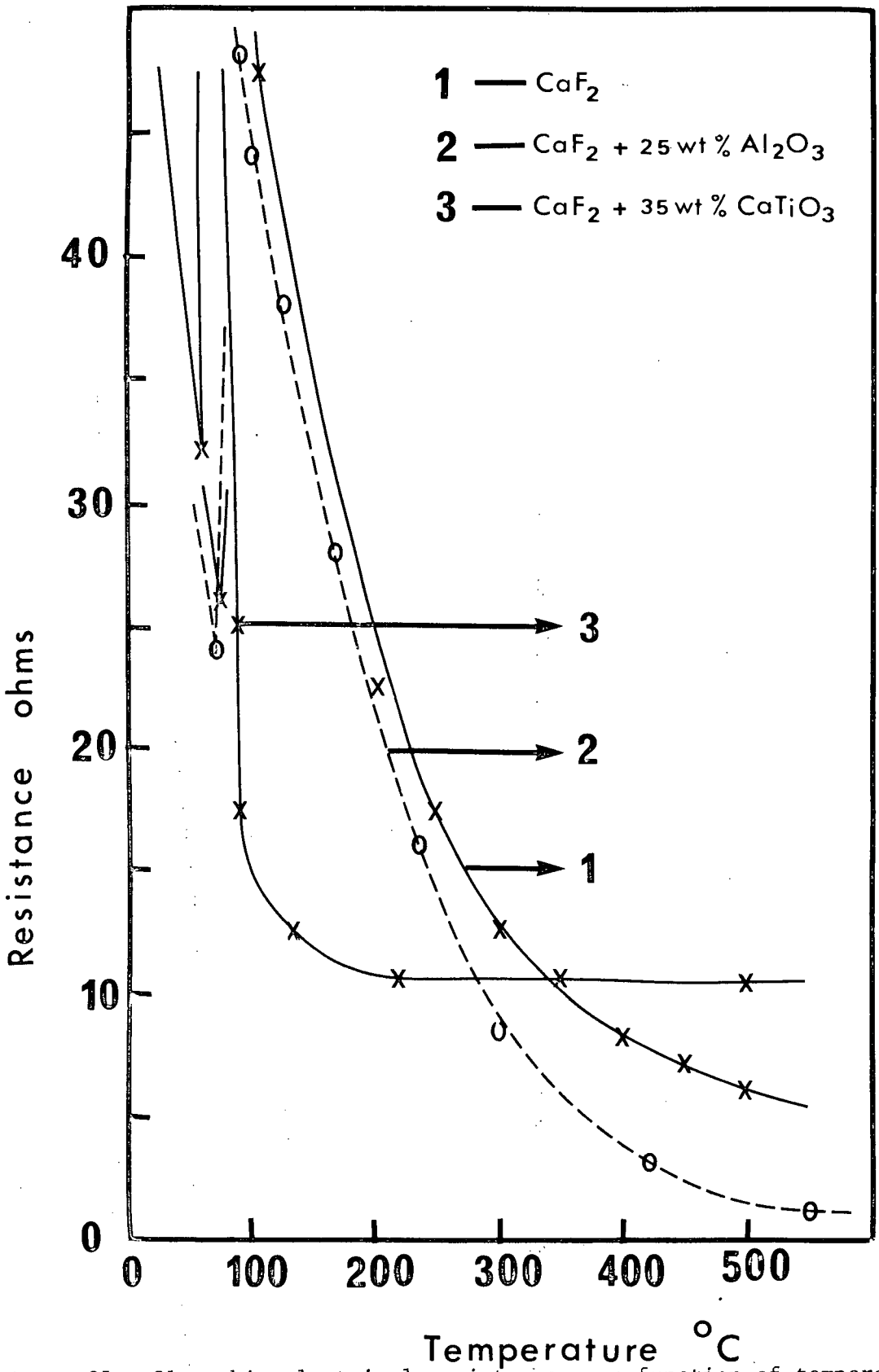

Figure 35. Slag skin electrical resistance as a function of temperature (slag temperature constant at 1600°C).

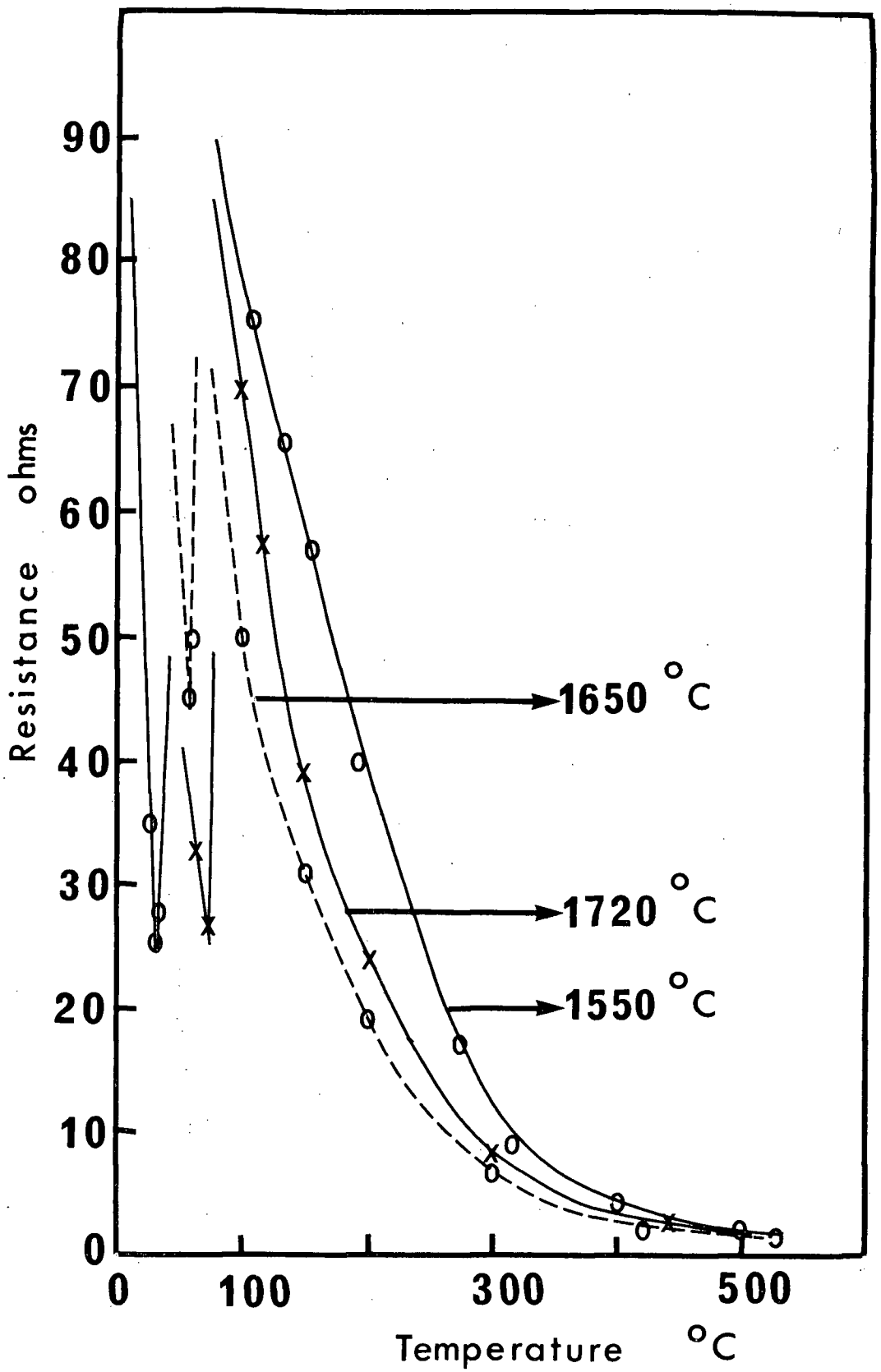

Figure 36. Slag skin electrical resistance as a function of temperature for CaF_2 slag at different slag bath temperatures.

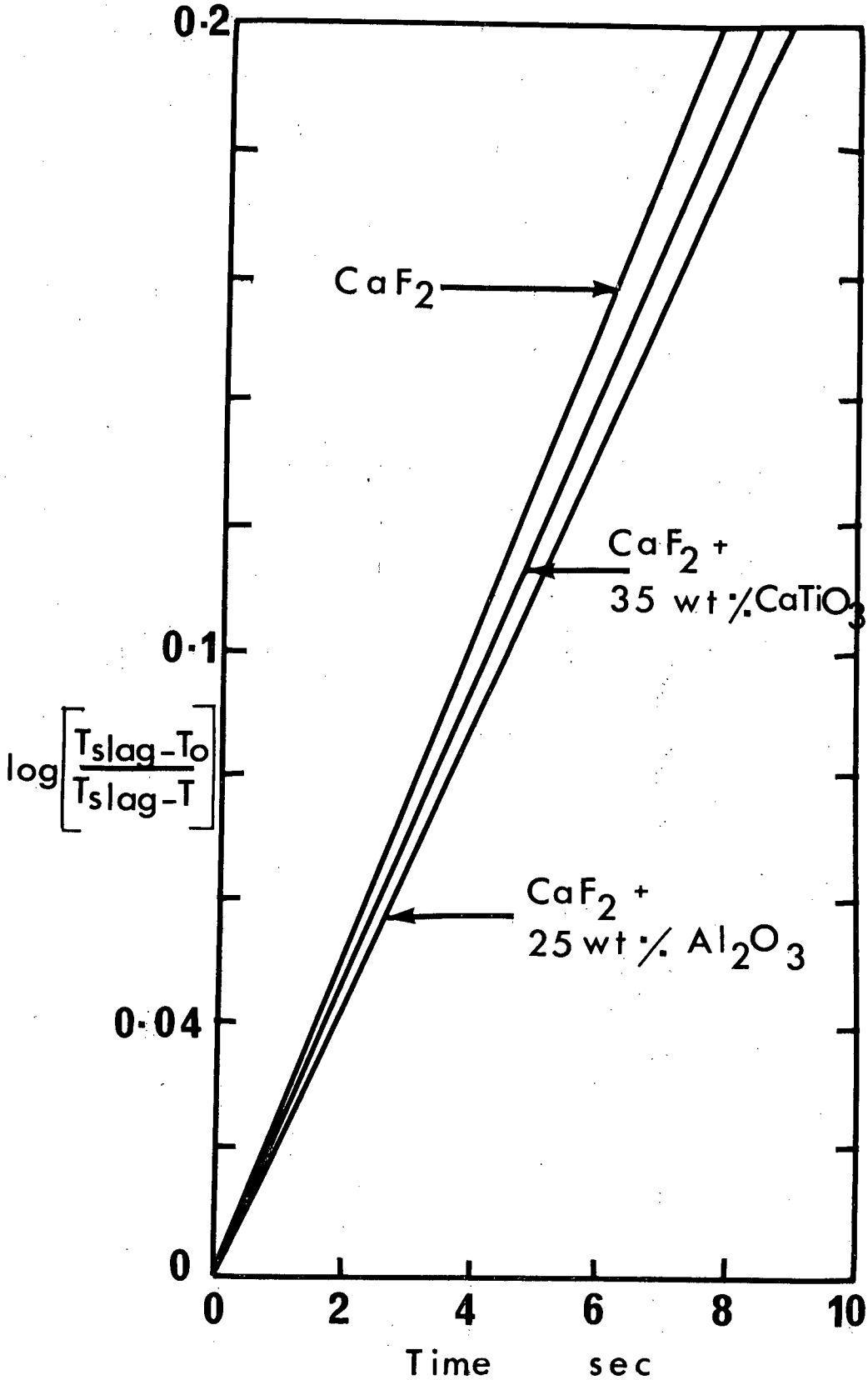

Figure 37. Time dependence of cylinder thermal parameter; slag temperature constant at 1650°C.

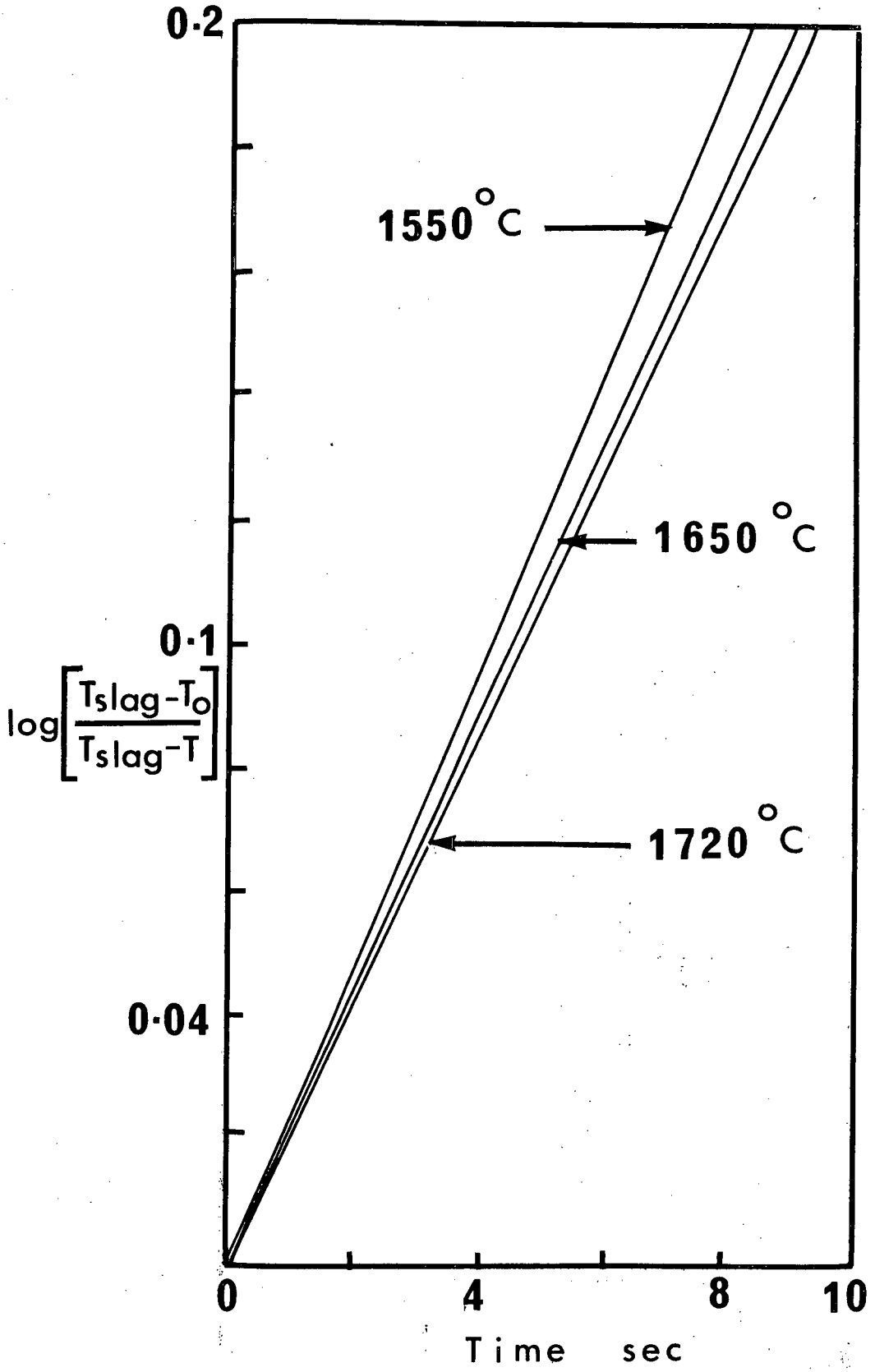

Figure 38. Time dependence of cylinder thermal parameter; slag composition constant at CaF_2 + 25 wt.% Al_2O_3.

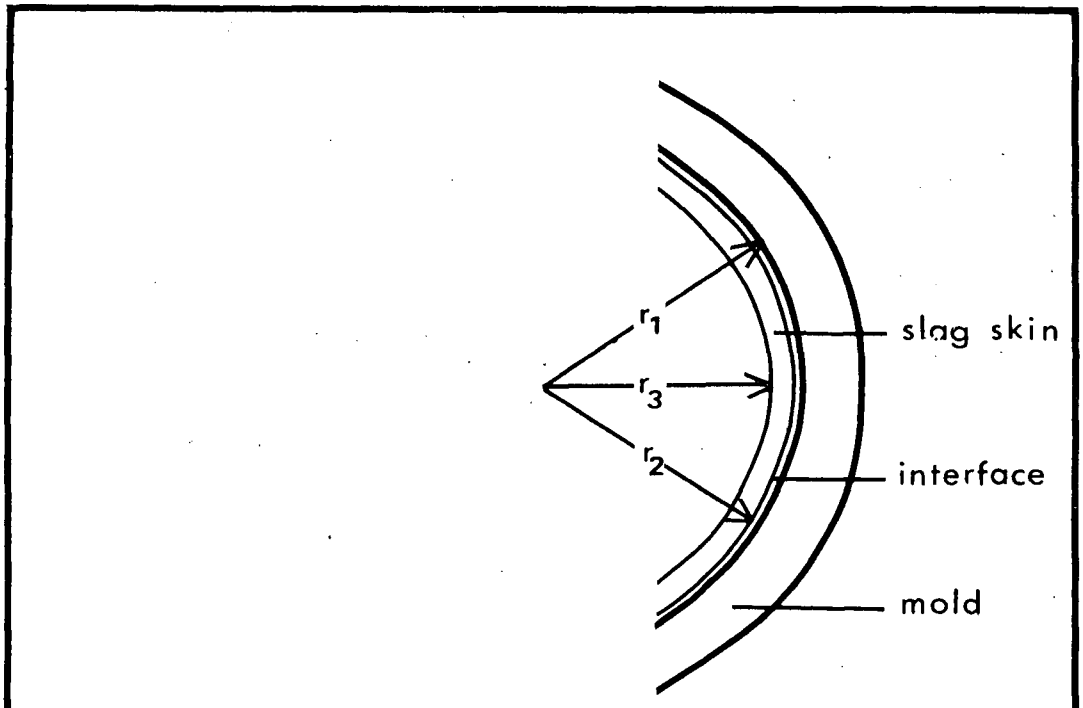

Figure 39. Radial dimensions of the mold-slag skin system.

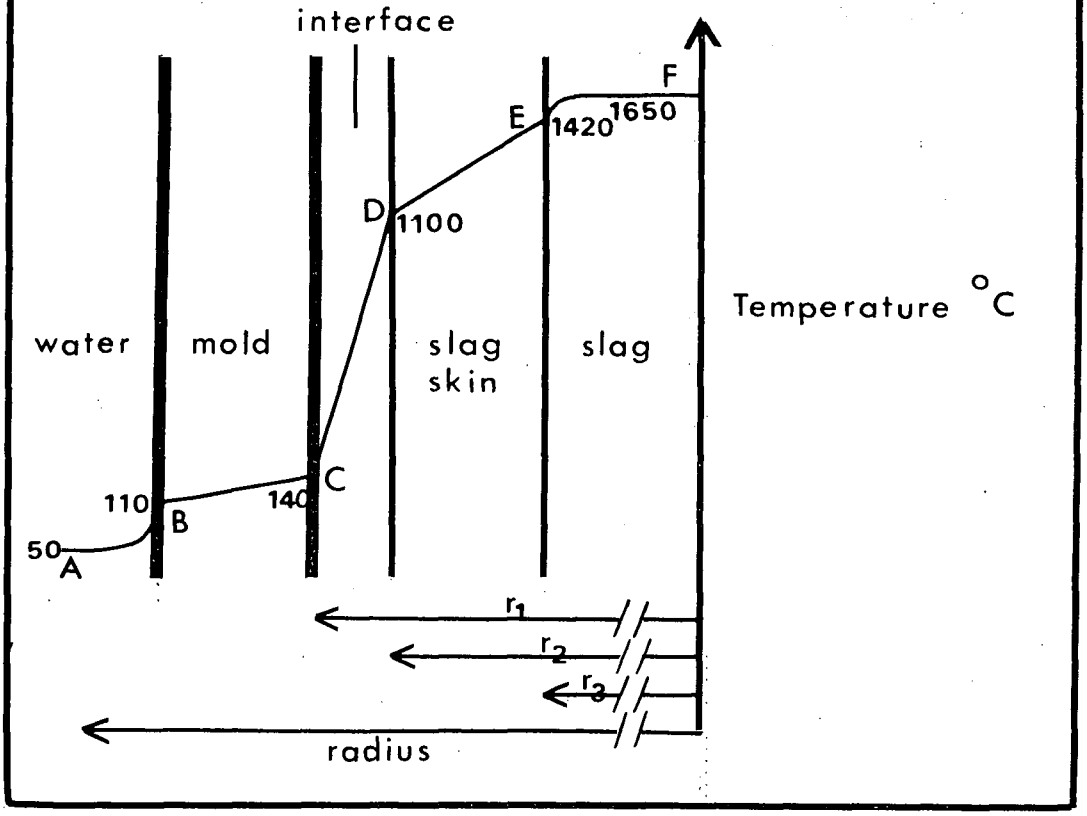

Figure 40. Mold region temperature profile derived from eq. (4.8) by assuming that $k_{slag} = 0.8 \times 10^{-2}$ cal $cm^{-1}{}^{\circ}C^{-1}sec^{-1}$.

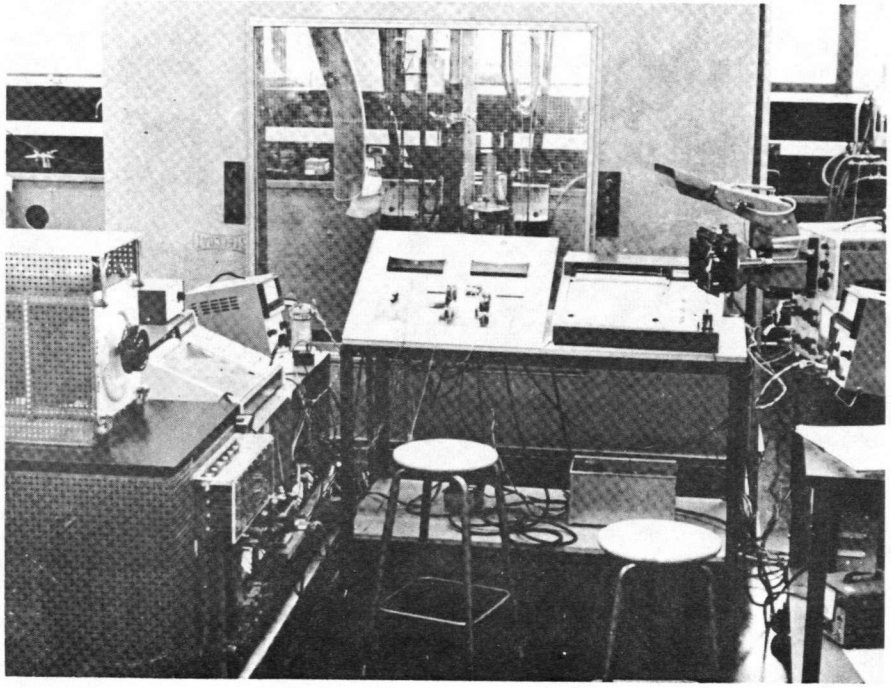

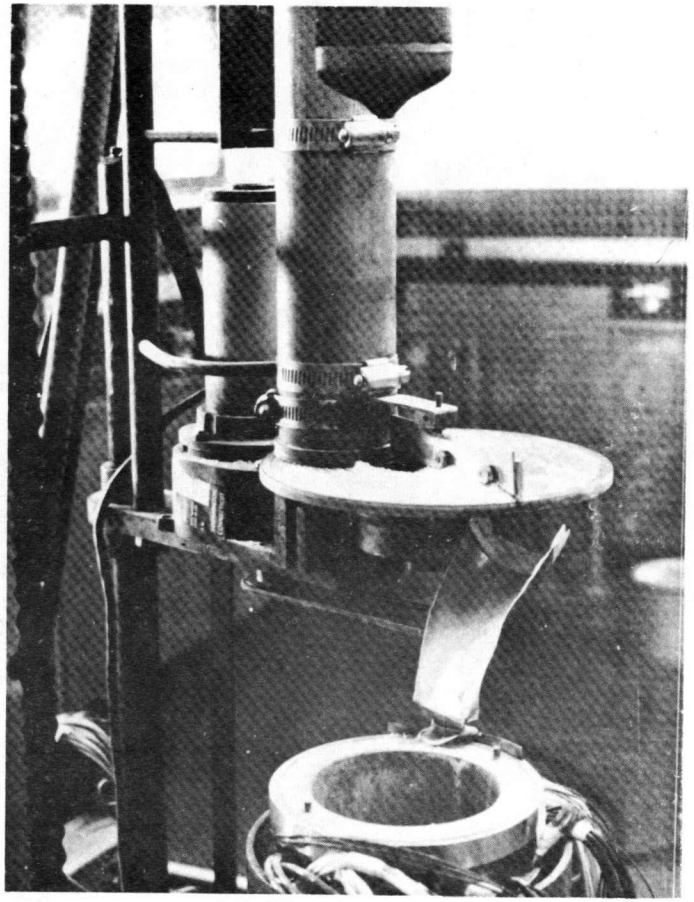

Figure 41. (a) View of the laboratory ESR unit. (b) Powder feeder

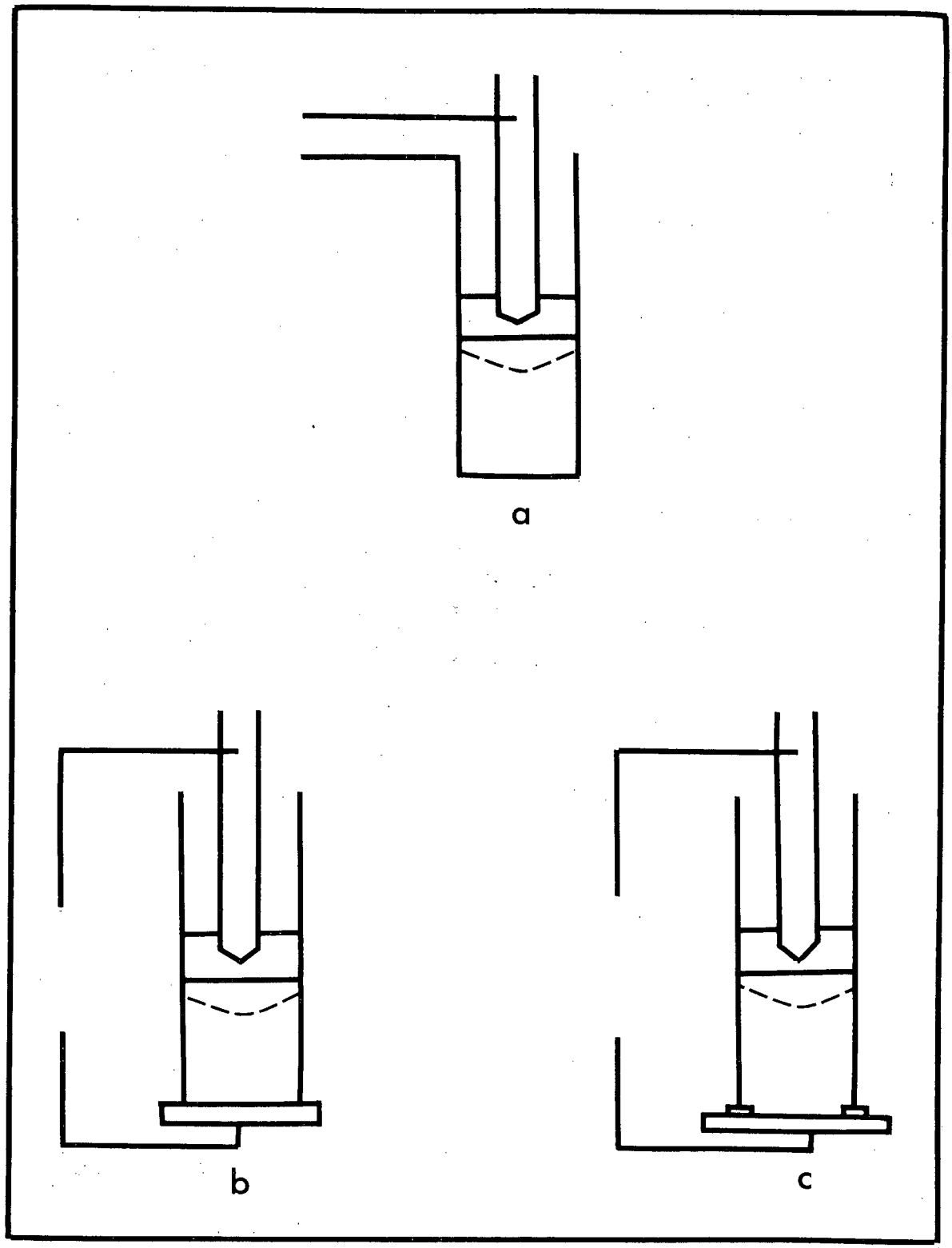

Figure 42. Mold connection in ESR practice.
(a) live (b) floating (c) insulated

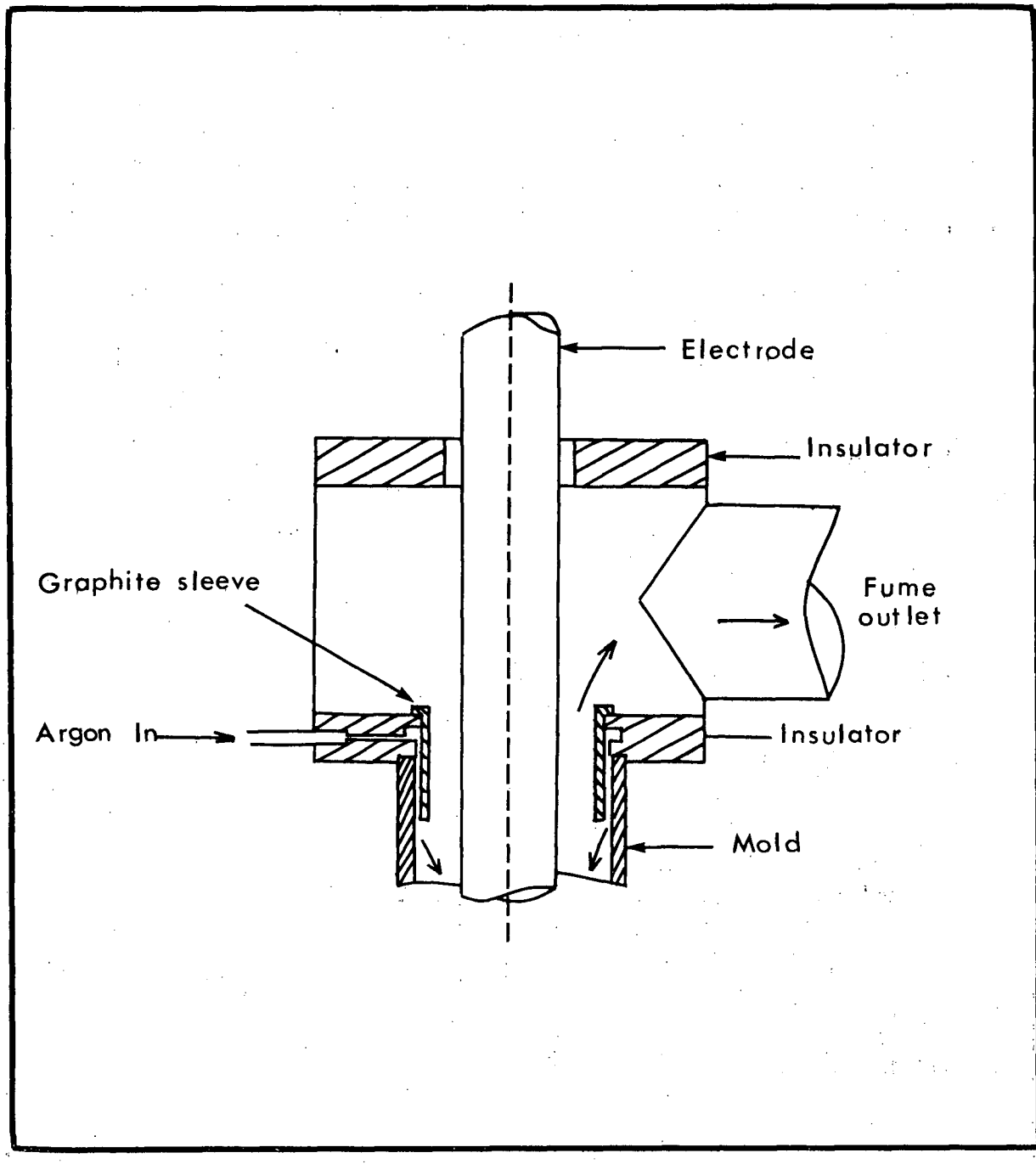

Figure 43. Atmospheric shield (type (I)).

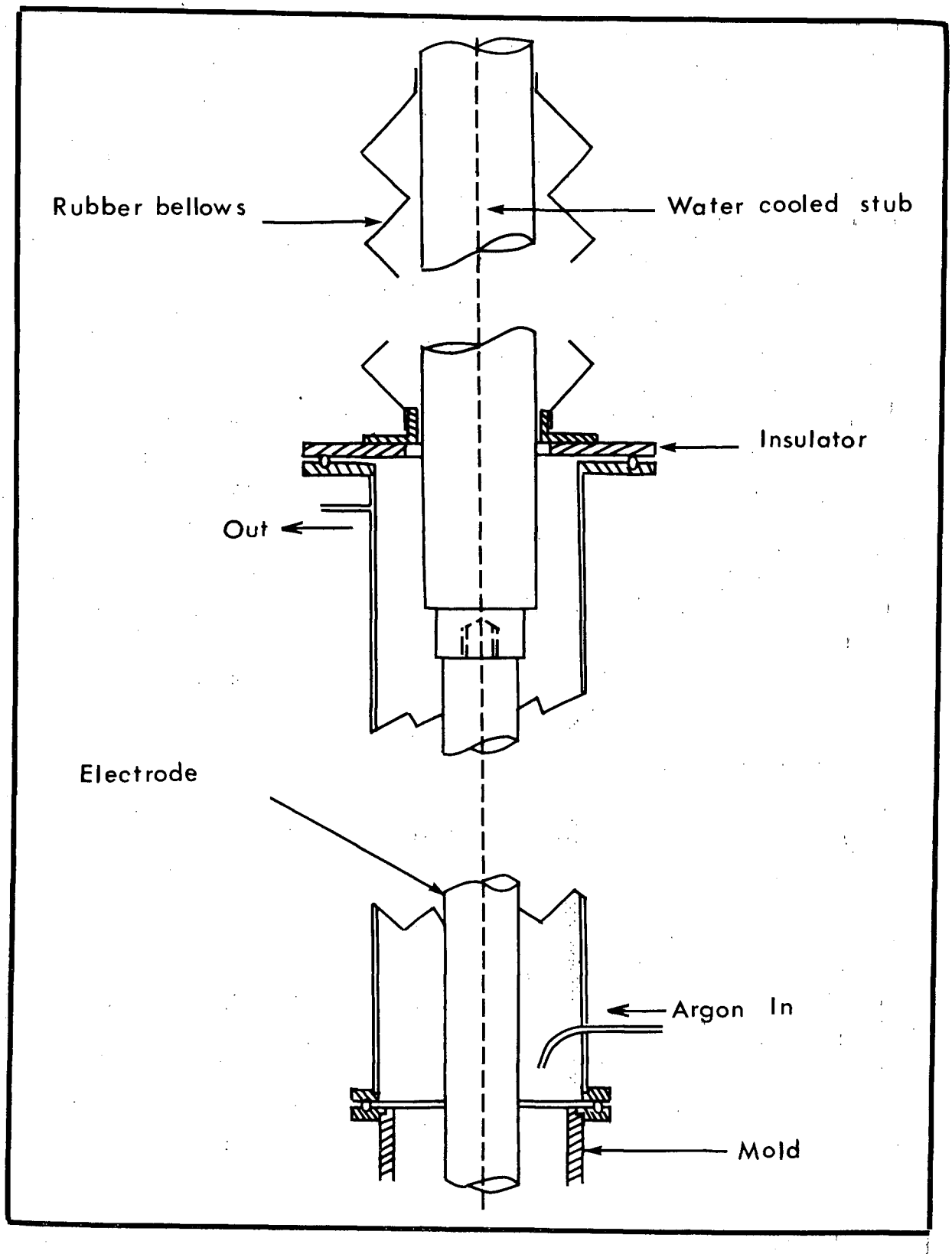

Figure 44. Atmospheric shield (type (II)).

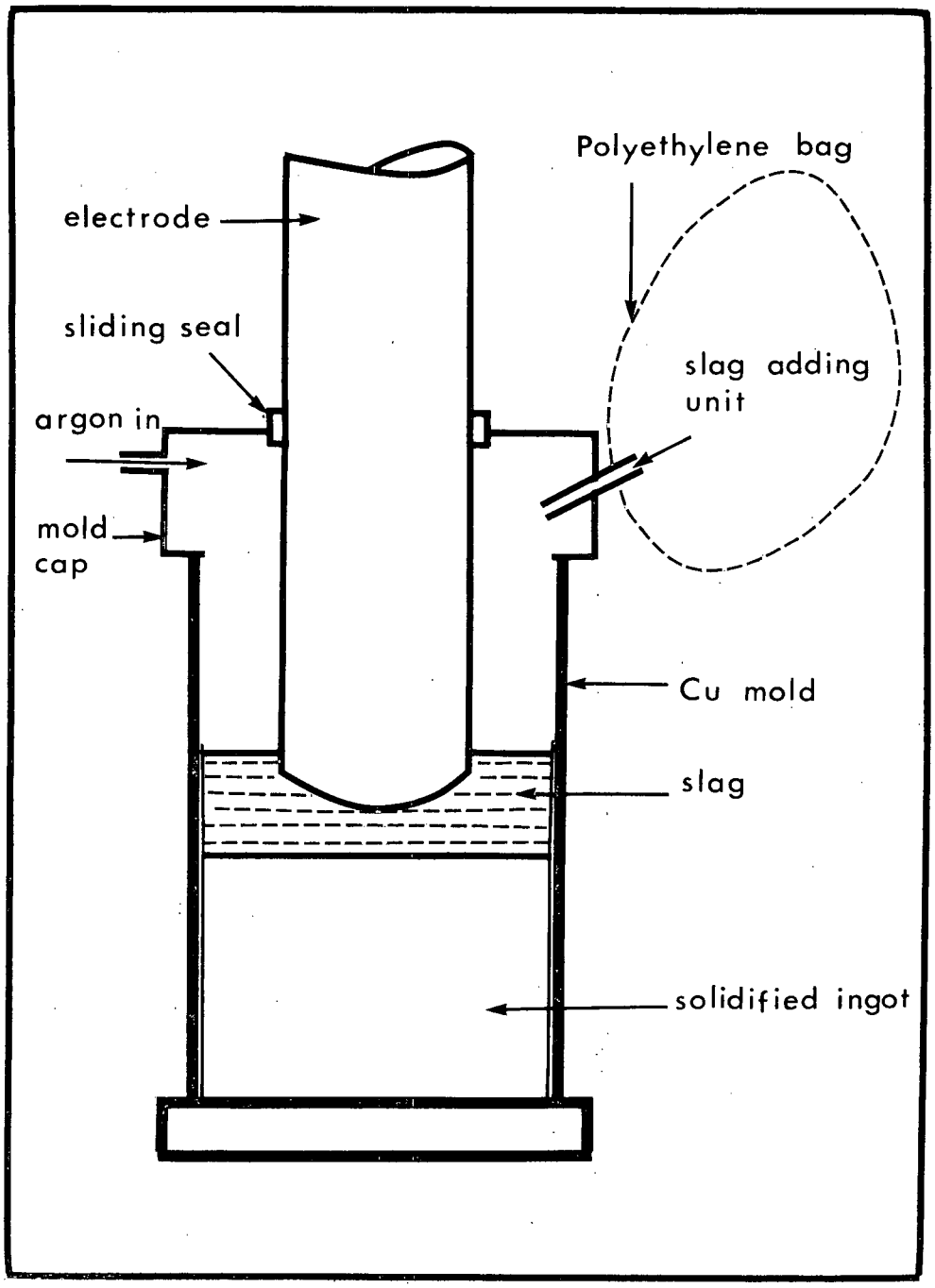

Figure 45. Atmospheric shield (type (III)).

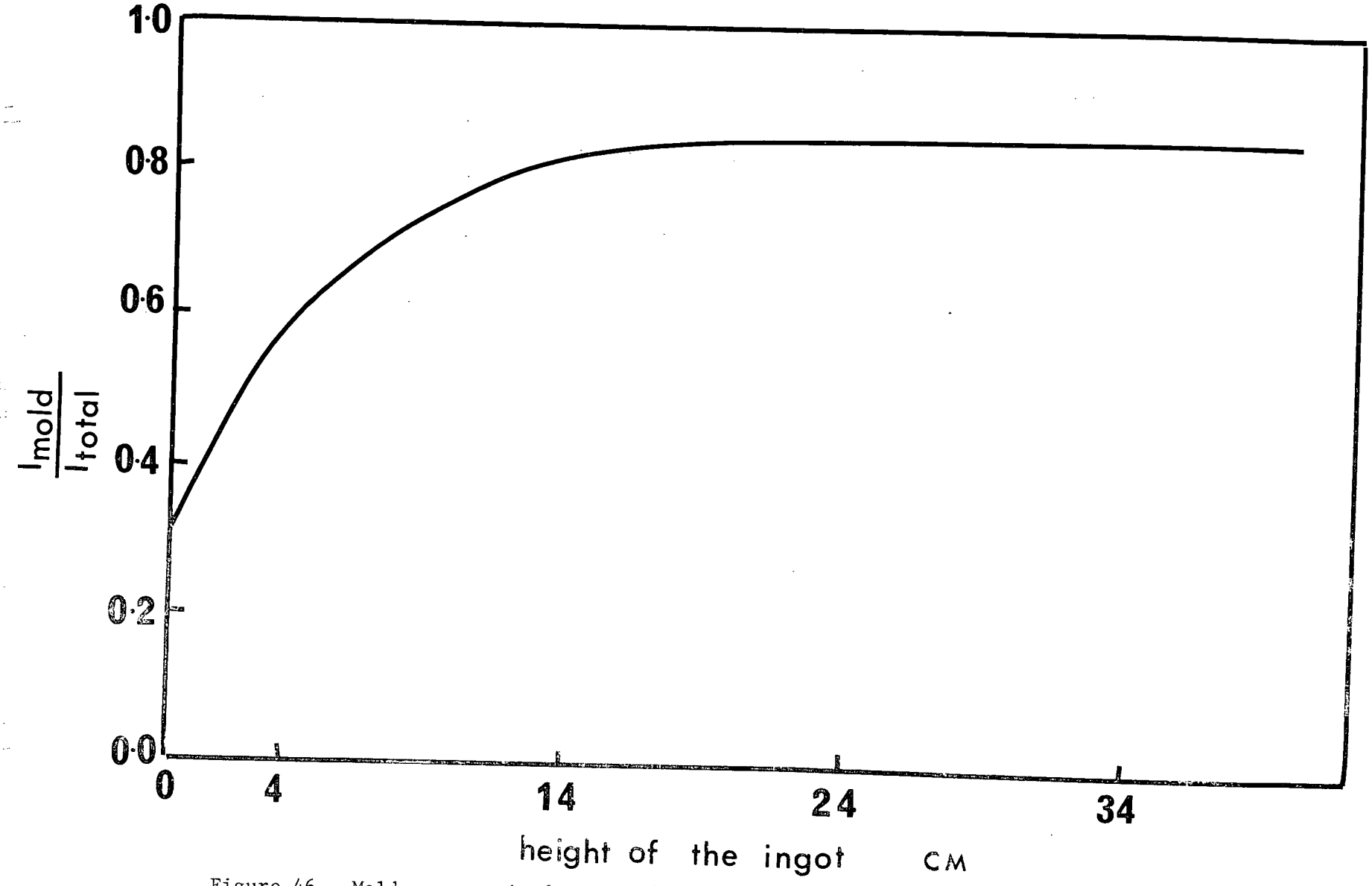

Figure 46. Mold current in d.c. +ve 'live' operation.

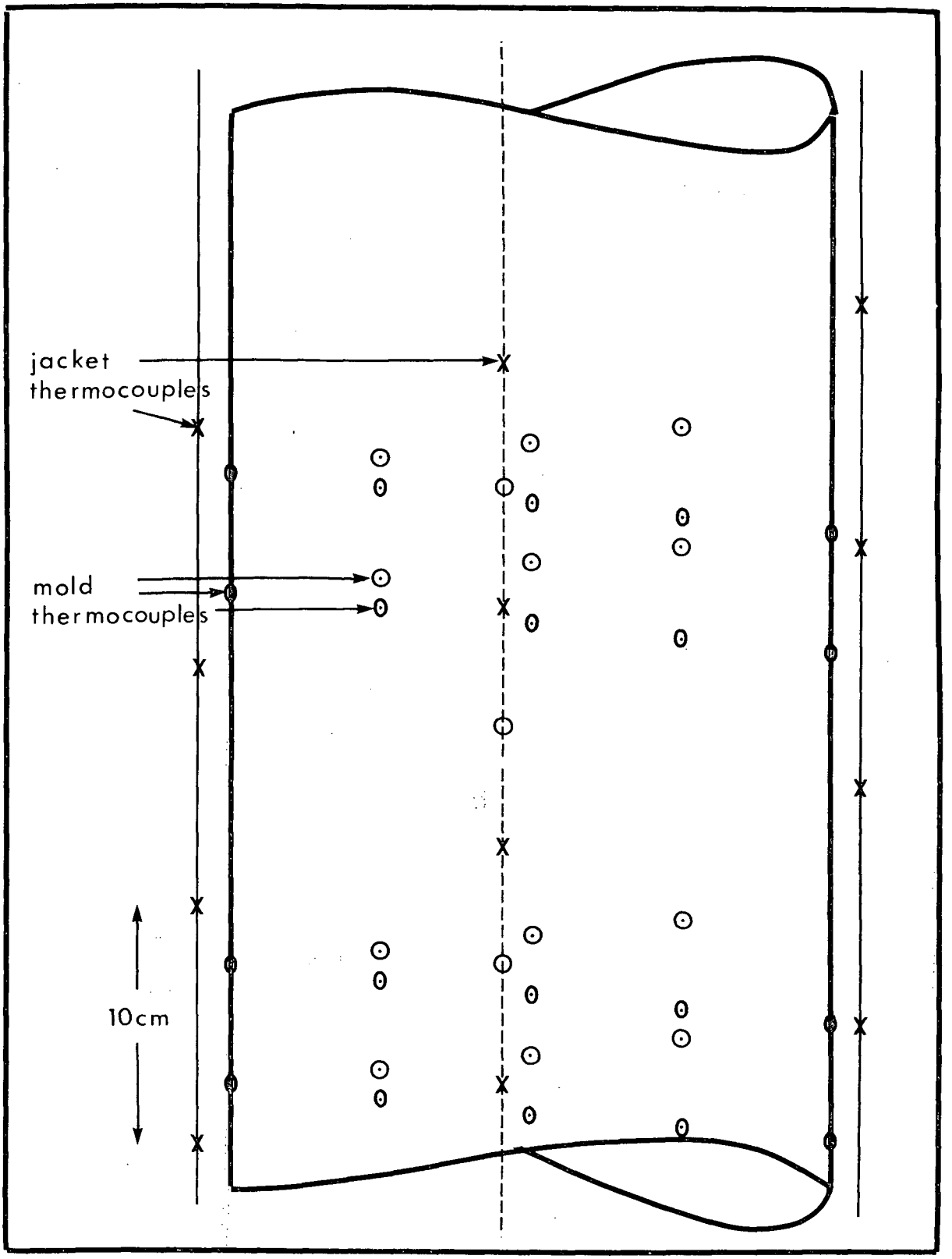

Figure 47. Thermocouple arrangement on the mold.

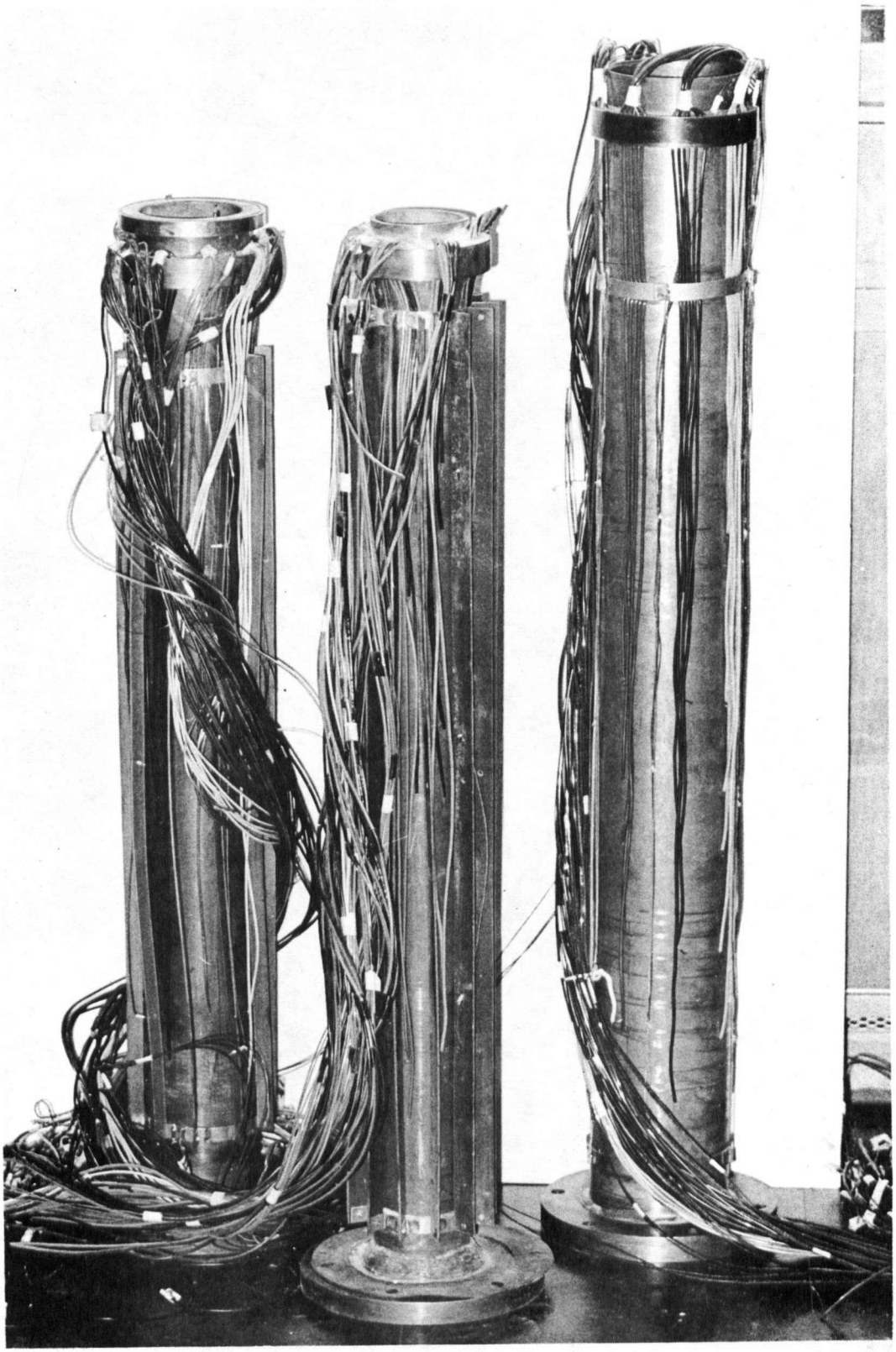

Figure 48. Thermocouples clad copper molds.

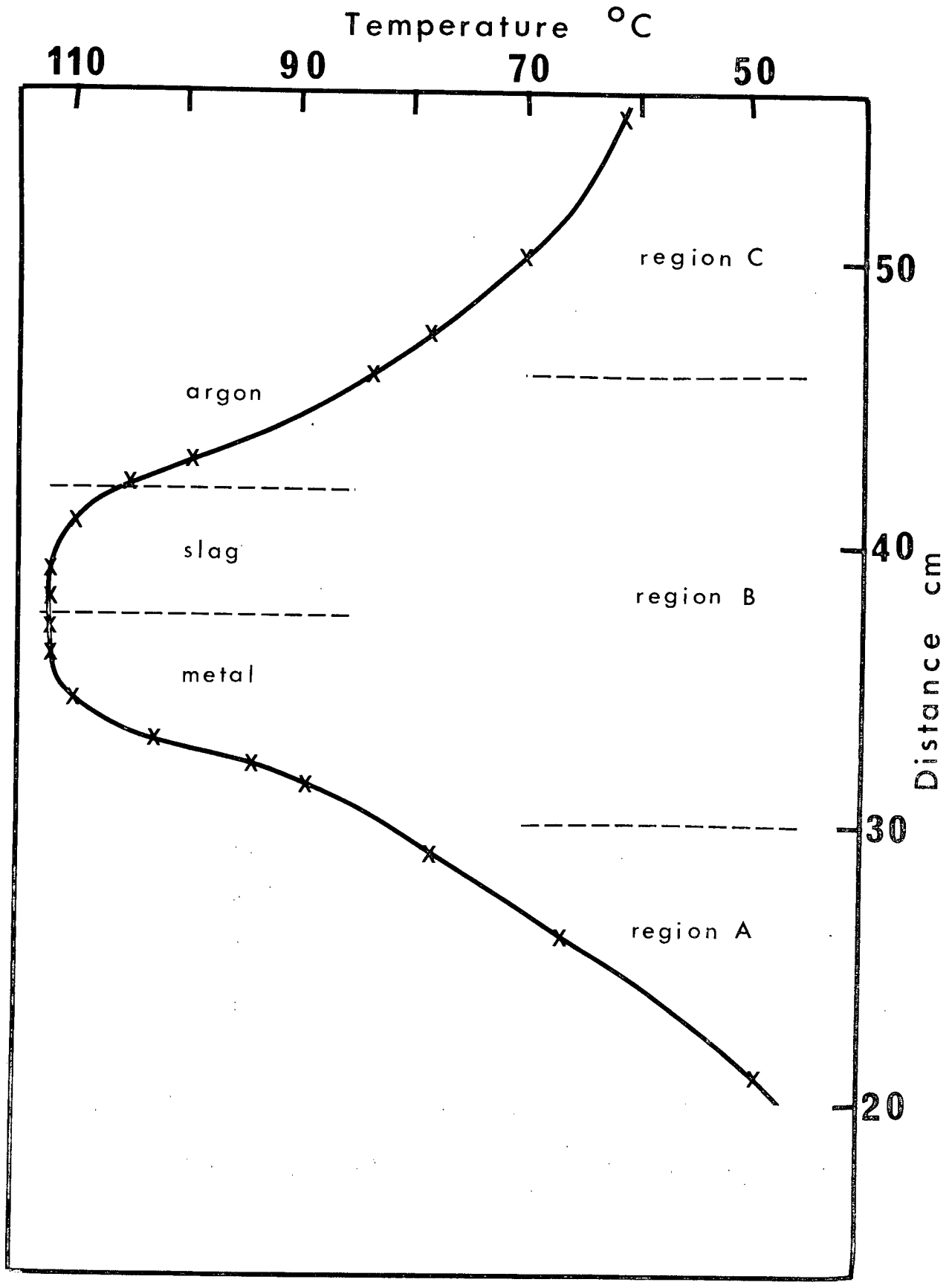

Figure 49. Temperature profile on the mold for ingot no. 1.

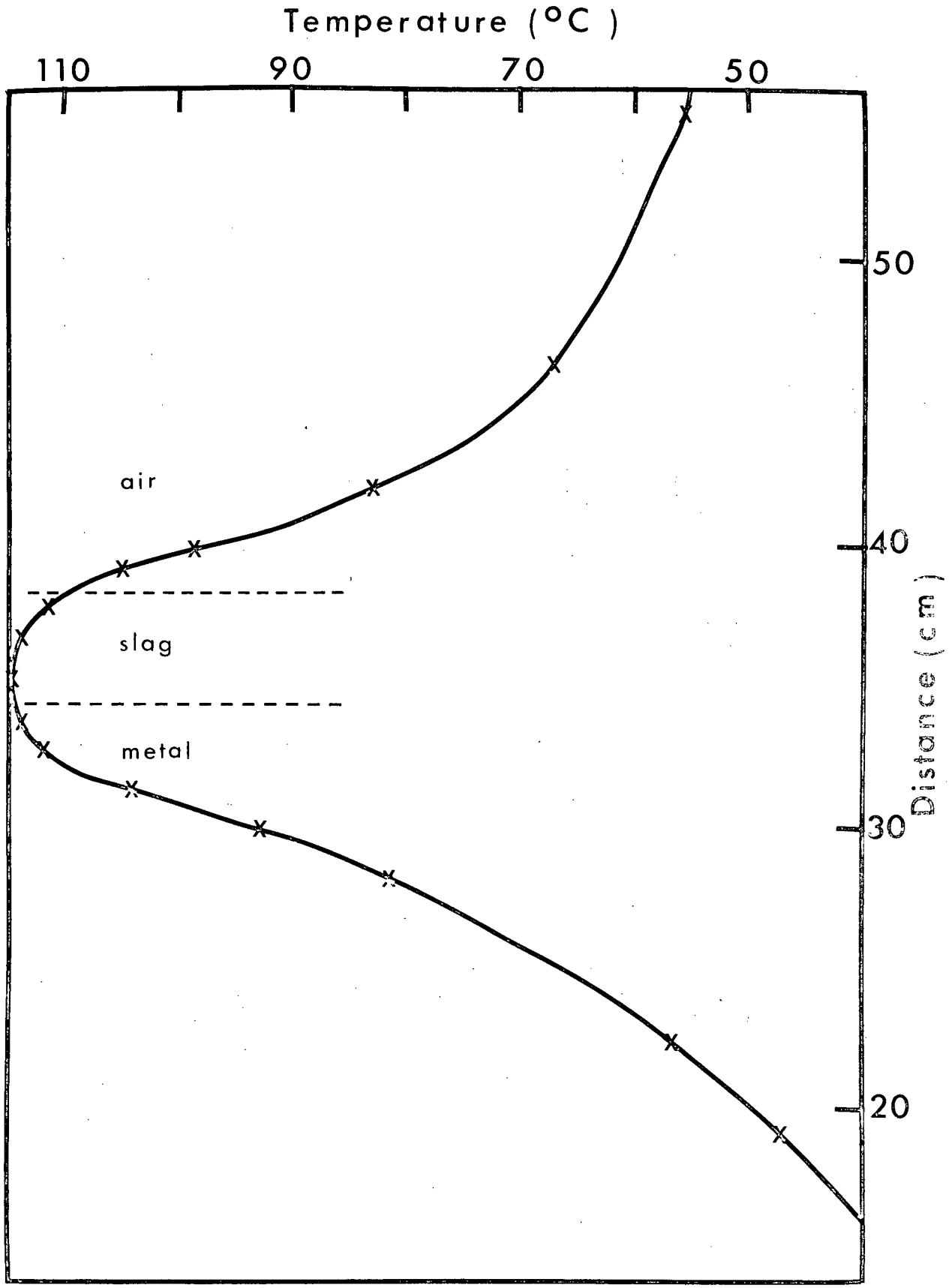

Figure 50. Temperature profile on the mold for ingot. no. 3.

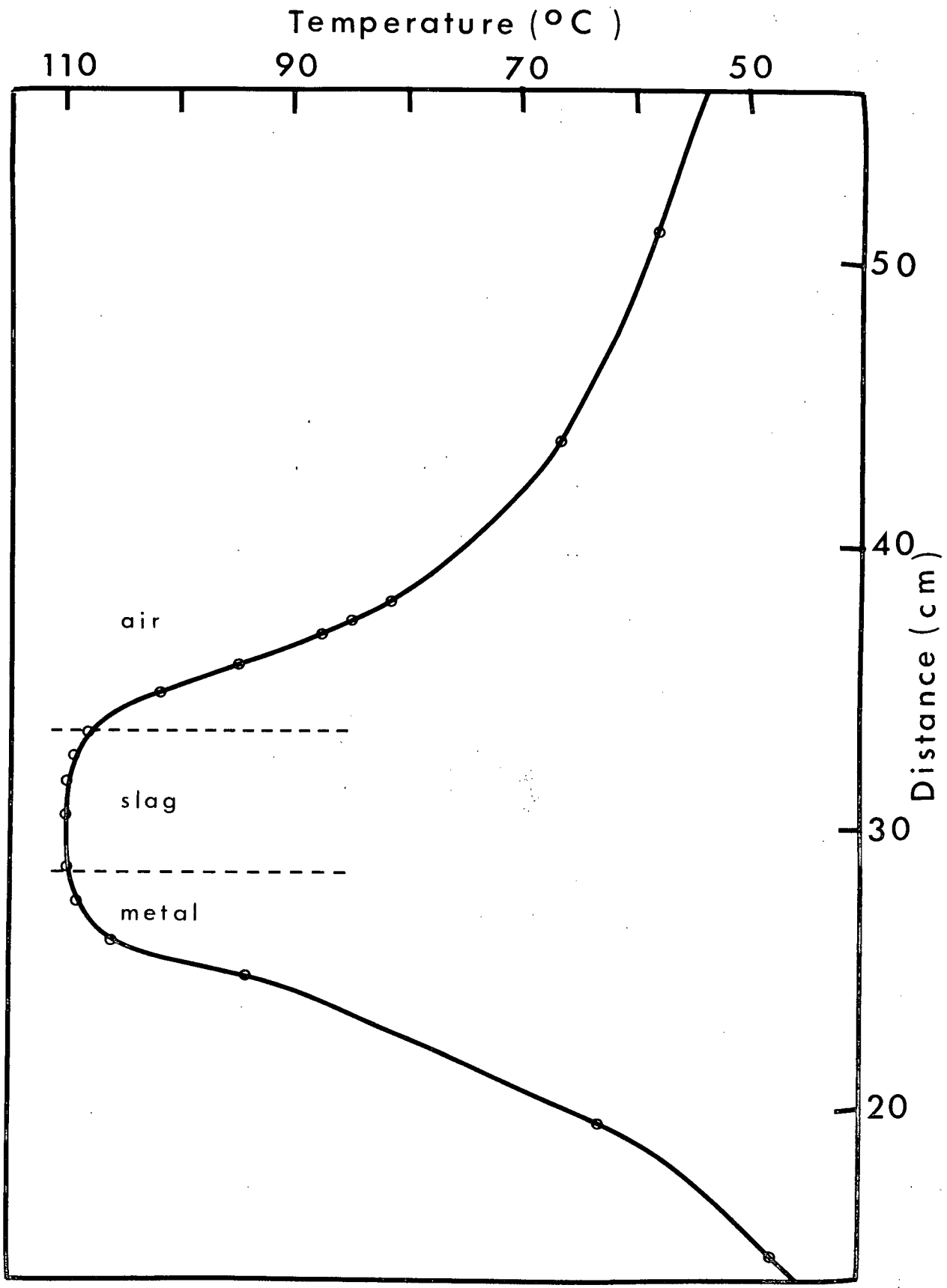

Figure 51. Temperature profile on the mold for ingot no. 8.

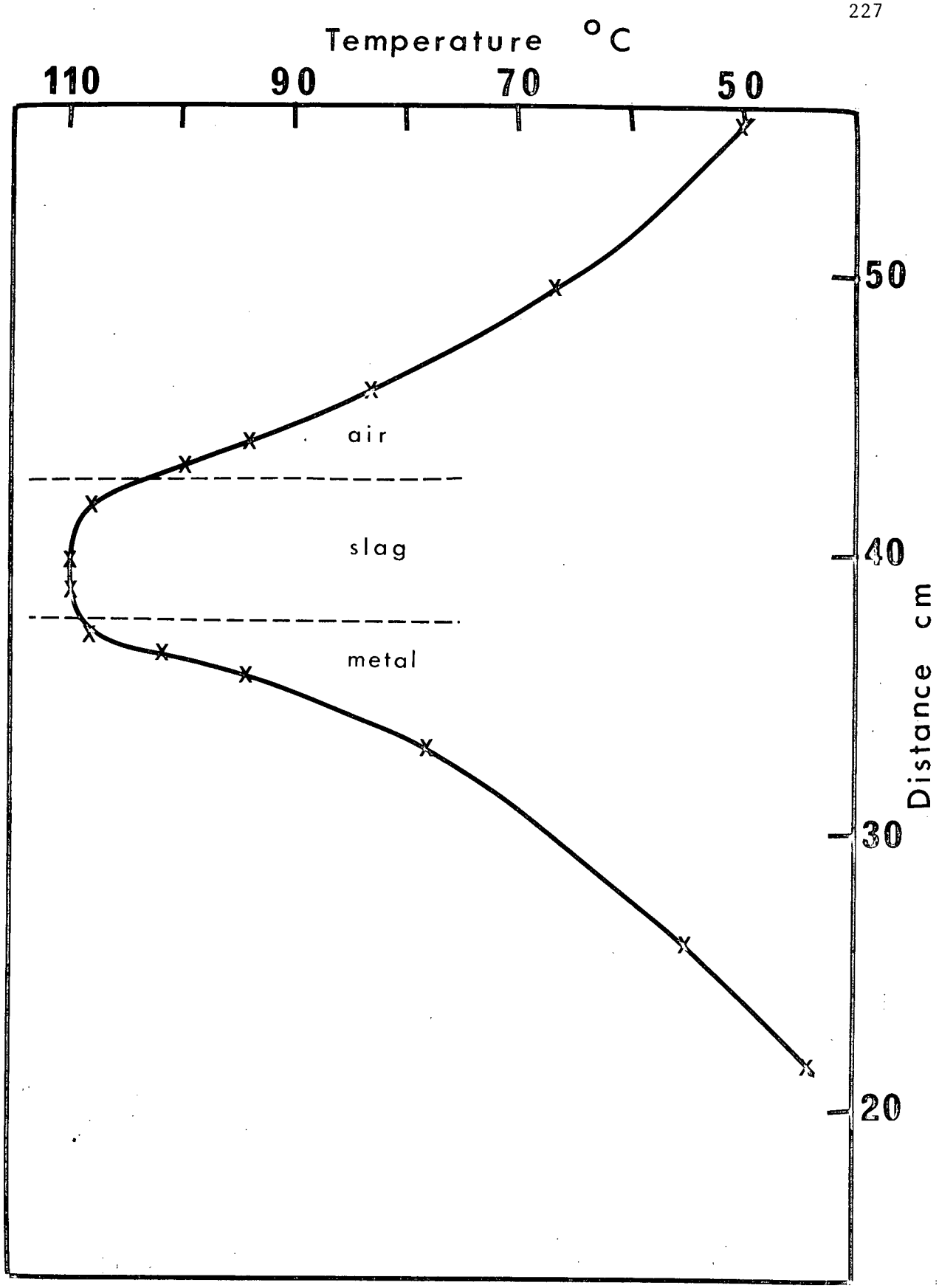

Figure 52. Temperature profile on the mold for ingot no. 9.

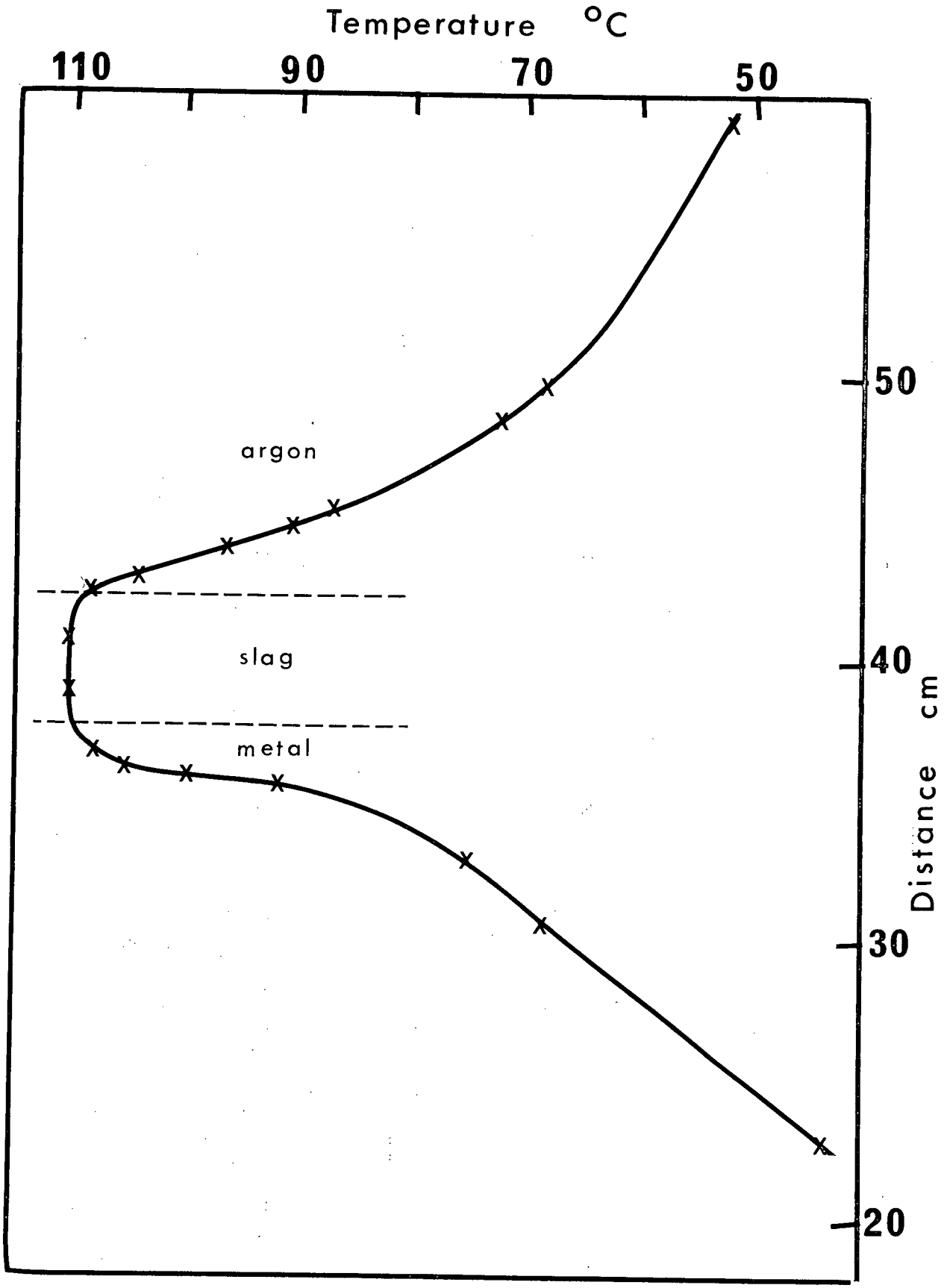

Figure 53. Temperature profile on the mold for ingot no. 10.

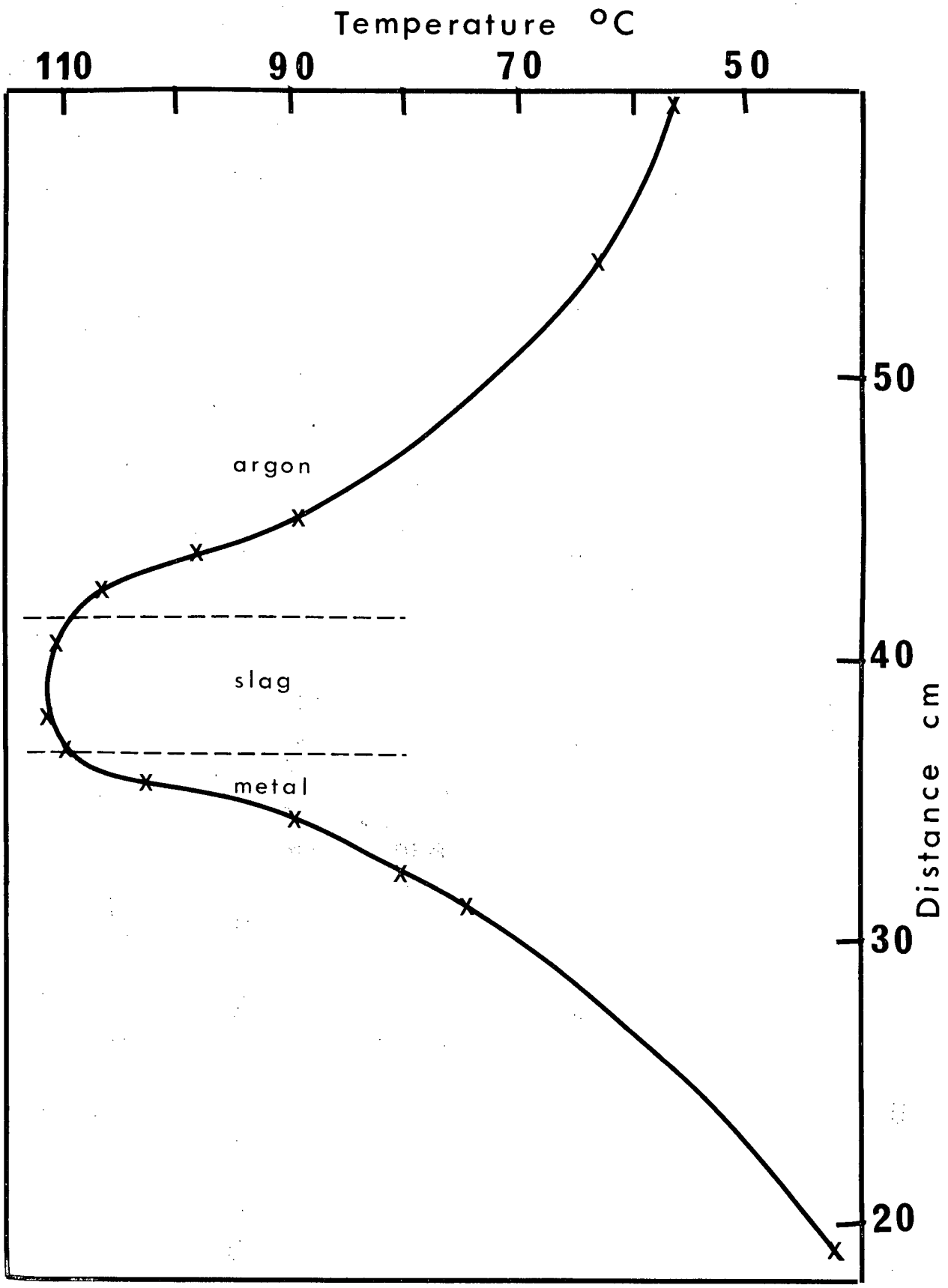

Figure 54. Temperature profile on the mold for ingot no. 13.

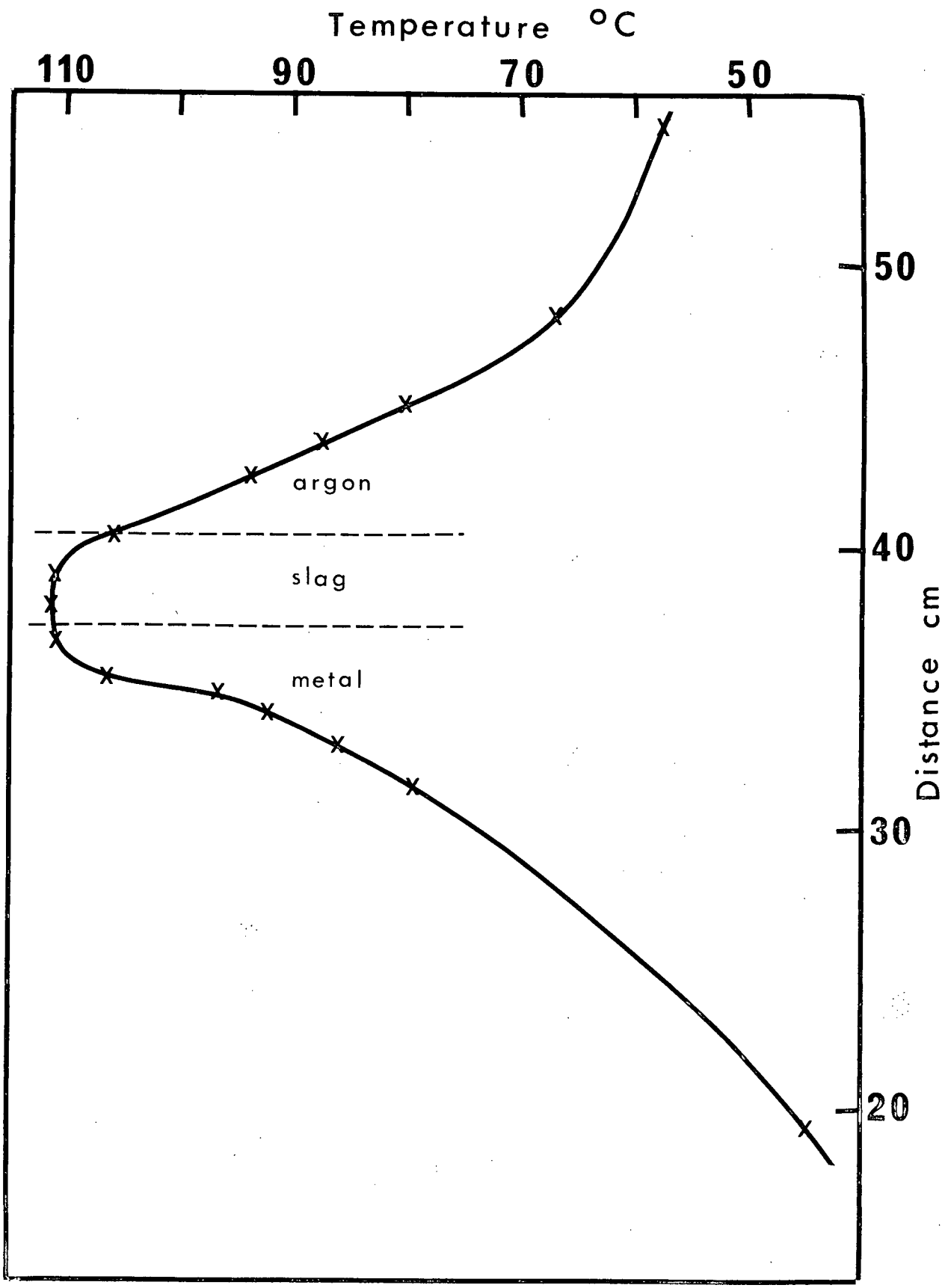

Figure 55. Temperature profile on the mold for ingot no. 16.

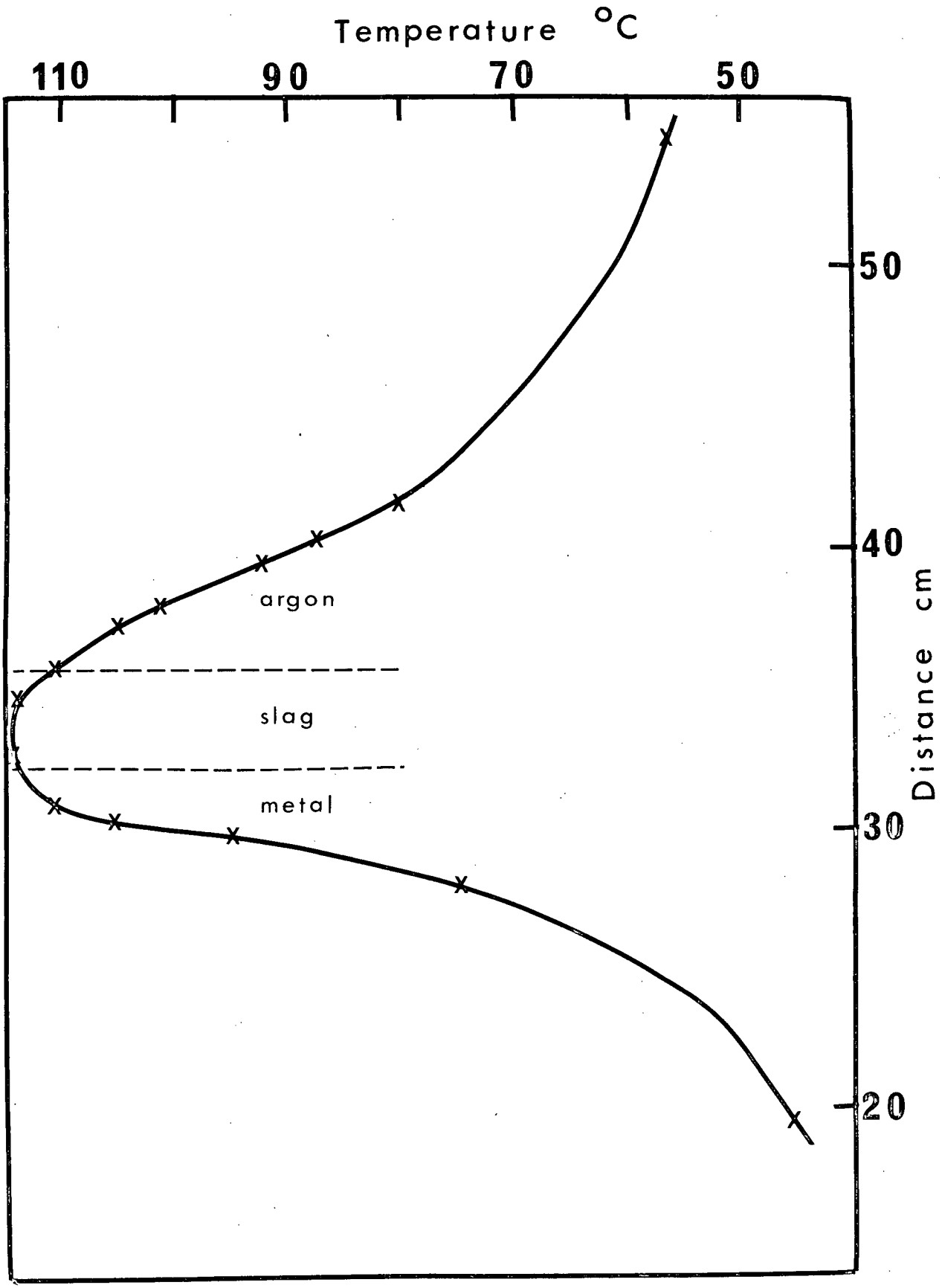

Figure 56. Temperature profile on the mold for ingot no. 19.

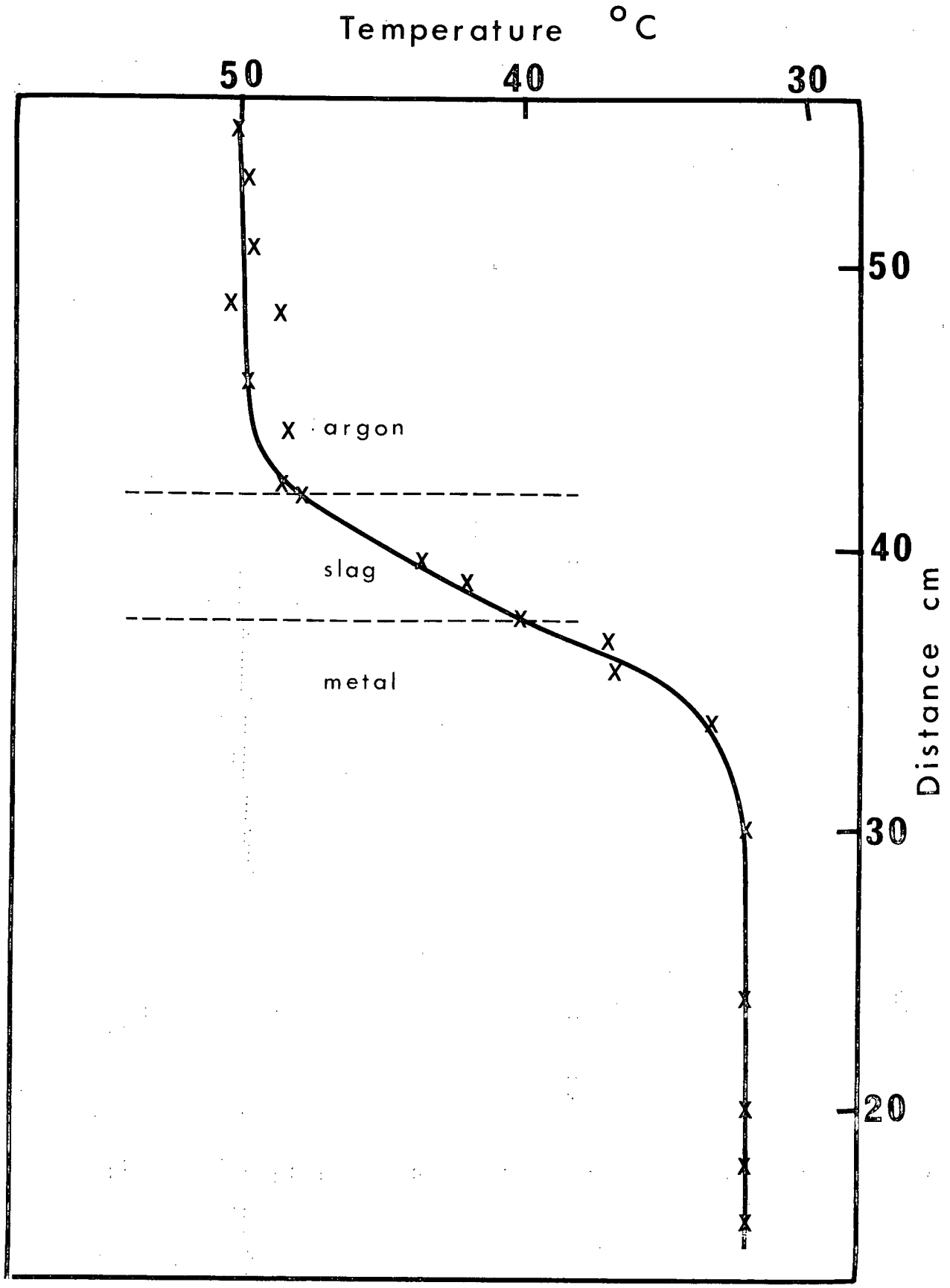

Figure 57. Temperature distribution in the mold cooling water for ingot no. 1.

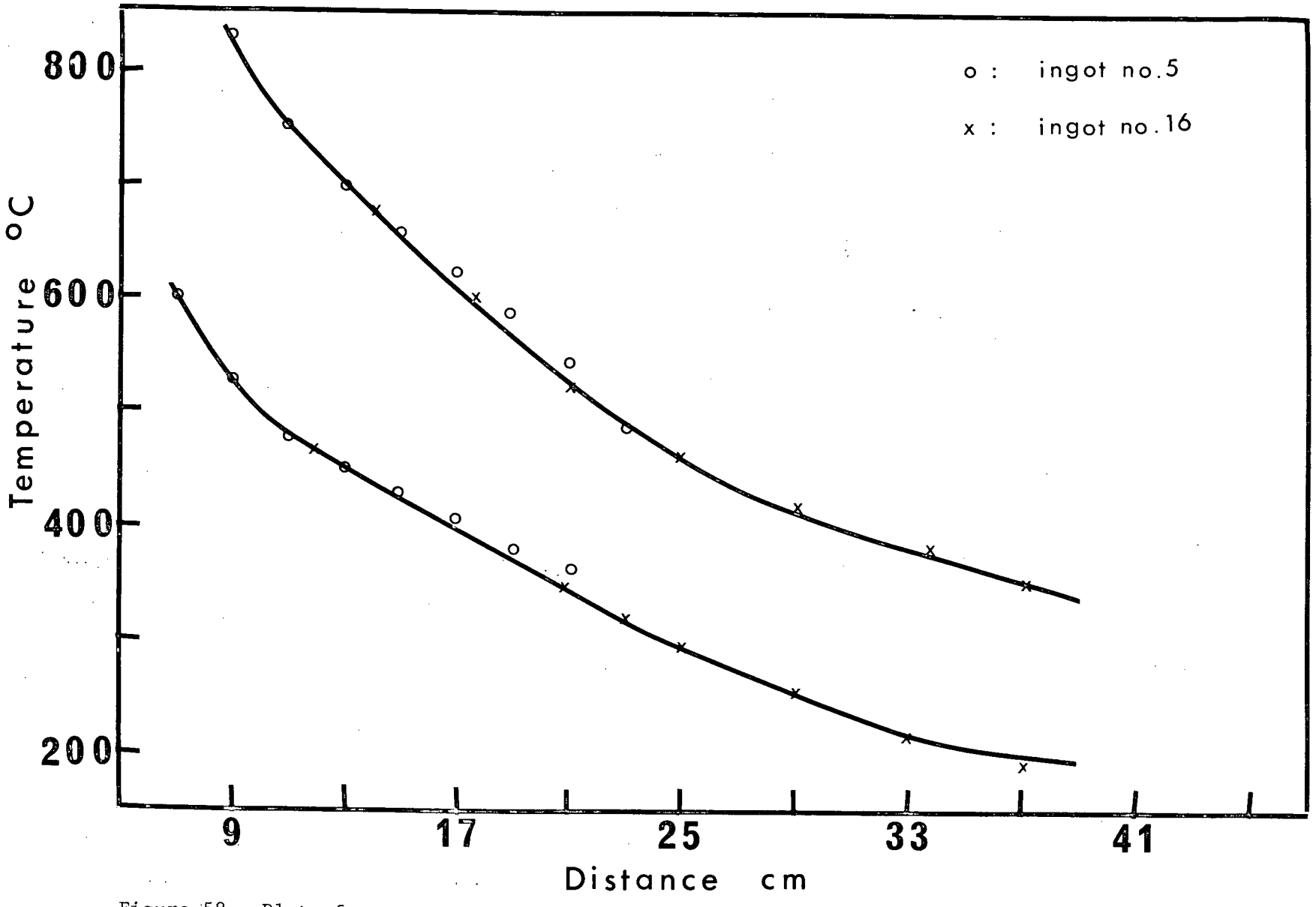

Figure 58. Plot of temperature vs. distance from the slag/metal interface for base plate thermocouples.

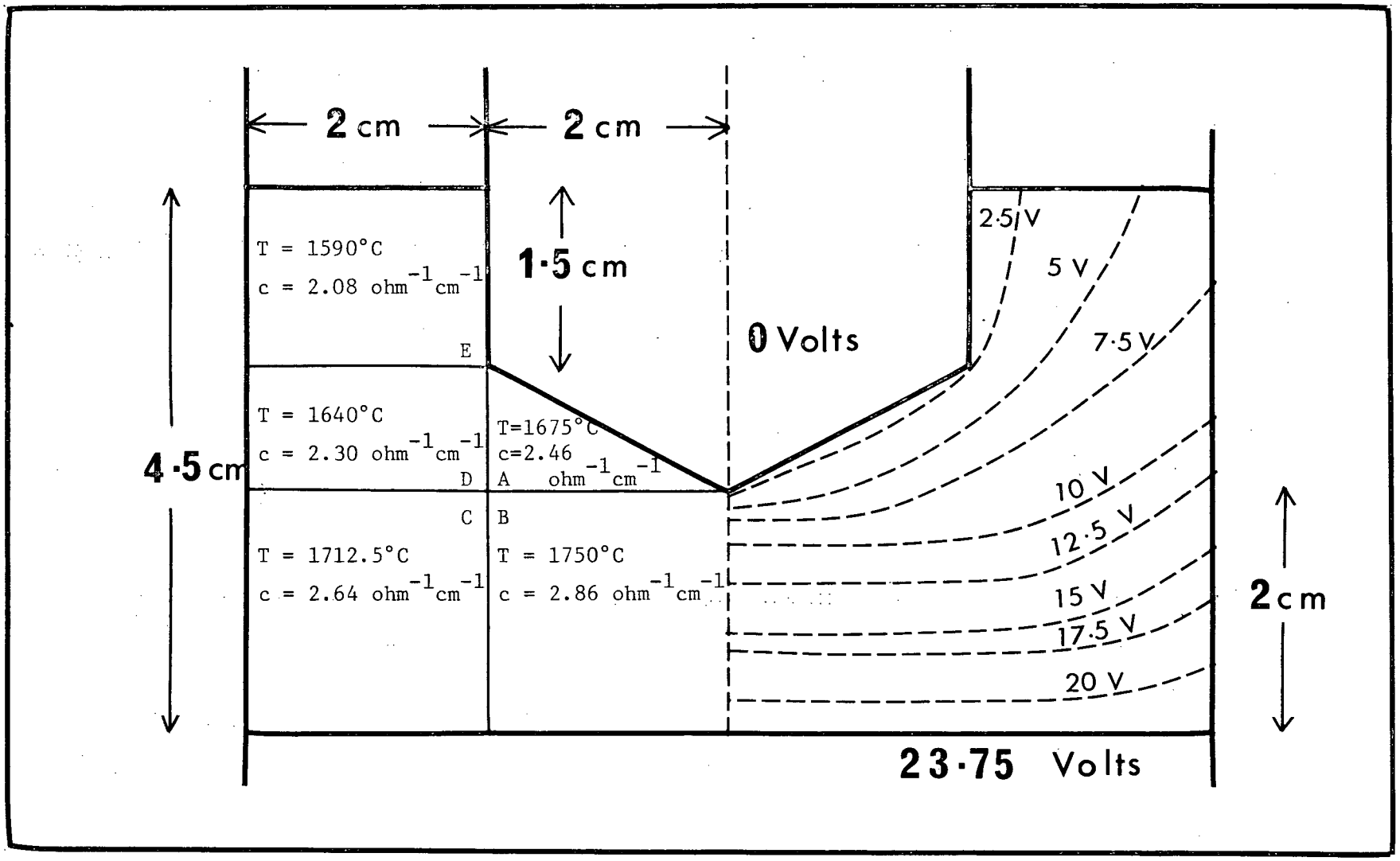

Figure 59. Voltage gradients in the slag bed for ingot no. 1.

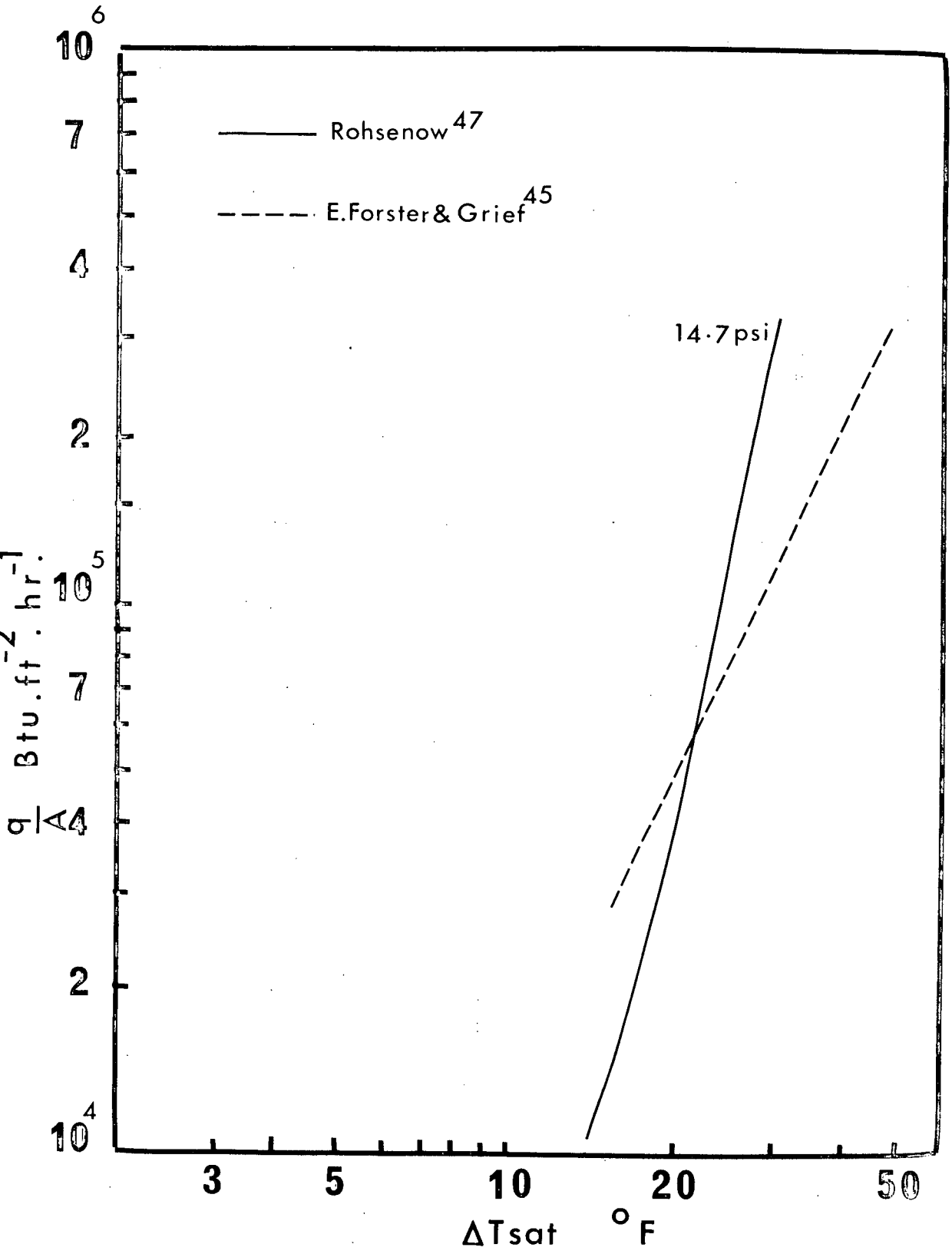

Figure 60. Plot of heat flux vs. excess temperature.[45,47]

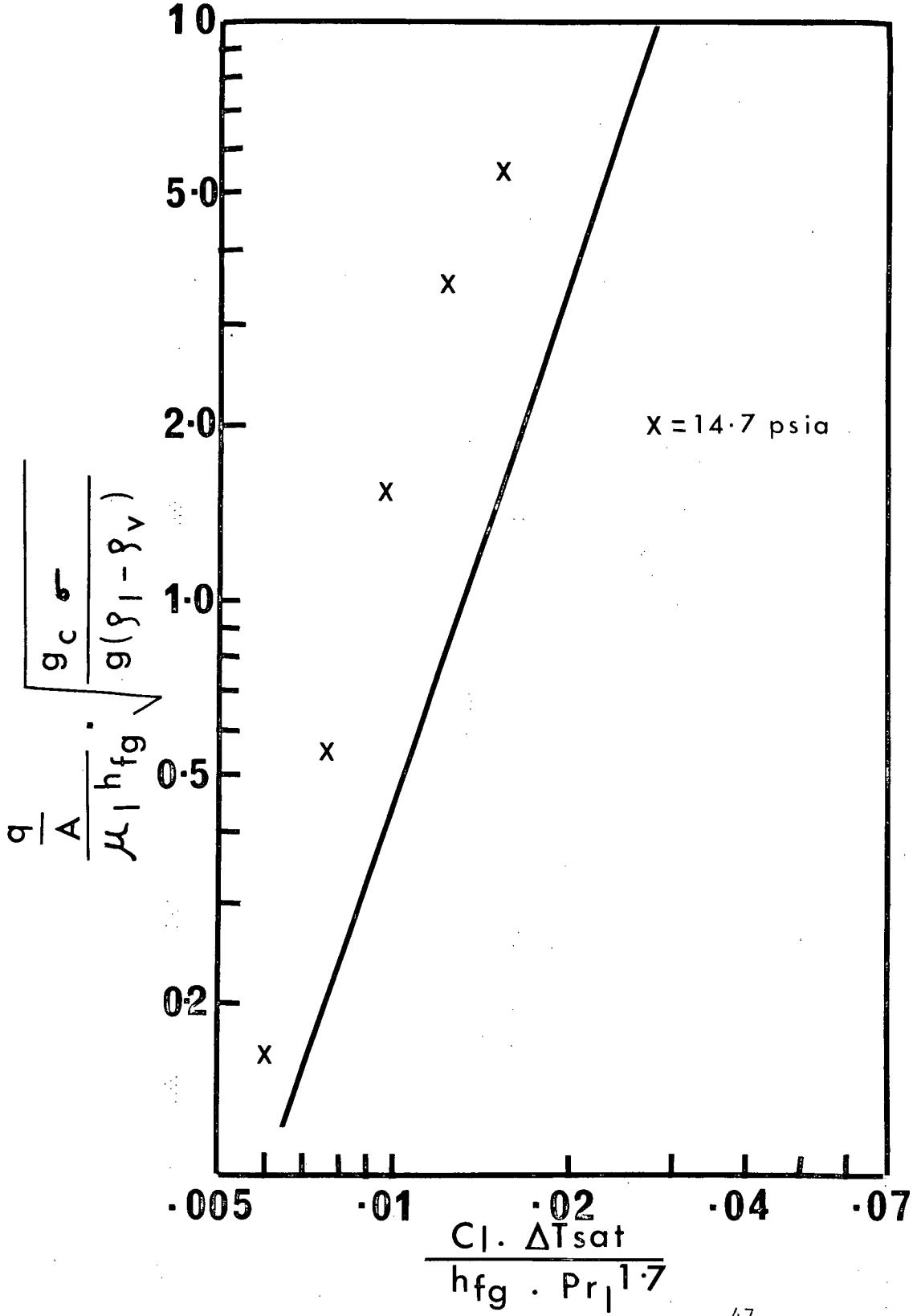

Figure 61. Correlation of pool-boiling heat transfer data.[47]

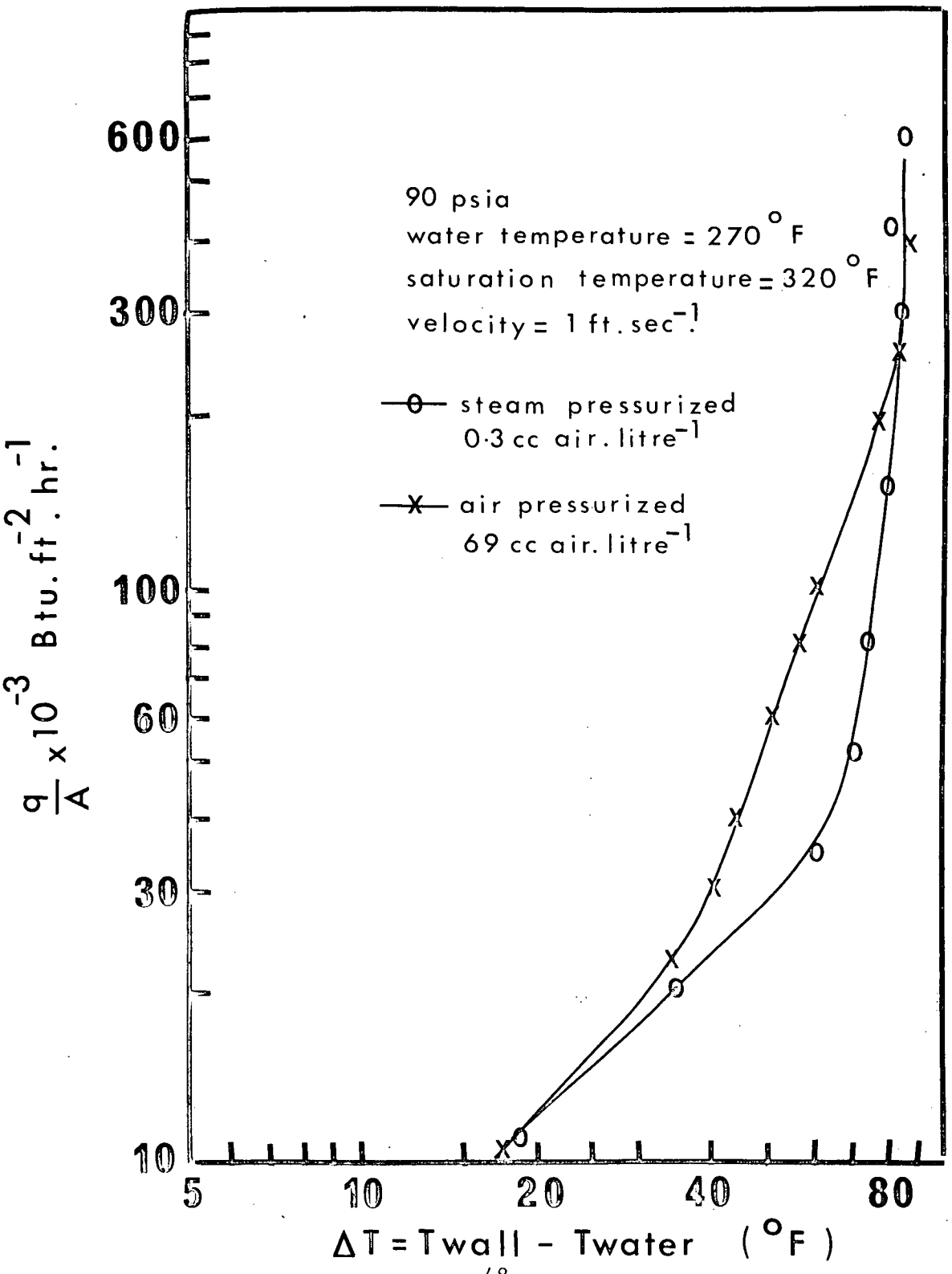

Figure 62. Effect of dissolved air[48] on the heat flux.

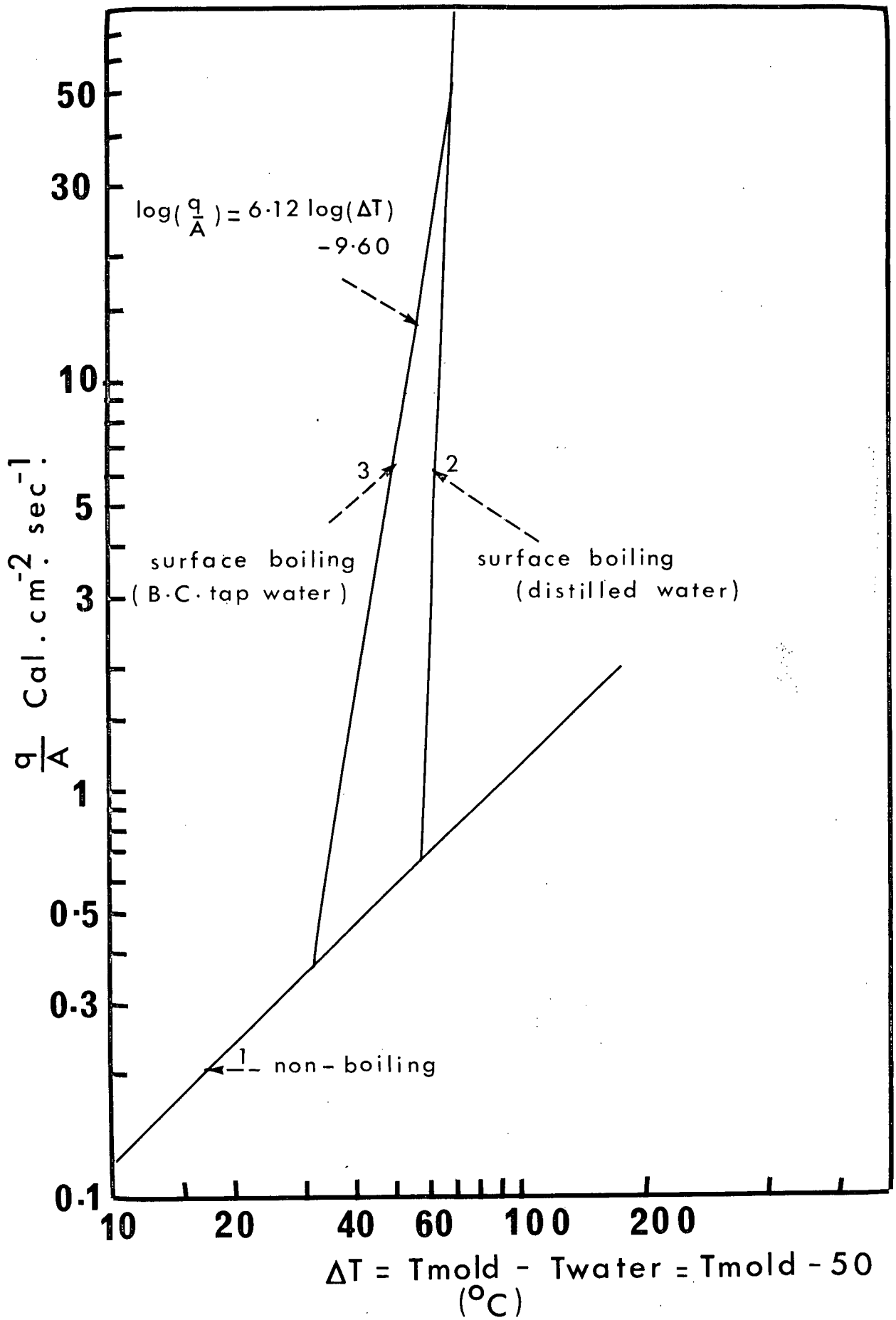

Figure 63. Plot of (q/A) vs. ΔT for (a) non-boiling and (b) surface boiling conditions.

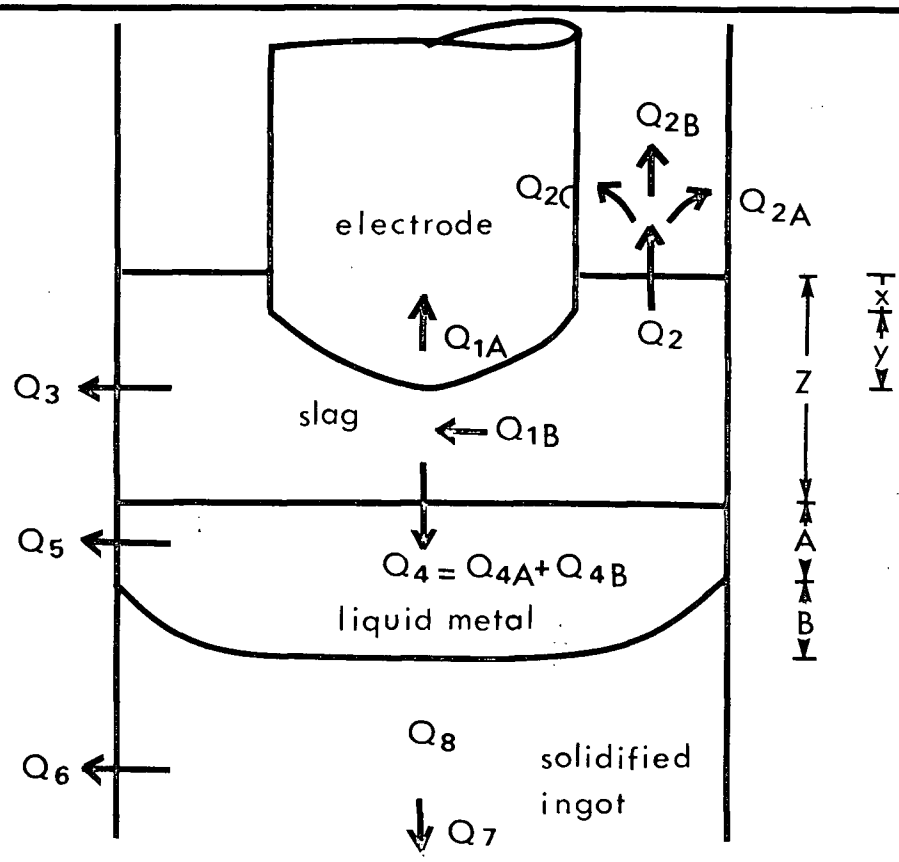

Q_{1A} = heat required to melt the electrode

Q_{1B} = heat required to superheat the liquid metal drops

Q_2 = heat lost by radiation from the slag surface to (A) mold cooling water, (B) gases, (C) electrode

Q_3 = heat lost to mold cooling water across the slag bed

Q_{4A} = heat transferred across S/M interface as sensible heat of the falling metal drops

Q_{4B} = heat transferred across S/M interface by convective heat transfer

Q_5 = heat lost to mold cooling water across the liquid metal pool

Q_6 = heat lost to mold cooling water across the solidified ingot

Q_7 = heat lost to base plate cooling water

Q_8 = sensible heat retained by the solidified ingot.

Figure 64. Heat distribution in an ESR unit.

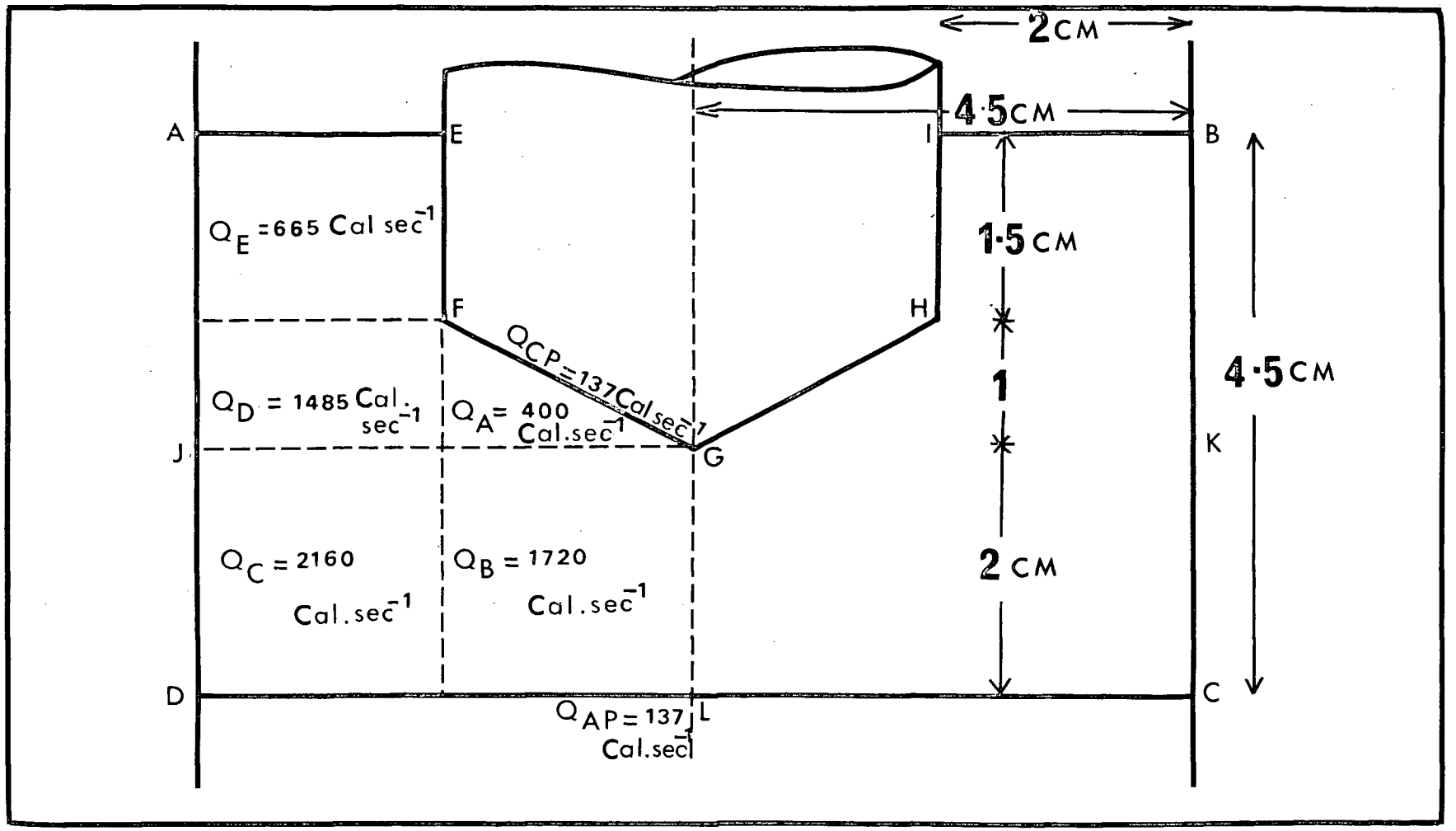

Figure 65. Heat generation distribution in the slag bed (for ingot no. 1).

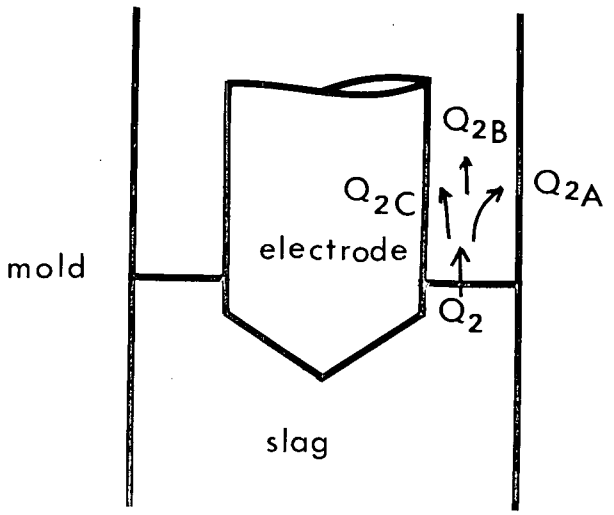

Figure 66. Heat lost by radiation from the slag surface.

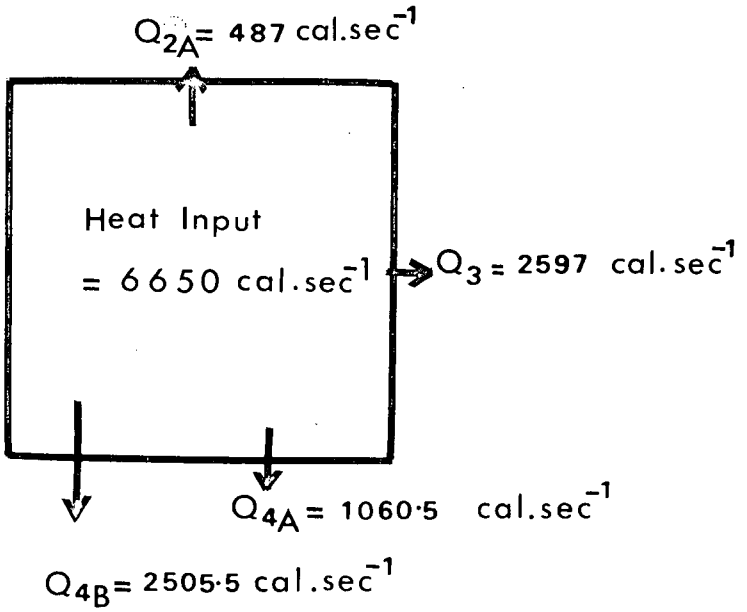

Figure 67. Block diagram for the heat balance of the slag region.

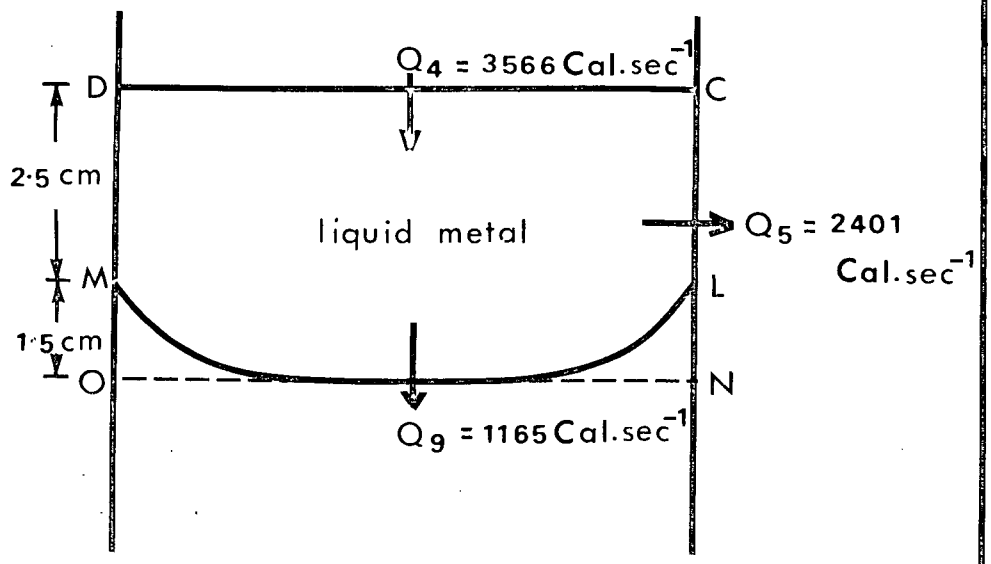

Figure 68. Block diagram for the heat balance of the liquid metal region.

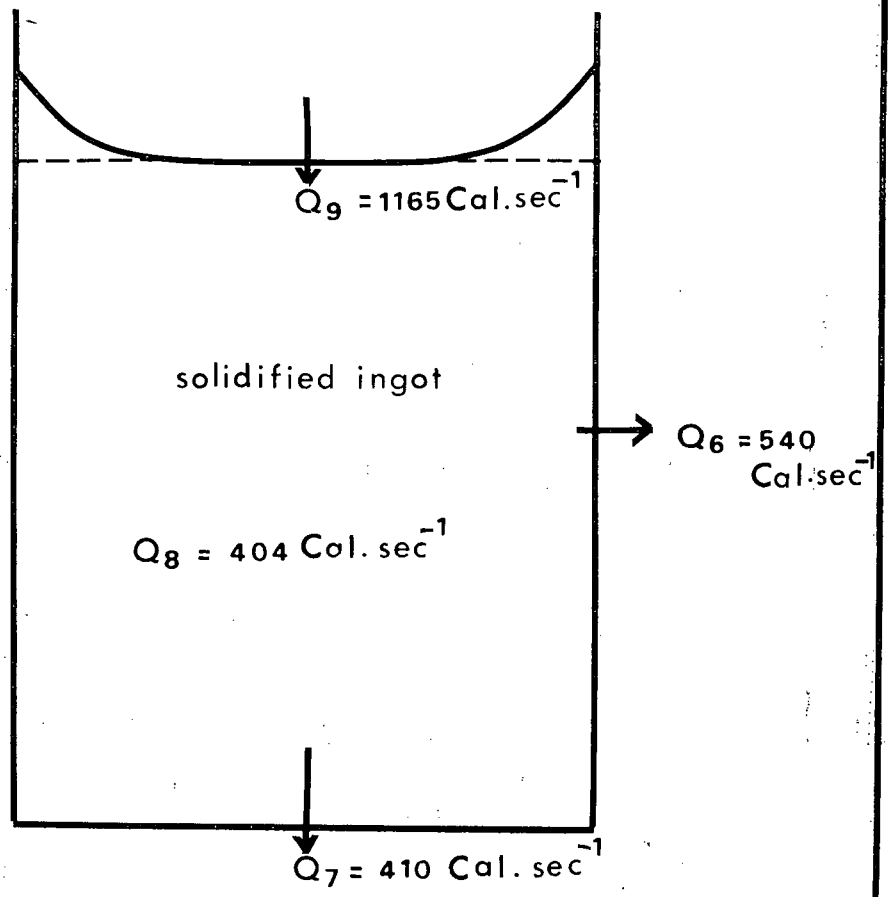

Figure 69. Block diagram for the heat balance of the solidified ingot.

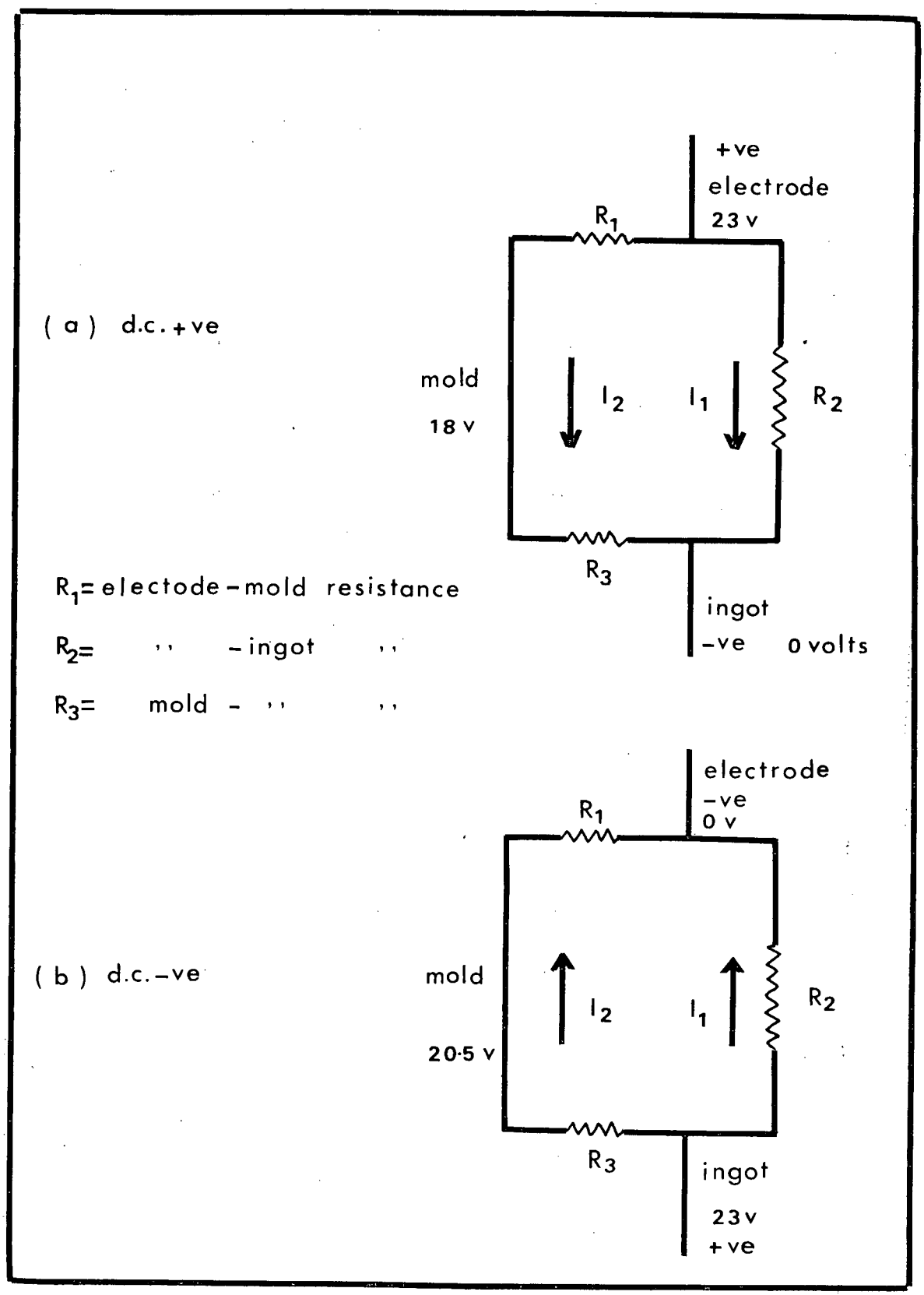

Figure 70. ESR unit's analog circuit.

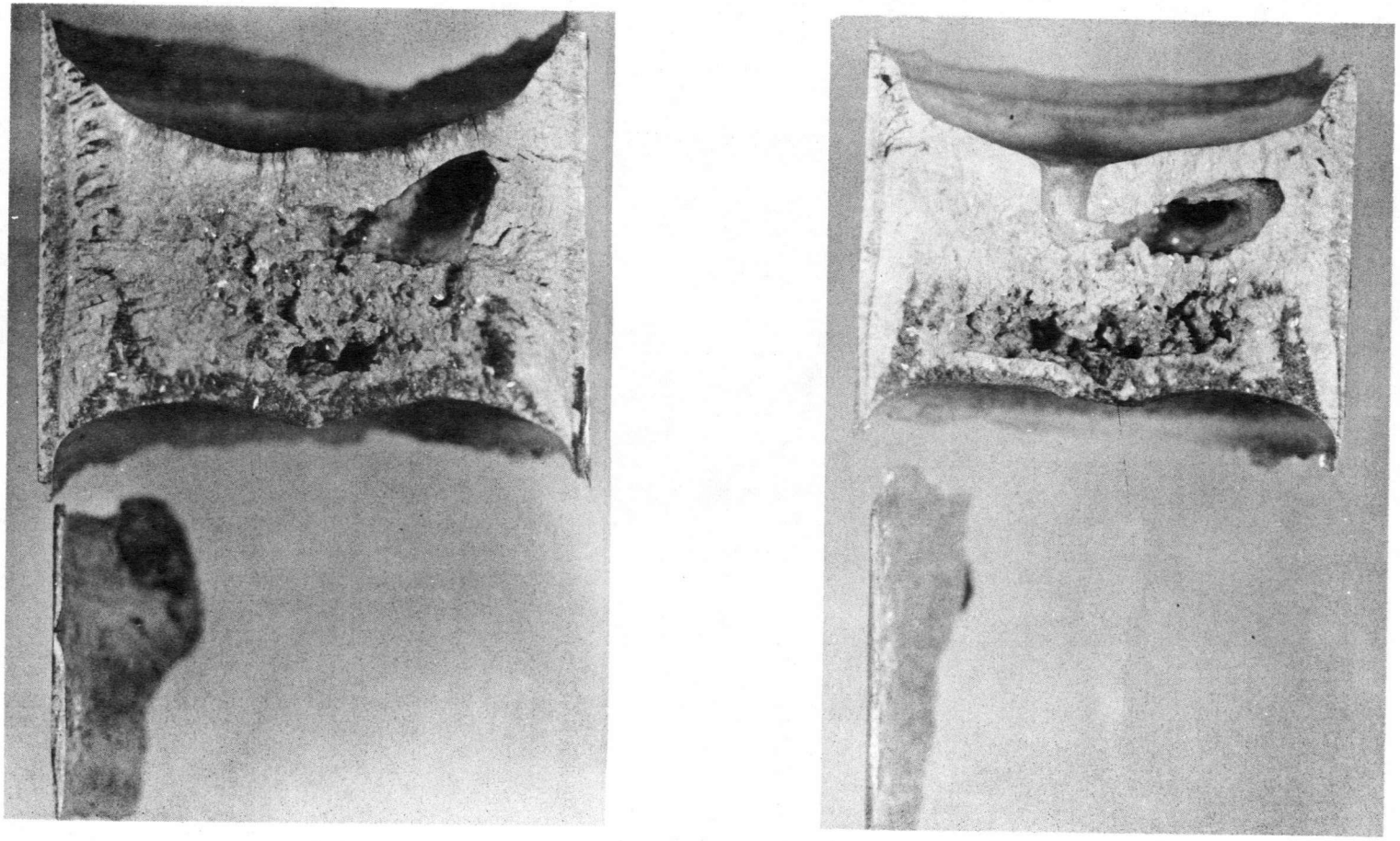

(a) I.N. 27

(b) I.N. 29

Figure 71. Pictures of slag cap and slag skin of some of the ESR melts of FVE

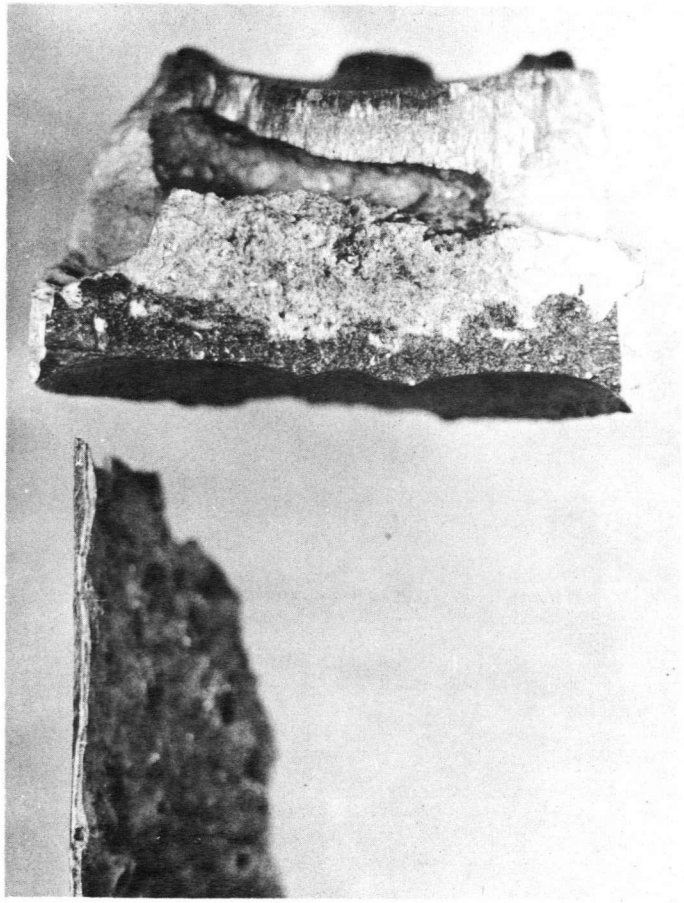

(c) I. N. 25

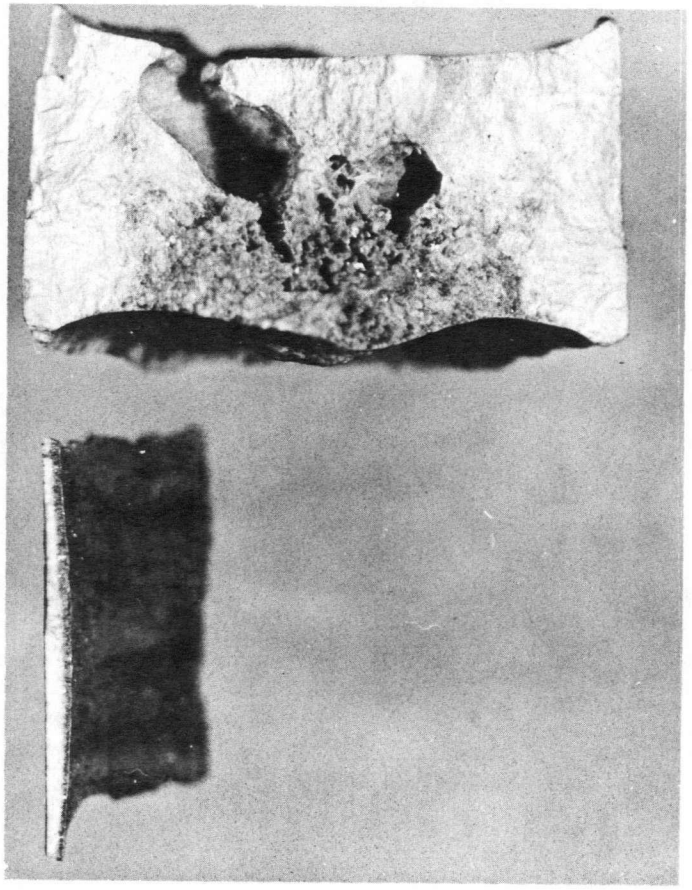

(d) I. N. 26

Figure 71. (Continued) Pictures of slag cap and slag skin of some of the ESR melts of FVE

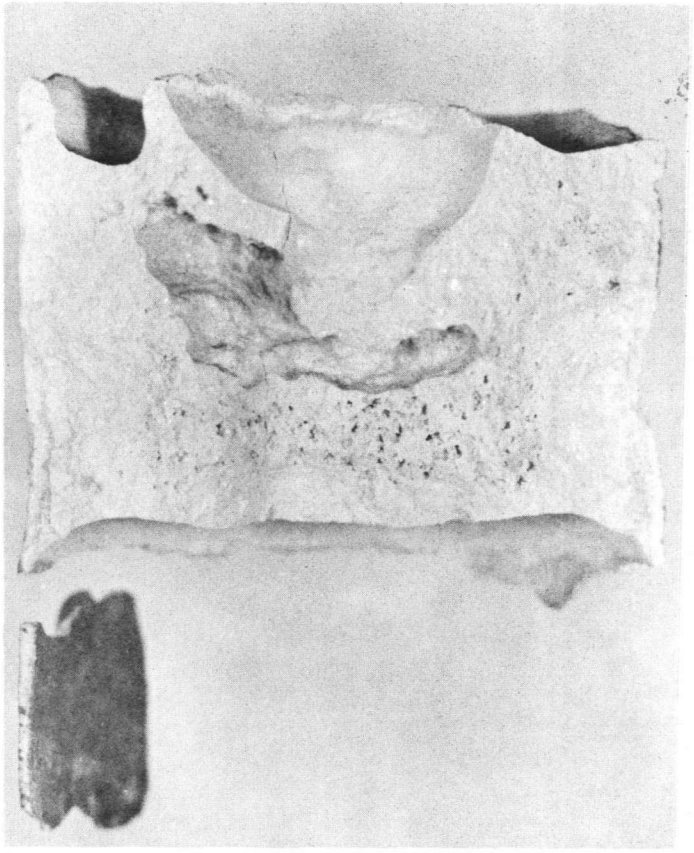

I. N. 6

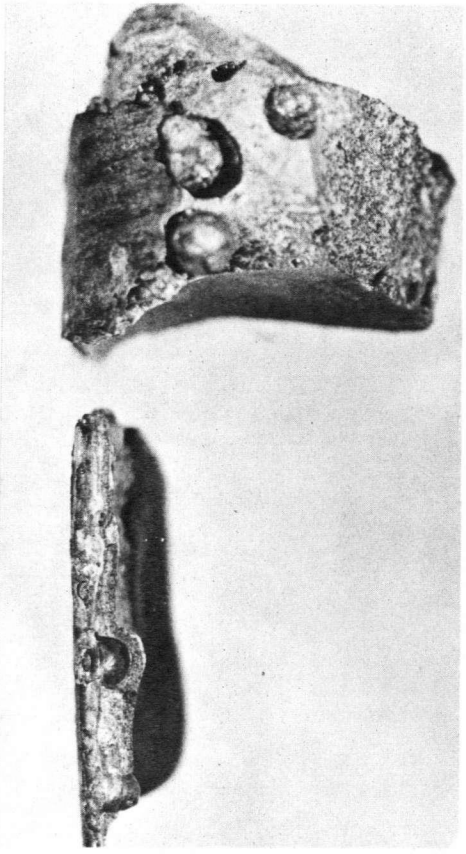

I.N. 13

Figure 72. Pictures of slag cap and slag skin of some of the ESR melts of EN 25 steel.

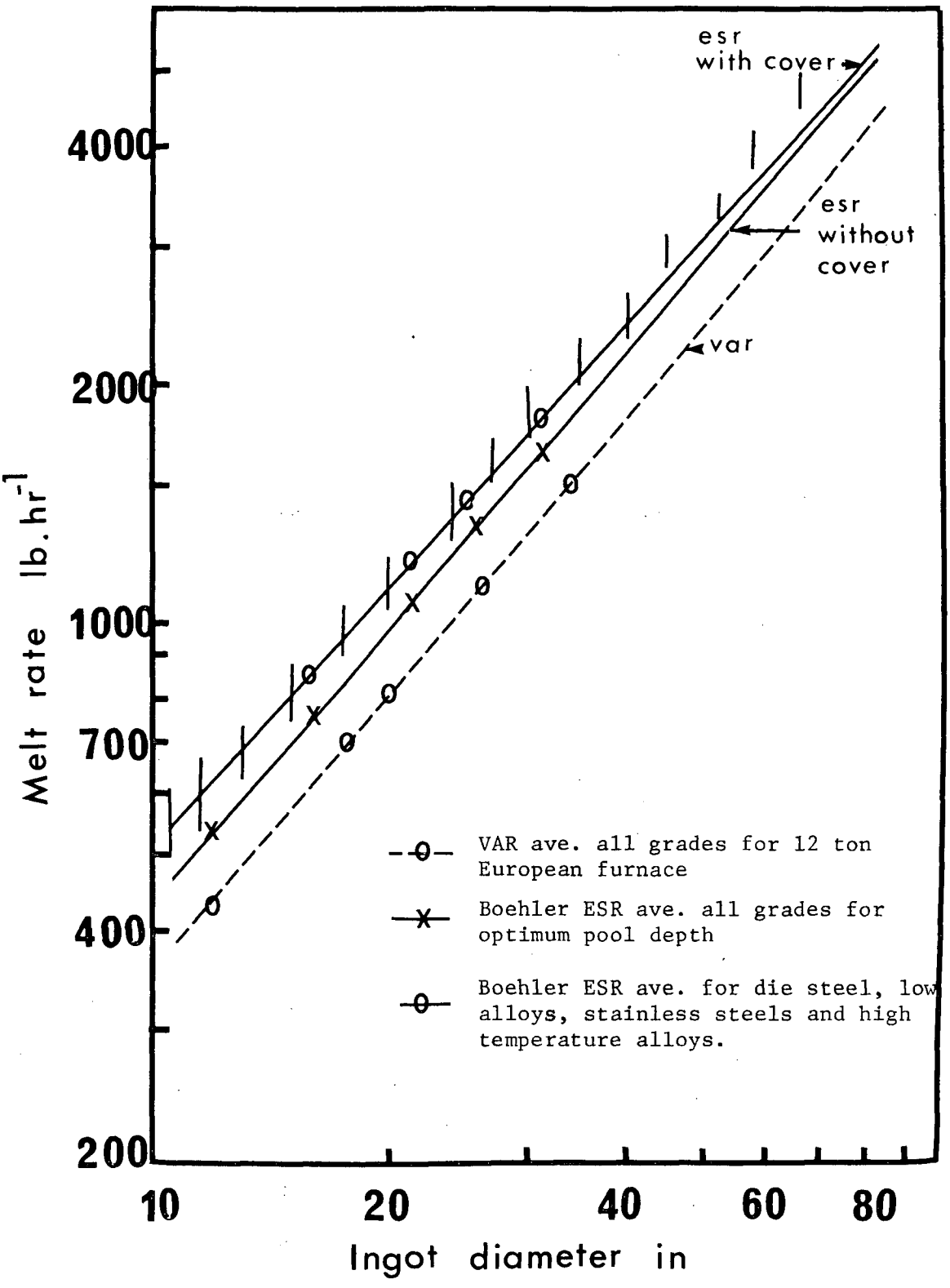

Figure 73. Boehler single phase a.c. ESR melt rate vs. ingot diameter.[6]

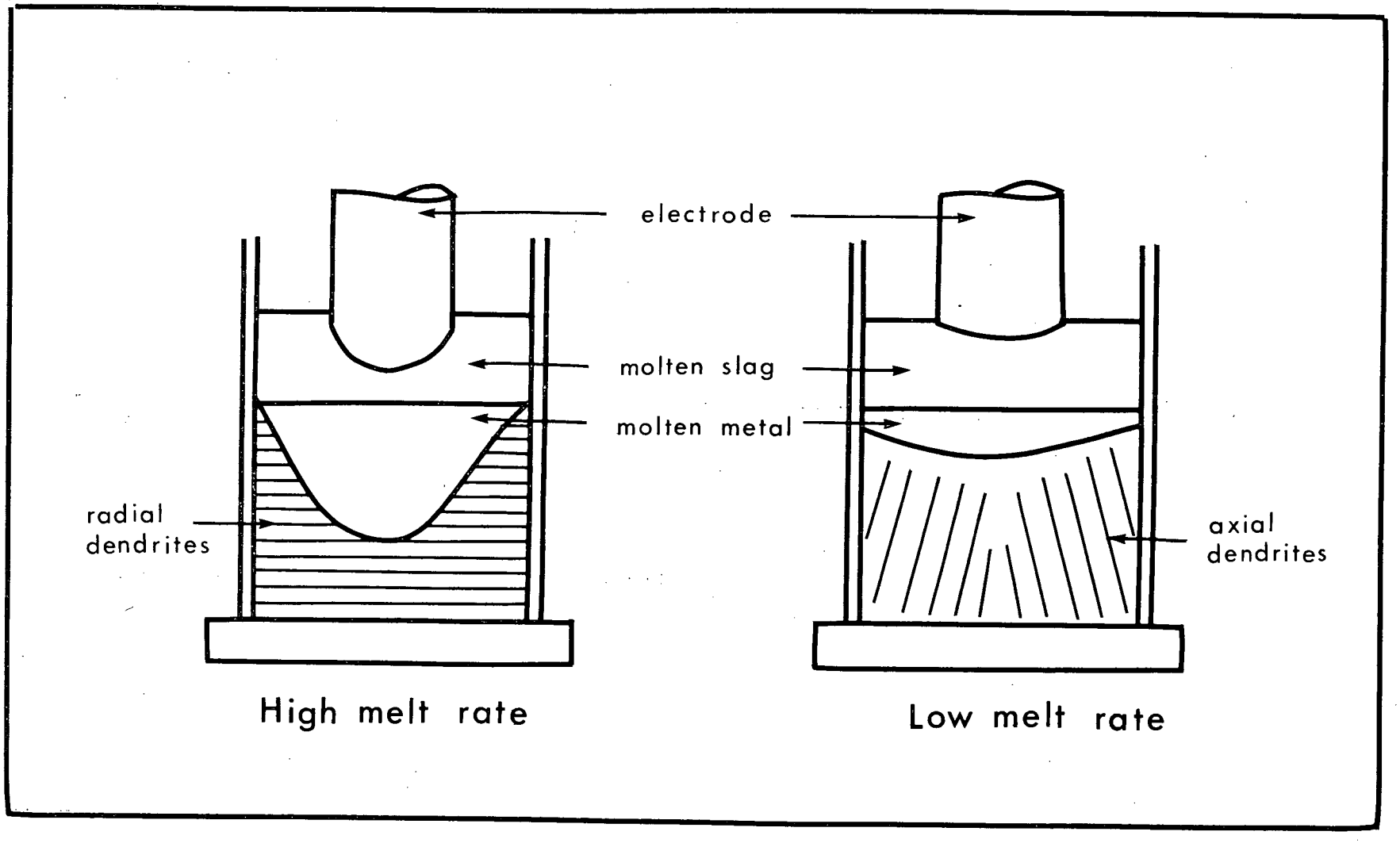

Figure 74. Effect of melt rate on the shape of the liquid metal pool.

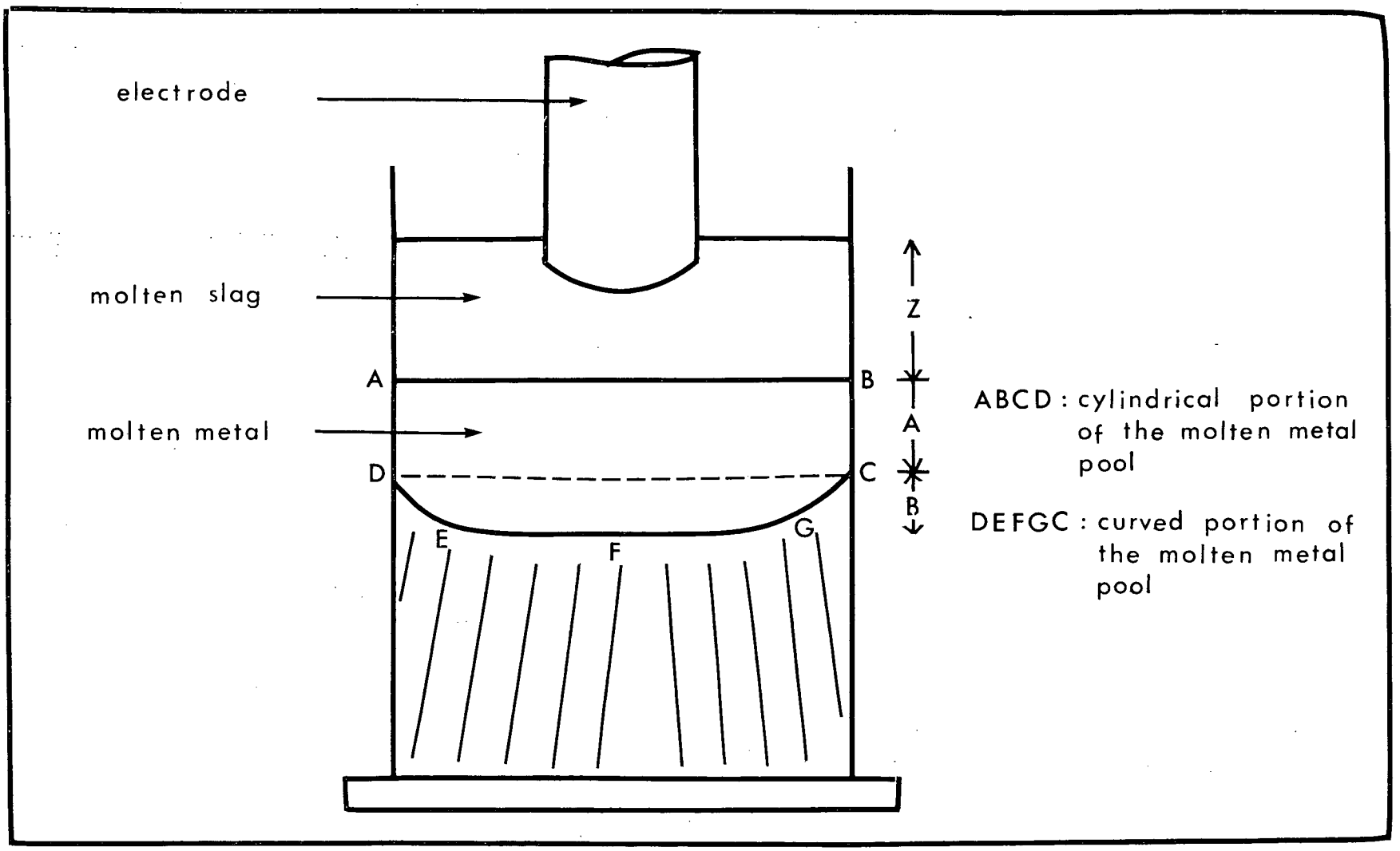

Figure 75. Subdivision of the molten metal pool.

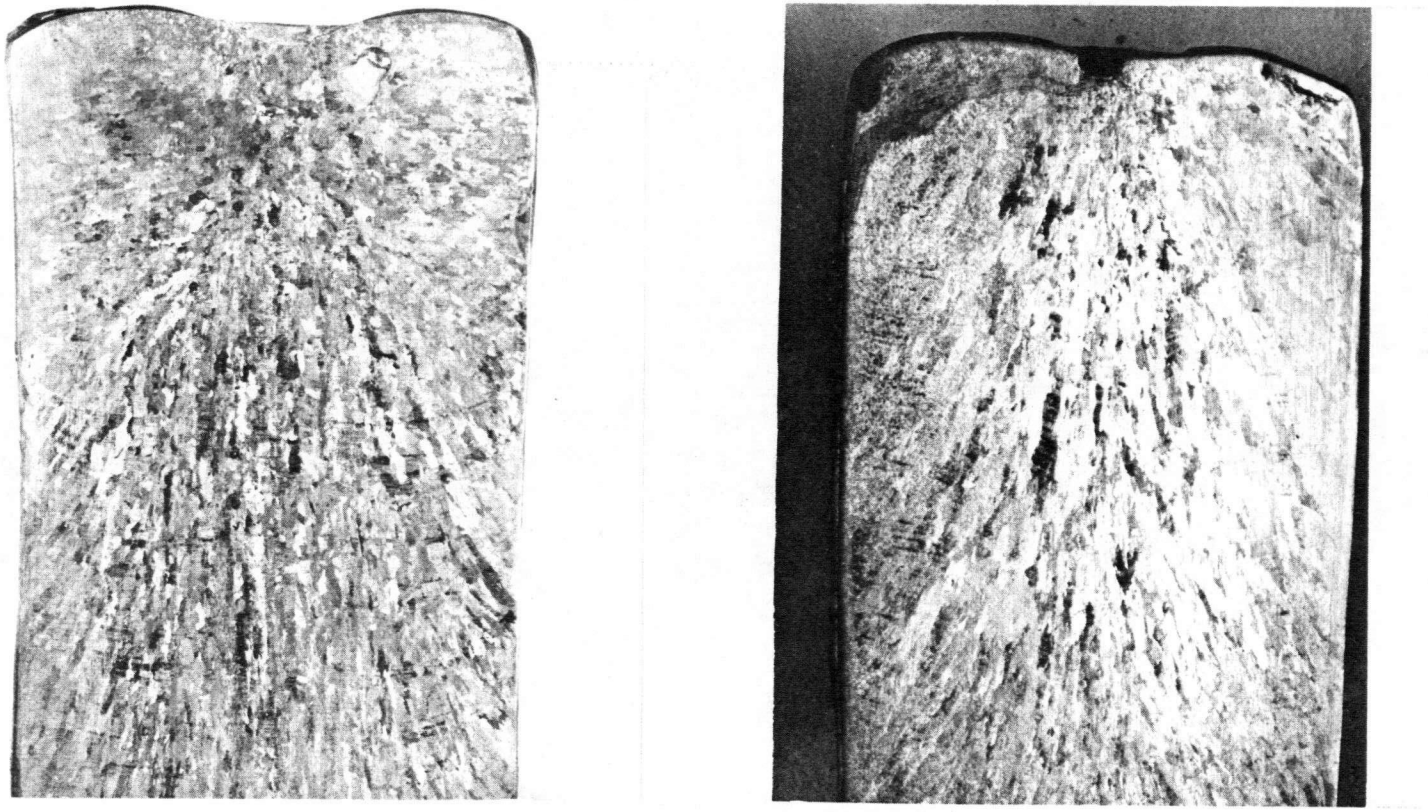

Figure 76. Macrographs of ingot no. (26) and (32).

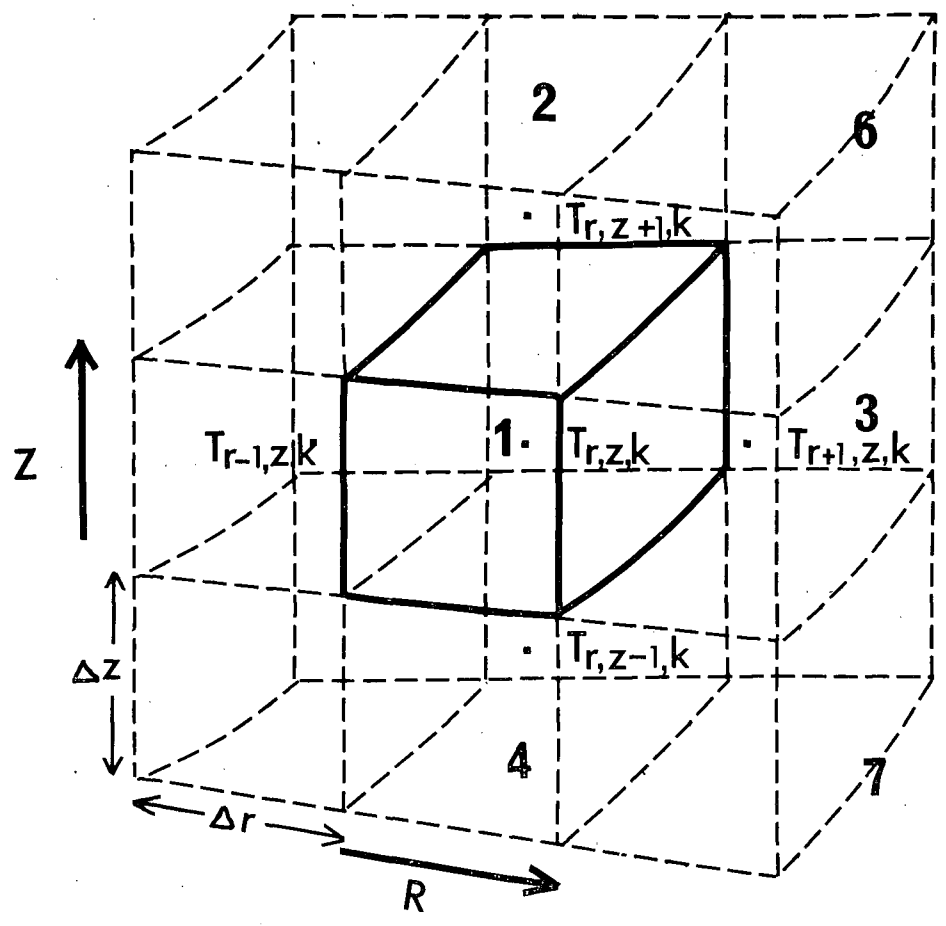

Figure 77. Subdivision of the ingot.

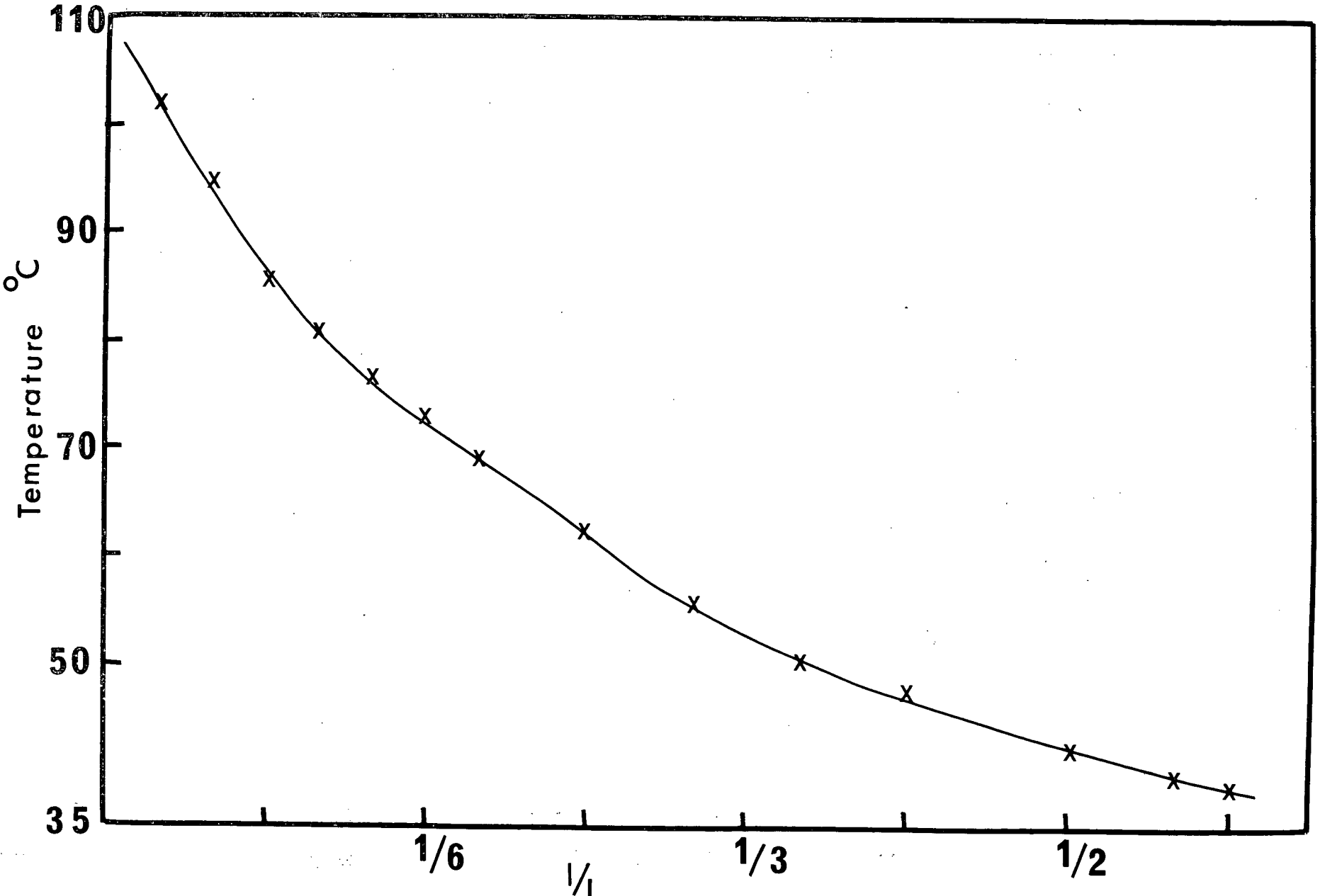

Figure 78. Average temperature distribution on the mold across the solidified ingot.

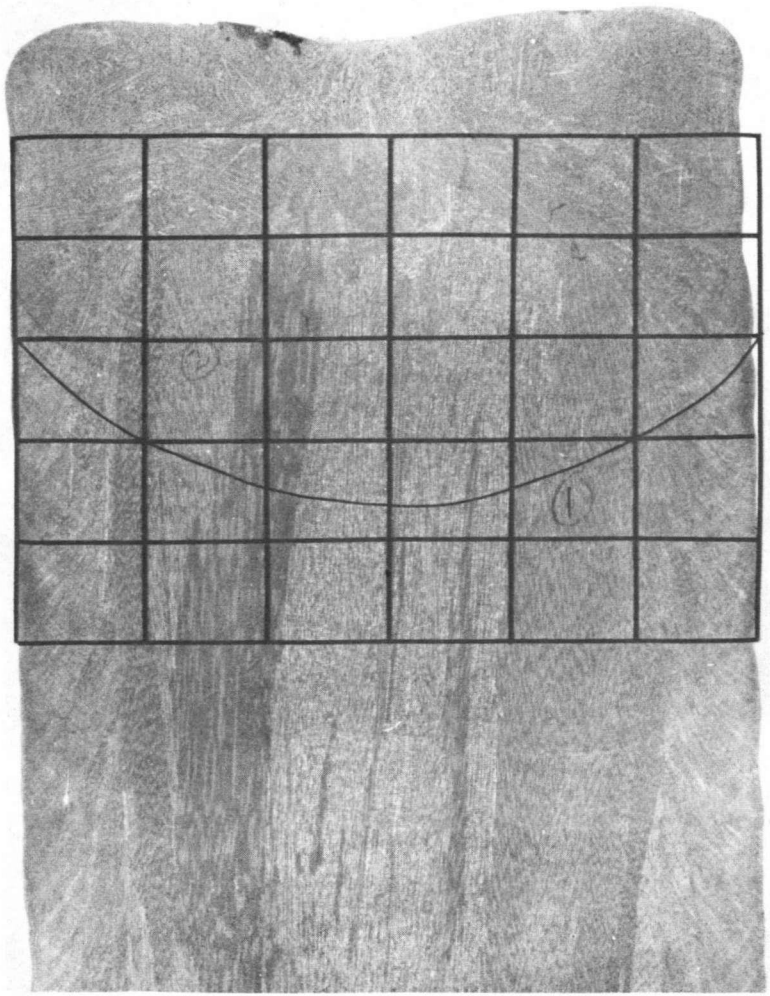

Figure 80. Predicted pool profile for ingot no. (1).

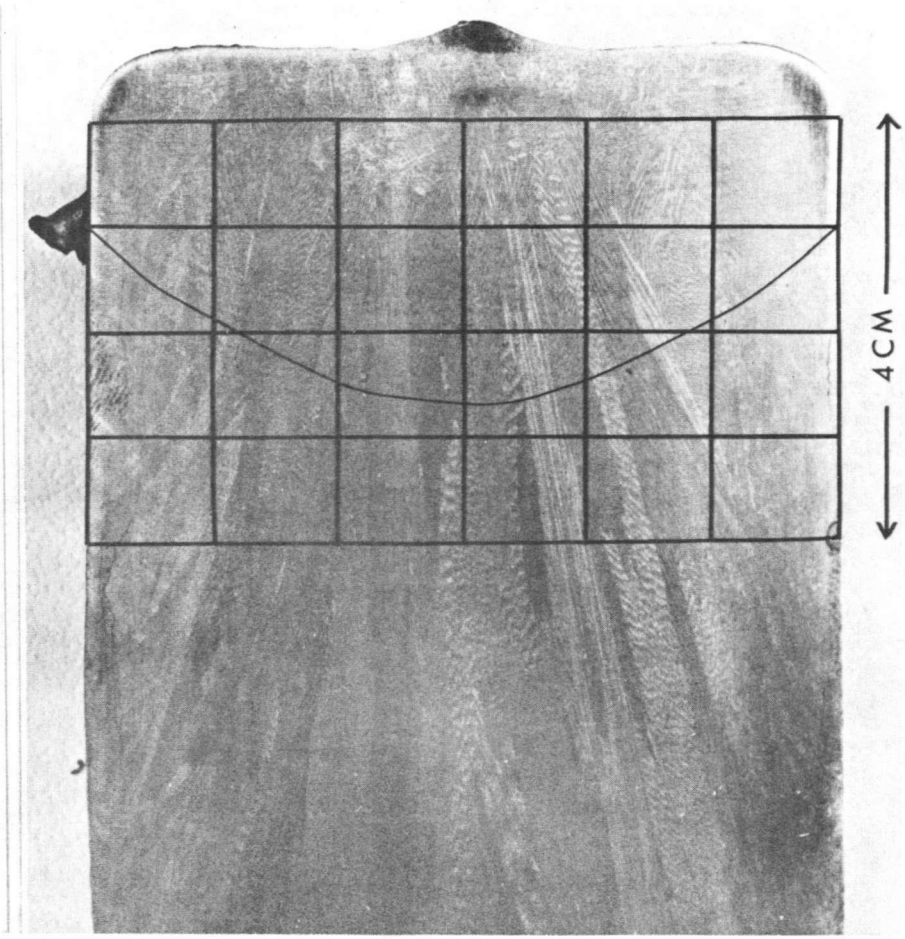

Figure 81. Predicted pool profile for ingot no. (10).

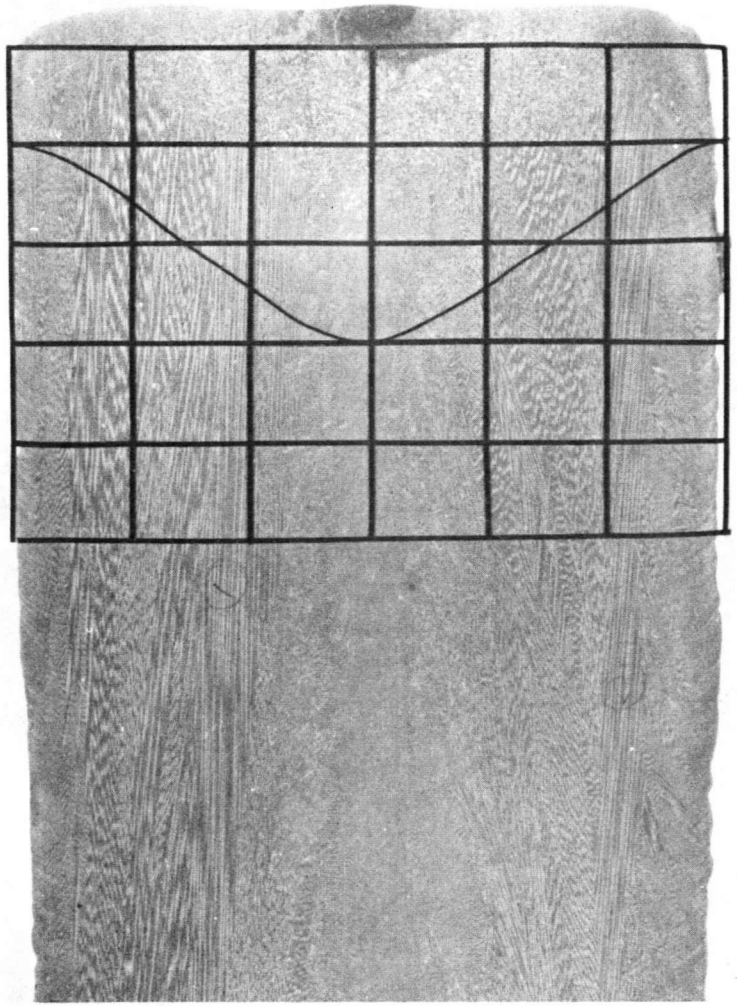

Figure 82. Predicted pool profile for ingot no. (16).

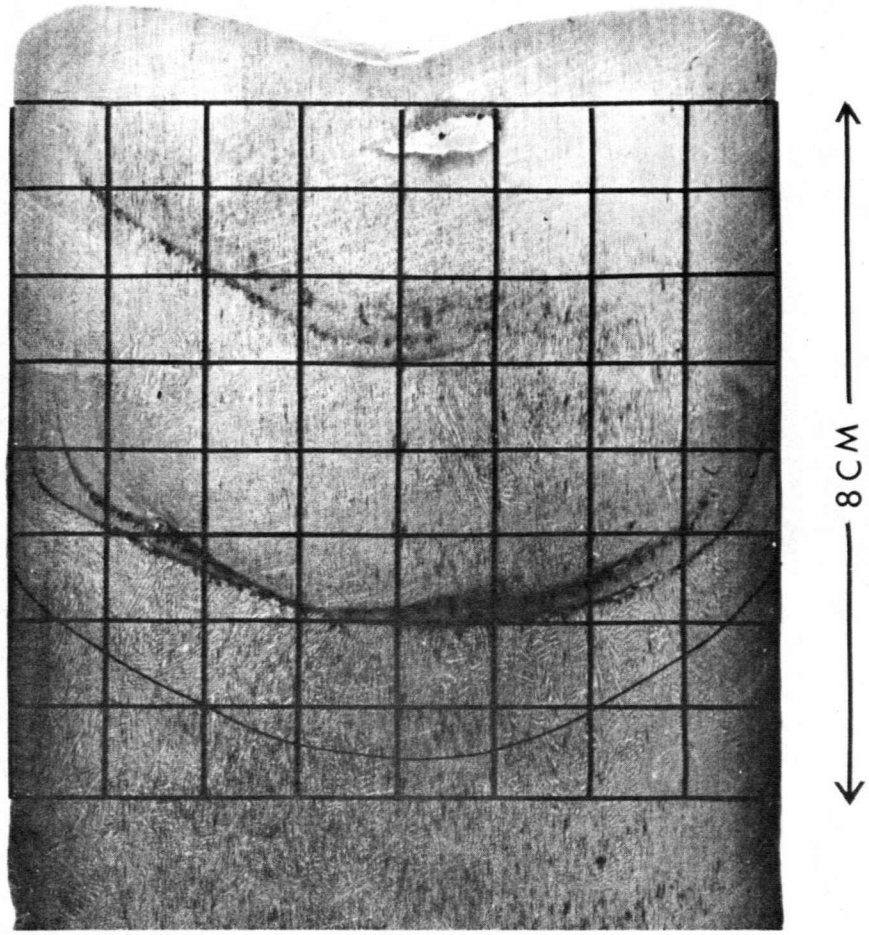

Figure 83. Predicted pool profile for ingot no. (21).

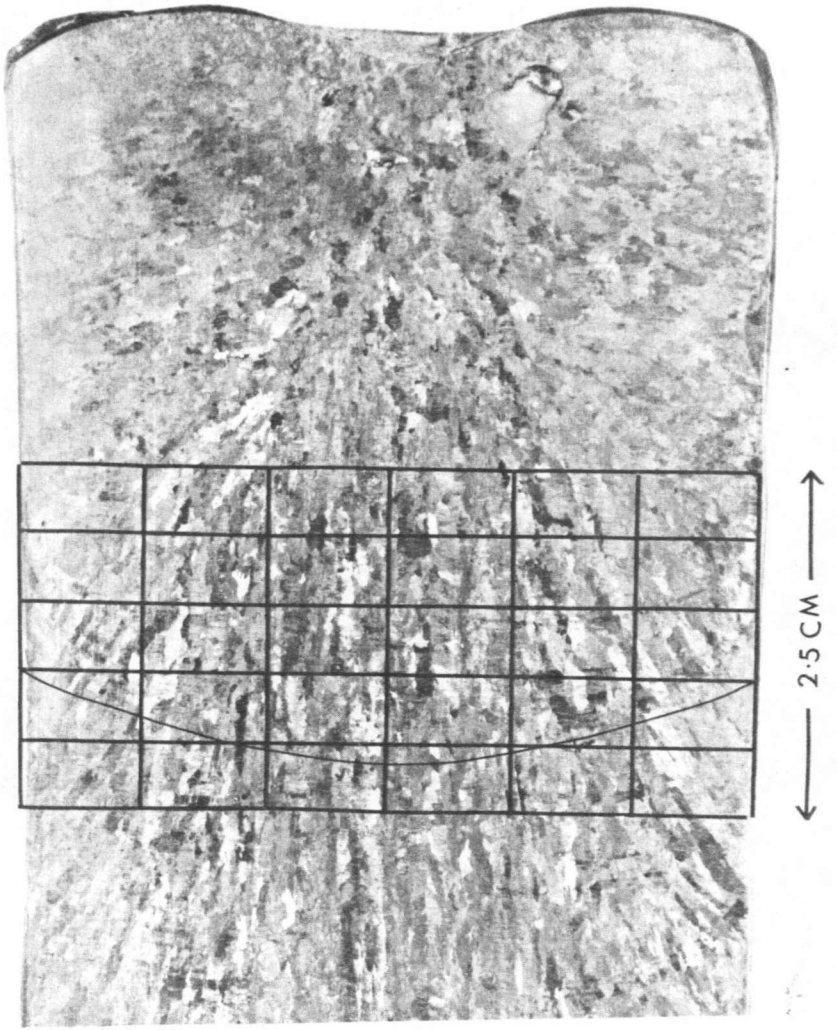

Figure 84. Predicted pool profile for ingot no. (26).

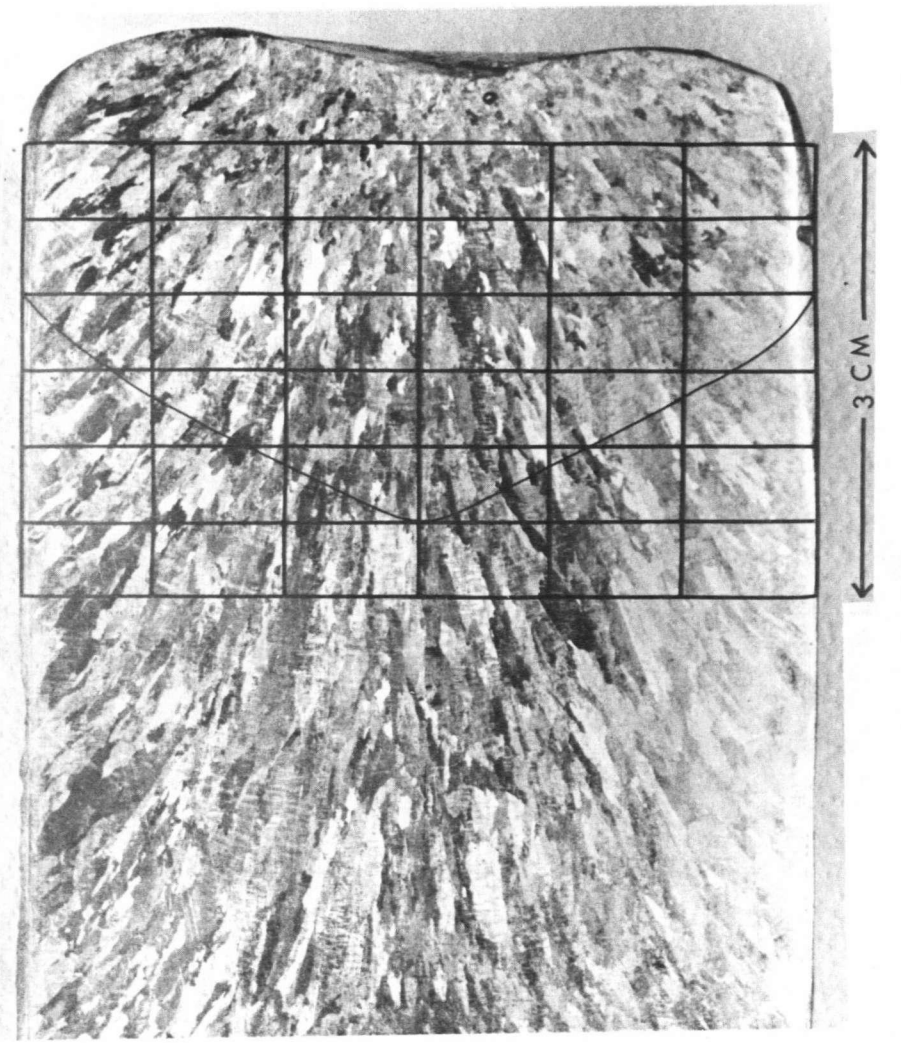

Figure 85. Predicted pool profile for ingot no. (28).

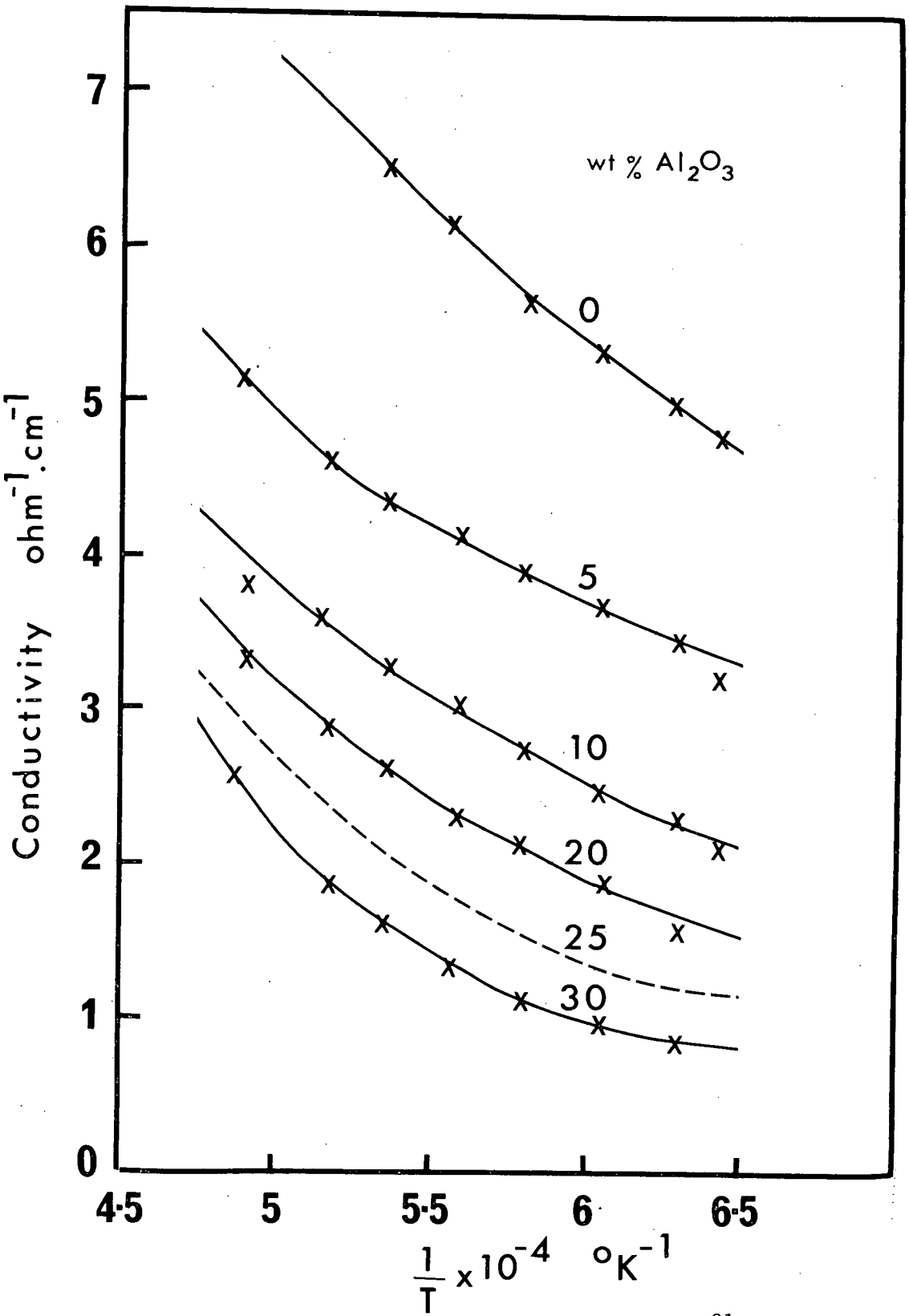

Figure 86. Electrical conductivity of CaF_2-Al_2O_3 slags.[21]

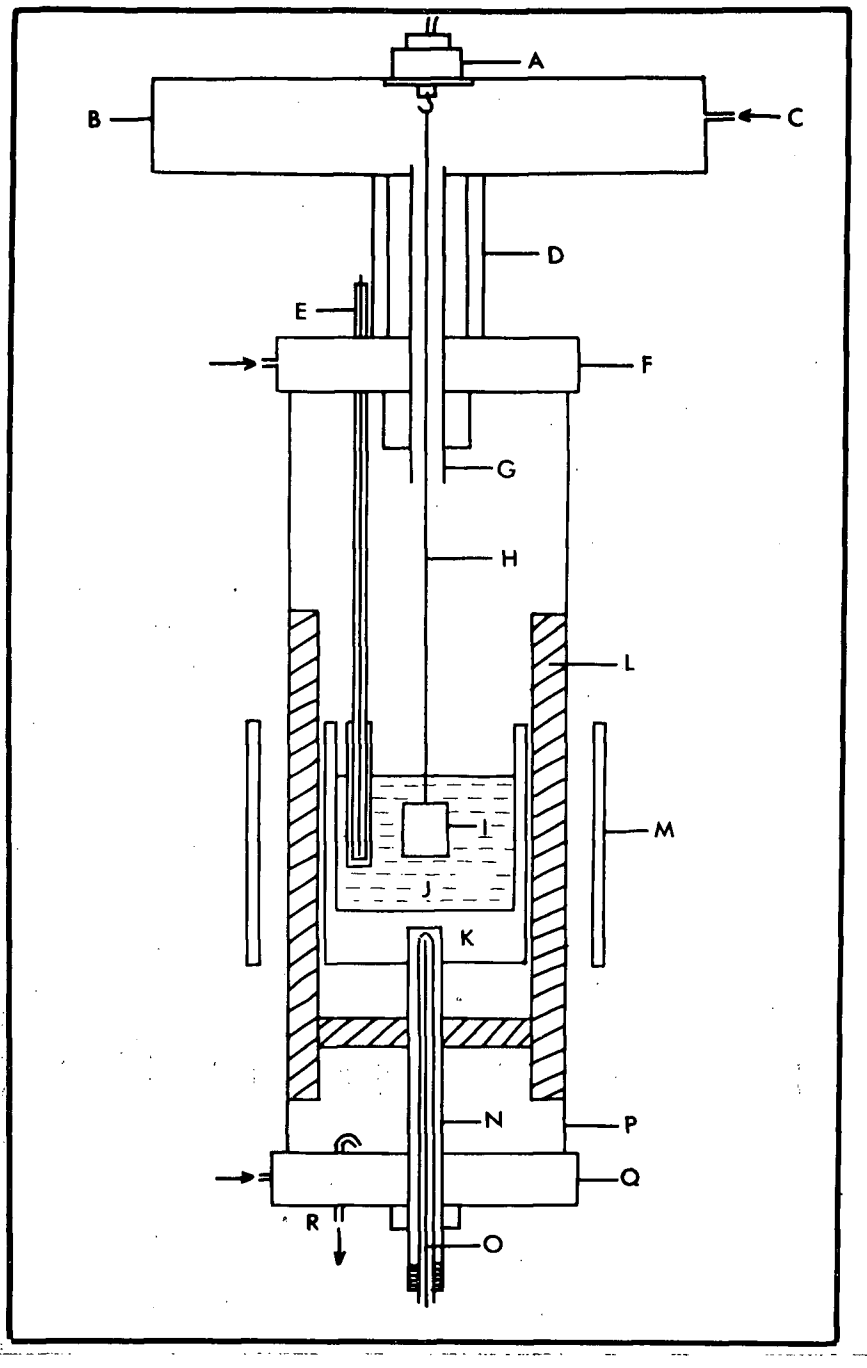

Figure 87. A schematic diagram of the apparatus of the measurement of density of CaF_2 based slags.

(A) transducer, (B) lucite box, (C) argon gas inlet, (D) stainless steel support, (E) thermocouple, (F) water cooled stainless steel lid, (G) Al_2O_3 tube, (H) 0.025 cm diameter tungsten wire, (I) molybdenum bob, (J) liquid slag, (K) molybdenum lined graphite crucible, (L) graphite felt, (M) induction coil, (N) Al_2O_3 tube to support the crucible, (O) thermocouple connected to induction f/c controller, (P) vycor glass tube, (Q) water cooled stainless steel base, (R) argon gas exit.

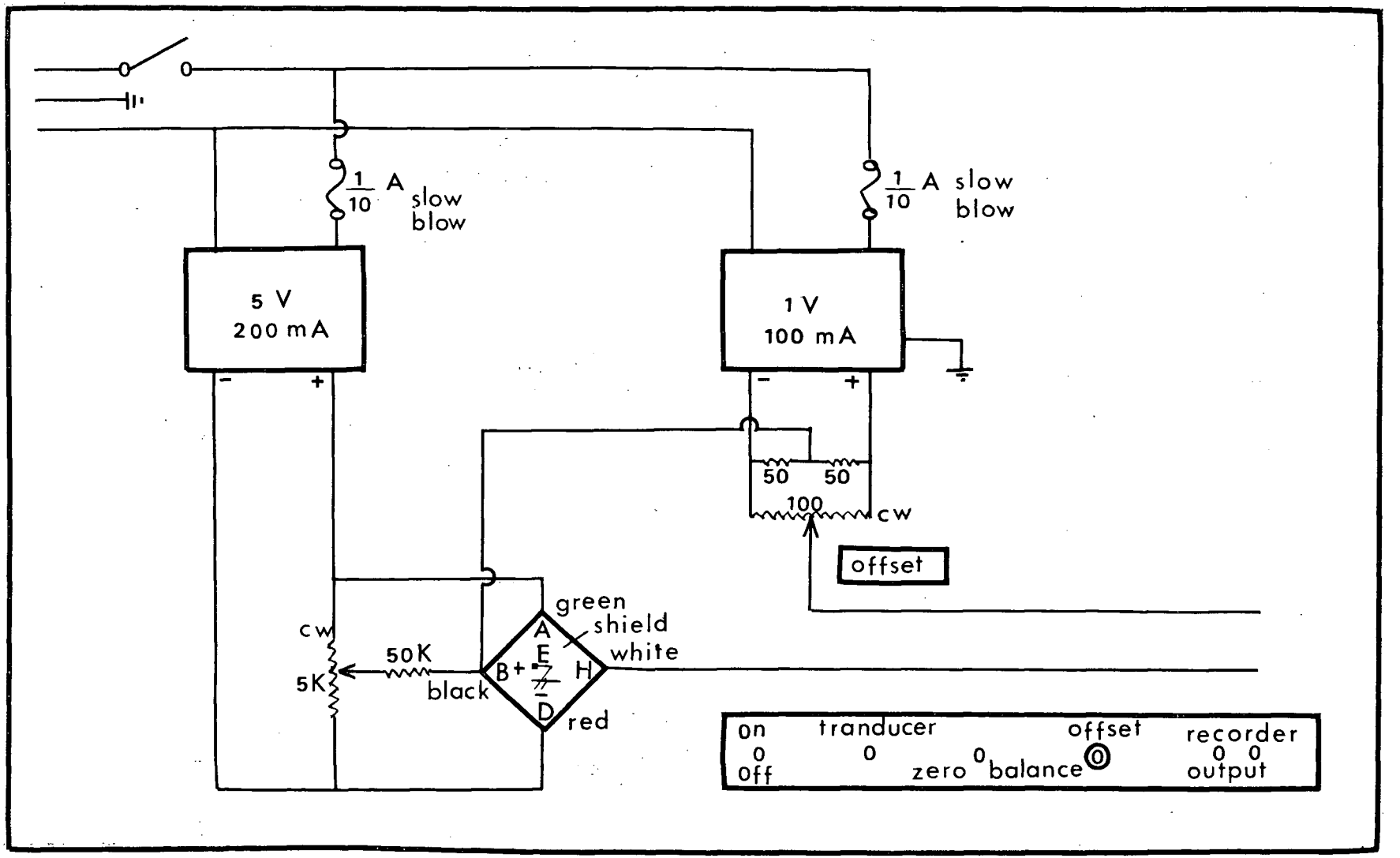

Figure 88. External circuitry required to operate the transducer.

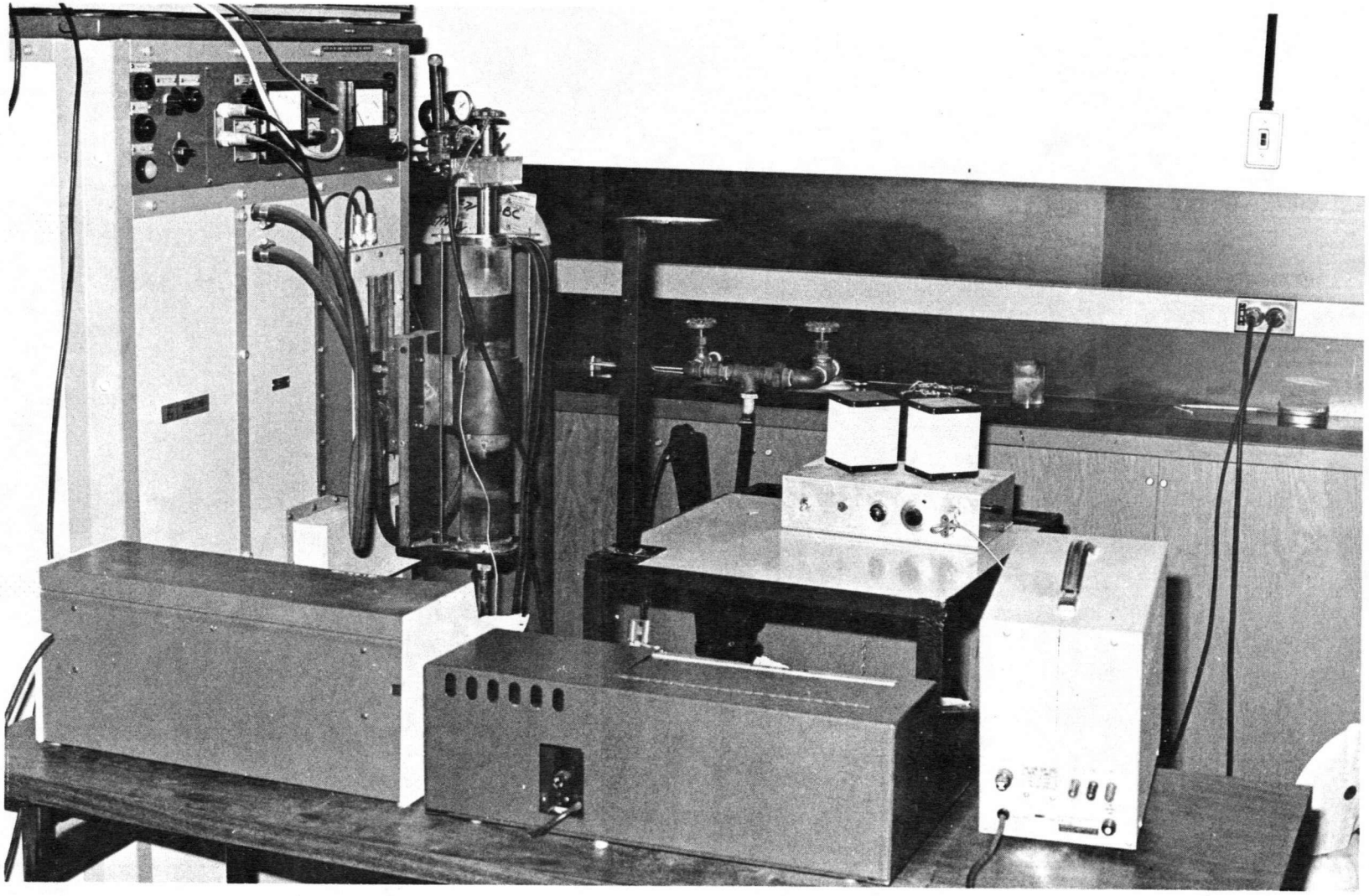

Figure 89. The density measurement apparatus.

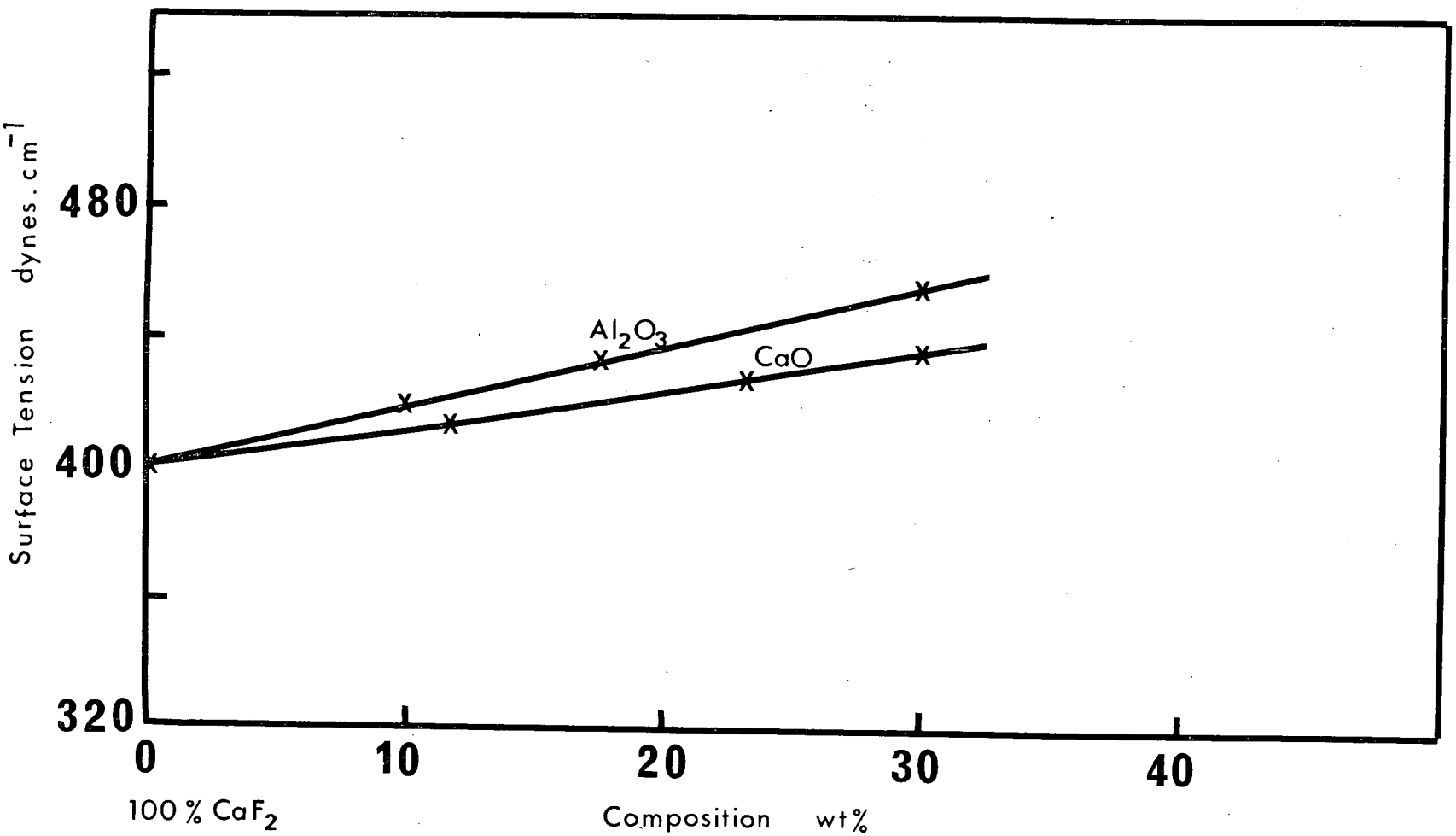

Figure 90. Effects of oxides on the surface tension of CaF_2.[70,71]

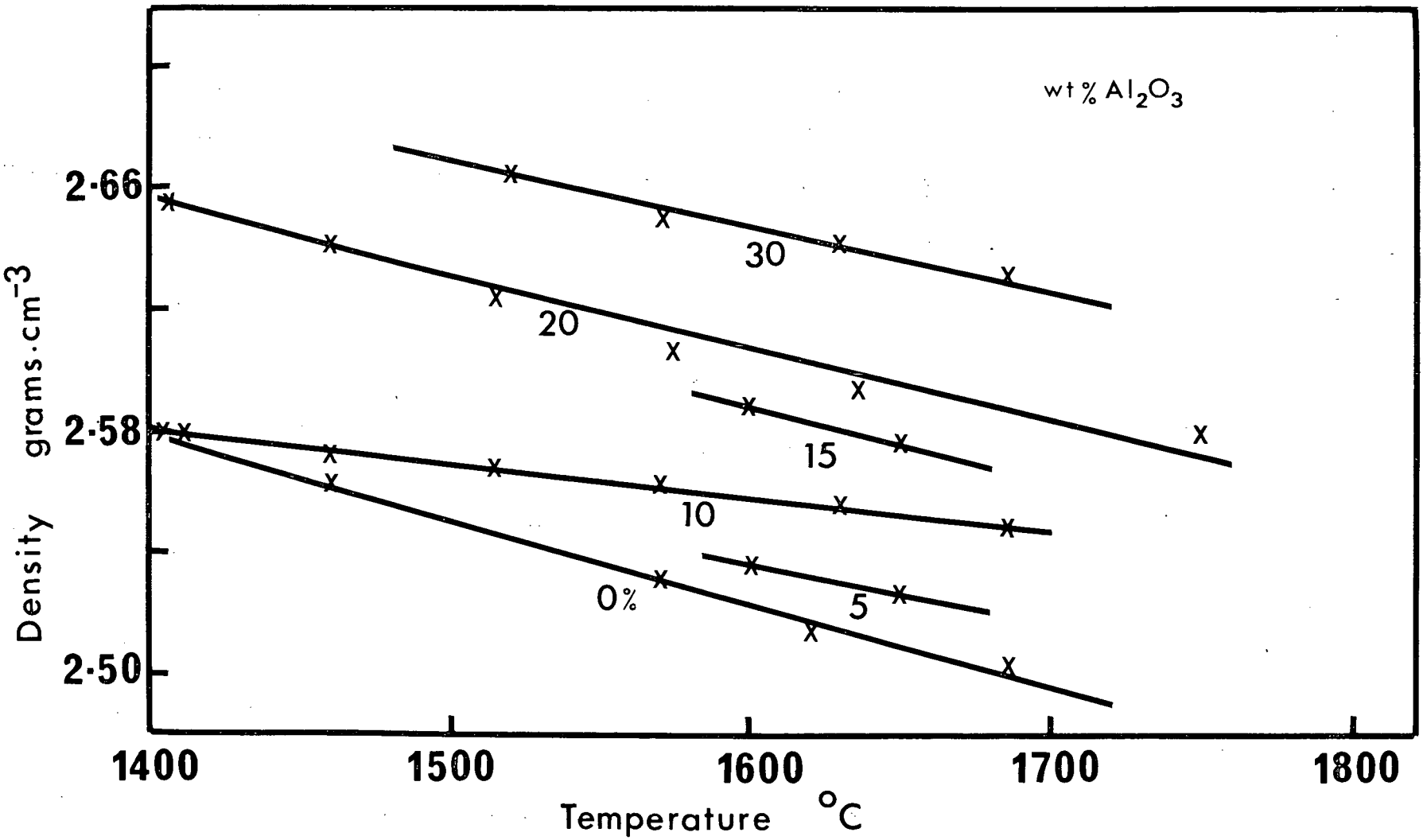

Figure 91. Density vs. temperature for CaF_2-Al_2O_3 system.

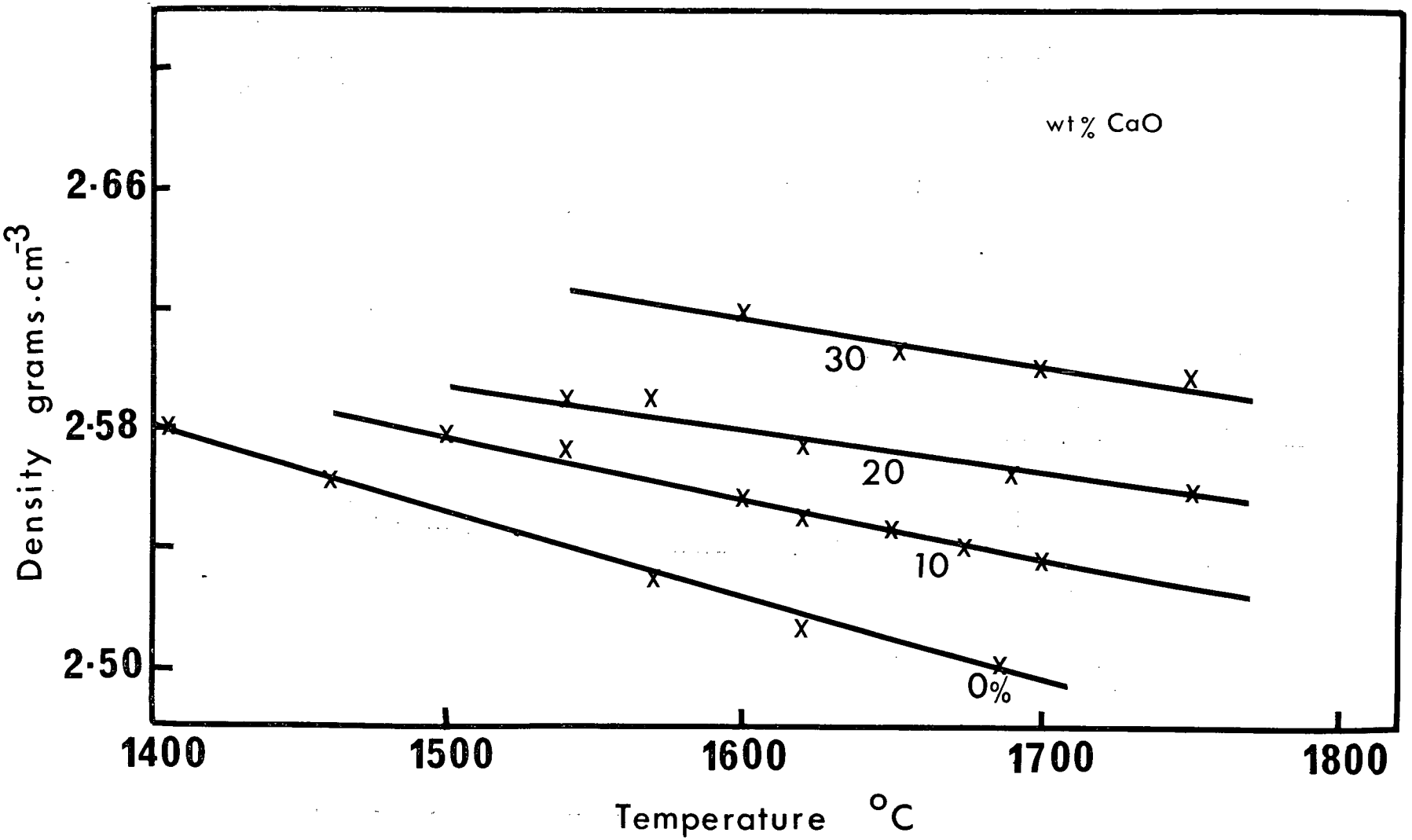

Figure 92. Density vs. temperature for CaF_2-CaO system.

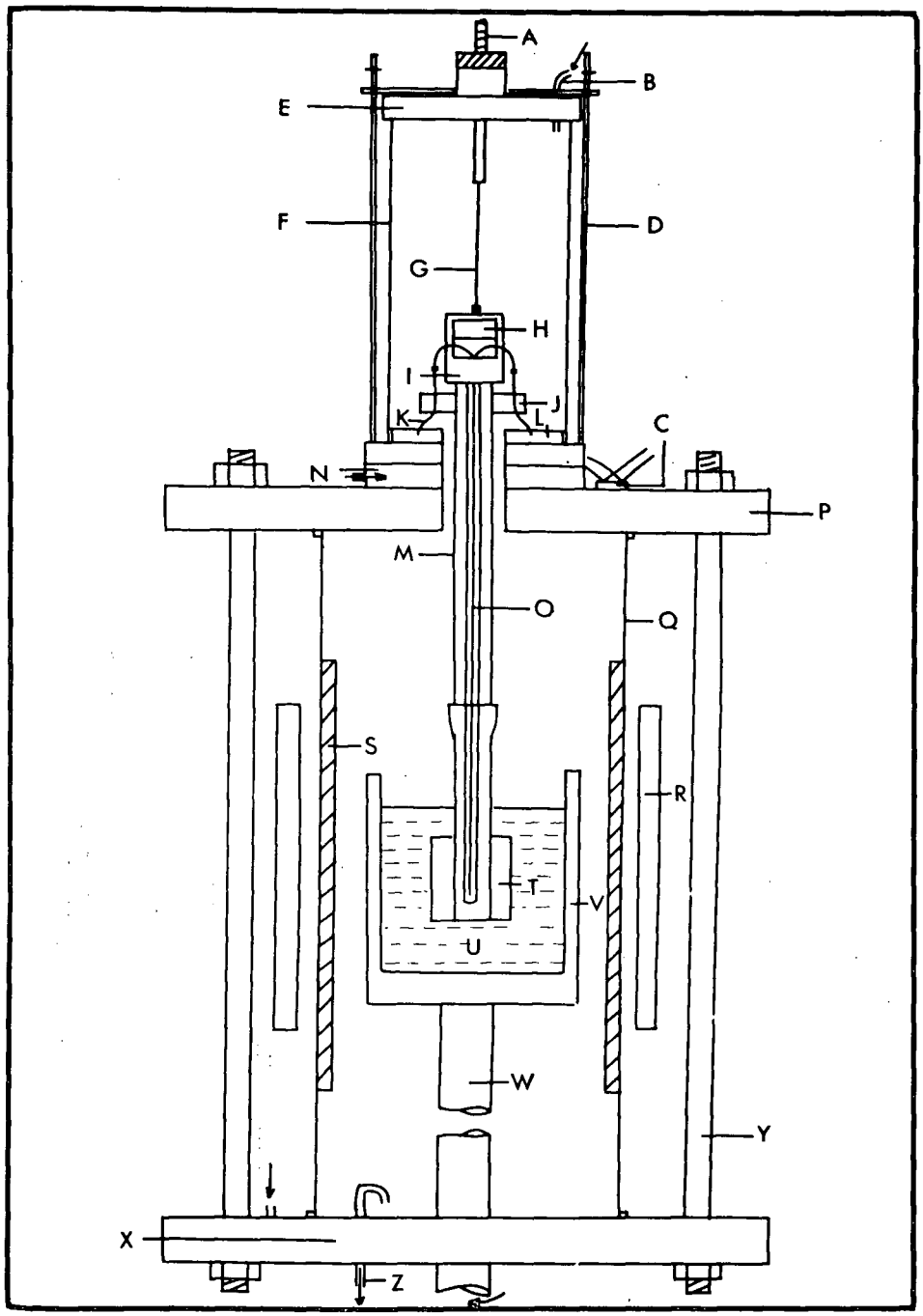

Figure 93. A schematic diagram of the apparatus for the measurement of viscosity of CaF_2 based slags.

(A) graduated stem, (B) argon gas inlet, (C) thermocouple junction,(D) steel frame support, (E) brass lid, (F) vycor glass tube, (G) suspension wire (5 thou W), (H) mirror, (I) stainless steel frame, (J) brass ring to support thermocouple leads, (K) molybdenum thermocouple leads, (L) mercury pool, (M) alumina tube, (N) water cooled base, (O) thermocouple (W-W-26% Re), (P) steel lid for the glass tube Q, (Q) vycor glass tube, (R) water cooled copper induction coil, (S) graphite wool, (T) inner molybdenum cylinder, (U) liquid slag, (V) outer molybdenum lined graphite cylindrical crucible, (W) shaft connected to the motor, (X) water cooled base, (Y) steel frame to support the lid P, (Z) argon gas outlet.

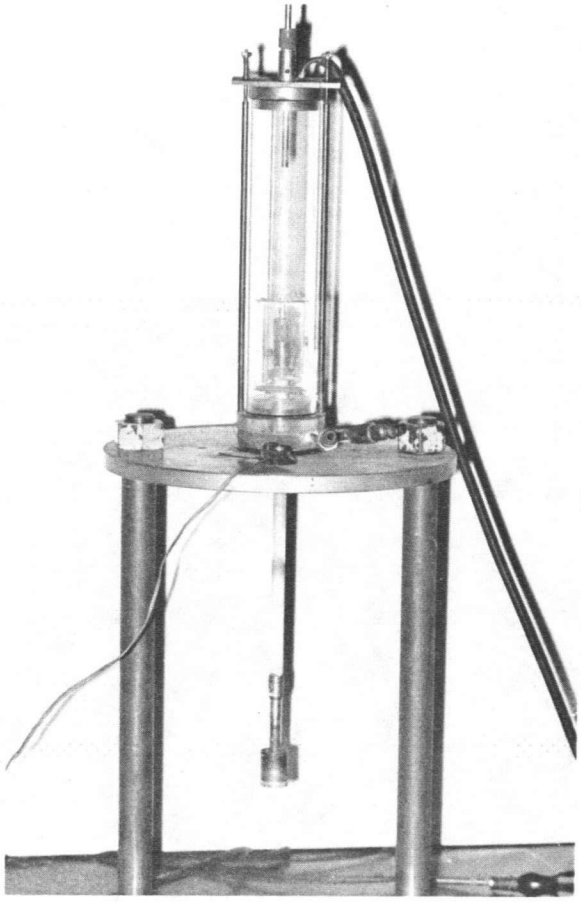

Figure 94. A closeup view of the viscosity measurement apparatus.

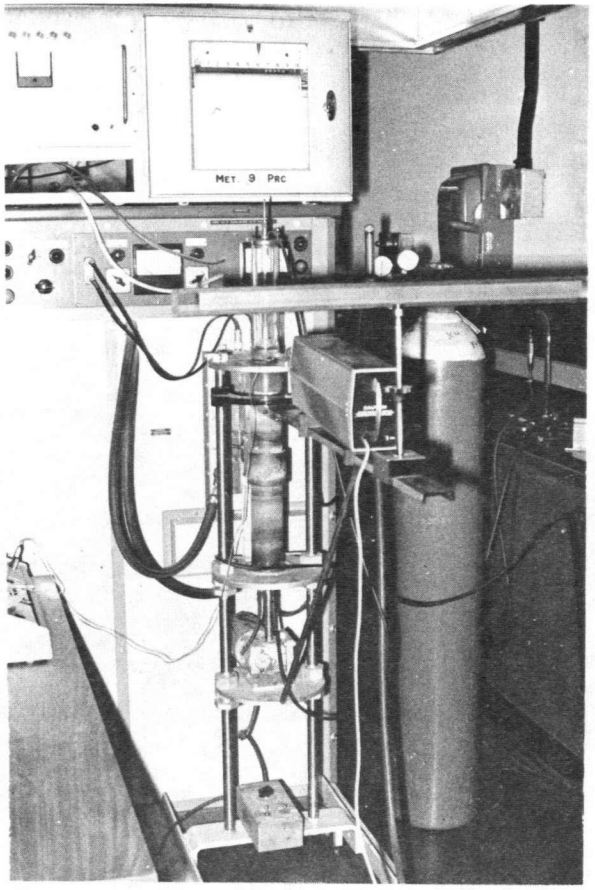

Figure 95. The viscosity measurement apparatus.

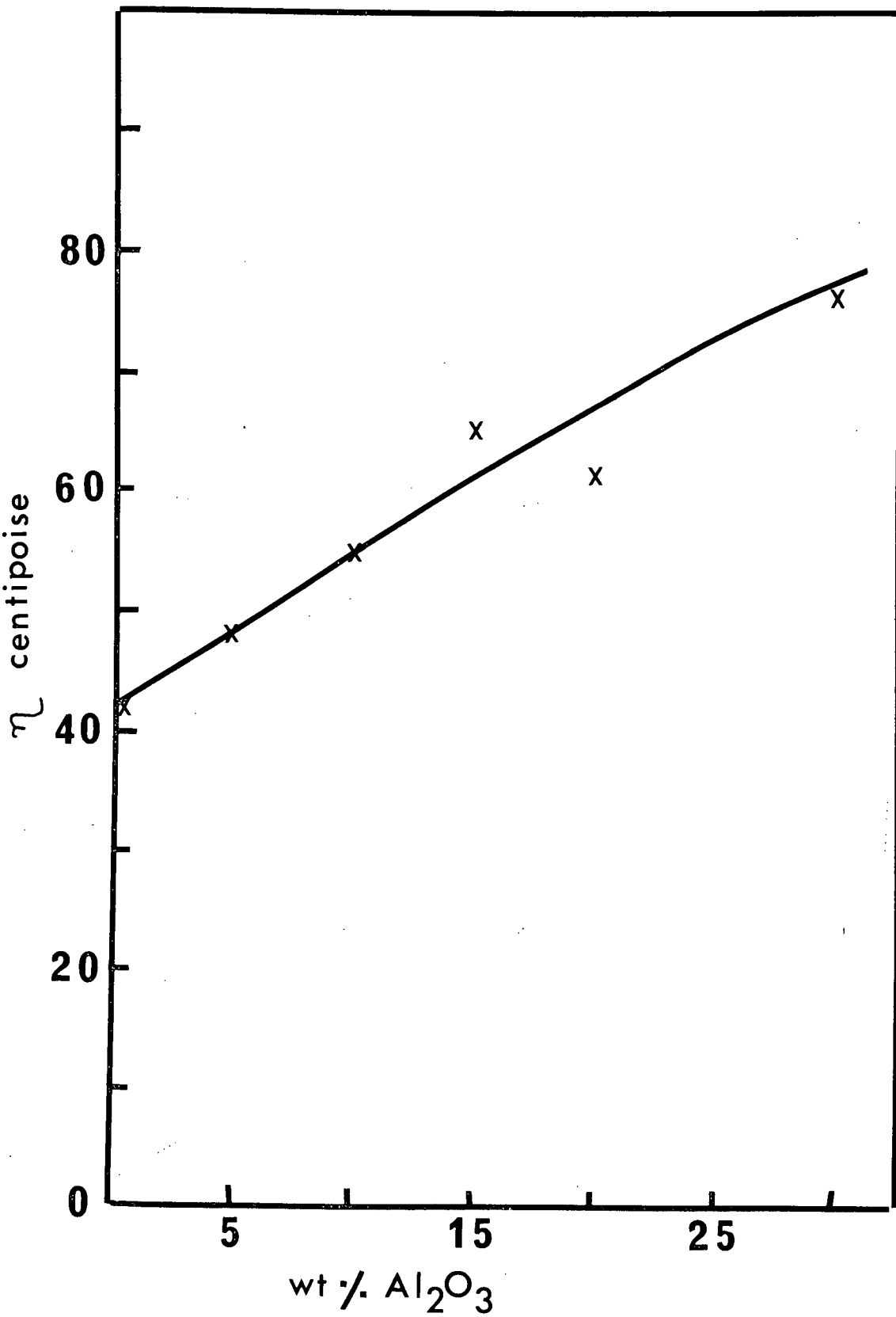

Figure 96. Variation of coefficient of viscosity with % Al_2O_3 at 1600°C.

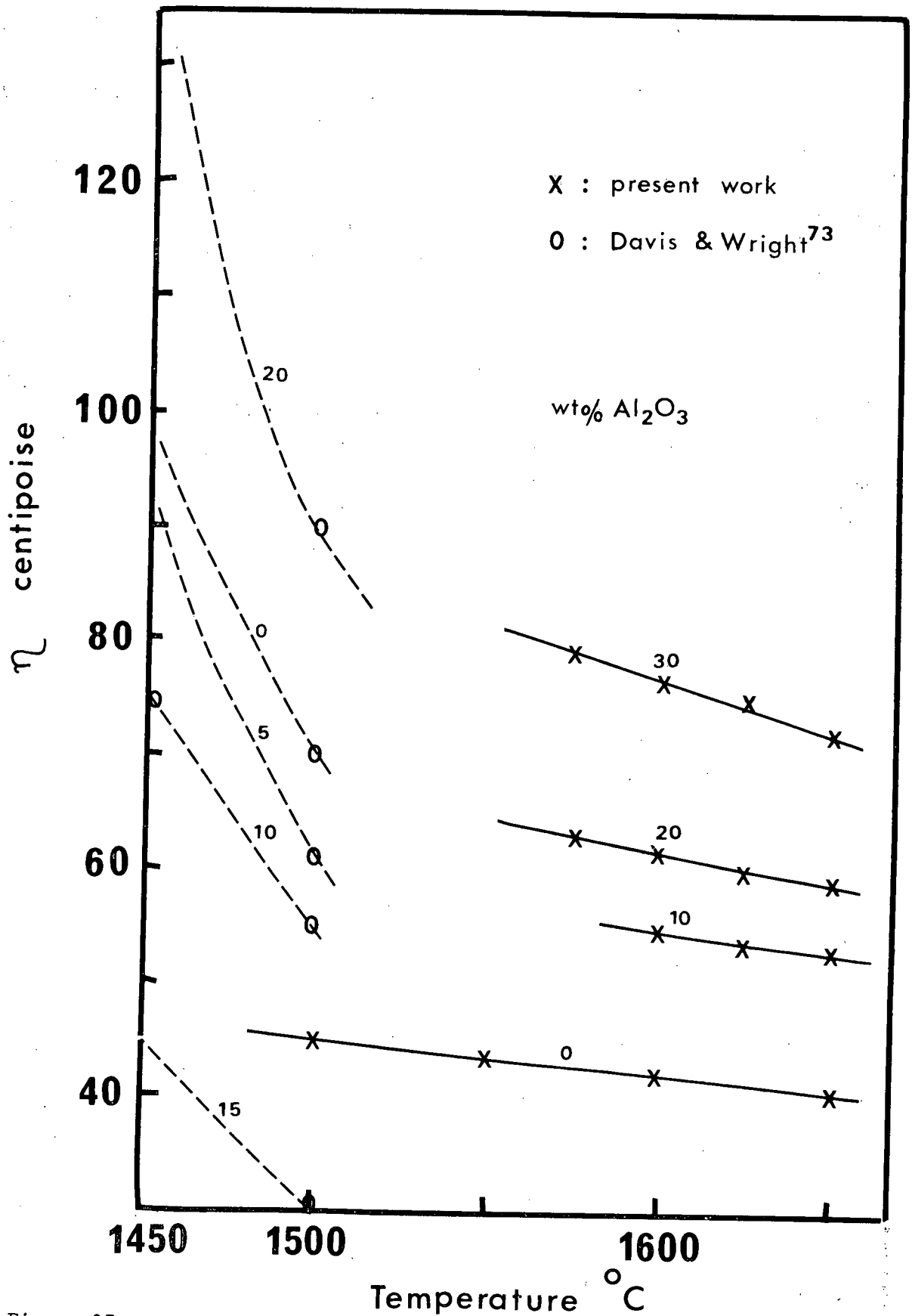

Figure 97. Variation of coefficient of viscosity with temperature for CaF_2-Al_2O_3 system.

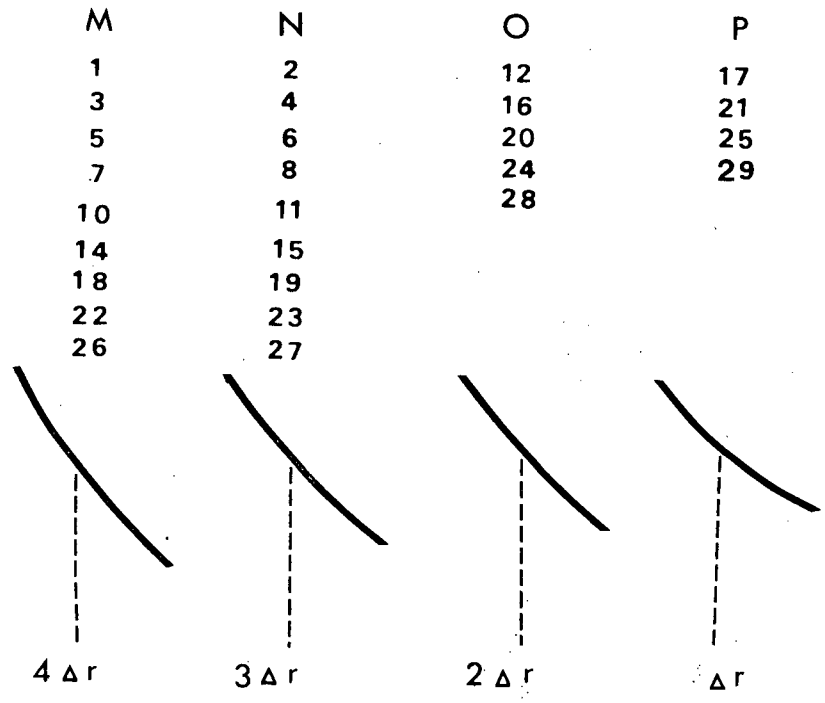

Figure 98. Schematic diagram of the section of the slag bath.

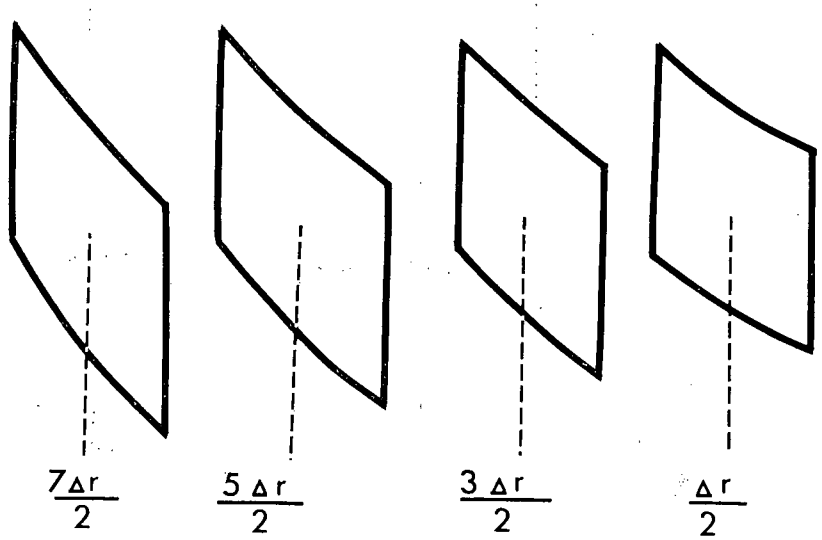

Figure 99. Schematic diagram of the section of the slag bath.

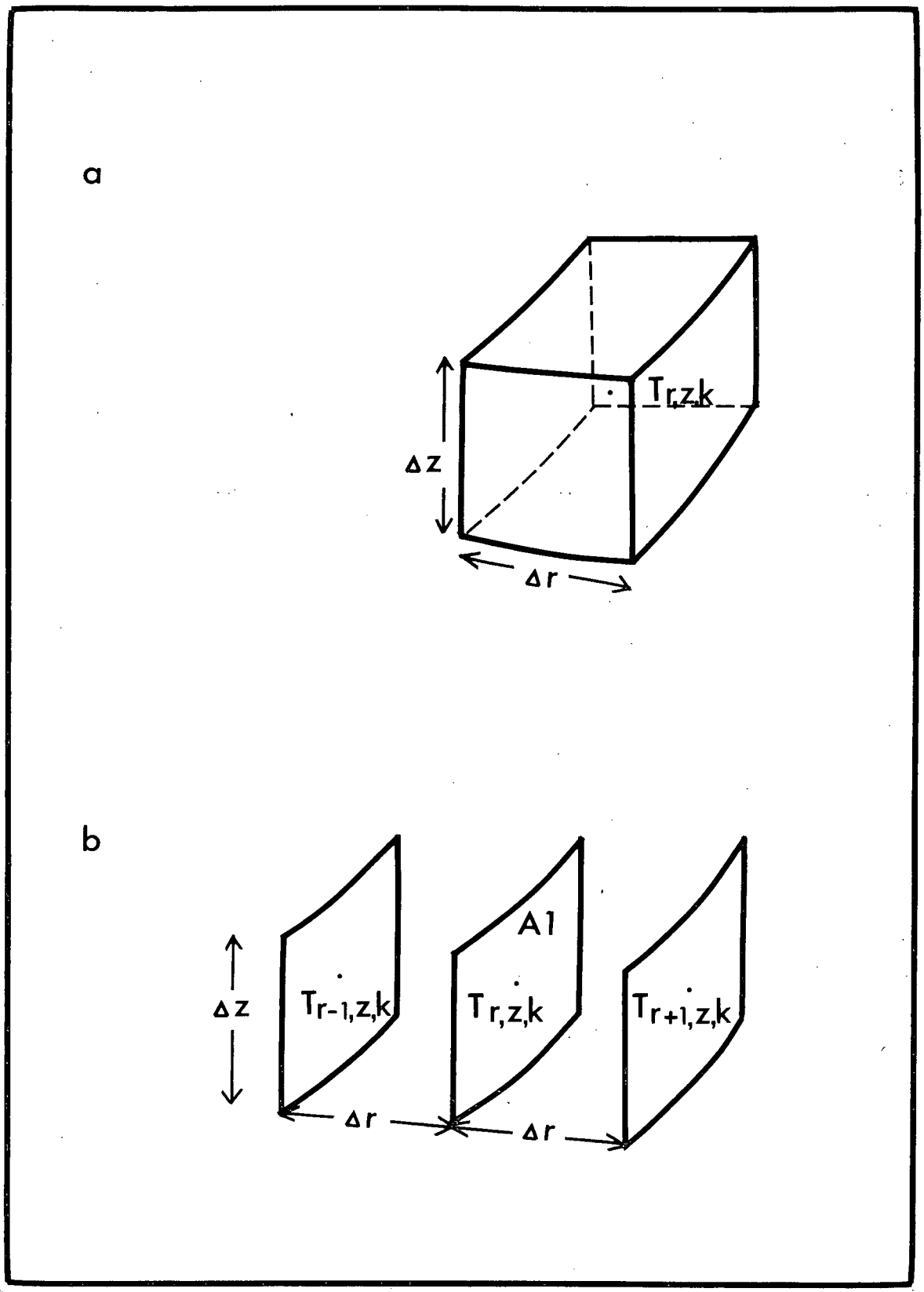

Figure 100. General element for case 1.

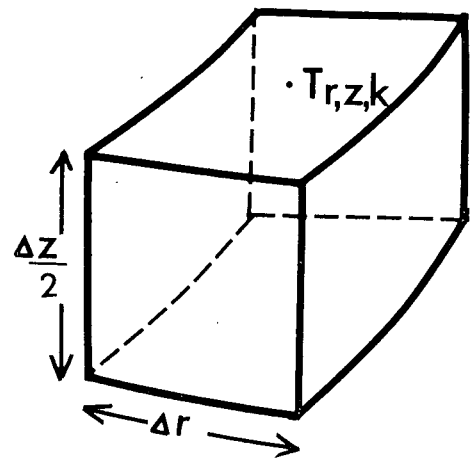

Figure 101. General element for case 2.

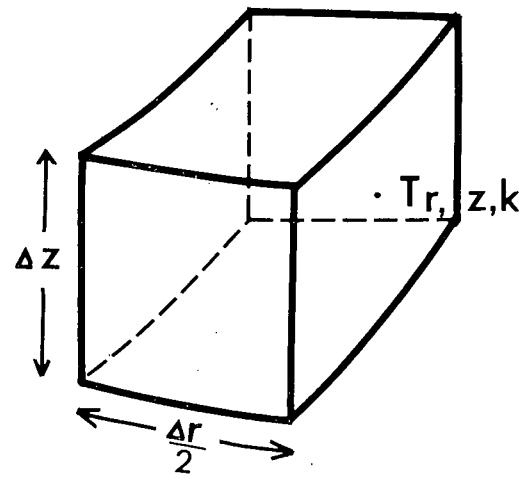

Figure 102. General element for case 3.

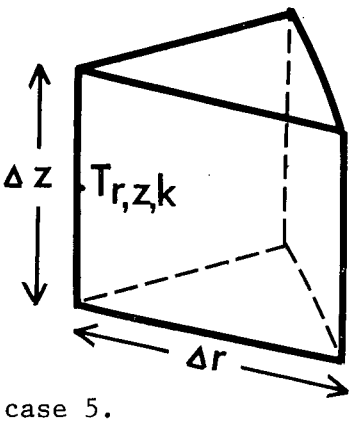

Figure 103. General element for case 5.

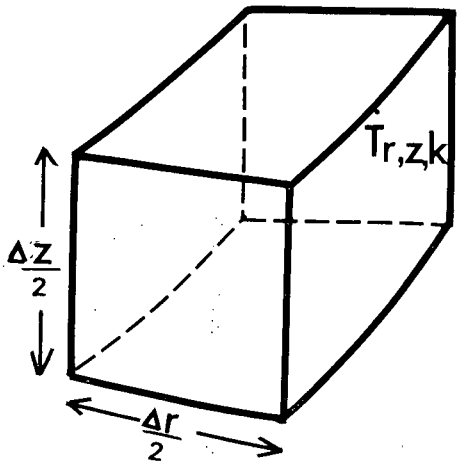

Figure 104. General element for case 6.

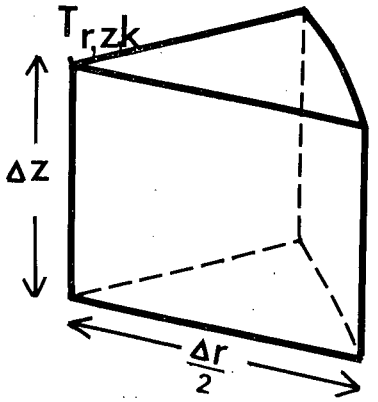

Figure 105. General element for case 8.